Study of the structural dynamics of phase transitions using time resolved electron and X-ray diffraction

Isabel Gonzalez Vallejo

université PARIS-SACLAY

UNIVERSITÉ PARIS SUD
Comprendre le monde, construire l'avenir

NNT : 2019SACLS496

Thèse de doctorat

Study of the structural dynamics of phase transitions using time resolved electron and X-ray diffraction

Thèse de doctorat de l'Université Paris-Saclay
préparée à l'Université Paris-Sud

École doctorale n° 564: Physique en Île-de-France (PIF)
Spécialité de doctorat: Physique

Thèse présentée et soutenue à Orsay, le 18 décembre 2019, par

MME. ISABEL GONZALEZ VALLEJO

Composition du Jury :

Arnaud Arbouet Directeur de recherche, CNRS (CEMES)	Président
Eric Collet Professeur, Université Rennes (IPR)	Rapporteur
Kai Rossnagel Professeur, University of Kiel (KNSIS)	Rapporteur
Claire Laulhé Maitre de conferences, Université Paris Sud (SOLEIL)	Examinatrice
Germán Sciaini Directeur de recherche, University of Waterloo (UeIL)	Examinateur
Jérôme Faure Directeur de recherche, CNRS (LOA)	Directeur de thèse
David Le Bolloc'h Directeur de recherche, CNRS (LPS)	Directeur de thèse
Vincent Jacques Chargé de Recherche, CNRS (LPS)	Invité

Acknowledgements

First of all, I would like to thank my supervisors for giving me the opportunity of working with them and for making me a part of this fascinating project. To Jérôme Faure at LOA for the trust he placed in me managing the experimental setup. Thank you for everything you have taught me (that was definitely much more than just ultrafast diffraction!) for your guidance, support and for all your patience during these three years. To my supervisors David Le Bolloc'h and Vincent Jacques at LPS for giving me the chance to participate in various experiments in different synchrotrons worldwide. Although beamtimes were sometimes long and difficult, you have never lost your enthusiasm and optimism. Whenever I see a diffraction peak now, I am unable not to think "c'est trop beau!!" despite the few pixels lighten on the detector or even a "c'est dingue!!" if its intensity goes beyond the expectation. Working with you has been a pleasure. Thanks to the three of you for sharing with me all your knowledge and experience.

I am immensely grateful to my thesis committee. Thanks to Claire Laulhé, Eric Collet, Kai Rossnagel, Arnaud Arbouet and Germán Sciaini for the exhaustive reading of my thesis, for the very interesting questions and discussions during the day of my defense, and for their suggestions to improve this manuscript.

Working in a collaboration between two labs gave me the opportunity to have an enriching scientific exchange and to get to know a lot of people who have helped me during my thesis. At LPS, Antonio Tejeda is probably the person to whom I owe the most. Thanks to him I came to France and started the master in Paris Saclay followed by my internship at LPS. It has been always a pleasure to discuss with you the experimental data and I am enormously grateful for your ideas, good advice and encouragement. I would also like to thanks Sylvain Ravy for his interest in my work, the valuable discussions on my results and the talks about topological defects. Thanks to Alexandra Mougin and Marco Aprili for accepting to be part of my "comité de suivi" each year.

Thanks to all the members from the LUCE/LUTECE group; Marino Marsi, Nicolás Moisan, Evangelos Papalazarou, Luc Ortega for their help during the beamtimes or simply for the nice day to day conversations during lunch or coffee breaks. Thanks to the fantastic group of PhD students at LPS; to Ewen Bellec for the sleepless nights we were working together during the beamtimes, Jonathan Caillaux, Abraham Campos Contreras and to my beloved "LPS girls" Lama, Rebeca, Min-I, Niloufar and Arlen for all the insightful conversations about practically everything, for your support and your friendship.

I would like to acknowledge and thank to all the local contacts in the beamtimes in which I have participated. Special thanks to Claire Lauhlé at CRISTAL for her support during and after the experiments and to Gerardina Carbone at Nanomax that nothing stopped her even if the entire synchrotron was shut down.

The experiments I performed with the UED setup would not have worked without the help of Geoffrey Gallé, the person who developed and taught me all the details of the experimental setup. Working with you was certainly the best start I could ever have had; it was not only instructive but quite fun as well! Without the proper samples my experiments at LOA would have

certainly not been possible neither. I thank our collaborators Max Lagally and Shelley Scott for providing us the high quality silicon nanomembranes. I acknowledge the help and collaboration of Brice Arnaud who performed theoretical simulations on silicon in order to better understand our experimental data. Special thanks to Florent Houdellier who welcomed me in Toulouse and measured the silicon samples by CBED, I appreciate not only his valuable experimental help but also the insightful discussions and the recommendations of further bibliography on dynamical theory of diffraction. Thanks to Giancarlo Rizza for the time he spent to teach me how to deal with the ultramicrotome and with the delicate diamond knifes without shaking a millimeter! Thanks for transferring me that sense of detail and accuracy from which I finally managed to get the perfect samples for our experiments. I thank Pierre-Eugene Coulon for the TEM measurements to verify the quality of the samples prepared with the ultramicrotome and for his help in preparing the samples for the CBED measurements.

Most of my time as a PhD student I was working at LOA and I had the great chance to be in contact with great researchers. Thanks to Guillaume Lambert for his perfect management of the salle argent and salle corail and for ensuring that our laser was always in perfect conditions. To Davide Boschetto for the stimulating discussions and interesting ideas for future experiments. Thanks to all the PhD students and postdocs that have been or are now part of LOA and contributed to the good environment in the lab; Mariusz, Domynikas, Lucas, Julius, Jean-Baptiste, Marie, Jaismeen, Carla, Elena, Raj, Ginevra, Siyi, Lena and the coolest office mates ever, Neïl and Aline. Special thanks to Aline for finding always some time to help me whenever I was struggling in salle argent. Thanks to Domenico Alj who has been always a great help whenever I needed a piece, tool or advice in the lab. Por supuesto, doy las gracias a mis españoles favoritos en LOA Hugo y Pablo con los que siempre he podido contar para una pausa café en español y desconectar un poquito.

Bien évidemment, l'équipes des secrétaires du LPS, Véronique Thieulart et du LOA, Patricia Touiller, Sandrine Tricaud, Carole Gratpanche et Catherine Buljore ne peuvent pas être absentes de ces remerciements. Sans vous, la bureaucratie française, les transactions d'achat ou les commandes d'azote liquide n'auraient pas été aussi faciles! Je suis également très reconnaissant pour toutes les pièces réalisées pour notre manip et pour toute l'aide de l'équipe de l'atelier mécanique; Jean-Lou Charles, Bernard Allali et Florian Oper. Je tiens également à remercier l'équipe de soutien Mouhcine Adraoui, Thomas Lavergne et Maxence Le Sourd.

A mis queridos Fernanda y Andrea, desde luego los mejores vecinos, amigos y familia que jamás hubiese podido imaginar encontrar al llegar a Francia. Vou sentir muita saudade de vocês em Berlim!

Gracias a mi familia, mis padres y mis hermanos por apoyarme cuando me embarqué en este viaje, por ser fuente de inspiración, alegrías y continua admiración.

And of course, thanks to Peter. Thank you for your unconditional support and for being always by my side. With your encouragement and love nothing is impossible!

Contents

Chapter 1

Introduction

Contents

Humankind has created the abstract concept of time as a way of tracking and ordering events into past, present and future. Therefore, the notion of time is deeply rooted in our understanding of the natural world. In an attempt to explain what *time* is, we could define it as a measure of change, or more precisely as the period needed for anything to develop from a state A to a state B. This gives rise to the obvious question: what is then the shortest period of time we can measure? Is there a limit at which changes start to become significant? From a physical point of view, this challenging question found an answer in quantum mechanics and the theory of relativity. The minimum imaginable interval of time is given by the Planck time [1], which sets an order of magnitude of the duration of the shortest changes in nature. It is given by three physical constants, the Planck constant $\hbar$, the gravitational constant G and the speed of light c:

$$t_P = \sqrt{\frac{\hbar G}{c^5}} = 5.39 \cdot 10^{-44} s \tag{1.1}$$

This value is, of course, far away from what we could ever be able to perceive or even detect. To the human eye, the window of time to perceive dynamical processes in nature is limited to a fraction of a second, somewhere around 50 ms. Within this temporal resolution we are able to detect and describe "by eye", for example, the wing motion of large birds. Faster wing beats, such as those of hummingbirds (around 80 beats per second), are out of reach and so we need to make use of fast shutter cameras to be able to fully describe the wing motion during flight.

Another example for which a fast detection can be useful is shown in a beautiful experiment performed by Xu *et al.* with a high-speed video camera. Figure 1.1 shows a series of snapshots of the fall of a liquid drop collected at 47000 fps. These short time scales permit to describe the drop geometry and how the impact of the drop against the flat surface is influenced by external factors, such as the environmental pressure [2].

The drop arrives in all cases with the same spherical geometry to the flat substrate, which finally covers its surface after about 2.5 ms. The largest changes happen between a third and a

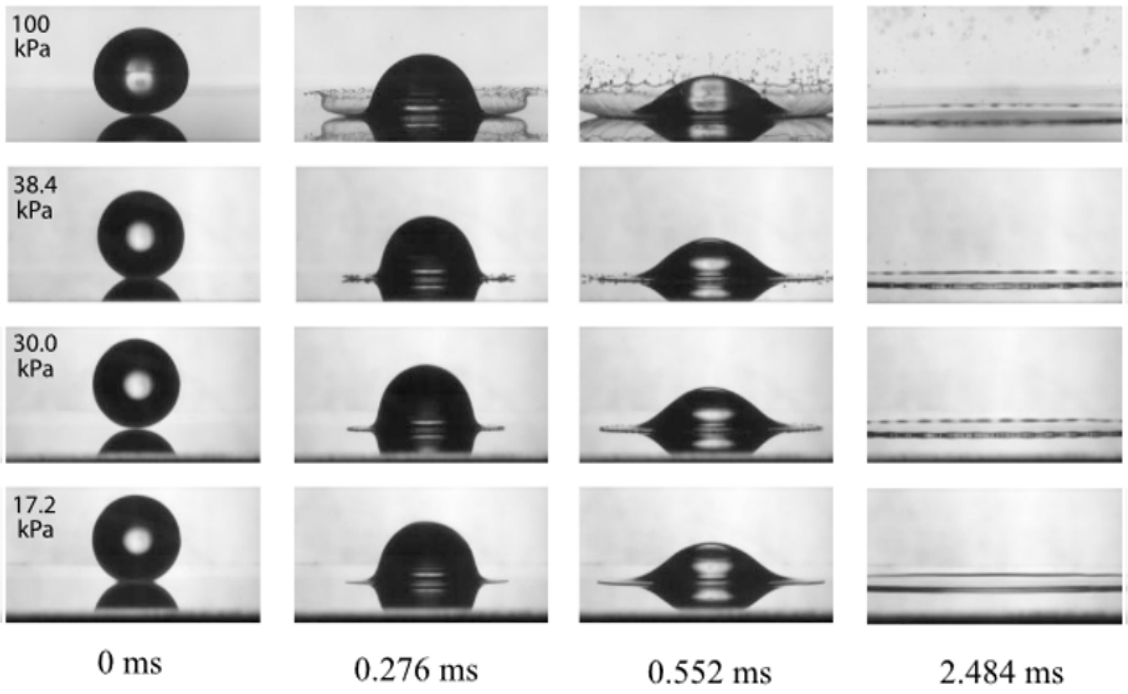

Figure 1.1: Time lapse of a falling drop on a substrate at different environmental pressures collected at 47000 fps [2].

half of a millisecond, shorter than the blink of an eye. The fast detection of this simple process allows to precisely measure the threshold pressure at which the drop splashes after the impact, to P = 38.4 kPa. This discovery, as well as being interesting for its own sake, might also find applications in industrial processes such as ink-jet coating.

Material scientists, on their side, are mostly interested in the atomic dynamics in matter, which are by far much faster processes. For instance, the atomic motion in crystals has typical time scales given by the speed of sound in solids, on the order of 1000 m/s, with atomic length scales of few Ångstroms. According to these numbers, the temporal resolution required to detect the dynamical processes should be on the order of 100 fs, i.e., 10^{-13} seconds.

The development of femtosecond laser pulses in the 1980s has enabled scientists to access these time scales to explore the ultrafast dynamics of the structure of matter. First indirectly from time resolved spectroscopic techniques, and then followed by direct structural techniques such as diffraction. In order to detect the atomic motion from diffracted beams, sufficiently short incident wavelengths are necessary, which are only achievable either from electron ($\lambda \sim$ pm) or hard X-ray ($\lambda \sim$ Å) sources. The first electron diffraction pattern generated from a pulsed electron source was reported by Mourou and Williamson in 1982 [3] followed one year later by the first stroboscopic electron diffraction experiment performed by Ischenko *et al.* in a gaseous sample [4]. These works set the beginning of the *molecular movie* era. The time resolved diffraction scheme permits the study of out-of-equilibrium photoinduced processes such as non-

thermal melting, structural phase transitions, coherent atomic vibrations or chemical reactions. In the past decades, tremendous progress have been achieved thanks to the pioneering works of A. Zewail, who was awarded the Nobel prize in chemistry in 1999 [5, 6]. An important work which pushed the limits of temporal resolution below picosecond was performed by R. J. D. Miller and co-workers with further progress in the development of ultrafast electron sources [7, 8]. In the X-ray domain, the development of table-top X-ray plasma sources [9] allowed temporal resolutions of few hundreds of femtoseconds. The first experiments monitoring the dynamics of solids at these time scales was reported at the Laboratoire d'Optique Apliquée (LOA) [10, 11]. On the other hand, large scale facilities such as synchrotrons in slicing mode [12, 13] or X-ray free electron lasers (FELs) are the other type of sources able to achieve the subpicosecond time resolution [14].

1.1 The pump-probe technique and temporal scales in condensed matter

The study of structural dynamics relies on pump-probe diffraction experiments (also known as time resolved diffraction techniques). In a first step, a laser beam known as the *pump*, impinges on the sample and triggers a cascade of photoinduced processes. A second diffracting beam of either electrons or X-rays, known as the *probe*, takes a snapshot of the diffraction pattern at different times after the pump initiation (a frame of the movie). A comparison between snapshots allows to draw the followed pathway until full relaxation.

Generally, the arrival of the optical pump prompts electrons to high energy bands, resulting in an out-of-equilibrium electron distribution. Within the first tens to hundred femtoseconds, the electron population thermalizes via electron-electron scattering, leading to a very high electron temperature. This process is followed by electron-phonon scattering in hundreds of femtoseconds and phonon-phonon scattering in picosecond time scales, eventually leading to a rise of the lattice temperature. The increase of temperature in the lattice is finally released by heat diffusion, a longer process that takes from nanoseconds to microseconds, depending on the sample geometry. This avalanche of events is well understood within the two temperature model, presented in this thesis in section 2.2.1. When the energy of the pump is low enough, the structural dynamics of the system is usually reversible. In this case, a possible observation following photoexcitation is coherent atomic vibrations such as optical phonons. A good example of this mechanism has been measured in bismuth by time resolved X-ray diffraction [15, 16] in which the optical pump activates coherent atomic motion belonging to the A_{1g} optical phonon. Another possible response after excitation is photoinduced stress at high incident energies resulting in lattice strain waves propagating through the sample within tens of picoseconds [17, 18]. In a wider range of time scales, we might find structural phase transitions such as the monoclinic to rutile crystal structures observed in vanadium dioxide in few picoseconds [19, 20, 21], or the charge density wave (CDW) phase transition in blue bronze

or transition-metal dichalcogenides materials, occurring in several hundreds of femtoseconds [22, 23, 24]. The time scales of these processes may vary since they usually depend on the properties of the material under study and the excitation fluence. Irreversible processes such as thermal and non-thermal melting, on the other hand, have been reported in organic materials, indium antimonide, bismuth, silicon or in gold at high incident fluence with time scales from few hundreds of femtoseconds to picoseconds [10, 11, 25, 26, 27, 28]. On longer time scales, as already mentioned, we can find heat diffusion as the lattice cools down. This process greatly depends on the sample geometry. In the case of nanomembranes, for example, the characteristic time scale of heat diffusion can exceed a few microseconds [29]. Figure 1.2 presents a schematic time arrow with the time scales corresponding to the different photoexcited processes.

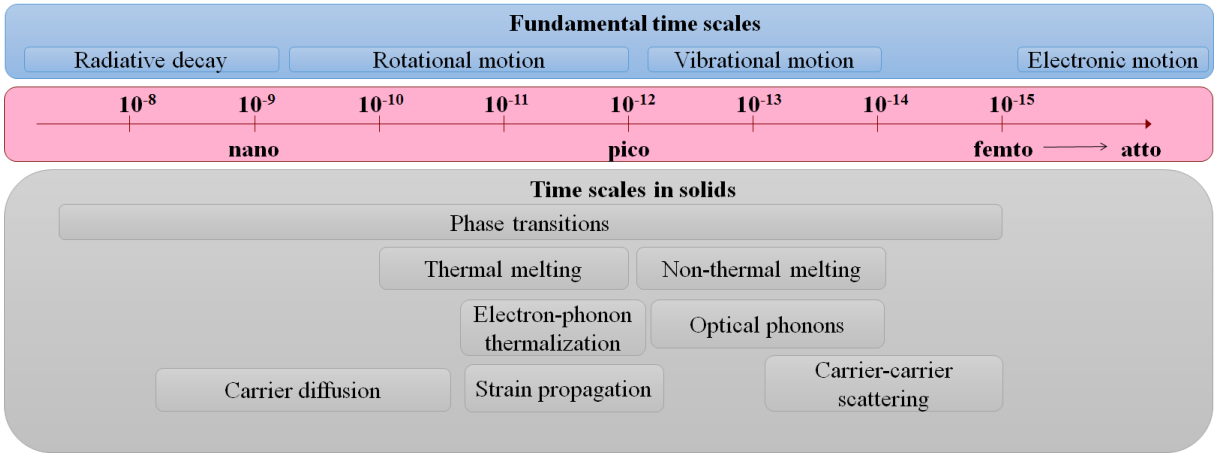

Figure 1.2: Temporal scales of different photoinduced processes.

1.2 Context and motivation of the thesis

The understanding of the physical mechanisms behind photoinduced structural phase transitions has become a central question in the ultrafast community. Systems displaying strong cooperation between the different degrees of freedom (charge, spin, orbitals and lattice) are of particular interest. The main questions regarding this type of phase transitions can be listed as follows:

What is the main driving force in a phase transition?

How strong is the coupling between the different degrees of freedom?

What are the different time scales associated to each degree of freedom and their coupling?

Does the understanding of the dynamics help us to better comprehend the basic physics of the phase transition?

Time resolved experiments, with their capability to follow the dynamics within the relevant time scales in solids, are the ideal techniques to shed light on these questions. A good example of a cooperative structural phase transition is found in charge density wave (CDW) systems. CDWs are stable macroscopic quantum states in low dimensional materials, that can only occur by the coupling between electronic and lattice subsystems.

When a metallic system undergoes a transition to the CDW phase, a gap opening emerges in its electronic structure accompanied by a lattice distortion. The latter results in the emergence of new spots in diffraction, known as satellite reflections. Their intensity is directly linked to the order parameter of the phase transition.

Optical excitation can result in the suppression of the CDW phase, as can be inferred from the satellite intensity decrease. Various relaxation pathways in this transition have been proposed. In some cases, these pathways have been attributed to mechanisms that are different from those observed at thermal equilibrium [30]. A good evidence of the increasing interest in these systems is reflected in the large amount of research works in the transition-metal dichalcogenides [23, 24, 31, 32, 33, 34, 35]. These compounds present high intensity satellite reflections that, from an experimental point of view, have a great advantage in terms of detection. One of the "drawbacks" of the transition-metal dichalcogenoides is their complex phase diagrams where several CDW phases might be present, depending on the elements that from compound. **Therefore, studies on materials with relatively simpler phase diagrams might give a more straightforward picture of the photoinduced phase transition into the metallic state.** Possible candidates with less complex phase diagrams are blue bronzes ($K_{0.3}MoO_3$) and Rare-Earth Tritelluride compounds (RTe_3).

This thesis is based on a collaboration between LOA and Laboratoire de Physique des Solides (LPS). Both laboratories are widely recognized for their expertise in ultrafast sources and solid state physics, respectively. The development of the first compact ultrafast electron diffraction (UED) setup in France at LOA opened the possibility to study the out-of-equilibrium structural dynamics of a well known topic at LPS: the CDW phase transition of the RTe_3 compounds. At the starting time of the work presented here (mid 2016), the structural dynamics of the photoinduced phase transition in RTe_3 compounds was poorly known, the collaboration between LOA and LPS thus provided the perfect conditions to study this matter.

The scope of this thesis was threefold:

First of all, we tested the capabilities of the recently developed UED setup at LOA. To do so, we performed a series of pump-probe experiments on a perfect silicon single crystal nanomembrane and discovered the large influence of multiple scattering effects on the time resolved diffracted intensities, an aspect that was pointed out before by other research groups but never studied in detail [29, 33].

The second and central aim of this thesis is focused on the study of the photoinduced phase

transition of $GdTe_3$ by UED. I thus addressed several questions:

- What are the main differences between the thermal equilibrium and photoinduced phase transitions?
- On which time scales does lattice dynamics take place?
- What is the response of the system to different excitation fluences?
- How does the initial temperature of the lattice influence the dynamics of the CDW?

Here, several challenges had to be faced. In particular, the preparation of suitable samples for the UED setup and the means to detect the low intensity satellite reflections. Another challenging aspect of the work presented here was its very timeliness, as a large number of high quality data was published on the topic as I was performing these experiments [36, 37, 38, 39, 40] (some of them still on *arXiv*).

The last aim of the thesis is to understand the dynamics of the structural phase transition on Nb_3Sn, a material that displays a *martensitic* phase transition driven by lattice distortive displacements. In this case, we centered our attention on the main differences between the structural transition at thermal equilibrium and after photoexcitation with temporal resolutions of several picoseconds. The experiments were performed in the CRISTAL beamline at SOLEIL synchrotron.

1.3 Outline

The thesis is divided in six chapters:

- Chapter two serves as an introduction to the theory of diffraction in the two existing formulations: kinematical and dynamical theories of diffraction. A brief comparison between X-ray and electron diffraction is given and then followed by the signatures of different photoinduced processes in a diffraction pattern.
- In chapter three, I introduce the experimental setups used in the development of my thesis. Firstly, I describe the ultrafast electron diffraction DC gun developed at LOA. The second part is devoted to the description of the CRISTAL beamline at SOLEIL Synchrotron where I performed two experiments with the LUTECE group from LPS.
- In chapter four, I present the results obtained in the UED setup on a high-quality silicon crystal nanomembrane from which we demonstrated that dynamical diffraction effects play an important role in time resolved electron diffraction.
- In chapter five, I show the time resolved electron diffraction results from nanomembranes of $GdTe_3$. Here, I shall give an analysis of the dynamics of the CDW at different incident

fluences and explore the implications of different initial sample temperatures, as a way of bringing more light to the conflicting interpretations given in the literature.

- Chapter six presents the results from time resolved X-ray diffraction experiments in SOLEIL in the structural phase transition in Nb_3Sn. Here, I compare the structural phase transition at thermal equilibrium with the results from the photoexcited phase transition.
- To conclude, the main results of this work are summarized and followed by a discussion of its limitations and future perspectives.

Chapter 2

Introduction to diffraction theory

Contents

The discovery of X-rays by Röntgen in 1895 led to scientific breakthroughs in several fields, from medicine to solid state physics and crystallography. In the case of the latter and thanks to the works of Laue, Ewald and specially W. L. and W. H. Bragg, with the use of X-ray diffraction it became possible to identify the structures of inorganic and organic crystals. Probably, one of the most famous milestones of X-ray diffraction was the discovery of the helical structure of DNA [41]. Furthermore, diffraction served as a support for the early theories of wave-particle duality of light, which was demonstrated as well with electrons as confirmed independently by G. Thomson and C. Davidson [42] corroborating the predictions from de Broglie.

This chapter serves as a brief introduction to basic notions of crystalline structures and diffraction. The description of kinematical and dynamical theory of diffraction is introduced along with the temperature effects in the diffraction patterns, followed by a description of the repercussions of the photoexcitation in the lattice and the diffraction pattern. Main bibliography covering in depth X-ray diffraction and crystalline structures can be found in [43, 44]. The lecture notes from S. Ravy [45] are particularly useful for those topics[1]. Electron diffraction and dynamical theory of diffraction are well described in [46] and especially in [47]. A good introduction of time resolved diffraction can be found in [48].

[1] Indeed, a good reason to start learning french.

2.1 Crystal structures and diffraction theories

We can imagine a solid crystal as an ensemble of ordered atoms, ions or molecules periodically arranged in the three dimensions of space. The smallest cell that can be used to create the entire crystal by translations is known as the *unit cell*. The crystal structure can be classified into 14 lattice types known as the *Bravais lattices*. Figure 2.1 shows the scheme of a Body Centered Cubic (BCC) crystal, with the atomic positions in the unit cell located at $\mathbf{r_1} = (0,0,0)$ and $\mathbf{r_2} = (1/2, 1/2, 1/2)$:

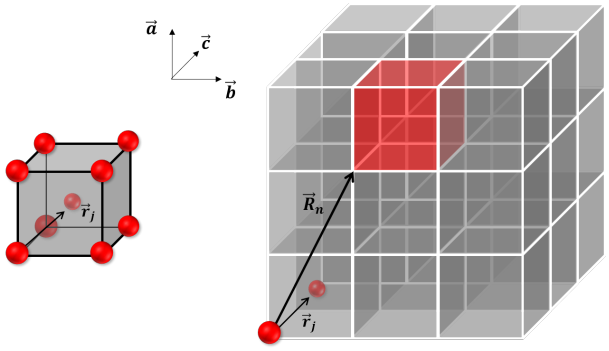

Figure 2.1: Schematic of a BCC crystal. The atomic positions in the unit cell are denoted by the $\vec{r}_j$ and the position of each unit cell is given by $\vec{R}$.

The atomic positions within the unit cell are given by:

$$r_j = x_j\mathbf{a} + y_j\mathbf{b} + z_j\mathbf{c}$$

with $\mathbf{a},\mathbf{b},\mathbf{c}$ the unitary cell vectors and j the type of atom. The position of each unit cell in the ensemble of the crystal is defined by :

$$R_n = u\mathbf{a} + v\mathbf{b} + w\mathbf{c}$$

with u,v,w integers.

In 1912, W. H. and W. L. Bragg (father and son) developed their famous law of diffraction; a simple, yet powerful geometrical approach widely used until now. While studying the interaction of a Zincblende sample and X-rays [49], they realized that certain reflections appeared in their detection screen and seemed to move when the crystal sample was rotated. They imagined the crystalline structure as a set of parallel planes with interplanar distances $d \geq \lambda$, which could reflect the X-rays as a mirror reflects light [50]. The appearance of such spots would only be possible if the reflected waves were interfering constructively, i.e., when the path difference between two set of waves was an integer of the incident wavelength λ (see figure 2.2):

$$n\lambda = 2d\,sin\,\theta_B \tag{2.1}$$

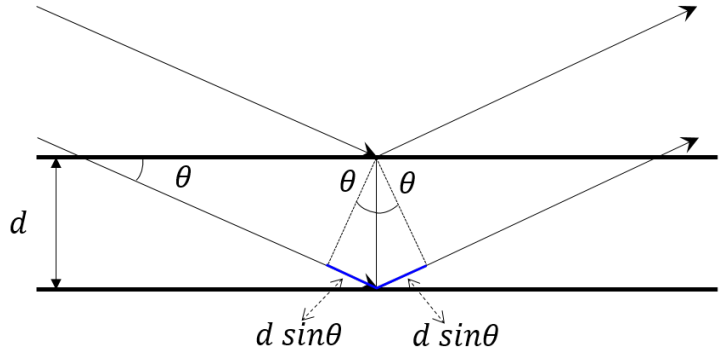

Figure 2.2: Schematic representation of Bragg's law. The path difference between two incident wave fronts of equal phase is given by the interplanar distance and the angle of incidence.

with n an integer, d the distance between the reflecting planes and θ_B the scattering angle (Bragg angle).

The resulting diffracted wave is what we term nowadays as a Bragg reflection. The position of such peaks in the detection screen corresponds to the interplanar distances in real space known as Miller planes. Real and reciprocal spaces in a crystal are related from their lattice parameters by:

$$\mathbf{a}^* = 2\pi \frac{\mathbf{b}\times\mathbf{c}}{\mathbf{a}\cdot(\mathbf{b}\times\mathbf{c})} \qquad \mathbf{b}^* = 2\pi \frac{\mathbf{c}\times\mathbf{a}}{\mathbf{a}\cdot(\mathbf{b}\times\mathbf{c})} \qquad \mathbf{c}^* = 2\pi \frac{\mathbf{a}\times\mathbf{b}}{\mathbf{a}\cdot(\mathbf{b}\times\mathbf{c})}$$

where $(\mathbf{a}^*,\mathbf{b}^*,\mathbf{c}^*)$ are the reciprocal unitary vectors, which fulfill the following relations:

$$\begin{aligned} &\mathbf{a}^*\cdot\mathbf{a} = \mathbf{b}^*\cdot\mathbf{b} = \mathbf{c}^*\cdot\mathbf{c} = 2\pi \\ &\mathbf{a}^*\cdot\mathbf{b} = \mathbf{a}^*\cdot\mathbf{c} = \mathbf{b}^*\cdot\mathbf{a} = \mathbf{b}^*\cdot\mathbf{c} = \mathbf{c}^*\cdot\mathbf{a} = \mathbf{c}^*\cdot\mathbf{b} = 0 \end{aligned} \tag{2.2}$$

In this way, we can define a reciprocal lattice vector by:

$$\mathbf{g}_{hkl} = h\,\mathbf{a}^* + k\,\mathbf{b}^* + l\,\mathbf{c}^*$$

which satisfies:

$$|g_{hkl}| = \frac{2\pi}{d_{hkl}}$$

with units of inverse length (usually in $\mathring{A}^{-1}$). Each family of planes in real space with an interplanar distance d is associated to the shortest reciprocal vector perpendicular to these planes. Figure 2.3 shows a scheme of the interplanar distances in real space (left) and the corresponding reciprocal space (right). With the relations given in 2.2, it is possible to demonstrate that a reciprocal lattice vector satisfies the condition $\mathbf{g}_{hkl}\cdot\mathbf{R}_{uvw} = 2\pi\,n$ when $n = (hu + kv + lw)$ integer.

Another equivalent geometrical description of the diffraction process was described by P. Ewald. Figure 2.4 depicts the scheme of the Ewald construction in 2D; consider the center of real space located at the point of incidence in the sample, and draw a sphere of radius $2\pi/\lambda$, i.e., the incident wavevector. We can find the center of reciprocal space lying on the sphere at

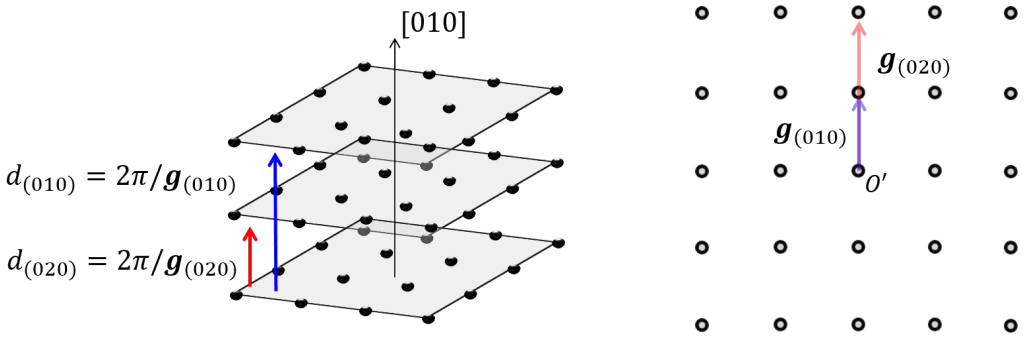

Figure 2.3: Schematic representation of the interplanar distances d along the crystallographic [010] *direction and the related scattering wavevectors* **g** *in reciprocal space.*

$\theta = 0$. The condition of constructive interference for the scattered wavesvector from the crystal takes place when the difference between incident and reflected wavevectors coincides with a reciprocal lattice vector (also known as the Laue condition):

$$\mathbf{\Delta k} = \mathbf{k}' - \mathbf{k_i} = \mathbf{g}_{hkl}$$

Schematically, when this condition is fulfilled **g** lies on the surface of the Ewald sphere, so

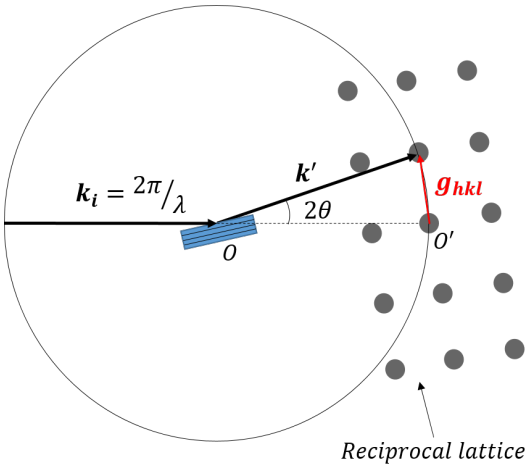

Figure 2.4: Schematic of the Ewald sphere with the radius given by the incident wavevector. The origin of real space is located at the point of incidence in the sample (blue rectangle) and O' *denotes the center of reciprocal space.*

that only those wavevectors satisfying $|\mathbf{g}_{hkl}| < 4\pi/\lambda$ are accessible in diffraction. This geometrical approach explains one of the main differences between electron and X-ray diffraction; in contrast to X-ray diffraction, high energy electrons with several keV have wavelengths of few picometers, leading to a smaller curvature of the Ewald sphere and thus to a larger number of spots intersecting its surface.

Bragg's law and the Ewald construction can only offer geometrical information on the position of the diffracted peaks but they do not provide a quantitative information of their intensities. When the interaction between the incoming electromagnetic wave and the crystal potential is weak, the probability of the incident beam to suffer two consecutive scattering events is really small. In this case, the kinematical theory of diffraction provides a suitable description of the process. The resulting diffracted intensities in this framework are much weaker than the intensity of the incident wave, as shown schematically in figure 2.5.

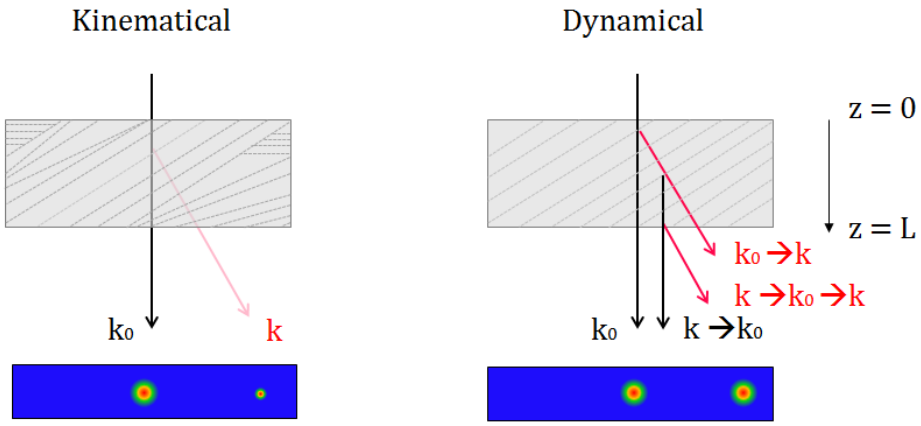

Figure 2.5: Schematic of kinematically (left) and dynamically (right) scattered intensity. In the kinematical case, the sample presents some domains, reducing the scattered intensity, and thus a weak intensity is diffracted. In the dynamical case the sample is a perfect single crystal, the diffracted beams are re-scattered into the incident beam multiple times through the sample thickness ($z = L$), resulting in a strong diffracted peak.

The theoretical description of diffraction departs from this formalism when the interactions between the incident wave and the crystal potential are strong. This is the case when the crystal potential is set by a perfect crystal. In the case of electrons, the incident beam is strongly affected by the Coulomb field of the atoms in the crystal. Therefore, the resulting diffracted intensity suffers multiple scattering events while traversing the thickness of the crystal gaining intensity as it propagates. As a result, it becomes comparable or even stronger than the incident intensity.

Figure 2.5 shows a schematic of both diffraction processes along with the expected diffracted intensities. Note that kinematical (dynamical) theory is not inherent of X-ray (electron) diffraction. Diffracted intensities from high quality single crystals will always be described by dynamical theory of diffraction. On the other hand, diffracted beams from samples with low crystal quality or with small thicknesses can be appropriately described within the kinematical framework in both techniques. In the following sections, a description of both theories is given.

2.1.1 Kinematical theory of diffraction

The scattered intensities predicted in the kinematical framework depend on two factors, namely the structure factor $F(\mathbf{\Delta k})$ which depends on the atomic positions in a single unit cell and their scattering power, and the shape factor $S(\mathbf{\Delta k})$ which depends on the external shape of the crystal, and thus on the number of probed unit cells:

$$S(\mathbf{\Delta k}) = \sum_{n}^{N} e^{-i\mathbf{\Delta k}\cdot\mathbf{R_n}} \qquad (shape\ factor) \tag{2.3}$$

$$F(\mathbf{\Delta k}) = \sum_{\mathbf{j}}^{n} f_{at}(\mathbf{\Delta k}) e^{-i\mathbf{\Delta k}\cdot\mathbf{r_j}} \qquad (structure\ factor) \tag{2.4}$$

Supposing a crystal formed by $N \times N \times N$ unit cells, the scattering amplitude from the shape factor is given by:

$$S(\mathbf{\Delta k}) = \sum_{u=1}^{N}\sum_{v=1}^{N}\sum_{w=1}^{N} e^{-i\mathbf{\Delta k}\cdot\mathbf{R_n}} = \sum_{u=1}^{N} e^{-i2\pi\Delta k_x u} \sum_{v=1}^{N} e^{-i2\pi\Delta k_y v} \sum_{w=1}^{N} e^{-i2\pi\Delta k_z w} \tag{2.5}$$

where every term is a geometric sum of the form $\sum_{u=1}^{N} e^{-i2\pi\Delta k_x u} = e^{-i\pi(N+1)\Delta k_x} \frac{sin(\pi N\Delta k_x)}{sin(\pi\Delta k_x)}$ so that the intensity becomes:

$$I(\mathbf{\Delta k}) = F\,F^*(\mathbf{\Delta k})\,S\,S^*(\mathbf{\Delta k}) = F(\mathbf{\Delta k})^2 \frac{sin^2(\pi N\Delta k_x)}{sin^2(\pi\Delta k_x)} \frac{sin^2(\pi N\Delta k_y)}{sin^2(\pi\Delta k_y)} \frac{sin^2(\pi N\Delta k_z)}{sin^2(\pi\Delta k_z)} \tag{2.6}$$

Then, the diffracted peaks display a shape of the form $sin^2(Nx)/sin^2(x)$ as depicted by the blue line in figure 2.6 with their width determined by the number of probed cells N and the intensity by the structure factor, which is given by:

$$F(\mathbf{\Delta k}) = \sum_{j} f_j e^{-i\mathbf{\Delta k}\cdot\mathbf{r_j}} = \sum_{j} f_j e^{-2i\pi(\Delta k_x a_j + \Delta k_y b_j + \Delta k_z c_j)} \tag{2.7}$$

where f_j is the scattering form factor of an atom j and r_j denotes the atomic position in the unit cell.

The structure factor gives information on the intensities and possible extinctions of the Bragg peaks. For instance, in the case of a BCC lattice, as the one shown in figure 2.1, the atomic positions can be fully described by the translation of two vectors: (0,0,0) and (½, ½, ½). The structure factor for any (hkl) plane becomes thus:

$$F_{hkl}^{BCC} = \sum_{j} f_j \left(1 + e^{-i\pi(h+k+l)}\right)$$

We will find a maximum at those reflections satisfying $(h+k+l) = 2n$, whereas it will be extincted for $(h+k+l) = n$.

Finally, the form factor f_j represents the scattering power of the atom. It depends on the number of electrons of the atom (Z), the scattering angle and the type of electromagnetic interaction, which in the case of X-ray diffraction is defined by:

$$f_{x,j}(\mathbf{\Delta k}) = \int \rho_{e,j}(\mathbf{r}) e^{-i\mathbf{\Delta k}\cdot\mathbf{r}} d^3r = \begin{cases} Z, & \mathbf{\Delta k} \to 0 \\ 0, & \mathbf{\Delta k} \to \infty \end{cases} \tag{2.8}$$

where $\rho_{e,j}$ is the atomic electron density. The analytical approximation of the form factor f_x is given by [44]:

$$f_{x,j}(\mathbf{\Delta k}) = \sum_i^4 a_{i,j} e^{-b_{i,j}\left(\frac{\mathbf{\Delta k}}{4\pi}\right)^2} + c \tag{2.9}$$

where a_i, b_i and c are the resulting constants obtained from theoretical calculations, tabulated in the *International tables of crystallography* [51]. The scattering form factor for electron diffraction, can be converted from the X-ray form factor by the Mott formula [47]:

$$f_{el}(\mathbf{\Delta k}) = \frac{2m_e^2}{\hbar^2}\gamma\frac{1}{\Delta k^2}(Z - f_x(\mathbf{\Delta k})) \tag{2.10}$$

with γ the relativistic mass correction factor. Figure 2.6 shows the resulting diffracted intensity of a crystal with the different factors intervening in the scattering process.

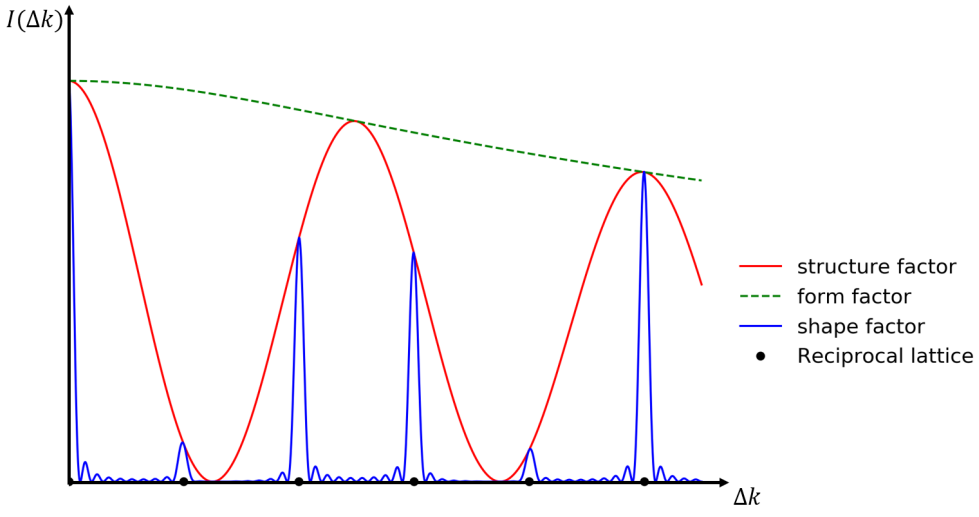

Figure 2.6: Total diffracted intensity (blue) of a crystal with N = 10 unit cells.

The Debye-Waller effect and Thermal Diffuse Scattering

Up to now we have described the diffraction from a crystal by considering a static crystal lattice. In reality, atoms are never fixed at a given position, but instead they vibrate as a consequence of thermal fluctuations. This even applies at $T = 0\,\mathrm{K}$ due to the quantum uncertainty principle, known as the *zero-point fluctuations*. The effect of such vibrations on the intensities of the Bragg peaks can be developed by considering the position of a n^{th} atom as the sum of a time averaged position R_n and a fluctuating term in time: $R(t) = R_n + \mathbf{u}_n(t)$ [2]. The more the temperature of the lattice increases, the larger the thermal fluctuations, affecting then the intensity of the diffracted peaks. Considering the fluctuating term, the structure factor becomes:

$$F(\mathbf{\Delta k}, t) = \sum_n f(\mathbf{\Delta k}) e^{-i\mathbf{\Delta k}\cdot(\mathbf{R}_n + \mathbf{u}_n(t))}$$

So that the intensity of the diffracted beam reads:

$$\begin{aligned} I(\mathbf{\Delta k}) &= \left\langle F(\mathbf{\Delta k}, \mathbf{t}) F(\mathbf{\Delta k}, \mathbf{t})^* \right\rangle = \left\langle \sum_n f(\mathbf{\Delta k}) e^{-i\mathbf{\Delta k}\cdot(\mathbf{R}_n + \mathbf{u}_n)} \sum_m f^*(\mathbf{\Delta k}) e^{i\mathbf{\Delta k}\cdot(\mathbf{R}_m + \mathbf{u}_m)} \right\rangle \\ &= \sum_n \sum_m f(\mathbf{\Delta k}) f^*(\mathbf{\Delta k}) e^{i\mathbf{\Delta k}\cdot(\mathbf{R}_m - \mathbf{R}_n)} \left\langle e^{i\mathbf{\Delta k}\cdot(\mathbf{u}_{\Delta k_m} - \mathbf{u}_{\Delta k_n})} \right\rangle \end{aligned} \tag{2.11}$$

where $\langle \ldots \rangle$ denotes temporal average and $\mathbf{u}_n = \mathbf{u}_{\Delta k_n}$ is considered for convenience, with the latter defined as a component of the displacement parallel to $\mathbf{\Delta k}$. By considering small displacements with equal positive and negative probabilities, it is possible to approximate the last term of the above equation with the Baker-Hausdorff theorem[3]:

$$\langle e^{ix} \rangle = e^{-1/2\langle x^2 \rangle}$$

whence:

$$I(\mathbf{\Delta k}) = \sum_n \sum_m f(\mathbf{\Delta k}) f^*(\mathbf{\Delta k})\, e^{i\mathbf{\Delta k}\cdot(\mathbf{R}_m - \mathbf{R}_n)}\, e^{-1/2\Delta k^2 \langle u^2_{\Delta k_m} \rangle}\, e^{-1/2\Delta k^2 \langle u^2_{\Delta k_n} \rangle}\, e^{\Delta k^2 \langle u_{\Delta k_n} u_{\Delta k_m} \rangle} \tag{2.12}$$

From translation geometry we can rewrite $\langle u^2_{\Delta k_n} \rangle = \langle u^2_{\Delta k_m} \rangle = \langle u^2_{\Delta k} \rangle$, and by defining $M = (\Delta k)^2 \langle u^2_{\Delta k} \rangle / 2$ it leads to:

$$\begin{aligned} I(\mathbf{\Delta k}) = &\sum_n \sum_m f(\mathbf{\Delta k})\, e^{i\mathbf{\Delta k}\cdot\mathbf{R}_m} e^{-M}\, f^*(\mathbf{\Delta k})\, e^{i\mathbf{\Delta k}\cdot\mathbf{R}_n} e^{-M} \\ &+ \sum_n \sum_m f(\mathbf{\Delta k})\, e^{i\mathbf{\Delta k}\cdot\mathbf{R}_m} e^{-M}\, f^*(\mathbf{\Delta k})\, e^{i\mathbf{\Delta k}\cdot\mathbf{R}_n} e^{-M} \left[e^{\Delta k^2 \langle u_{\Delta k_n} u_{\Delta k_m} \rangle} - 1 \right] \end{aligned} \tag{2.13}$$

[2] For simplicity, we consider one type of atom located at each lattice point.

[3] Demonstration of this approximation can be found in [52].

where

$$M = \frac{1}{2}(\Delta k)^2\langle u_{\Delta k}^2\rangle = \frac{1}{2}\left(\frac{4\pi}{\lambda}\right)^2 sin^2\theta\langle u_g^2\rangle = B_T\left(\frac{sin\theta}{\lambda}\right)^2 \tag{2.14}$$

is the Debye-Waller factor, with $B_T = 8\pi^2\langle u_g^2\rangle$. The first term of equation 2.13 accounts for the elastic scattering giving rise to the sharp diffracted Bragg peaks. The effect of the Debye-Waller factor tends to decrease the intensity with increasing temperatures (larger displacements) without changing the width of the peak. On the other hand, the term enclosed in brackets on the second part of equation 2.13 increases with increasing temperature, due to larger displacements with temperature. It arises from short distances in the crystal, resulting thus in a considerably diffused scattering in comparison to the diffracted Bragg peaks. This is the reason why it is known as *thermal diffuse scattering*, usually seen as a background signal in the diffraction patterns.

By inspecting the Debye-Waller factor M we can make a straight observation: large $\mathbf{\Delta k}$ will display weaker intensities at high temperatures[4]. An example of this effect is shown in figure 2.7, which shows the measured [h00] X-ray Bragg reflections of an aluminum sample at different lattice temperatures [53].

Considering the case of a monoatomic cubic crystal within the Debye approximation and as a collection of harmonic oscillators, it is possible to demonstrate (see [44] or [52] for a detailed development) that the mean squared displacement averaged over all modes:

$$\langle u^2\rangle = \frac{9\hbar^2T^2}{m_A k_B\theta_D^3}\int_0^{\theta_D/T}\left[\frac{1}{e^\xi - 1} + \frac{1}{2}\right]\xi d\xi \tag{2.15}$$

with m_A the average mass of the unit cell and where the Debye function is introduced as:

$$\phi(x) = \frac{1}{x}\int_0^x \frac{\xi}{e^\xi - 1}d\xi$$

with $x = \hbar\omega_D/k_BT = \theta_D/T$, θ_D the Debye temperature and $\xi = \hbar\omega/k_BT$. We can express the factor B_T given in equation 2.14 by:

$$B_T = 8\pi^2\langle u^2\rangle = \frac{6h^2}{m_A k_B\theta_D}\left(\frac{\phi(\theta_D/T)}{\theta_D/T} + \frac{1}{4}\right)$$

The $\phi(\theta_D/T)$ integral varies from 1 to 0.6 between $\theta_D/T \sim 0$ and $\theta_D/T = 2$, respectively.

[4]Note that the loss of Bragg peak intensity with temperature does strictly apply to the case of kinematical diffraction. As we will see in the following section, in the case of dynamical diffraction the intensities of the diffracted peaks do not necessarily decrease with temperature.

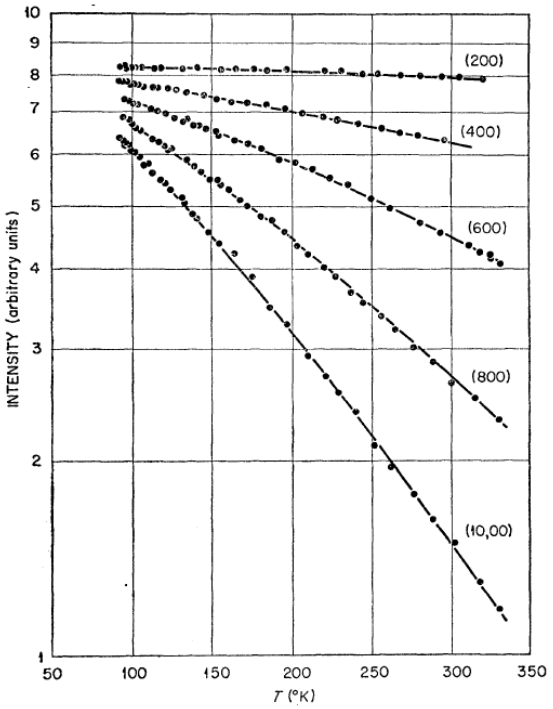

Figure 2.7: Diffracted intensities of the [h00] aluminum Bragg peaks as a function of the sample temperature. Image from [53].

2.1.2 Dynamical theory of diffraction

In order to illustrate the electron scattering processes under the dynamical framework, the derivation of the scattered amplitudes and its application to the two beam approximation in electron diffraction will be explained in the following. Results derived from a larger number of interacting beams will be presented in chapter 4 along with the experimental data.

The crystal potential can be viewed as the superposition of all atomic potentials, and thus described as the Fourier series of the crystal lattice. Following the notation in [47] the crystal potential is defined as:

$$V(\mathbf{r}) = \sum_{\mathbf{g}\neq 0} U_{\mathbf{g}} e^{i\mathbf{g}\cdot\mathbf{r}} + U_{00} \tag{2.16}$$

where $\mathbf{g}$ denotes the reciprocal lattice vector of the diffracted beam and U_{00} the static average crystal potential.

When the electron enters the crystal potential, its kinetic energy is altered due to the interaction with the average crystal potential U_{00}, thus from the energy conservation law:

$$\frac{\hbar^2}{2m}(k_i^2 - k^2) = U_{00} \tag{2.17}$$

with k_i the electron wavevector in vacuum and k in the crystal.

The electron wavefunction inside of the crystal potential is then defined by:

$$\Psi(\mathbf{r}) = \sum_{\mathbf{g}} \phi_{\mathbf{g}}(z)\, e^{i(\mathbf{k}+\mathbf{g})\cdot\mathbf{r}} \tag{2.18}$$

where $\phi_{\mathbf{g}}(z)$ is the Fourier coefficient corresponding to the scattered amplitude associated to $\mathbf{g}$ through the sample.

By introducing the above quantities into the Schrödinger equation:

$$-\frac{\hbar^2}{2m}\nabla^2\Psi(\mathbf{r}) + V(\mathbf{r})\Psi(\mathbf{r}) = E\Psi(\mathbf{r}) \tag{2.19}$$

considering $e^{i(\mathbf{k}+\mathbf{g})\cdot\mathbf{r}} = e^{i[(k_x+g_x)\cdot x+(k_y+g_y)\cdot y+k_z\cdot z]}$[5] and by inserting the Fourier development of $\Psi(\mathbf{r})$ and $U(\mathbf{r})$, the solution to the Schrödinger equation becomes after multiplying by $\frac{2m}{\hbar^2}e^{-i(\mathbf{k}+\mathbf{g})\cdot\mathbf{r}}$ and integrating on $\mathbf{r}$:

$$(2k_xg_x + g_x^2 + 2k_yg_y + g_y^2)\phi_{\mathbf{g}}(z) - \frac{\partial^2\phi_{\mathbf{g}}(z)}{\partial z^2} - i2k_z\frac{\partial\phi_{\mathbf{g}}(z)}{\partial z} + \frac{2m}{\hbar^2}\left(\sum_{\mathbf{g}'\neq\mathbf{g}}\phi_{\mathbf{g}'}(z)U_{\mathbf{g}-\mathbf{g}'}\right) = 0 \tag{2.20}$$

The summation enclosed in parenthesis in the first term of the solution is known as the *"deviation parameter"* or *"excitation error"* $s_{\mathbf{g}}$, which depends on sample orientation. Following the same notation as in figure 2.8 we can retrieve the relation for the deviation vector in 1D:

$$s = \frac{-g_x^2 - 2k_xg_x}{2k} = \frac{k_x^2 - (g_x+k_x)^2}{2k}$$

Figure 2.8 a) depicts a schematic of a portion of the Ewald sphere and the reciprocal lattice plane

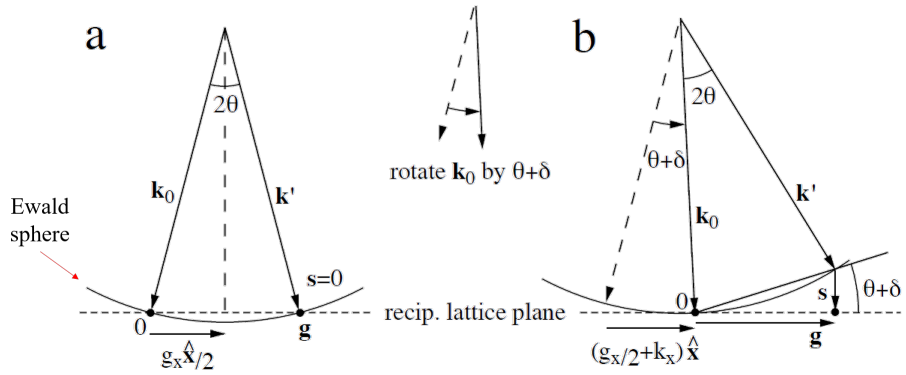

Figure 2.8: Schematic of the deviation parameter. a) geometry for $s = 0$ (Bragg condition) and b) after rotating the sample by $\theta+\delta$. For convention, $s < 0$ in this case. Image taken from [47].

[5]Here, we consider that $g_z \sim 0$ since for high energetic electrons the curvature of the Ewald sphere is highly reduced, so $\mathbf{g} \perp z$.

in 1D in symmetric condition i.e., at Bragg condition. By rotating the incident wavevector by an angle of $\theta + \delta$ the Ewald sphere is deviated by s from the reciprocal lattice plane, as depicted in figure 2.8 b). Thus, as its name suggests, the deviation vector gives information on how far we are from diffraction condition, i.e., $s_{\mathbf{g}} = \Delta\mathbf{k} - \mathbf{g}$.

The second term of equation 2.20 can be neglected when considering a slowly varying beam along the sample thickness. Finally, the last term can be rewritten by considering the *"extinction distance"* parameter, which is related to the crystal potential by:

$$\frac{1}{\xi_{\mathbf{g}-\mathbf{g}'}} = -\frac{2m}{\hbar^2 k_z} U_{\mathbf{g}-\mathbf{g}'} \tag{2.21}$$

The extinction distance is the period of oscillation of intensity for the diffracted beams (this definition becomes clearer in the simple case of the two-beam approximation shown in the following).

The solution of the Schrödinger equation leads then to a system of coupled differential equations known as the Howie-Whelan equations:

$$\frac{\partial \phi_{\mathbf{g}}}{\partial z} = i s_{\mathbf{g}} \phi_{\mathbf{g}}(z) + \sum_{\mathbf{g}' \neq \mathbf{g}} \frac{i}{2\xi_{\mathbf{g}-\mathbf{g}'}} \phi_{\mathbf{g}'}(z) \tag{2.22}$$

The simplest picture of dynamical theory of diffraction can be explained by considering only two interacting beams, known as the two-beam approximation, with the incident electron beam ϕ_0 and a diffracted beam $\phi_{\mathbf{g}}$. By imposing the condition of intensity conservation $|\phi_0|^2 + |\phi_{\mathbf{g}}|^2 = 1$ and boundary conditions $\phi_0(z=0) = 1$, $\phi_{\mathbf{g}}(z=0) = 0$, the solutions of the scattered amplitudes become:

$$\phi_0(z) = e^{i\pi z s_{\mathbf{g}}} \left[cos\left(\pi z \sqrt{\frac{1}{\xi_{\mathbf{g}}^2} + s_{\mathbf{g}}^2}\right) - \frac{i\xi_{\mathbf{g}} s_{\mathbf{g}}}{\sqrt{1 + \xi_{\mathbf{g}}^2 s_{\mathbf{g}}^2}} sin\left(\pi z \sqrt{\frac{1}{\xi_{\mathbf{g}}^2} + s_{\mathbf{g}}^2}\right) \right] \tag{2.23}$$

$$\phi_{\mathbf{g}}(z) = e^{i\pi z s_{\mathbf{g}}} \left[\frac{i}{\sqrt{1 + \xi_{\mathbf{g}}^2 s_{\mathbf{g}}^2}} sin\left(\pi z \sqrt{\frac{1}{\xi_{\mathbf{g}}^2} + s_{\mathbf{g}}^2}\right) \right] \tag{2.24}$$

and their respective intensities:

$$I_{\mathbf{g}} = \frac{1}{(1 + \xi_{\mathbf{g}}^2 s_{\mathbf{g}}^2)} sin^2\left(\pi z \sqrt{\frac{1}{\xi_{\mathbf{g}}^2} + s_{\mathbf{g}}^2}\right) \tag{2.25}$$

$$I_0 = 1 - I_{\mathbf{g}} \tag{2.26}$$

The expressions for the intensities become particularly simple at the exact Bragg condition, where the deviation parameter becomes $s_{\mathbf{g}} = 0$, so that the intensities of the transmitted and diffracted beams are simplified to:

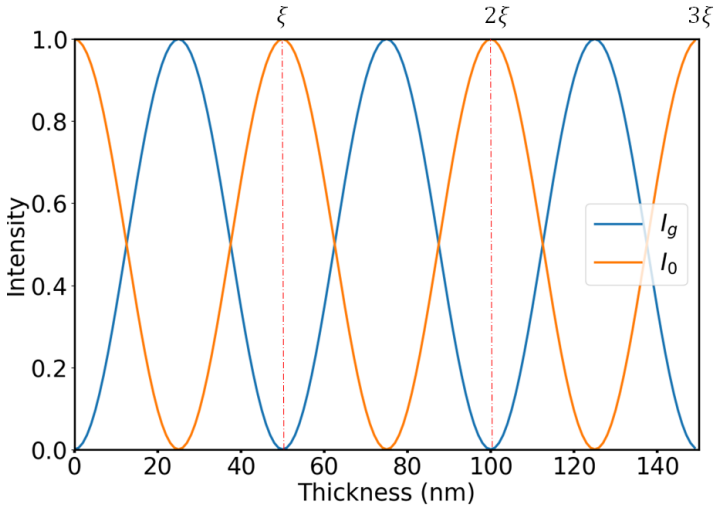

Figure 2.9: Pendellösung effect in the two-beam approximation. The intensities of diffracted (blue) and transmitted (orange) are calculated over a thickness of 150 nm. The extinction distance $\xi = 50\,nm$ corresponds to the period of extinction of the diffracted beam.

$$I_{\mathbf{g}} = \phi_{\mathbf{g}}\phi_{\mathbf{g}}^{*} = sin^2\left(\frac{\pi z}{\xi_{\mathbf{g}}}\right) \tag{2.27}$$

$$I_0 = \phi_0\phi_0^{*} = cos^2\left(\frac{\pi z}{\xi_{\mathbf{g}}}\right) \tag{2.28}$$

In this case, the intensities only depend on the thickness of the sample. More precisely, at $z = 0$ and at $z = n\xi_g$, with n integer, the intensity of the diffracted beam $I_g = 0$ and of the direct beam $I_0 = 1$. On the other hand, the diffracted intensity reaches its maximum ($I_g = 1$) when the thickness of the sample fulfills the condition $z = \frac{\xi_{\mathbf{g}}(2n+1)}{2}$, and consequently the transmitted beam is extincted ($I_0 = 0$), as shown in figure 2.9 for an extinction distance of $\xi_g = 50\,\text{nm}$.

This situation is analogous to a system of two coupled harmonic oscillators, also referred as the *Pendellösung effect*, transferring energy from one to another along the thickness of the sample. Furthermore, the full rocking curves as a function of $s_{\mathbf{g}}$ highlight the importance of the thickness in their shapes. To illustrate it, figure 2.10 shows the rocking curves for a given extinction distance of $\xi_{\mathbf{g}} = 50\,\text{nm}$ and at four different thicknesses. We can clearly observe that as the thickness of the sample is increased, the distance between the fringes in the rocking curves decreases. Note that the envelope (black dotted line) is constant for all thicknesses, as expected from the first factor in equation 2.25. It is interesting to remark that as the thickness of the sample is reduced and $\xi_g >> z$, the rocking curves recover the kinematical shape, as shown in figure 2.10 a).

Electron microscopists rely on the dynamical fringe pattern to accurately measure the thickness of the samples by convergent beam electron diffraction (CBED) technique [54]. Figure 2.11 shows a typical CBED diffraction pattern of an aluminum foil of thickness $z = 100\,\text{nm}$ in nearly two beam condition [55], with the right diffracted spot corresponding to the (220) Bragg

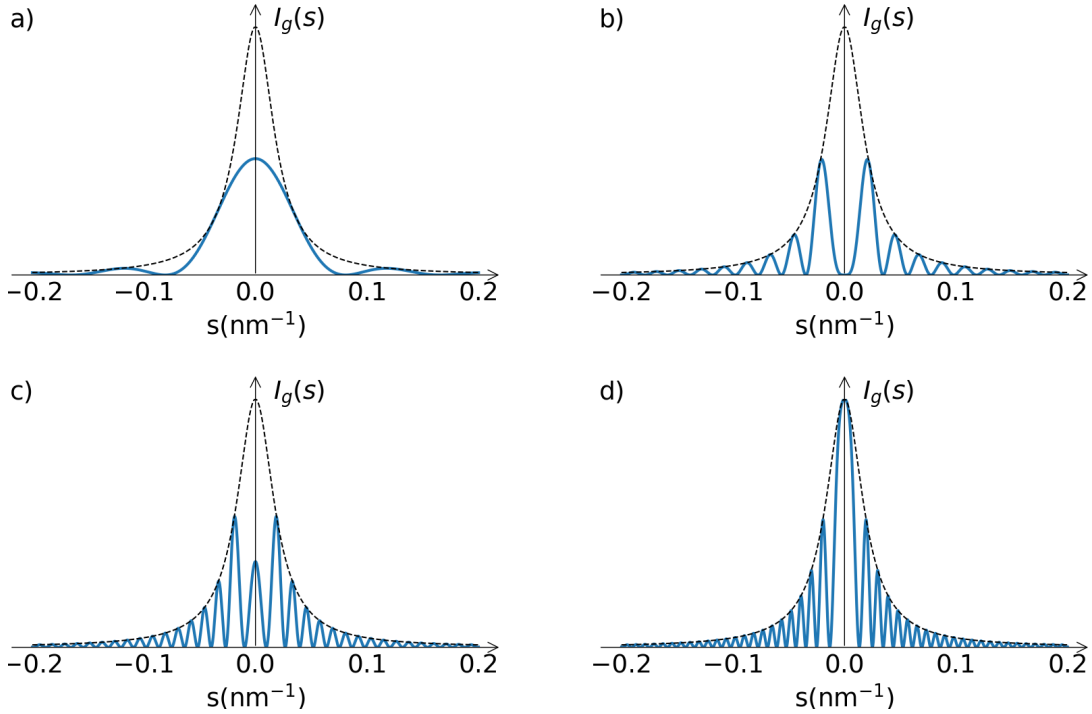

Figure 2.10: Rocking curves of the dynamically diffracted Bragg peak assuming $\xi = 50\,nm$ and different thicknesses a) $z = 12\,nm$, b) $z = 50\,nm$, c) $z = 90\,nm$, d) $z = 125\,nm$.

peak and the left to the transmitted beam. Below the CBED pattern a scheme of the profile lines is depicted highlighting the S_i distances and the Bragg angle, which is defined from the distance to the center of the transmitted beam. Notice the complementarity in their intensities. When the diffracted pattern is close to the two-beam condition, it is possible to relate the "interfringe" distance with the thickness of the sample from the following linear relation [55, 56]:

$$\left(\frac{S_i}{n_i}\right)^2 = -\frac{1}{\xi_{\mathbf{g}}^2 n_i^2} + \frac{1}{t^2} \tag{2.29}$$

In this case S_i denotes the deviation parameter of the i^{th} minimum from the exact Bragg position and n_i ($n_i = 1,2,3,4$) the position. The thickness is retrieved from the intercept of the linear fit.

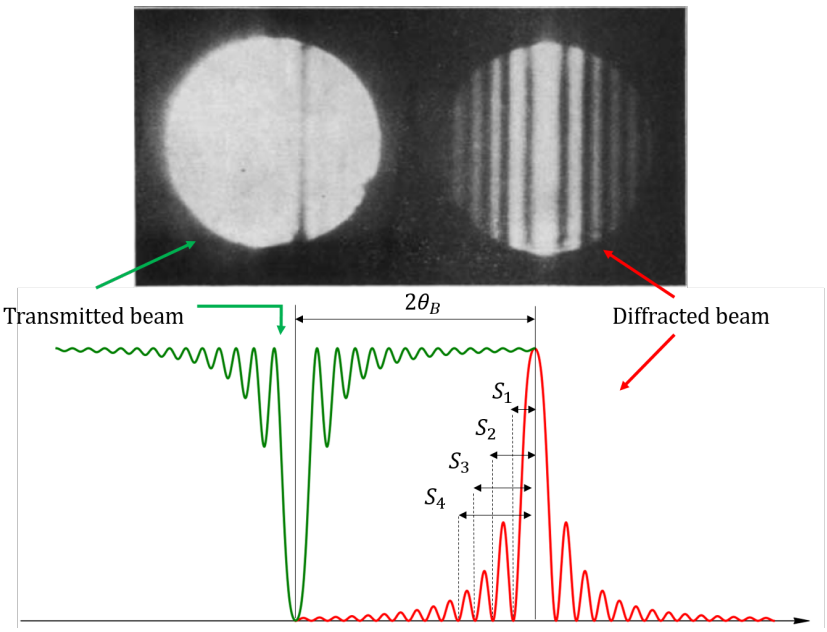

Figure 2.11: Up: CBED diffraction pattern of an aluminium foil in two-beam condition for the (220) Bragg peak [55]. Bottom: Simulated line profiles for an extinction distance of $\xi_g = 100\,nm$ and a thickness of 150 nm. The green curve represents the transmitted beam whereas the red curve is the diffracted peak.

Temperature effects in dynamical diffraction

We have seen that in the kinematical theory of diffraction, the effects of the temperature increase can be accounted for by the Debye-Waller effect, leading always to a decrease of the intensities. In the case of dynamically diffracted beams, the effects of temperature on the intensities are more complex since the crystalline potential as well as the extinction distance are subjected to the temperature changes (see equation 2.21). This can be easily shown by introducing another definition of the extinction distance, which reads [47, 46]:

$$\xi_{\mathbf{g}} = \frac{\pi V}{\lambda F_{\mathbf{g}}} \tag{2.30}$$

where V stands for the volume of the unit cell, λ the de Broglie electron wavelength and $F_{\mathbf{g}}$ the structure factor corresponding to the scattered $\mathbf{g}$ wavevector. Thus, when we take into account the Debye-Waller factor, the extinction distance becomes:

$$\xi'_{\mathbf{g}} = \frac{\pi V}{\lambda F_{\mathbf{g}} e^{-M}} = \xi_{\mathbf{g}} e^{M} \tag{2.31}$$

In certain cases, the relation between thickness and extinction distance may lead to the non-intuitive result of a larger intensity of the diffracted beam at higher lattice temperatures.

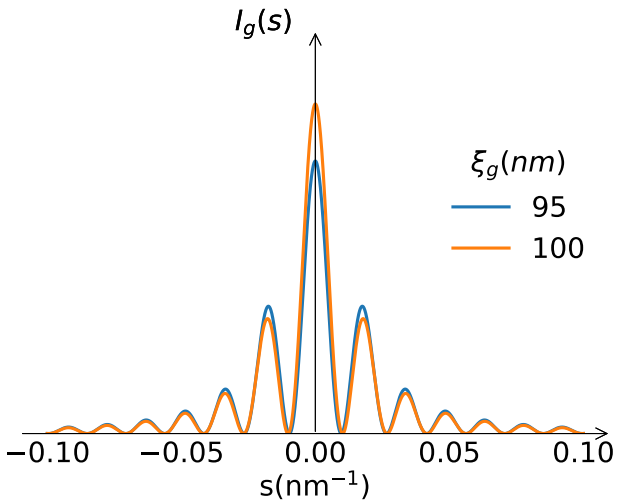

Figure 2.12: Simulated rocking curves for a 70 nm thick sample with two different extinction distances.

This effect is represented in figure 2.12, in which the rocking curves have been simulated for a constant thickness of 70 nm and with two different extinction distances: $\xi_g = 95$ nm and $\xi'_g = \xi_g e^M = 100$ nm with $M = 0.05$, which results in a higher intensity at the exact Bragg condition.

2.2 Time resolved diffraction

This section introduces diffraction considering the optical pump excitation, which allows to study matter as it relaxes back to the equilibrium state. First the two-temperature model that describes the temporal relaxation of the electrons and lattice is presented. In order to perform successful experiments, it is necessary to keep the excited volume matched to the probed volume. Therefore, the difference in the penetration depth from the pump and probe beams is discussed, followed by a more general comparison between electron and X-ray probes. Finally, the possible structural changes that the optical excitation may induce in the solid and the expected signatures in the diffracted pattern are discussed.

2.2.1 Two-temperature model

The two-temperature model is a phenomenological model that describes the relaxation dynamics of a photoexcited system by considering two coupled subsystems formed by electrons and phonons with distinct temperatures T_e and T_l, respectively [57]. The strength of the coupling between both dictates the temporal evolution of their temperatures until reaching thermal equilibrium. When the pulse width is shorter or comparable to the electron-phonon energy

transfer time, a non-equilibrium between electrons and phonons is achieved. Since the electron heat capacity is smaller than that of the lattice, the absorption of the laser pulse energy increases its temperature by several thousands of Kelvin while the lattice remains unaffected for the first tens of femtoseconds. After photoexcitation, the electronic system follows a rapid thermalization through electron-electron scattering transferring the energy to the phonons via electron-phonon coupling, which ultimately increases the lattice temperature by few tens of Kelvin depending on the laser incident energy. The temporal evolution of the temperature of both electrons and lattice can be modelled by considering a system of coupled non-linear differential equations describing the energy balance between both subsystems [57]:

$$\begin{aligned} C_e(T_e)\frac{\partial T_e}{\partial t} &= K\nabla^2 T_e - G(T_e - T_l) + f(r,t) \\ C_l\frac{\partial T_l}{\partial t} &= G(T_e - T_l) \end{aligned} \tag{2.32}$$

where $C_e(T_e)$ is the electron heat capacity which depends linearly on the electron temperature ($C_e = \gamma_e T_e$, with γ_e the electron heat capacity constant), K is the thermal conductivity, $f(r,t)$ the heat source term due to the laser pulse:

$$f(z,t) = -\sqrt{\frac{4\,ln2}{\pi}}\frac{(1-R)F_{inc}}{w\,\delta_L}\,exp\Big(-\frac{z}{\delta_L} - 4\,ln2\Big(\frac{t-2w}{w}\Big)^2\Big) \tag{2.33}$$

which corresponds to a gaussian profile with a full width half maximum w, propagating along the sample thickness z with an incident fluence F_{inc}, with reflectivity R and penetration depth δ_L. The electron-phonon coupling constant G is defined by:

$$G \sim \pi^2 mnv_s^2/6\tau_{ep} \tag{2.34}$$

with m the electron mass, n the electron density, v_s the sound velocity and τ_{ep} the electron-phonon collision time, which is proportional to $1/T_e$ (this assumption is valid when T_e and T_l are larger than the Debye temperature θ_D). Once the energy is transferred from the electron subsystem to the phonon bath within the first hundreds of femtoseconds, the lattice returns to the ambient temperature by heat diffusion. Experimentally, the temporal evolution of the temperatures can be accurately determined from ultrafast optical experiments, as reflectivity or transmissivity.

As the intensity of the laser pulse is increased, the amount of deposited energy on the system increases leading to longer electron relaxation times [58]. The temporal scales of the relaxation process might depend, on the other hand, on the strength of electron-phonon coupling. Materials displaying a strong electron-phonon coupling, i.e., large values of G, result in a faster relaxation of the process [59].

Although this model is generally suitable to describe non-equilibrium dynamics of metallic systems, some other systems as for instance magnetic samples, need a third degree of freedom

to fully describe the laser induced demagnetization dynamics: the spin. In this case, the description turns into a three temperature model accounting for electrons, spins and lattice [60]. The three temperature model has been also applied to more complex systems as high temperature superconductors [61].

2.2.2 Pump and probe penetration depths

One of the most important factors to consider in time resolved diffraction is the penetration depths of the pump and probe, which should be matched to ensure that the measured signal comes from a homogeneously excited volume. The majority of experimental setups are based on lasers with wavelengths lying in the visible range, which results in penetration depths of few tens of nanometers in solid state samples, depending on the material characteristics. Following the Beer-Lambert law, the intensity of the laser beam decreases exponentially as it propagates through the material:

$$I = I_0 e^{-\alpha L}$$

with α the attenuation constant and L the material thickness. The attenuation constant is inversely proportional to the penetration depth and so it can be linked as well to the extinction coefficient by:

$$\delta = \frac{1}{\alpha} = \frac{\lambda}{4\pi\kappa(\lambda)} \tag{2.35}$$

where λ is the wavelength and $N = n + i\kappa$ the refractive index[6].

In the case of electron diffraction, the condition of equally probed and excited volumes is easily fulfilled, since the large scattering cross section of electrons reduces considerably their elastic mean free path in the solid [63]:

$$\Lambda_e = \frac{A}{\rho N_o \sigma} \tag{2.36}$$

with A the atomic weight, σ the cross section in units of $events/e^-/(atom/cm^2)$, N_o the Avogadro number, ρ the material density. Typically, for samples with low atomic number, the elastic mean free path of an electron beam is on the order of ~ 100 nm for electron energies of 100 keV.

For X-ray diffraction the situation is quite different; X-rays provided by synchrotron radiation with energies of few keV have penetration depths as large as few microns in specular reflection, being thus several orders of magnitude larger than the optical pump depth. Performing a diffraction experiment in such conditions would hinder the dynamics of the photoexcited volume. This problem can be overcome by working at low angles of incidence or grazing incidence (see figure

[6]Appendix D gives the calculation of laser penetration depths from reflectivity measurements and optical conductivity [62], which is used to estimate penetration depths in chapter 5.

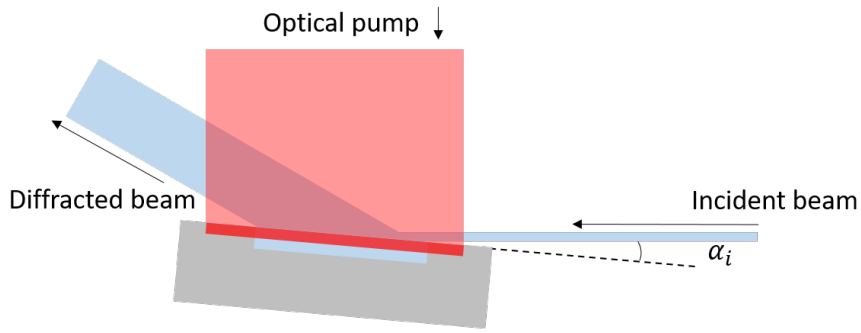

Figure 2.13: Schematic of the grazing incidence geometry in a pump-probe X-ray diffraction experiment.

2.13), which are about 1° to 3° above the critical reflection angle θ_c.

2.2.3 X-rays or electrons?

The choice of electrons or X-rays as a probe beam greatly depends on the focus of the study and the sample type. One of the fundamental differences between electron and X-ray diffraction arises from their interaction with matter; electrons interact strongly with the atomic potential formed by the crystal, X-ray beams undergo a much weaker scattering process from the comparatively diffuse electron density of the atoms. This results in electron beam cross-sections (σ_e) of the order of $\sim 10^6$ times larger than that one in X-ray beams (σ_X) [64]. Therefore, the electron beam flux necessary to obtain diffraction patterns with sufficiently good quality is highly reduced with respect to X-ray beams. In contrast, the inelastic scattering suffered by electrons within the sample is several orders of magnitude lower than that of X-rays, which makes electrons less damaging than X-rays [64]. Specifically in the case of biological samples this becomes an important factor. Another notorious difference between both probing beams is their wavelengths; as we have seen before, they determine the radius of the Ewald sphere and consequently the number of detected diffracted peaks is significantly larger in the case of electron with respect to X-ray diffraction.

Now, when considering the extra dimension of time into this comparison we find other essential differences. Electron bunches, as charged particles, are strongly affected by Coulomb repulsion effects, leading to unwanted beam divergence, which affects the spatial coherence and temporal resolution of the probing beam. On the other side, and as we have just seen, the penetration depths of electrons and X-rays are quite different. Electron diffraction is constrained to the study of thin samples (or surface dynamics in the case of reflectivity geometry) that become particularly challenging when the experiments are performed in the time resolved domain: the sample surface should be as large as the transverse size of the electron beam, i.e., few hundreds of micrometers. The preparation of samples with such geometrical characteristics in a free-standing fashion and with sufficient crystalline quality becomes of great difficulty. Moreover,

the presence of dynamical effects pushes the limits to reduce even more the sample thicknesses in order to avoid the complex interpretation of the dynamics with multiple scattering processes involved. On the opposite extreme, we find that the large penetration depths of X-rays along with the lower cross-section limits the experimental geometries to the reflection geometry at low angles of incidence (which ultimately limits the temporal resolution) or to the transmission geometry through thin film samples (which results in low diffraction intensities).

Finally, while electron diffraction can be easily performed in table-top experiments with temporal resolutions down to few hundreds of femtoseconds with fairly high intensities, time resolved X-ray diffraction usually requires the use of large scale facilities. Although table-top X-ray plasma sources by laser irradiation on solid targets have demonstrated to achieve temporal resolutions of the same order of magnitude [11], they are compromised by mechanical noise and a beam flux on sample of 10^6 photons/s, requiring long pump-probe measurements that can go up to weeks in the case of low diffracting samples [65]. Fast advances in temporal resolution and number of photons per bunch (with an average flux of 10^{12} photons/pulse in the case of European XFEL for instance [66]) are met in X-ray free electron laser facilities. Although FELs present promising outlooks, they have the main disadvantage of being large facilities. Only five of them are available to users nowadays (LCLS, European XFEL, SwissFEL, PAL-FEL and SACLA) limiting the allocation time for beamtimes to few experiments.

2.2.4 Photoinduced structural changes in the diffraction peaks

The arrival of the pump laser on the sample can have distinct effects on the structure that will be directly reflected on the diffraction pattern. Figure 2.14 shows the relation between real space changes and its signatures in the diffraction intensity.

The effects of lattice expansion or compression will shift the position of the diffracted peaks towards smaller or larger scattering wavevectors, respectively. Other possible structural changes after pump arrival is photoinduced disorder, divided in two kinds; first kind disorder which corresponds to thermal fluctuations as described by the Debye-Waller effect (depicted in figure 2.14 d)), or disorder of second kind, which implies long range correlated changes of the structure (figure 2.14 e)). Both types of disorder will tend to decrease the diffracted intensity, but while first kind maintains the width of peak constant, the second kind disorder will tend to broaden the Bragg peaks. The width of the diffracted peaks keeps information of the grain size and thus the crystal quality over the long range (provided the beam coherence length is sufficiently large) known as the correlation length ξ:

$$FWHM = \frac{1}{\xi}$$

The arrival of the pump pulse can trigger the excitation of coherent phonons. This coherent motion of atoms leads to atomic displacements in the crystallographic direction of the phonon and, contrary to the Debye-Waller effect, it will change the intensity of only certain Bragg peaks.

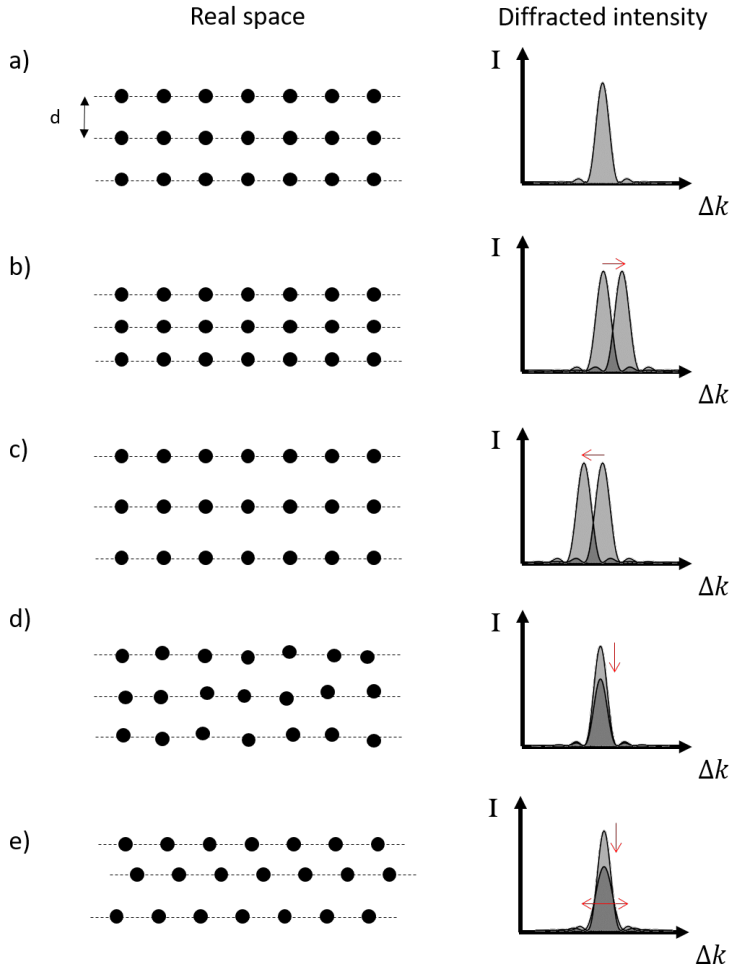

Figure 2.14: Real space (left) and corresponding diffracted intensity (right). a) Original crystal lattice, b) lattice compression, c) lattice dilatation, d) thermal disorder (kinematical diffraction), e) planar disorder.

The intensity changes as a function of delay time will present a damped oscillatory intensity with the frequency of the excited mode. In the particular case of thin films, the pump excitation can generate coherent acoustic modes that propagate along the thickness of the sample [67], also known as breathing modes. An example of this coherent phonon excitation is shown in figure 2.15 measured on a graphite sample by UED [68]. Time resolved diffraction becomes particularly useful when studying structural phase transitions. Systems displaying such phase transitions will give rise to the appearance/disappearance of diffracted peaks. As we will see, that is the case of the experiments presented in chapters 5 and 6.

The last possible photoinduced effects deal with irreversible processes, in which the strong intensity of the incident pump melts the crystal structure and thus the diffracted spots vanish completely [26, 69]. This type of experiments have another degree of complexity, since a new

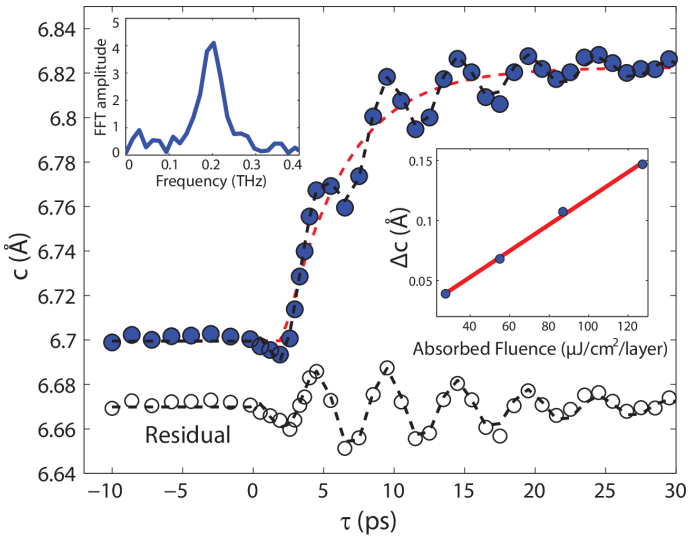

Figure 2.15: Coherent excitation of the thin film breathing mode in graphite. The c-axis lattice constant exhibits oscillatory dynamics in addition to simple expansion following photoexcitation. The measured frequency of 0.2 THz corresponds to a sample thickness of 10 nm. The overall c-axis expansion is linear in excitation fluence as shown in the inset. Image from [68].

region of the sample has to be probed at every pump pulse.

Chapter 3

Experimental setups

Contents

This chapter is devoted to the description of the experimental setups employed for the results presented in following chapters. The first part describes the main characteristics and performance of the ultrafast electron diffraction setup installed and developed at LOA. The second part serves as an illustration of a typical picosecond time resolved X-ray diffraction in a synchrotron beamline.

3.1 Experimental setup for UED

Figure 3.1 shows an image of our experimental UED setup at LOA with the three main components of the experiment: the electron chamber (1) connected to the sample and detector chamber (2) and the black box enclosing the CCD camera (3).

A more detailed scheme is shown in figure 3.2. The experiment relies on a commercial Ti:Sapphire regenerative amplifier (COHERENT, Legend Elite Duo) that delivers pulses with a FWHM of 30-35 fs centered at a wavelength of 800 nm with an energy of 1 mJ per pulse at 1 kHz repetition rate. The output beam from the compressor is divided into two arms: one dedicated

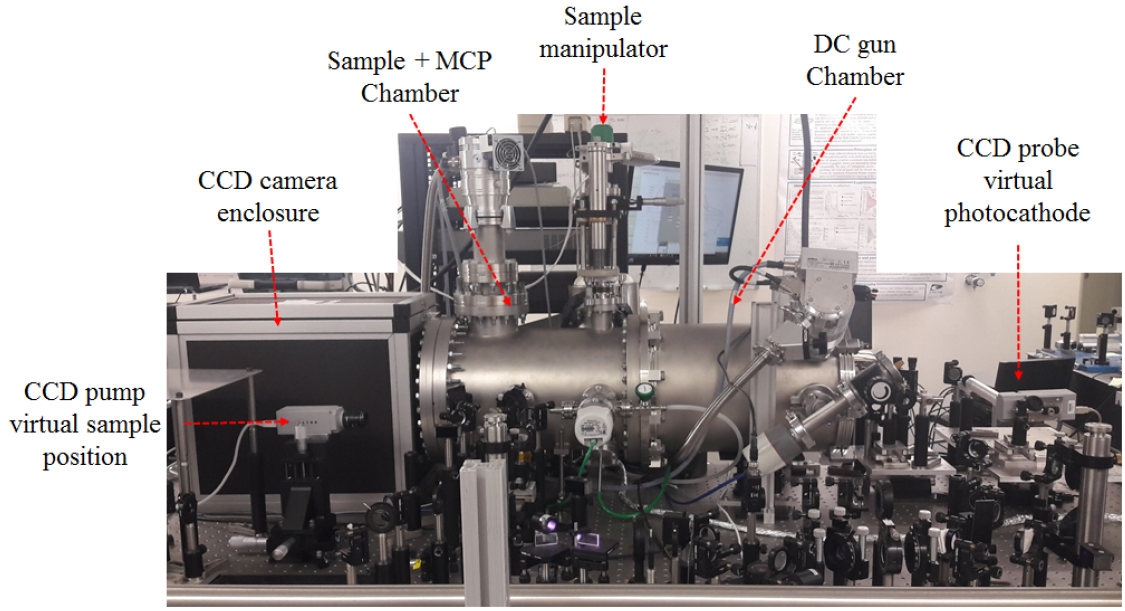

Figure 3.1: Picture of the experimental UED setup at LOA.

to the electron pulse generation by tripling its frequency, and the other to the excitation pump for the sample. The delay between pump and probe pulses is set by a delay stage with a maximum temporal range of 2 ns. The size of the pump beam at the sample can be adjusted with a lens to a maximum FWHM of about 1 mm at the sample position. The experiments are performed by taking two images per delay time; an image with the pump illuminating the sample and another with the pump blocked by the mechanical beam-blocker, so that the recorded intensity changes can be relatively compared (see section 3.1.5). Apart from the main components for electron acceleration and detection, the experimental system is equipped with two main beam diagnostics. By placing flip mirrors (noted as FM in figure 3.2) it is possible to adjust the size and position of the beam at crucial sites, at the photocathode and at the sample virtual positions. Moreover, a beam pointing system monitors continuously the beam position to optimize the pointing stability by piezo-actuated mirrors. This system allows to correct any possible thermal drifts that may arise during long acquisition experiments.

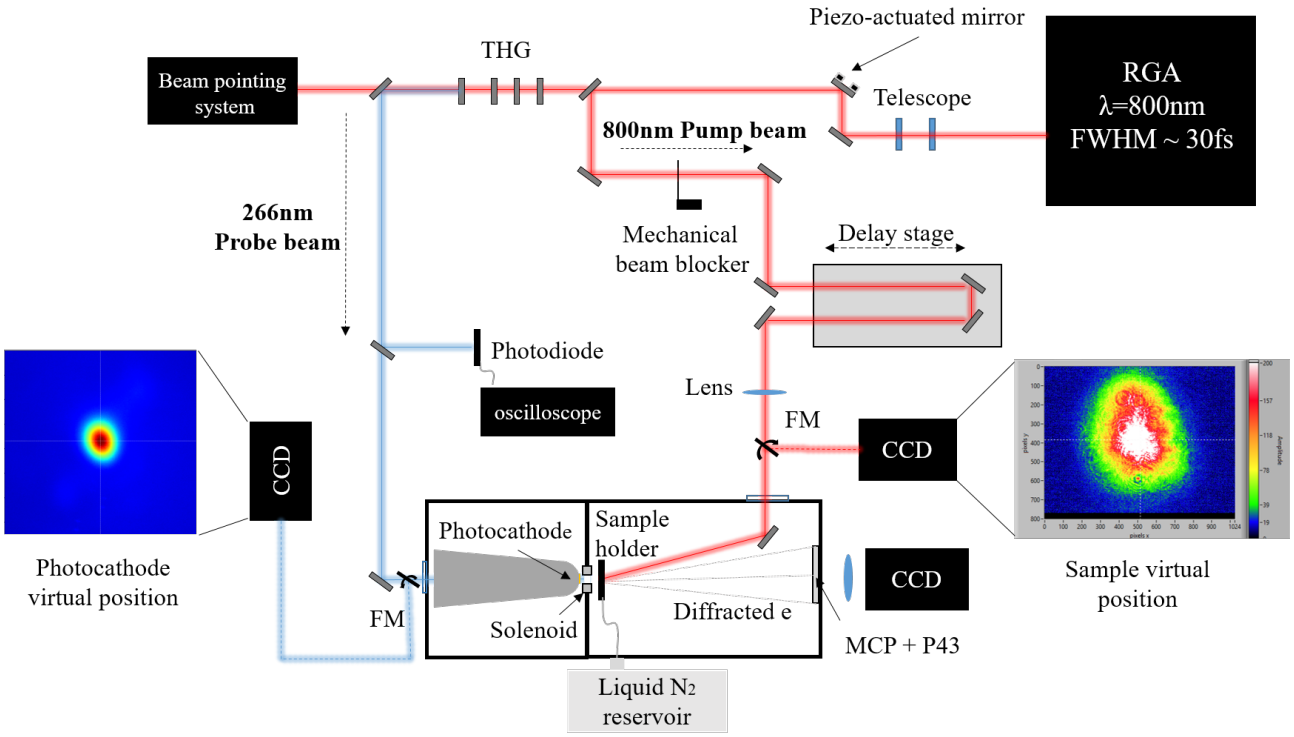

Figure 3.2: Schematic of the experimental setup. FM stands for flip mirrors and THG for third harmonic generation.

3.1.1 DC electron gun

The compact DC accelerator installed in the experimental setup was designed and developed by O. J. Luiten's group at Eindhoven University [70].

Figure 3.3 shows a scheme of the DC gun design with its main components: the inner conductor, the insulating cone, the photocathode and the anode. The chamber enclosing the DC gun is maintained under a pressure of $2{\cdot}10^{-6}$ mbar.

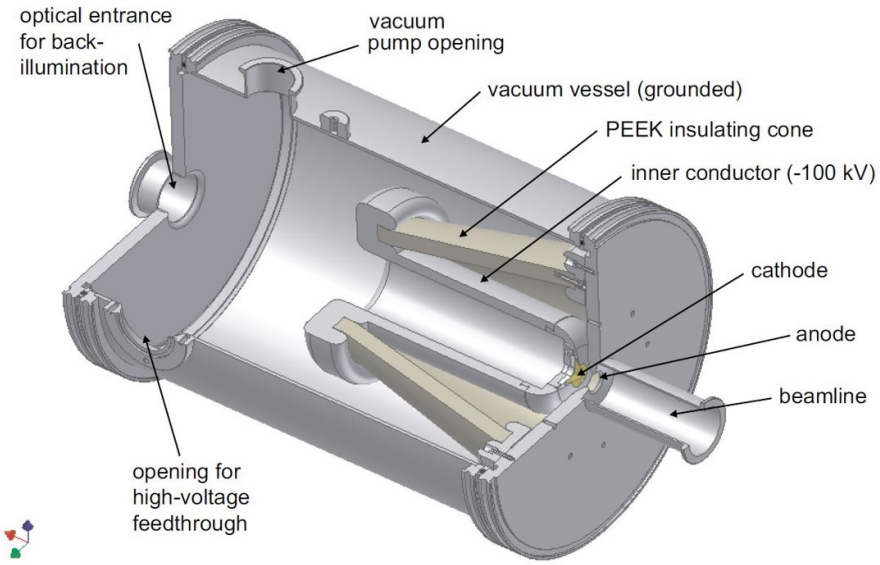

Figure 3.3: 3D design of the DC electron gun. Image taken from [70].

The frequency-tripled pulses of the laser enter the chamber through an optical aperture allowing back-illumination of the photocathode which is clamped to the aluminum cylinder. The latter is connected to a high voltage supply (Matsusada, AU-100) delivering voltages down to -100 kV. In order to insulate the chamber from the accelerating structure, a PEEK (a vacuum compatible insulating material) insulating cone covers the inner conductor. The grounded anode is perforated with an aperture of 1.6 cm diameter and located at a distance of 1.1 cm from the cathode. Finally, a solenoid (not shown in the figure) collimates the resulting electron beam.

A more detailed description of the design and operation of the DC gun can be found in reference [70].

3.1.1.1 Third Harmonic Generation and Photocathode

The laser frequency output from the compressor is tripled by a set of non-linear crystals as depicted in Figure 3.4. The 800 nm laser wavelength is focused on a barium borate (BBO) crystal for second harmonic generation followed by a calcite plate to compensate group velocity delay between the 800 nm and 400 nm wavelengths. To tune the laser intensity, a dual waveplate

is inserted before the second BBO crystal that finally generates third harmonic centered at 266 nm. A few dichroic mirrors positioned after the last BBO reflects only the contribution of the UV 266 nm.

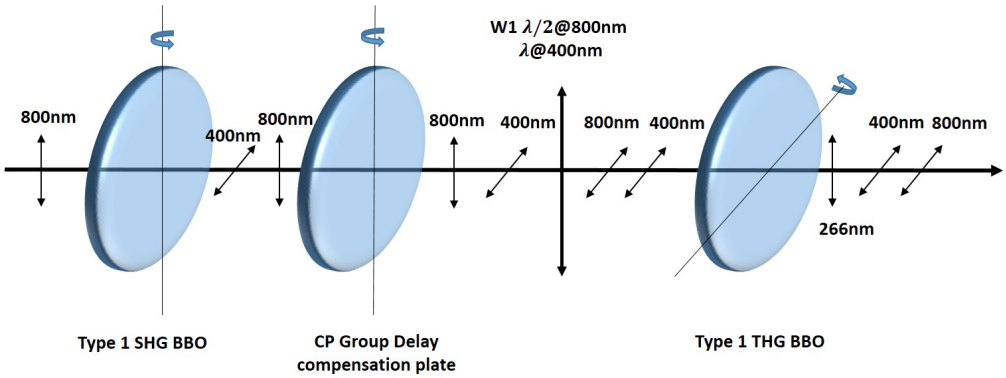

Figure 3.4: Third harmonic generation (THG) set, adapted from [71].

The generated UV beam with a pulse duration of 120 fs is then focused onto a 15 nm gold coated fused silica substrate (with 2 nm Cr to ensure adherence of the gold film) with a FWHM of 40 μm. To extract electrons from the photocathode, the incident photon has to trigger the photoemission process. The photoemission process is divided in three main steps; (1) absorption of the photon energy by an electron, (2) drift of the electron to the surface of the metal overcoming the surface potential, i.e., the work function of the material, and (3) finally escaping from the surface. The effective work function of the photocathode depends on the applied acceleration voltage following the Schottky effect [72]:

$$\phi_{eff} = \phi_{wf} - \phi_{Schottky} = \phi_{wf} - e\sqrt{\frac{eF_a}{4\pi\varepsilon_0}} = \phi_{wf} - 0.037947\sqrt{F_a[MV/m]}$$

with ϕ_{wf} = 4.61 eV the work function of gold, ε_0 the vacuum permittivity, e the elementary charge and F_a the applied field. For example, an applied voltage of -50 kV results in an effective workfunction of 4.52 eV, which is below the incident photon energy (4.65 eV), ensuring single-photon photoemission process [73].

The back-illumination of the photocathode has the advantage of an easier alignment procedure although it limits the working acceleration voltages to 55 keV. Above this value, the gun started to arc and the photocathode has shown clear signs of damaging. Possible reasons that might induce damage in this type of photocathodes is the reduced thickness of the deposited gold coating which needs to be sufficiently thin to allow photoemission. Surface roughness and impurities in the thin film also increase the probability of inducing electrical breakdowns. Because of this limitation, all the experiments presented in the thesis were performed with absolutes values of the voltage below 50 kV.

3.1.1.2 Temporal resolution

One of the most important characteristics of a pump probe diffraction experiment is its temporal resolution. Capturing ultrafast structural dynamics requires electron pulses with a temporal duration below 1 ps. Indeed, the electron bunch duration is the most limiting factor for the temporal resolution, which is given by:

$$\sigma_{resol} = \sqrt{\sigma_{e^-}^2 + \sigma_{laser}^2 + \sigma_{\alpha}^2}$$

where σ_{e^-} denotes the electron bunch duration, σ_{laser} the duration of the optical pump and σ_{α} the difference of arrival time arising from different angles of incidence and velocity mismatch between pump and probe. The latter is negligible in the case of transmission geometry, and so the temporal resolution is greatly dependent on the electron pulse duration. The electron beam temporal duration is mainly dominated by space-charge effects. Coulomb repulsion effects inherent to charged particle beams broaden the pulses up to several picoseconds depending on the number of electrons contained in the bunch. As a way of reducing the space-charge effects, different parameters can be tuned to achieve temporal resolutions below 1 ps:

- the laser intensity on the photocathode.
- the electron acceleration voltage.
- the distance between the photocathode and the sample.

The first parameter can be adjusted by reducing the laser intensity at the photocathode: the yield of photoemitted electrons will be proportional to the number of incident photons. In the case of this setup, the intensity of the third harmonic is tuned by changing the position of the waveplate in the set of third harmonic generation. See section 3.1.3 and Appendix A for more details. Secondly, since higher energy of the electron bunches reduce the space-charge effects, an increase of the electron velocity can considerably shorten the pulse duration. This effect can be directly observed in the results shown in Figure 3.5, which presents beam dynamics simulations performed with the General Particle Tracer (GPT) code [74].

Finally, within the electron beam propagation its longitudinal spatial dimension will tend to elongate requiring a short distance between the cathode and the sample to achieve the shortest temporal resolution. The minimum attainable distance (considering the anode and the solenoid) is 40 mm.

In order to estimate the duration and spatial dimensions of the pulse, particle tracer simulations with the GPT code [74] are implemented with the beam characteristics listed in table 3.1 and by considering an initial energy spread given by the difference between the laser energy and the workfunction of gold, i.e. $\Delta\varepsilon \sim 0.13$ eV. The results provided by the simulation are depicted in figure 3.5.

Parameter	Value
Laser spot size (FWHM)	$40\mu m$
Laser pulse duration (FWHM)	120 fs
Laser wavelength	266 nm
Photocathode - solenoid distance	18 mm
Photocathode - sample distance	40 mm

Table 3.1: Parameters used in the particle tracer (GPT) simulations.

These results clearly show that the duration of the electron pulse is largely influenced by the number of electrons contained in the bunch as well as the acceleration voltage, where the shortest pulse duration is achieved at higher accelerations voltages in bunches containing few thousands of electrons.

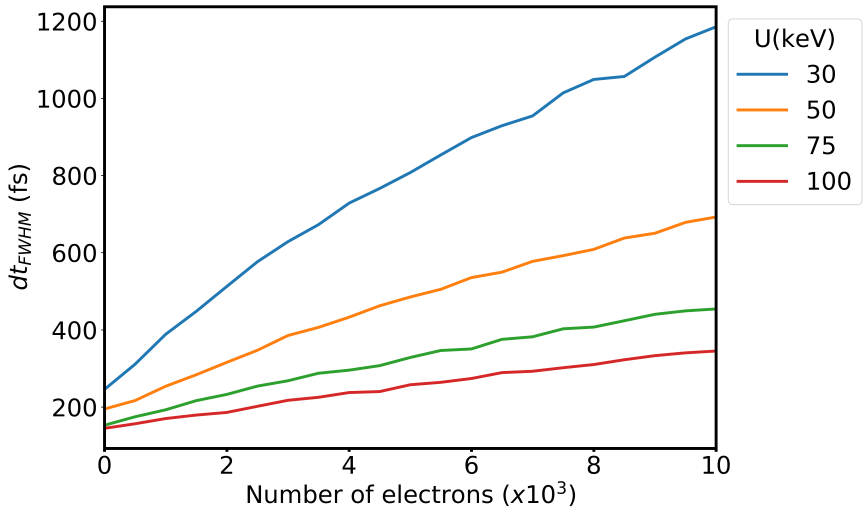

Figure 3.5: FWHM temporal duration of the electron pulses at the sample position as a function of the number of electrons at different acceleration voltages. Results are obtained from GPT simulations with values listed on table 3.1 .

3.1.1.3 Spatial resolution

Detection of structural dynamics at the atomic level requires, along with a short temporal resolution, sufficiently short probing wavelengths and a spatial coherence covering several unit cells.

The de Broglie wavelength of electrons accelerated to voltages in the range of V = [10 -100] keV is λ = [12.3 - 3.9] pm, calculated with $\lambda = h/\sqrt{2m_e \cdot eV + (eV)^2/c^2}$, where h is the Planck constant, m_e the electron mass at rest, V the acceleration voltage, e the elementary charge and c the speed of light. These values are sufficiently small to probe interplanar distances, which

are usually on the order of several Angstroms. The resulting momentum transfer is given by the Bragg law:

$$g = \frac{4\pi \cdot sin\theta}{\lambda}$$

where g is the scattering wave vector and θ the Bragg angle. If we consider for example an electron beam of 40 keV energy, the diameter of the detector of d = 40 mm and a distance between the sample and the detector of L = 28 cm, we obtain a maximum momentum transfer of $g = 7.3\,\mathring{A}^{-1}$.

While short electron wavelengths ensure the probability of scattering from the atomic planes, the transverse coherence length of the electron beam will finally dictate the quality of the diffraction pattern. The coherence length represents the maximum resolvable distance in the sample in which the electron wave functions are in phase. It is inversely proportional to the angular spread σ_θ of the beam, following the relation:

$$L_\perp = \frac{\lambda}{2\pi\sigma_\theta} \tag{3.1}$$

A more commonly used parameter in electron beam accelerators is the transverse normalized emittance which describes the parallelism and focusability of the beam. Hence, it is used as a parameter of the beam quality. It is defined as [75] [76]:

$$\varepsilon_{n,x} = \frac{1}{mc}\sqrt{\langle\sigma_x^2\rangle\langle\sigma_{p_x}^2\rangle - \langle\sigma_x\,\sigma_{p_x}\rangle^2} \tag{3.2}$$

where x is the transverse position and p_x the transverse momentum. The sample is placed at the waist of the electron beam where the covariance term in equation 3.2 becomes zero resulting in a normalized transverse emittance of $\varepsilon_{n,x} = \frac{\sigma_x\sigma_{p_x}}{mc}$, where σ_x is the RMS bunch radius, and σ_{p_x} the RMS transverse momentum spread. The effects from the space-charge will not only tend to elongate longitudinally the electron beam, but also transversely as shown in Figure 3.6, which represents the GPT results obtained for the FWHM of the transverse size as a function of the number of electrons and beam energy. It is important to point out that due to the large transverse size that the electron beam acquires (several hundreds of μm), the dimensions of the samples of study should have a comparable surface of at least $100 \times 100\,\mu m^2$, with a thickness of less than 100 nm to ensure transmission of the electrons through the sample.

The transverse coherence length in terms of its normalized transverse emittance at the sample position becomes [75, 77] :

$$L_\perp = \frac{\hbar}{m_e c}\frac{\sigma_x}{\varepsilon_{n,x}} \tag{3.3}$$

The GPT results lead to a normalized transverse emittance of $\varepsilon_{n,x} \sim 0.007$ mm·mrad at the sample position. This value along with the spotsize given in Figure 3.6 finally result in a coherence length of the order of $L_\perp = 5$ nm, meaning that the diffraction pattern reflects coherent interference from, for example, 10 unit cells with a lattice parameter of 5 $\mathring{A}$ each.

It should be noted that apart from the source characteristic coherence length, the reciprocal space resolution will ultimately depend on the sample quality [75, 77, 78], $\Delta g = 2\pi\frac{\sigma_{peak}/L}{\lambda}$, where σ_{peak} denotes the RMS width of the diffracted peak and L the distance between the

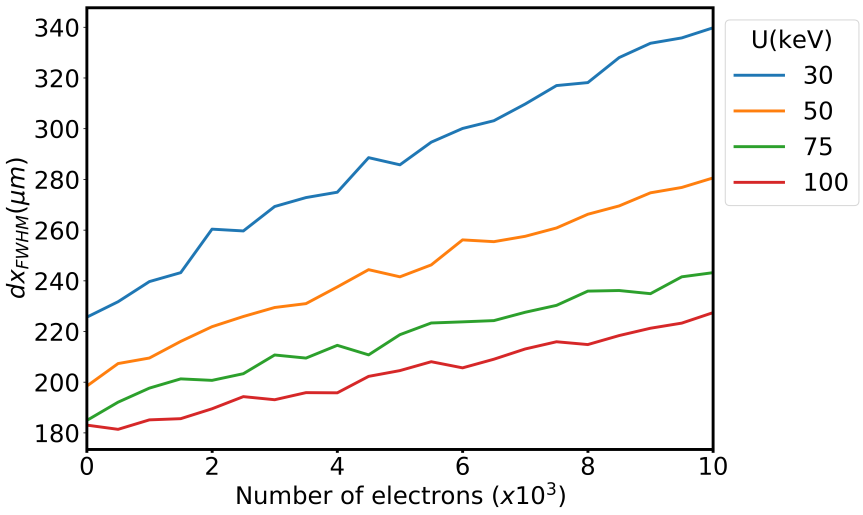

Figure 3.6: GPT simulation results for the beam size at the sample position at different electron energies.

sample and the detector. Defects on the crystal lattice, presence of domains or the grain size will enlarge the Bragg width degrading proportionally our spatial resolution. In order to get an estimation considering sample quality effects, we have recorded a diffraction pattern of a monocristalline silicon sample (considered as a nearly perfect crystal) oriented along the [001] crystal axis. Figure 3.7 shows a Voigt fit of the (220) Bragg peak, giving a value of σ_{peak} = 119.8 μm, resulting on a reciprocal space resolution of $\Delta g \sim 0.053\,\mathring{A}^{-1}$, i.e., $\Delta g/g = 0.015$.

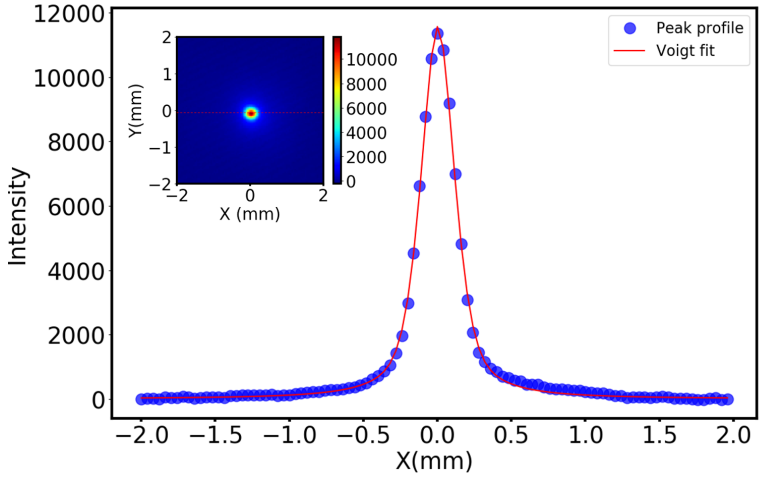

Figure 3.7: (220) Bragg peak from a 70 nm monocristalline membrane of silicon [001] and the corresponding line profile Voigt fit (marked in inset with a red line). The diffraction pattern was measured with an electron beam energy of 45 keV.

3.1.2 Sample holder

The sample holder consists of a piece of copper with 5 apertures. Four of them are used to place the TEM grids holding the thin sample sections under study, whereas the fifth is a large aperture for electron beam alignment. The TEM grids are clamped with a thin holed copper plate screwed to the main copper body (see figure 3.8, front size). The sample holder is then mounted to the rotation and translation stage which permits to align the sample and adjust the angle of incidence between the incoming electron beam and the sample surface.

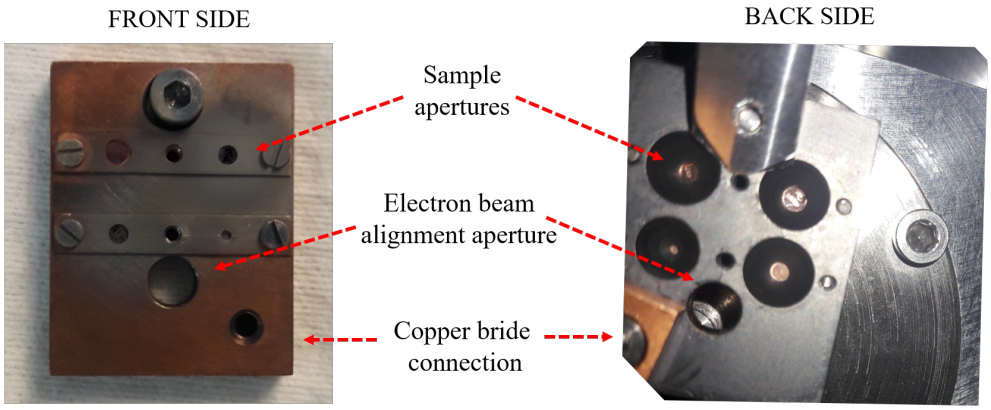

Figure 3.8: Front side and back side of the sample holder.

Crystalline samples undergoing structural phase transitions are of great interest in UED. An extensive number of materials are subjected to such transitions with critical temperatures below room temperature. For this purpose, the experimental setup has a liquid Nitrogen cold finger that extends down to the chamber and connects with a braided copper wire to the sample holder. The temperature of the sample can be monitored by connecting a type *K* thermocouple in the junction between the copper bride and the sample holder. The minimum registered temperature with this cooling system reaches 150 K.

3.1.3 Detection system

In order to detect the scattered electrons from the sample under study, a set of two microchannel plates (MCP) in Chevron configuration (consisting of two biased MCP detectors) and an alluminized phosphor plate (P43), are placed in the second vacuum chamber at a distance of L = 28 cm from the sample.

MCPs are widely used as image amplification devices of charged particles. It is composed by arrays of miniature electron multipliers tubes with a diameter of 10 μm, see figure 3.9. Their working mechanism relies on secondary electron emission within the microchannel tubes, in which an incident electron produces a cascade of δ secondary electrons giving an overall gain of G = 10^7 in the case of a Chevron configuration at 1 kV [79].

As the voltage of the MCP detector is increased, the number of counts recorded will increase exponentially. Furthermore, it is worth mentioning that this will also lead to an exponential increase of the noise on the images. This background noise usually results from ion-feedback instabilities when operating at high voltages or a high background pressure, effects that are well known in MCP amplifiers [80]. Since high background pressure could also lead to damages in the device, the chamber pressure is maintained at 10^{-7} mbar. Figure 3.10 shows an example of the intensity increase of the unfocused electron beam, plotting the maximum number of counts recorded as a function of the MCP voltage. The top left inset shows the mean value of the intensity in a small region of interest of 100x100 pixels (marked in low right inset) showing that the same effect is present in the background signal.

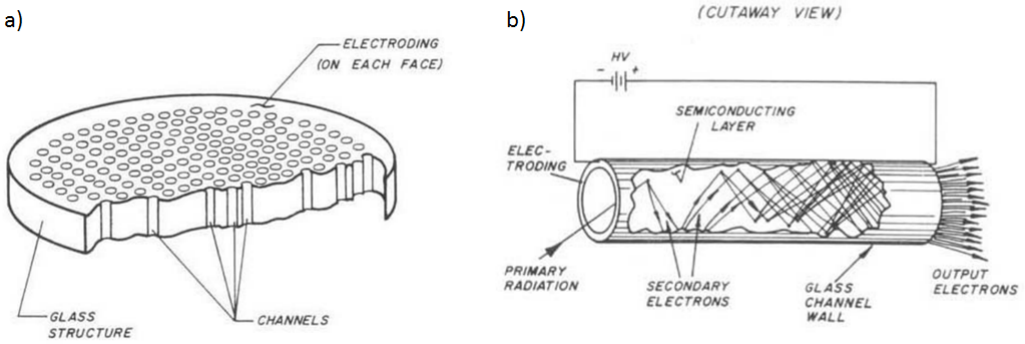

Figure 3.9: a) Schematic of a multiple channel plate showing the array of electron multipliers, b) schematic of a single electron multiplier tube. Images taken from [79].

Since MCP have a large detection efficiency of low energy electrons (50 to 85 %) the first MCP plate is coated with 200 nm of aluminum and connected to a -90 V voltage to reduce as much as possible the contribution of low energy electrons without limiting the detection of high energy electrons. Low energy electrons, usually arising from inelastic scattering processes, contribute to the background signal which lowers considerably the signal to noise ratio of low intensity diffraction spots.

The diffracted signal amplified at the MCP and the phosphor plate set is subsequently demagnified and recorded with an air cooled CCD camera (Andor, iKon-M) with arrays of 1024x1024 pixels, allowing an spatial resolution of 40 μm per pixel. To counterbalance any contribution from the ambient light or reflected pump light from the sample holder, a green band pass filter is placed in front of the camera chip to selectively transmit the phosphor plate 545 nm signal.

A homemade AND gate collects the signal from the delay pulse generator with the repetition rate of the laser and the exposure time of the camera shutter. The output of the AND box is sent to the voltage trigger of the MCP.

One of the main advantages of using MCP detectors consist in their compactness and their large detecting area; the plates have a diameter of 40 mm allowing the detection of several

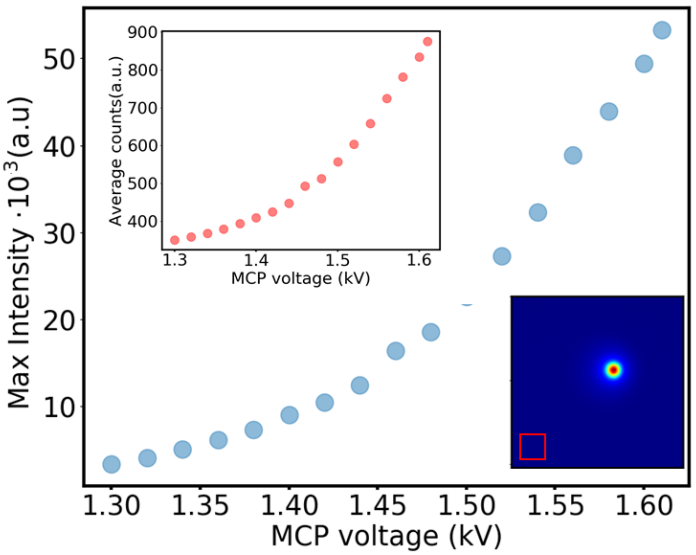

Figure 3.10: Maximum number of counts of the electron beam as a function of the MCP input voltage. Top inset shows the average number of counts for the background (corresponding to the region highlighted in the red square in the bottom inset).

diffraction orders. Moreover they are inexpensive electron detection systems. On the other hand, and as mentioned before, their detection efficiency of high energy electrons is lower in comparison to low energy electrons; it falls down to 10-60% for energies ranging from 2 keV to 50 keV. The Chevron configuration with a high input voltage on the MCP and Phosphor plates (up to 2 kV and 5 kV respectively) and gating the MCP with the camera shutter improves the signal to noise ratio.

Detector calibration: Temporal resolution

As seen in previous sections, a high charged beam does not only increase the diffraction intensity, but also elongates transversely and longitudinally the electron bunches, and consequently its duration. In order to have a direct estimation of the temporal resolution, we have calibrated the detection system by measuring the charge of the beam and simultaneously the number of counts on the detector.

The current of the electron beam was measured as a function of the laser intensity with a Faraday cup placed at the sample position and connected to a picoammeter (Keithley Series 6400) with a resolution of ±0.5 pA which corresponds to ± 590 electrons . Figure 3.11 shows the resulting maximum number of detected counts as a function of the number of electrons in the bunch. With the purpose of better estimating the maximum number of counts, the beam spot on the detector is fitted by a Voigt function along the vertical and horizontal axes after averaging over five consecutive images. Figure 3.11 clearly illustrates the linear relation between both parameters, with the value of the slope given by the linear fit m = 1.642± 0.016.

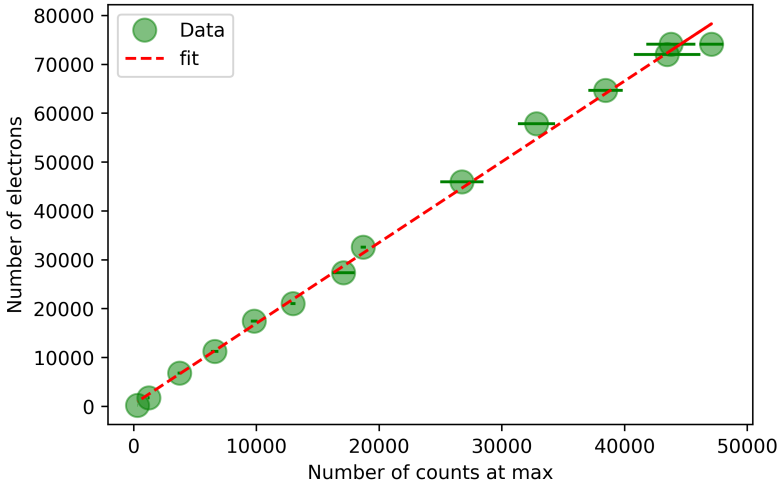

Figure 3.11: Number of electrons contained in the bunch and number of maximum counts in the detector, measured for 30 keV electron energy and 1 kV input on the MCP detector. The error bars in the number of counts are calculated from the standard deviation from the five collected images.

With the results from the fit shown in figure 3.11 it is possible to have a relation between the number of electrons and the number of counts, giving us the possibility of a direct estimation of the electron pulse duration with the GPT simulation results. The resulting conversion of number of electrons into number of counts is shown in figure 3.12. Further details on the parameters and the procedure followed are given in Appendix A.

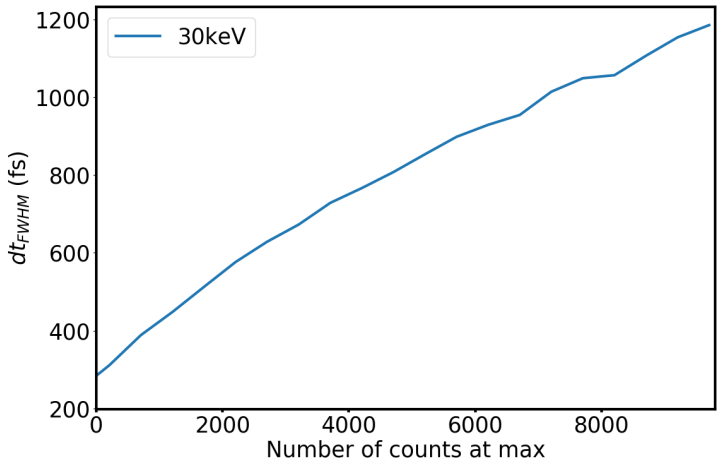

Figure 3.12: Electron pulse duration at the sample position as a function of the number of counts at maximum intensity on the detector for 30 keV electrons. The pulse duration is extracted from the GPT simulation results shown in figure 3.5.

3.1.4 Spatio-temporal pump-probe overlap

The spatio-temporal overlap between the electron beam probe and the pump is carried out by means of transient electric field effect [81]. A copper TEM grid with 400 mesh is placed at the sample position and imaged with the uncollimated electron beam. To ensure spatial overlap, the pump beam is focused on the position of the copper grid approximately from the chamber's view port. The arrival of a laser pulse of about 100 mJ/cm^2 initiates a multiphoton photoemission process on the grid surface generating a high density electron cloud. The Coulomb interaction between this electron cloud and the electron probe beam will lead to a space charge effect which deforms the image of the TEM grid, as shown in figure 3.13.

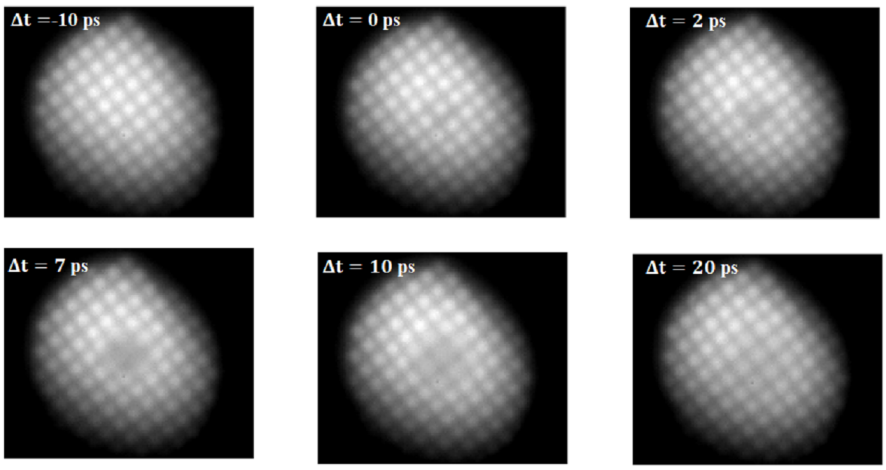

Figure 3.13: Unfocused images of the copper TEM grid at different pump-probe delays, the shadow corresponds to the region with high density of charged particles created by the arrival of intense pump pulse.

The effect of the transient electric field generated on the TEM grid is shown at different delay stage positions for the pump. As observed in the figure, this effect lasts for several picoseconds. An analysis of the RMS image changes as a function of the delay line position allows to accurately set the temporal pump-probe overlap with a precision of 500 fs [82].

3.1.5 Pump probe scan procedure

Diffraction scans on low diffracting samples can take up to several hours during which laser power drifts are unavoidable. As a way of correcting these fluctuations, the scans are performed by taking two diffracted patterns per delay time; an image with the pump illuminating the sample followed by a second image with the pump blocked. This procedure allows us to relatively compare both diffracted images and correct any possible laser fluctuations. As a way of illustrating the procedure, figure 3.14 shows the integrated intensity per position of the delay line on the direct electron beam (i.e., without sample) for one hour.

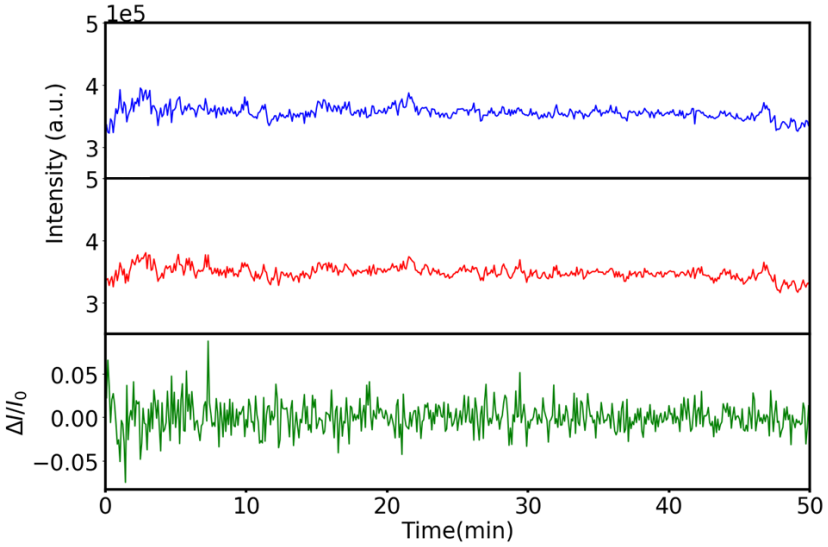

Figure 3.14: Top: Integrated intensity of the direct beam with pump (red) and without pump (blue). Bottom: relative intensity changes between images taken with and without pump, I_0 stands for the intensity recorded without pump.

The energy of the beam is 35 keV with 10000 electrons and each image is recorded with 1 second exposure time. As in the case of a regular scan, two images were taken at every position of the delay line; the blue curve depicts the integrated intensity of the direct beam with the pump beam blocked whereas the red curve represents the integrated intensity with the pump. During the length of the scan, intensity changes of the order of 5% are clearly visible. By normalizing the intensity of the pumped image with respect to the unpumped one, these changes are flattened with a RMS of 1.7% in the intensity, shown in green in figure 3.14. Thus, the lowest achievable sensitivity of intensity changes $\Delta I/I_0$ is limited to this RMS value.

3.2 Synchrotron based X-ray diffraction: CRISTAL beamline at Soleil

Since the early 1950s, the development of synchrotrons as large scale facilities has opened the door to the research of matter at the molecular and atomic scale in a vast number of fields; ranging from biology to condensed matter physics. With the recent progress in time resolved techniques, the possibility to study matter under out-of-equilibrium conditions became a reality.

In this section I give a brief introduction to a typical experimental setup for pump probe X-ray diffraction. The description is based on the CRISTAL beamline in Soleil Synchrotron, a third generation synchrotron located in France.

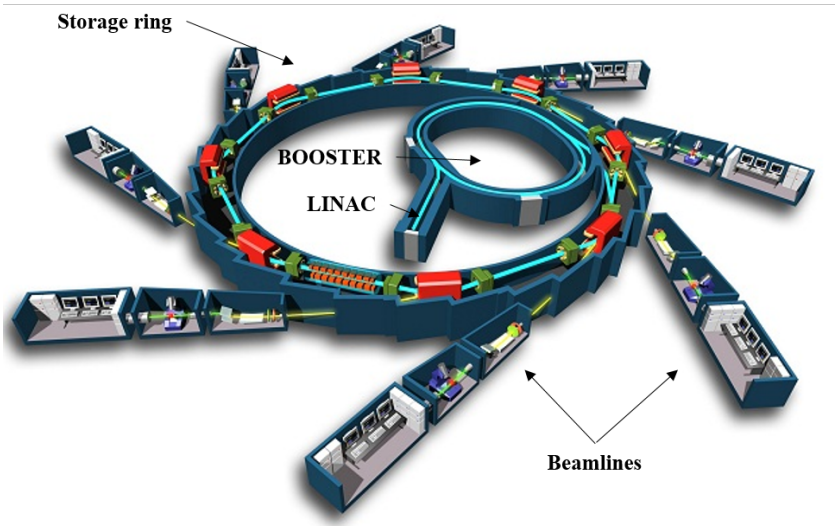

Figure 3.15: Schematic overview of the synchrotron main components.

3.2.1 Synchrotron X-ray radiation in SOLEIL

In a first step, electrons emitted from an electron gun are accelerated in a 16 meter linear accelerator (LINAC) reaching energies up to 100 MeV. The resulting beam is then inserted into a first ring called the Booster, which further accelerates the electron beam to an energy of 2.75 GeV. Finally, the accelerated electrons are injected into the storage ring with a diameter of 113 m, in which they circulate with a period of 1181.4 ns. The high energy beam is subjected to deflection and oscillation in bending magnets and undulators or wigglers. This process will ultimately control their trajectory or make them oscillate, resulting in a loss of energy into high energy photons by means of synchrotron radiation. The energies of the resulting photons range from Terahertz to hard X-ray energies. Each of the 29 beamlines in SOLEIL has optical systems that select and shape the beam into the desired wavelengths suitable for various experimental techniques. Figure 3.15 shows a scheme of the main parts of the synchrotron.

The beamline CRISTAL works within the hard X-ray range, with energies between 4 keV and 30 keV. A monocrystalline silicon monochromator, Si(111), permits to selectively choose the wavelength of interest with an energy resolution of $\Delta E/E = 10^{-4}$ and a maximal photon flux of 10^{13} photons/s in the case of 8 keV. Further technical details are given in [83].

3.2.2 Pump probe diffraction in CRISTAL

The inherent pulsed structure of the synchrotron X-ray beams allows to perform time resolved experiments. SOLEIL has four different operational modes for such experiments: hybrid mode, single bunch mode, 8 bunch mode and the low alpha mode. All of them feature an isolated bunch, i.e. a bunch that is separated from its first neighbours by at least 147 ns. The number of emitted photon per isolated pulse at a beamline depends on the current carried by the isolated

bunch. The CRISTAL beamline has the following performances:

- Hybrid mode (5 mA + 445 mA, 5 mA in the isolated bunch) // Pulse duration: 62 ps FWHM // 3.7e5 ph/pulse in a bandwidth ΔE/E = 2.4e-4
- Single-bunch mode (1×15 mA, 15 mA in the isolated bunch) // Pulse duration: 93 ps FWHM // 1.1e6 ph/pulse in a bandwidth ΔE/E = 2.4e-4
- 8-bunch mode (8×12.5 mA, 12.5 mA in an isolated bunch) // Pulse duration: 87 ps FWHM // 9.1e5 ph/pulse in a bandwidth ΔE/E = 2.4e-4
- Low-alpha mode (67 µA + 18 mA, 67 µA in the isolated bunch) // Pulse duration: 12 ps FWHM // 4700 ph/pulse in a bandwidth ΔE/E = 2.4e-4

The experimental results discussed in chapter 6 were obtained with the last two modes.

A 6-circle diffractometer in Kappa geometry is installed at the beamline. It allows controlling the orientation of the sample along four angular degrees of freedom and three translations. The accuracy of the sample positioning is of 1.5 10^{-3} degrees in the case of the rotations and 1.0 μm for the translations. The detector arm of the diffractometer can be rotated around both a vertical axis (azimuthal angle) and a horizontal axis perpendicular to the incident X-ray beam (elevation angle). This peculiarity of the diffractometer enables pump-probe diffraction experiments in grazing incidence.

The beamline is equipped with a cryostat that can lower the sample environmental temperature down to 5 K. The cryostat has three windows, a top silica window for the pump beam entrance and two Kapton windows for the entrance and exit of the scattered X-ray beam. An image and a scheme of the experimental setup in the time-resolved configuration are shown in figures 3.16 and 3.17.

The laser system source for the pump pulses has a repetition rate of 1 kHz delivering 5 mJ per pulse with a central wavelength of 800 nm with a pulse duration of 35 fs.

The illuminated area on the sample is 3.5×1.0 mm^2 by the pump beam and 1.7×0.5 mm^2 by the X-ray beam with one degree incidence with respect to the sample surface. Since the penetration depth of 8 keV X-rays is much larger than the 800 nm pump beam, the experiment is performed in grazing incidence, i.e. the angle between the probe beam and the sample surface does not exceed $\alpha_i = 2°$, translated into a penetration depth of few tens of nanometers. In this way, we ensure that the probed volume matches the photoexcited volume.

The laser and X-ray pulses are synchronized on the 352 MHz signal that runs the RF cavities of the synchrotron. The temporal overlap is achieved with a fast photodiode which is sensitive to both X-rays an IR photons (G7096-03 model from Hamamatsu). The spatial overlap is established with a fluorescent card and monitored with a camera.

The detection system consists of a 2D hybrid pixel detector, the XPAD3.2. It was developed by the collaboration between SOLEIL, the European synchrotron radiation facility (ESRF) in France, and the Centre de Physique des Particules de Marseille (CPPM). The detector is

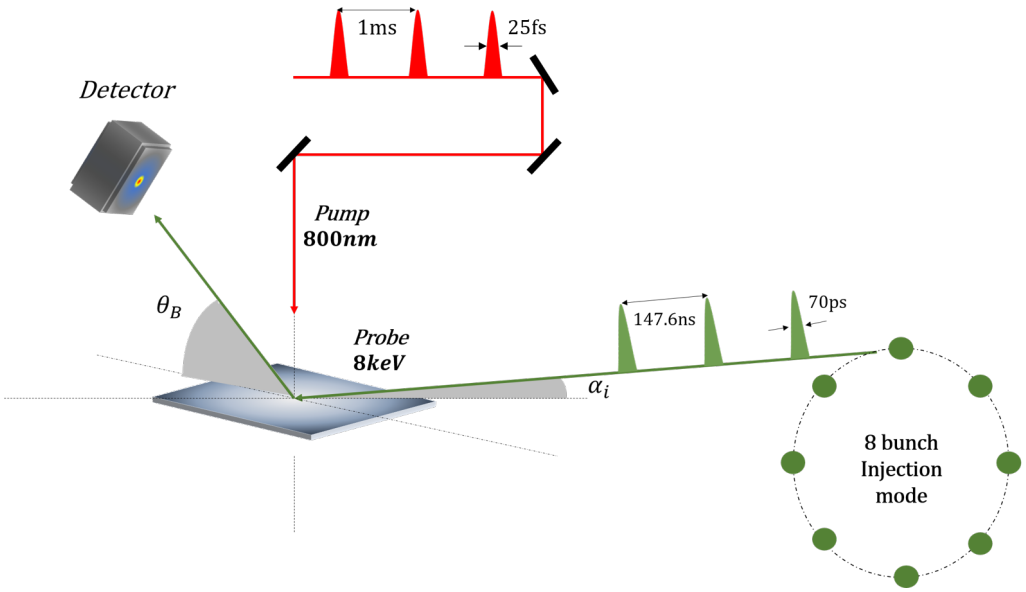

Figure 3.16: Schematics of the pump probe experimental setup in CRISTAL beamline at SOLEIL.

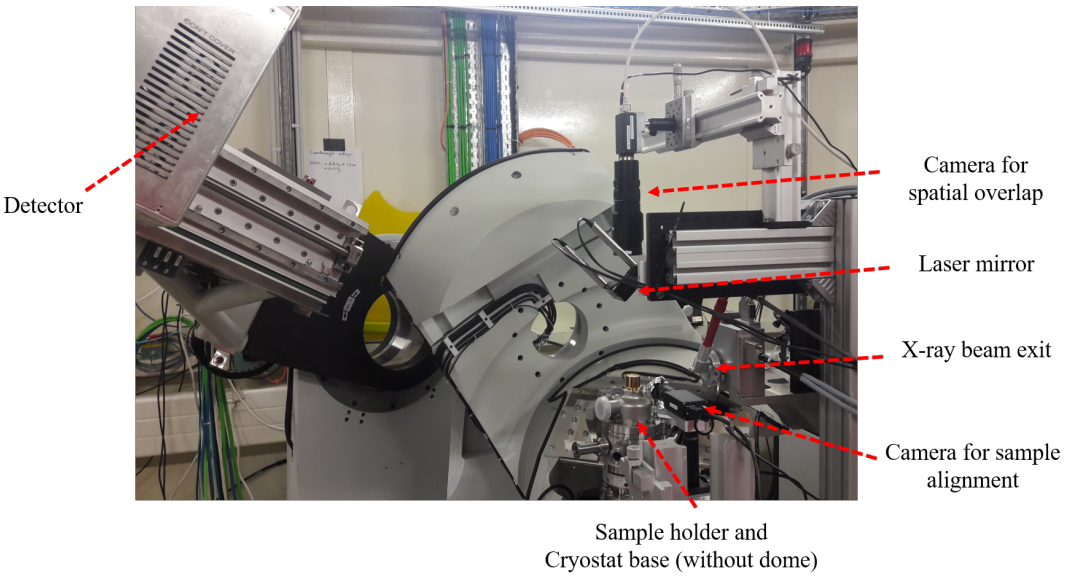

Figure 3.17: Experimental hutch at CRISTAL in time resolved diffraction mode.

divided into 8 main modules, each of them composed by 7chips of 120x80 pixels bonded to a 500 μm silicon sensor. The entire area of the detector becomes then 560x960 pixels, with a size of 130x130 μm^2 per pixel. In the time resolved experiments, the detector is triggered by an external signal in order to synchronize it with the incoming pulses. The number of counts per pixel per second in the triggered mode is reduced to few photons/pixel/s, meaning that several images must be collected per delay time in order to get sufficient intensity.

The temporal resolution of the pump-probe diffraction in CRISTAL allows us to study the structural dynamics in the picosecond range with a reciprocal spatial resolution of $\Delta Q \sim 5{\cdot}10^{-4}\mathring{A}^{-1}$. At these temporal time scales, we can mainly have access to structural phase transitions, thermal processes or strain wave propagation. Chapter 6 presents the results obtained on a second order structural phase transition performed at CRISTAL.

Chapter 4

Multiple scattering effects demonstrated in UED with free standing Si nanomembranes

Contents

The use of ultrafast electron diffraction in pump-probe experiments has proven to be very efficient for studying the dynamics of photoinduced phase transitions by measuring the relative changes of the diffraction pattern following photoexcitation [20, 21, 23, 69, 84]. Indeed, in the case of a structural phase transition, the change in the crystal symmetry can be monitored through the appearance/disappearance of Bragg peaks [21, 23].

However, a wealth of additional information is contained in the diffraction pattern, e.g., lattice heating can be estimated through the change of the Bragg peak intensity due to the Debye-Waller effect. Quantitative analysis mostly relies on the use of kinematical diffraction theory, which assumes that the scattering potential of the crystal lattice is a small perturbation, so that the probing electrons undergo a single elastic scattering event, leading to a weak diffracted intensity compared to the incident electron beam. This theory gives satisfactory results when applied to the case of polycrystalline samples where the grain size is only a few nanometers [21, 85]. It led to quasi-direct measurements of the lattice temperature with subpicosecond resolution in several materials [8, 85]. However, as high quality single crystal samples adapted to UED experiments are becoming available, kinematical theory does not appear sufficient to

explain all experimental results. Several UED studies on high quality crystals, such as silicon [29] and graphite [86], have reported large photoinduced changes of the Bragg peak intensity that cannot be explained by kinematical theory. The authors proposed that multiple scattering of the electrons must be at play but no quantitative analysis was performed to fully confirm this hypothesis.

In electron microscopy, multiple scattering is taken into account in the framework of dynamical diffraction theory [46, 47]. In high quality crystals, multiple scattering needs to be considered due to the very high elastic scattering cross section of electrons. Despite this, little attention has been given to these effects in time-resolved electron diffraction experiments. To our knowledge, multiple scattering was considered in detailed only in [87] in a UED experiment in reflection geometry designed to study surface dynamics. In this chapter we show that multiple scattering completely dominates the dynamics of the diffraction pattern in the commonly used transmission geometry.

4.1 Sample description and silicon properties

The samples presented in this chapter were fabricated by M. G. Lagally's group from University of Wisconsin-Madison. They consist of a grid of single crystal silicon nanomembranes oriented along the [001] crystallographic axis thinned out of a silicon wafer as shown in figure 4.1. The area of each membrane is $350\times\ 350\mu m^2$ with a thickness of $70\,\text{nm} \pm 2\,\text{nm}$, which was characterized by convergent beam electron diffraction [56] at the CEMES laboratory in Toulouse (see Appendix C for details). Their high quality, reduced thickness and large surface, make these samples the perfect candidates for ultrafast electron diffraction.

The crystalline structure of silicon is arranged in a diamond cubic lattice with a lattice parameter of a = 5.431 $\AA$ at T = 300 K. From a diffraction point of view, it is interesting to keep in mind the value of its structure factor. The diamond unit cell is described by two FCC cells with atomic positions located at (000), $(0\frac{1}{2}\frac{1}{2})$, $(\frac{1}{2}0\frac{1}{2})$, $(\frac{1}{2}\frac{1}{2}0)$ and $(\frac{1}{4}\frac{1}{4}\frac{1}{4})$, $(\frac{1}{4}\frac{3}{4}\frac{1}{4})$, $(\frac{3}{4}\frac{1}{4}\frac{3}{4})$, $(\frac{1}{4}\frac{3}{4}\frac{3}{4})$,

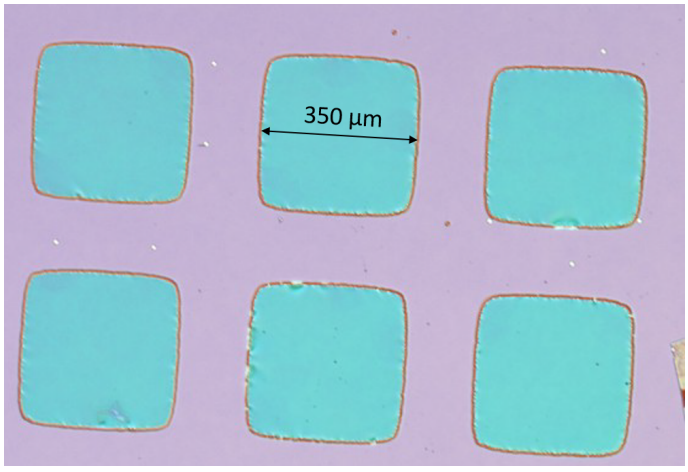

Figure 4.1: Optical microscope image of the free standing 70 nm membranes of single crystal silicon on a silicon wafer matrix. The size of each membrane is $350\,\mu m \times 350\,\mu m$.

resulting in a structure factor of:

$$F_{hkl} = f_{Si}(1 + e^{i\pi(h+k)} + e^{i\pi(k+l)} + e^{i\pi(h+l)} + e^{i\pi(h+k+l)/2}[1 + e^{i\pi(h+k)} + e^{i\pi(k+l)} + e^{i\pi(h+l)}])$$
$$= f_{Si}[1 + e^{i\pi(h+k+l)/2}][1 + e^{i\pi(h+k)} + e^{i\pi(k+l)} + e^{i\pi(h+l)}]$$

where f_{Si} is the atomic form factor of silicon. Therefore, diffraction occurs for those planes which fulfill the following conditions:

- $h+k+l = 4n$ and all h,k,l even
- $h+k+l = 4n+1$ and all h,k,l odd.

with n integer. In the case of our sample, oriented along the [001] axis, $l = 0$, so diffraction condition occurs with $h+k = 4n$, where h, k are both even, resulting in a structure factor of $F_{hkl} = 8f_{Si}$, which is the maximum attainable value in this structure. This means that the intensity of our diffracted peaks can only decrease after pump arrival. As we will see, this is quite different to what we have measured.

The electronic band structure of monocristalline silicon, on the other side, is characterized by an indirect bandgap of $E_g = 1.12\,\text{eV}$ and a direct bandgap along the Γ point of about 3 eV as shown in figure 4.1. In order to excite electrons from the conduction band to the valence band, the energy of the pump beam should be comparable to the direct bandgap, hence in our experiments we work with a pump wavelength of $\lambda = 400\,\text{nm}$, i.e., $\hbar\omega \sim 3\,\text{eV}$.

Some other relevant parameters of silicon which will be used in the chapter (related to thermal, optical or elastic properties) are listed in the table below.

Parameter	Value
Lattice parameter $a(\mathring{A})$	5.43
Debye temperature $\theta_D(K)$	645
Density $\rho(g/cm^3)$	2.33
Absorption coefficient $\alpha(cm^{-1})$	$2{\cdot}10^5$
Stiffness constant $C_{11}(dyn/cm^2)$	$16.60 \cdot 10^{11}$
Penetration depth $\delta(nm)$	50

Table 4.1: Silicon thermal, optical and elastic values. ***Note****: values given for the absorption coefficient and the penetration depth correspond to a wavelength of* $\lambda = 400\,nm$.

Expected lattice dynamical response

Before discussing the experimental results, the expected response of the lattice following photoexcitation is reviewed. It can be divided into:

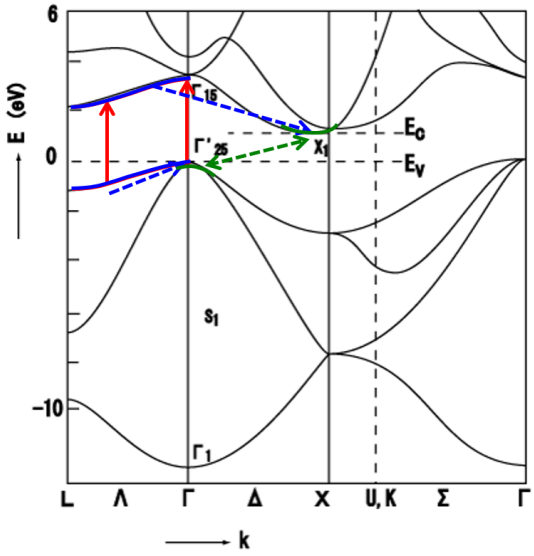

Figure 4.2: Calculated electronic band structure of silicon, adapted from [88]. Red, blue and green arrows represent the schematic excitation and relaxation pathways after pump arrival.

- Carrier excitation upon pump arrival creating two subsystems of hot electrons and holes (red arrows in figure 4.2).
- Carrier thermalization via electron-electron scattering within the first 100 fs, leading to an increase of the electronic temperature [89].
- Relaxation of excited carriers through electron-phonon coupling causing an increase of the lattice temperature (blue arrows) [85, 90]: electrons (holes) relax to the bottom (top) of the conduction (valence) band.
- Excitation of longitudinal acoustic modes propagating along the thickness of the sample [29].
- Further lattice temperature increase results from electron hole pair recombination through the gap, via Auger recombination [91] (green arrow).
- Long thermal diffusion process in a scale of $\sim 100\,\mu$s [29].

Thus, the expected lattice dynamics will display in the diffracted pattern the effects of lattice temperature increase and the presence of excited coherent modes.

The lattice temperature increase can be estimated from the following relation [85]:

$$\Delta T = F_{abs}\left(1 - \frac{E_g}{h\nu}\right)\frac{1}{L\rho}\frac{1}{C_v} \tag{4.1}$$

where E_g denotes the band gap energy, L the thickness of the sample, ρ the material density and C_v the heat capacity, with F_{abs} the absorbed fluence given by:

$$F_{abs} = F_{inc}(1-R)(1-e^{-\alpha L})(1+Re^{-\alpha L})$$

where α is the absorption coefficient, $R = 0.5$ the reflectivity. The estimated lattice temperature increase from equation 4.1 results in $\Delta T = 280$ K. The lattice temperature increase after Auger

recombination becomes:

$$\Delta T = F_{abs}\frac{1}{L\rho}\frac{1}{C_v} \tag{4.2}$$

Ab initio calculations [92] performed by our collaborator B. Arnaud from Université du Mans, confirmed this value. By assuming that the number of electron-holes pairs remains constant after their relaxation to the top of the valence band and bottom of the conduction band [93], respectively, the temperature lattice increase was derived from:

$$\int_{T_{l,0}}^{T_{l,max}} C_V(T_l)dT_l = \Delta E(T_{e,max}) - \Delta E(T_{l,max})$$

where $\Delta E(T_{e,max}) = F_{abs}\frac{v}{L} = 2690\,K$, being $v = a^3/4$ the volume of the primitive cell and L the thickness of the membrane. The specific heat $C_v(T_l)$ per unit cell was calculated from the phonon spectrum of silicon, leading to a lattice temperature increase of $\Delta T_l \sim 240$ K, in good agreement with the estimated value above.

Additional lattice heating occurring from Auger recombination through the band gap is known as the dominant recombination mechanism [91]. The number of initial excited carriers can be estimated from:

$$n_{exc_0} = \frac{F_{abs}}{L\hbar\omega} = 1.8\cdot 10^{21}\,cm^{-3}$$

with L the thickness of the sample and $\hbar\omega$ the energy of the pump pulse. The dynamics of the excited carriers is governed by the following equation $dn_{exc}/dt = -(C_e + C_h)n_{exc}^3$ where C_e and C_h are the Auger coefficients for electrons and holes respectively. Following Dziewior and Schmid [94], we used $C_e + C_h = 3.8\cdot 10^{-31}$ cm^{6}s^{-1}, and solving the equation from the excited carriers:

$$n_{exc}(t) = \frac{n_{exc_0}}{\left(1 + {}^{t}/_{\tau}\right)^{1/2}}$$

where

$$\tau = \frac{1}{2Cn_{exc_0}^2}$$

and

$$C = C_e + C_h$$

We find that the 94% of the Auger recombination occurs within the first 100 ps. Therefore, at this time delay we estimate a lattice temperature increase of $\Delta T_l = 460$ K. After Auger recombination, the system reaches a metastable state as heat diffusion occurs on the microsecond time scale for our sample geometry. This results are in agreement with those obtained by Harb *et al.* in a polycrystalline silicon sample [95].

Under the precedent assumptions, a decrease of the Bragg peak intensities is expected through the well known Debye-Waller effect (see section 2.1.1); the lattice temperature increase

results in atomic vibrations characterized by a mean-squared displacement $< u^2 >$, which in the case of a cubic crystal within the Debye model becomes [44]:

$$< u^2 >= \frac{9\hbar^2 \Delta T^2}{m_A k_B \Theta_D^3} \int_0^{\frac{\Theta_D}{T}} \left[\frac{1}{e^{\xi}-1} + \frac{1}{2}\right] \xi d\xi$$

where m_A is the atomic mass and Θ_D the Debye temperature. The diffracted intensity of a given *(hkl)* Bragg peak at a certain temperature T_l reads:

$$I_{hkl}(T_l) = I_{hkl}(T_0) e^{-\frac{1}{2}<u^2> g_{hkl}^2} = I_{hkl}(T_0) e^{-M}$$

with $T_0 = 300\,\mathrm{K}$ the initial lattice temperature, g_{hkl} the scattering vector corresponding to the *(hkl)* plane and M the Debye-Waller factor.

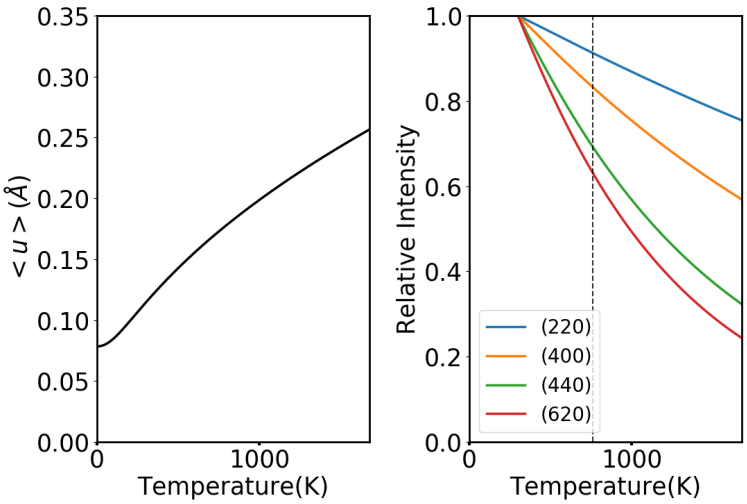

Figure 4.3: Left: Mean squared displacement of a single silicon atom as a function of the temperature. Right: Relative intensity of the Bragg peaks as a function of the temperature. The dashed line indicates $\Delta T = 460\,K$.

By assuming a lattice temperature increase of ΔT_l =460 K, the intensity of the first order diffracted peaks, i.e., the (220) peaks should decrease by about 10 % (see figure 4.3). Furthermore, temperature increase leads to thermal expansion of the lattice parameter. Considering the linear thermal expansion coefficient of silicon given by [96] $\kappa = 2.6 \cdot 10^{-6}\,K^{-1}$, an increase of $\Delta T_l = 460\,\mathrm{K}$ leads to a lattice parameter change of $da/a = \kappa \Delta T_l = 0.12\,\%$, which is in any case, below our experimental resolution, as shown in chapter 4.

Finally, optical excitation of acoustic coherent modes are expected as reported in the work of M. Harb et al. [29]. In their experimental results, the authors observed clear oscillations in the time resolved curves arising from the excitation of transverse and longitudinal acoustic

modes, characterized by sound velocities of $v_T = \sqrt{\frac{C_{44}}{\rho}} = 5850\,\text{m/s}$ and $v_L = \sqrt{\frac{C_{11}}{\rho}} = 8440\,\text{m/s}$, respectively.

Summarizing, following photoexcitation, we expect to observe a decrease of the Bragg peaks intensities due to lattice heating. Contrary to these expectations, and as shown in our experimental results, we observed a giant photoinduced response with an unexpected increase of the diffraction intensities, which, as we have seen, is in contradiction to the Debye-Waller effect.

4.2 Experimental results

All the experimental results presented here were obtained at room temperature with a different set of incident fluences ranging $F \in [4-12]\,\text{mJ/cm}^2$ and an electron energy of U = 45 keV. The charge of the electron bunch beam is <1 fC, resulting in a temporal resolution of ~300 fs and an electron spot size of 150 μm. The pump spot size at the sample is adjusted to a FWHM = 500 μm to ensure homogeneous excitation of the nanomembranes.

4.2.1 Bragg dynamics on nanosecond time scale

We start by analyzing the photoexcited response of the (2-20) Bragg peak and the transmitted electron beam on the nanosecond time scale. The sample was oriented so that the Bragg condition was fulfilled for the (2-20) peak. The left side of figure 4.4 shows the relative changes of the integrated intensity of the Bragg and direct peak as a function of the delay time between pump and probe at different incident fluences[1]. The right side shows the corresponding diffraction pattern before pump excitation.

The first paramount observation is the intensity of the diffracted Bragg peak, which is of the same order of magnitude as the transmitted beam. This clearly violates the kinematical diffraction assumptions, in which the diffracted intensity should be several orders of magnitude weaker than the transmitted beam. Moreover, the intensity changes on the Bragg peak become positive after photoexcitation and increase with incident fluence. On the contrary, and as seen before, the expected dynamics pointed rather to an increase of the lattice temperature manifested in the diffraction pattern by a decrease of the Bragg peak intensities due to the Debye-Waller effect. On the other hand, the transmitted beam shows the opposite behaviour; larger negative intensity changes for higher incident fluences.

The dynamics of the peaks can be fitted by the phenomenological function involving three

[1] I_0 stands for the integrated intensity of the peaks with the pump beam blocked.

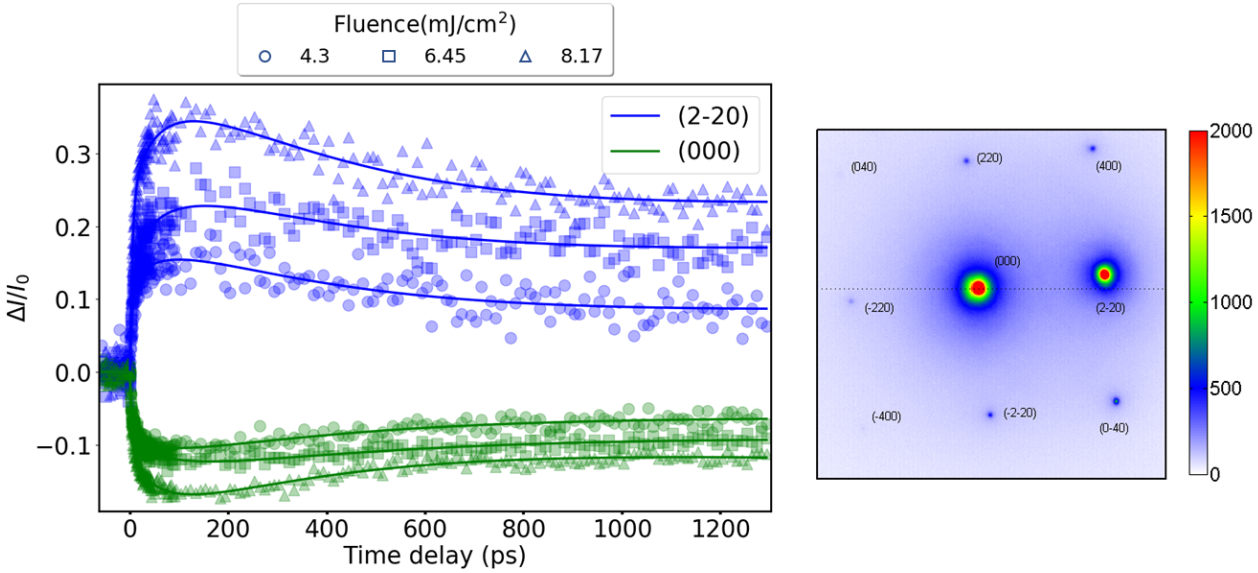

Figure 4.4: ***Left:*** *Temporal dynamics of the relative Bragg intensities (blue) and the direct beam (green) as a function of the incident fluence.* ***Right:*** *Diffraction pattern with the (2-20) peak in Bragg condition. The direct beam is referred as the (000).*

processes of the form:

$$\frac{\Delta I}{I_0} = A_1(1-e^{-t/\tau_1})H(t) + A_2\left(1-\frac{1}{\sqrt{1+(t-t_0)/\tau_2}}\right)H(t-t_0) + A_3(e^{-t/\tau_3}-1)H(t-t_0) \qquad (4.3)$$

where $H(t)$ accounts for the Heaviside function centered at $t_0 = 0$. Under the assumptions made for the photoexcitation and relaxation processes, the first term accounts for electron-phonon scattering with a typical time scale of τ_1 =5 ± 1 ps. The second term accounts for the dynamics of Auger recombination which takes the form of the solution to the equation $\frac{dn_{exc}}{dt} = -Cn_{exc}^3$, resulting in a time constant of $\tau_2 = 53 \pm 5$ ps and followed by a slower cooling process with $\tau_3 = 450 \pm 50$ ps. Note that we impose that the second and third processes occur after the first process through the use of the Heaviside function $H(t-t_0)$ with $t_0 = 2\tau_1$.

Although this phenomenological model fits accurately the temporal dynamics of the Bragg and the transmitted peaks, the mechanism behind the intriguing large positive changes of the Bragg peak remains unexplained. In order to get further insights, we have performed pump-probe scans at different angles of incidence between the electron beam and the sample.

4.2.2 Bragg dynamics at different angles of incidence

Firstly, we start by analyzing the dynamics of the symmetric diffraction pattern, i.e., the sample is oriented normal to the electron beam, as shown in figure 4.5. Strikingly, the behaviour at this

angle of incidence is opposite to the one presented in figure 4.4. The relative intensity $\Delta I/I_0$ of all Bragg peaks starts with a sharp decrease on the picosecond time scale which is followed by a slower roll-off and further decrease on the 10 ps time scale. The transmitted electron beam, on the other hand, shows an increase of the intensity with similar time scales.

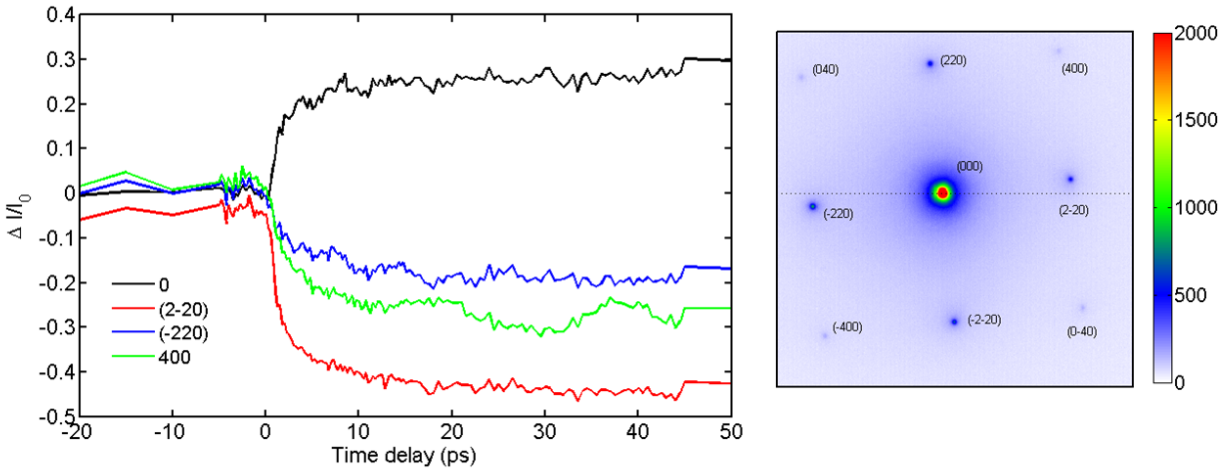

Figure 4.5: Result of a pump-probe scan with incident fluence $F = 12\,mJ/cm^2$ showing the relative intensity changes of various Bragg peaks $\Delta I/I_0$ and the corresponding diffraction pattern.

Figure 4.6 illustrates the integrated intensity changes at different angles of incidence between the electron beam and the normal to the surface. The top graph shows the direct beam whereas the (2-20) peak is depicted in the bottom. These results highlight the importance of sample orientation; it can lead to changes of $\Delta I/I_0$ from -40% to +60% depending on the angle of incidence. Moreover, the intensity of the transmitted beam decreases or increases in a manner that is complementary to the Bragg peak intensity.

In this case, since the scans were taken on a much shorter temporal range, the fits were performed by neglecting the last term in equation 4.3. The effect of the angle of incidence on the time constants is only marginal with values of $\tau_1 = 3-5$ ps being shorter when the peak is out of Bragg condition. The second time constant remains $\tau_2 = 59$ ps for all cases. Only the curve with $\theta_B + \delta\theta$ results in longer time decays with $\tau_1 = 18$ ps. Overall, this shows that the angle of incidence does not play an important role in the temporal dynamics of the diffracted Bragg peaks.

The signature of excitation of coherent acoustic modes can be observed in the temporal evolution of the intensity of the (400) Bragg peak, which was clearly visible only at certain angles as shown in figure 4.7. Although the scans were not taken in a sufficiently long range, it is possible to discern a first period with T~17 ps. Considering a strain pulse bouncing back and forth between the Si-film edges, its velocity can be calculated from the thickness of our sample and the period

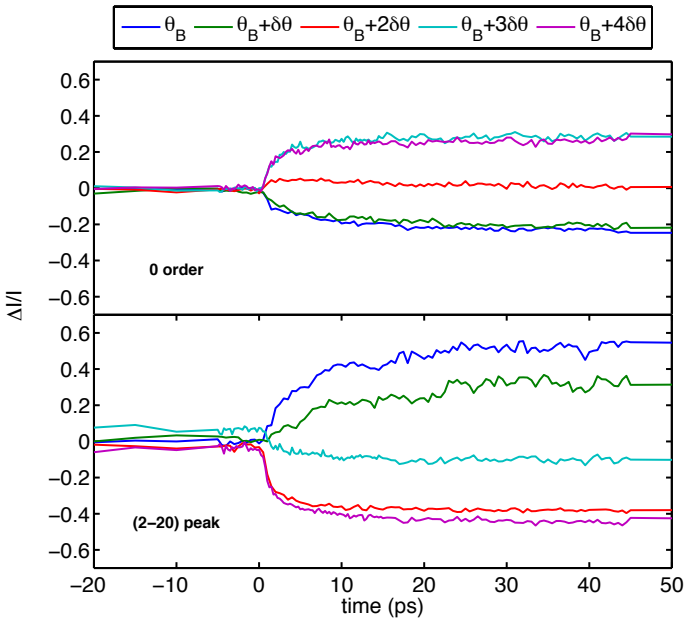

Figure 4.6: Photo-induced dynamics for various angles of incidence. The blue curve is obtained when the sample is exactly at the Bragg angle for the (2-20) peak; the other curves are obtained by tilting the sample by steps of $\delta\theta = 0.26°$. The incident fluence is $F = 12\,mJ/m^2$ with an electron energy of 45 keV. Top: dynamics of the direct beam. Bottom: dynamics of the Bragg peak.

of oscillation by $v = \frac{2L}{T}$ resulting in a value of $v \sim 8235$ m/s, which is in close agreement with the longitudinal acoustic mode of silicon with $v = 8440$ m/s [43].

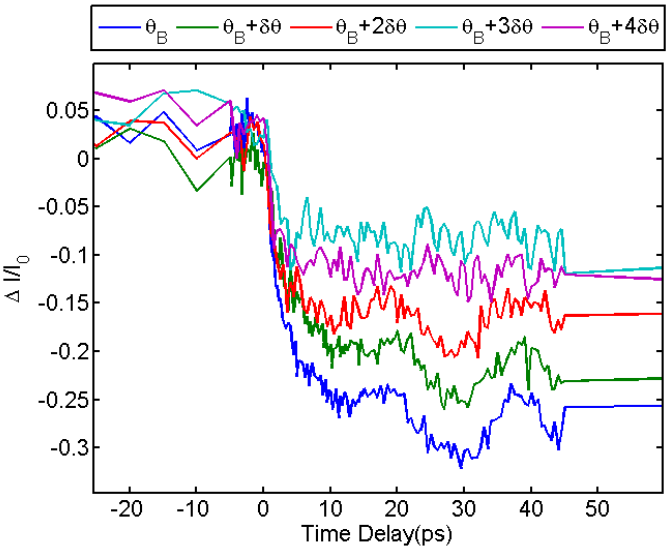

Figure 4.7: Photo-induced dynamics for various angles of incidence on the (400) Bragg peaks. Note that the angles of incidence are those corresponding to the (2-20) Bragg, as in figure 4.6. The incident fluence is $F = 12\,mJ/m^2$ with an electron energy of 45 keV.

4.2.3 Rocking curve scans

The precedent results show the need of study in more depth the behaviour of the sample as a function of the incidence angle. To do so we have performed rocking scans, which consist

in tilting the sample around its center of rotation. The sample was mounted in a way that the $(h+k)$ planes were lying horizontally on the diffraction pattern. For the purpose of comparing equilibrium and photoexcited states, we chose the temporal range in which the lattice dynamics are in the quasi-equilibrium state due to the long thermal diffusion process (of the order of $\sim$100 μs) involved in the relaxation. Accordingly, the delay line was fixed at a delay time between pump and probe of 150 ps, and the sample was scanned from $\Delta\theta \sim -0.5°$ to $\Delta\theta \sim 2.5°$.[2]

Figure 4.8 shows the diffraction pattern at different angles of incidence. In the same way as in figure 4.6, the intensity of the diffracted peaks are strongly dependent on the angle of incidence between the electron beam and the surface plane.

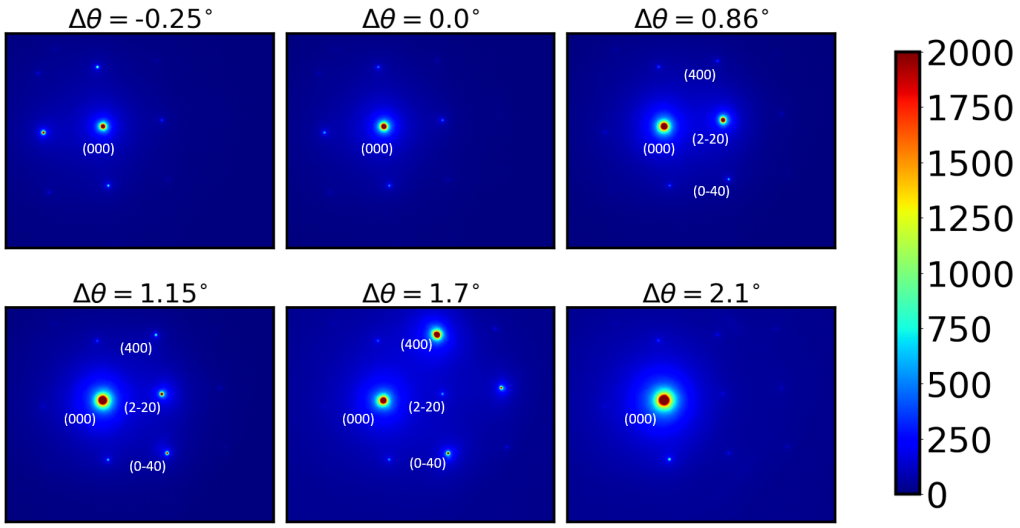

Figure 4.8: Static diffraction patterns at different angles of incidence acquired with an electron beam energy of 45 keV on a 70 nm silicon membrane. $\Delta\theta = 0°$ is assigned to the symmetric pattern.

As the angle of incidence is increased, new planes come into the Bragg condition. Remarkably, the intensity of the transmitted beam is of the same order of magnitude as the peaks at Bragg condition, as clearly seen at $\Delta\theta = 0.86°$ and $\Delta\theta = 1.7°$. These effects are the primary signature of multiple scattering in a dynamical diffraction process.

Figure 4.9 depicts the rocking curve of the (2-20) peak at equilibrium (i.e., at 300 K, blue curves) and in the photoexcited state (red curves) taken 150 ps after the arrival of the pump pulse, i.e., after thermalization of the sample has occurred. Rocking curves are shown at two

[2]Here we consider $\Delta\theta = 0°$ as the symmetric diffraction pattern.

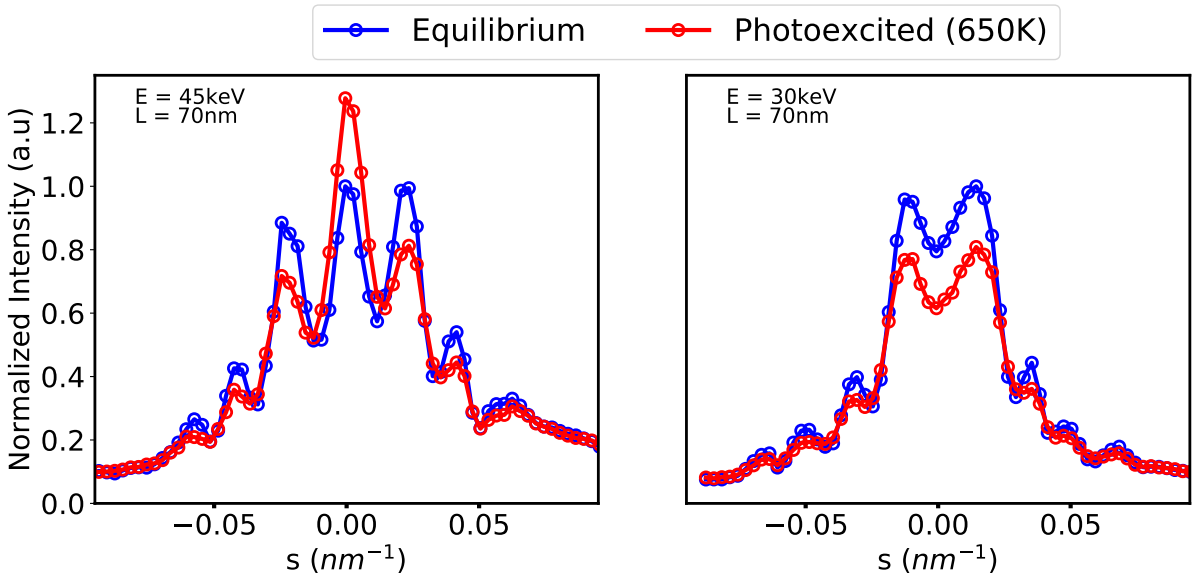

Figure 4.9: Left: Experimental rocking curves for the (2-20) peak taken with 45 keV electrons, at equilibrium $T = 300\,K$ (blue curve) and in the photoexcited state (red curve), taken at $t = 150\,ps$ delay with an incident fluence of $F = 12\,mJ/cm^2$. Right: Same but using 30 keV electrons as a probe. The rocking curves were normalized relative to the equilibrium case.

different electron energies. We plot the Bragg peak intensity $I(s)$, where s is the amplitude of the deviation vector $\mathbf{s} = \Delta\mathbf{k} - \mathbf{g}$ and $\mathbf{g}$ the lattice reciprocal vector corresponding to the (2-20) peak. Figure 4.9 clearly shows that the shape and magnitude of the rocking curve change upon photoexcitation. However, there is no angular shift of the rocking curve upon photoexcitation, so we can assure that lattice expansion and sample distortion are not the main mechanisms taking place. In addition, the results of figure 4.9 summarize and clarify the surprising features of figure 4.4: for 45 keV electrons, the intensity change is positive at the Bragg angle, whereas it is negative for most off-Bragg cases. For 30 keV electrons, the behavior is quite different: here the intensity change is always negative after photoexcitation. The shape of these rocking curves, by departing from the usual sin^2x/x^2 line shape of kinematical theory, indicates that dynamical effects are dominating the physics of electron diffraction, even at equilibrium, presenting the oscillatory fringe pattern characteristic of multiple scattering.

Another way of corroborating the presence of multiple scattering effects, is by plotting the intensities of all diffracted and transmitted peaks as a function of the angle of incidence, as shown in figure 4.10. The intensity of the transmitted beam is strongly dependent on the diffracted peaks, showing a complementary fringe pattern with respect to the Bragg peaks. Furthermore, the shape of the transmitted curve displays a clear asymmetry around the θ_B(2-20); this effect is another characteristic of dynamical effects arising from inelastic scattering (known as anomalous absorption or simply absorption) [46, 97].

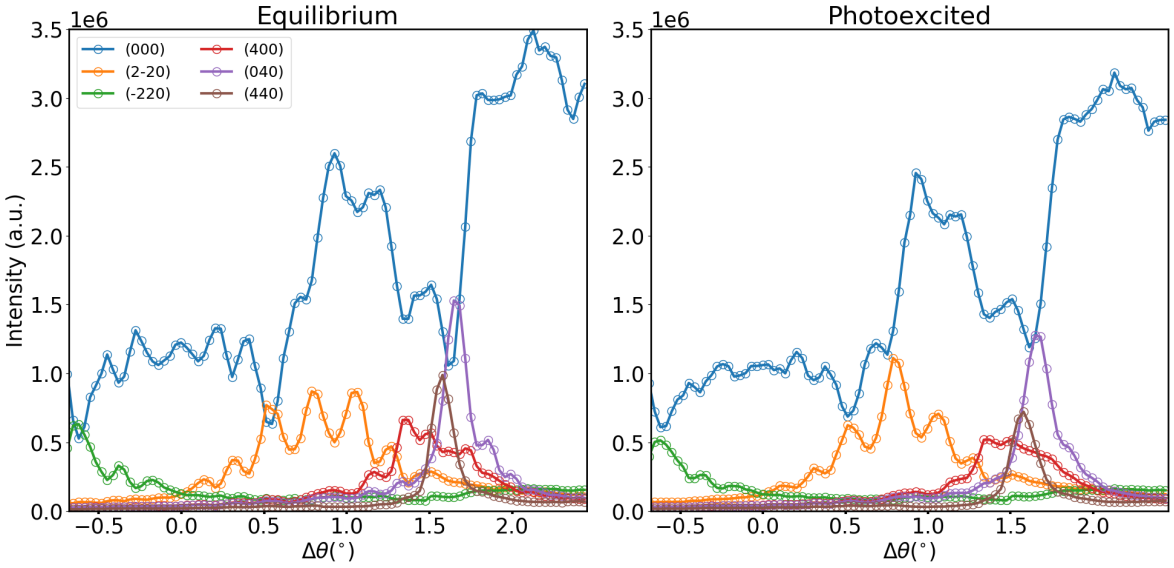

Figure 4.10: Integrated intensity of the diffracted peaks as a function of the angle of incidence, at equilibrium (left) and after photoexcitation at 150 ps time delay with an incident fluence of $F = 12\,mJ/cm^2$ (right). The sample is 70 nm, the diffraction pattern was recorded with an electron energy of 45 keV.

4.3 Discussion

As seen in chapter 2, dynamical diffraction is characterized by the strong interaction between the atomic potential and the electrons, which due to the charged particle nature of the beam, are much stronger than the X-ray-crystal interactions (usually described in terms of kinematical diffraction). Contrary to the simple two-beam approximation presented in section 2.1.2, our experimental data clearly shows the presence of other strongly diffracted beams. This becomes evident in figure 4.10 where the intensity of the (2-20) Bragg peak is influenced by other Bragg peaks as the (400), (040) and (440). The diffracted intensity of the (2-20) Bragg peak is transferred back and forth between several beams along the thickness of the sample. In order to properly fit our data, we have therefore to consider several beam solutions for the Howie-Whelan equations 2.22.

Moreover, the presence of inelastic scattering increases the background signal on the diffracted (2-20) peak, also apparent from the asymmetry of the transmitted beam around the Bragg angle θ_B(2-20). The absorption factors in dynamically diffracted intensities are usually modelled by considering the crystal potential as a complex value (and so, the extinction distance). The imaginary part of the extinction distance becomes then the *absorption distance* [46, 47, 97]. Since other effects might contribute as well to the increase of the background signal, we will use instead a phenomenological gaussian background to model the experimental (2-20) rocking curves [54].

Simulated dynamical diffraction rocking curves

In order to simulate the rocking curves in the equilibrium and photoexcited states, we have solved the Howie-Whelan equations which describe the evolution of the scattered wave intensities during the propagation of the electron beam into the sample with the form [46, 98]:

$$\frac{\partial \phi_{\mathbf{g}}}{\partial z} = i s_{\mathbf{g}} \phi_{\mathbf{g}} + \sum_{\mathbf{g}' \neq \mathbf{g}} \frac{i}{2\xi_{\mathbf{g}-\mathbf{g}'}} \phi_{\mathbf{g}'} \tag{4.4}$$

Here, $\phi_{\mathbf{g}}$ is the amplitude of the scattered wave in diffraction peak corresponding to vector $\mathbf{g}$, z the thickness of the sample, $s_{\mathbf{g}}$ the deviation error which depends on the crystal orientation and $\xi_{\mathbf{g}-\mathbf{g}'}$ the extinction distance. As seen before, the extinction distance is directly related to the crystal scattering potential by the following relation:

$$\xi_{\mathbf{g}-\mathbf{g}'} = \frac{1}{\lambda} \frac{2\hbar^2}{m_e U_{\mathbf{g}-\mathbf{g}'}} \tag{4.5}$$

where $U_{\mathbf{g}}$ is the Fourier component corresponding to $\mathbf{g}$, which describes the entire crystal potential as $V(r) = \sum_{\mathbf{g}} U_{\mathbf{g}} e^{i\mathbf{g}\cdot\mathbf{r}}$. In our case, we extracted the $U_{\mathbf{g}}$ matrix for the silicon potential from the code JEMS [99].

To account for the changes of the intensity in the photoexcited curves, we have simply considered the Debye-Waller factor M in the crystal scattering potential as [100, 101]:

$$V'(r) = V(r)e^{-M} = \sum_{\mathbf{g}} U_{\mathbf{g}} e^{i\mathbf{g}\cdot\mathbf{r}} e^{-M}$$

Therefore, the influence of temperature changes in the crystal potential increases the extinction distance (see equation 2.31), which ultimately determines the intensity of the diffracted beam. This mechanism is responsible for the non-intuitive intensity increase with temperature.
The system of N coupled differential equations can be written in matrix form:

$$\frac{d\Phi}{dz} = iM\Phi \tag{4.6}$$

where Φ is a column vector of length N and M is a $N \times N$ matrix that can be decomposed as

$$M = \begin{pmatrix} 0 & 0 & 0 & \cdots \\ 0 & s_{g_1} & 0 & \cdots \\ 0 & 0 & s_{g_2} & \cdots \\ \vdots & \vdots & & \ddots \end{pmatrix} + \frac{\gamma m_e}{2\pi\hbar^2}\lambda \begin{pmatrix} 0 & U_{-g_1} & U_{-g_2} & U_{-g_3} & \cdots \\ U_{g_1} & 0 & U_{g_1-g_2} & U_{g_1-g_3} & \cdots \\ U_{g_2} & U_{g_2-g_1} & 0 & U_{g_2-g_3} & \cdots \\ \vdots & \vdots & & \ddots & \end{pmatrix}$$

where $\gamma = 1 + E/mc^2$ is the Lorentz factor of an electron with kinetic energy E.
The left matrix is diagonal and its elements are the amplitudes of the deviation vectors for each diffraction peak $s_{\mathbf{g}-\mathbf{g}'}$. The right matrix is composed of the Fourier amplitudes $U_{\mathbf{g}-\mathbf{g}'}$. This is an eigenvalue problem and the solution is found by diagonalizing matrix M. If D is the diagonal

matrix in the basis of eigenvectors and C is the matrix for changing basis, we have $M = CDC^{-1}$ and the solution of the problem is given by

$$\Phi(z) = Ce^{iDz}C^{-1}\Phi(0)$$

This general solution allows us to compute the amplitude of the various diffracted peaks $\phi_{\mathbf{g}}(L)$ at the output of the crystal, $z = L$. We modelled the experiment considering $N = 26$ beams, including all (220), (400), (440), (620) peaks and a few higher order peaks as well. Such a high number of beams was necessary to ensure the convergence in the shape of the (220) rocking curve. Note that there are no free parameters in this model.

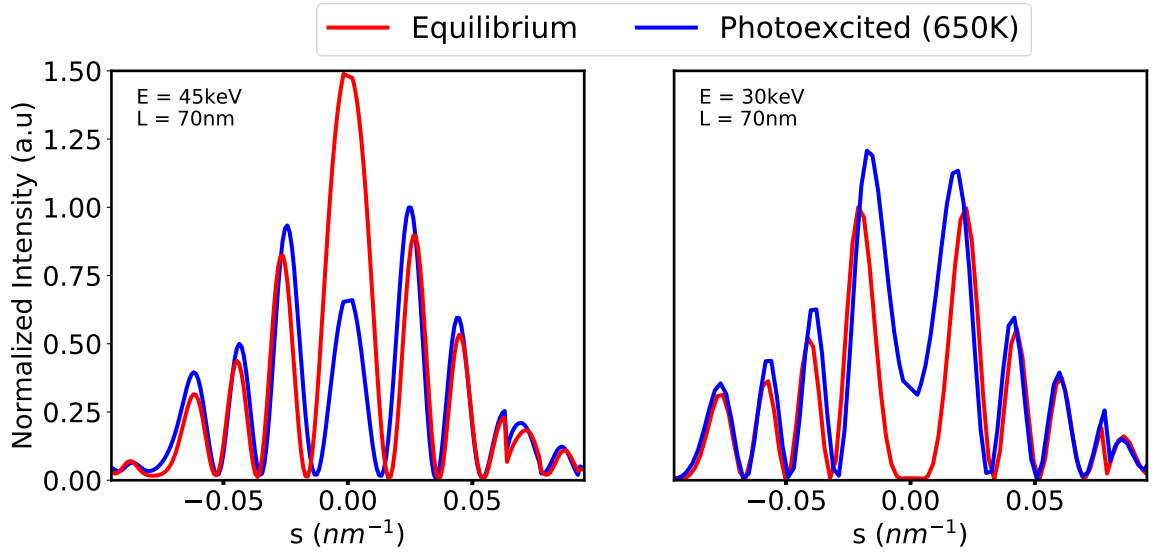

Figure 4.11: Simulated rocking curves via dynamical diffraction theory with the parameters from the experimental rocking curves without background contribution.

Figures 4.11 and 4.12 show the results of the calculations with the experimental electron energies and thickness parameters. The experimental trends are well reproduced: the shapes of the calculated rocking curves are similar to the experimental ones. In particular, the signs of the relative intensity changes are well reproduced.

It is important to point out that the results given directly by the Howie-Whelan equations (considering only the real part of the crystalline potential) do not consider the influence of anomalous absorption or thermal diffuse scattering [102], as seen in figure 4.11, which generally gives rise to a background intensity in the rocking curves. Experimentally, the background signal may arise from many factors, such as inelastic scattering (on phonons, plasmons, defects...), surface contamination or surface amorphization. Because of the difficulty of modeling all these effects, we turn to a phenomenological approach and model the background using a simple

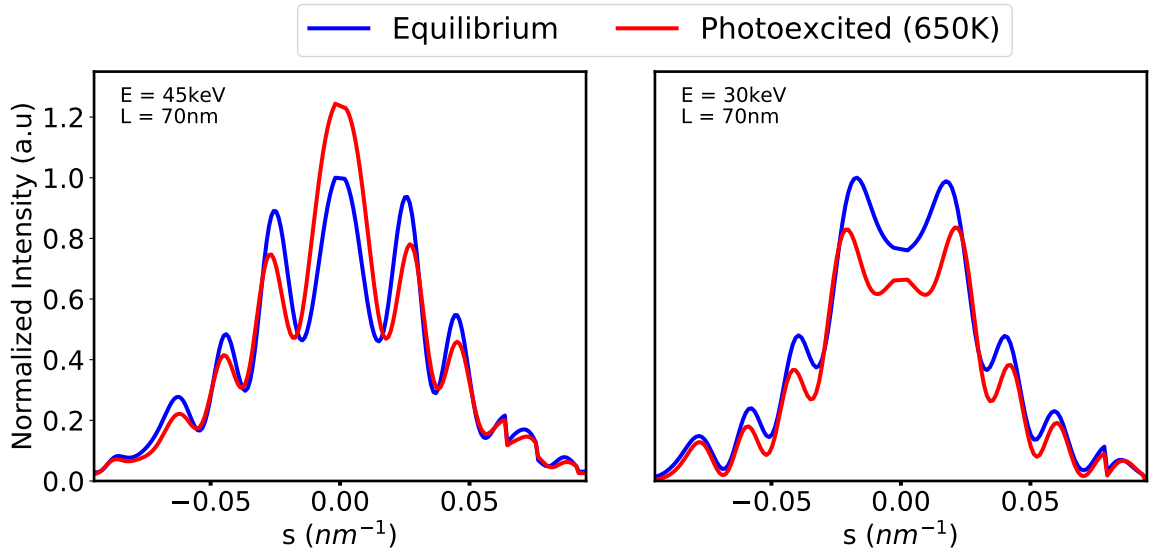

Figure 4.12: Modelled rocking curves via dynamical diffraction theory with the parameters from the experimental rocking curves considering a phenomenological background.

gaussian distribution. We were able to obtain a quantitative fit of the experimental data using the following function:

$$I(s) = AI_{dyn} + Be^{-s^2/\sigma^2}$$

where I_{dyn} is given by dynamical theory (no free parameters) and A, B and σ are free parameters. The presented model allowed us to simulate quite accurately the shapes of the experimental rocking curves at equilibrium and photoexcited states at the different electron energies, as shown in figure 4.12.

4.4 Results on a 30 nm thickness sample

In order to test the robustness of our interpretation, we performed measurements on a 30 nm sample at 30 keV with an incident fluence of 12 mJ/cm^2. Figure 4.13 shows the rocking curve including the intensities of several diffracted peaks in a range from $\Delta\theta = -2.5°$ to $\Delta\theta = 2.5°$. As in the previous sample, the intensity of the transmitted beam is strongly dependent on the intensities of the diffracted peaks, which have as before, an intensity of the same order of magnitude.

The estimated lattice temperature increase from equation 4.2, results in $\Delta T = 650$ K. The measured and simulated rocking curves of the (2-20) at equilibrium and after photoexcitation are displayed in figure 4.14 considering a photoexcited lattice temperature of $\Delta T = 450$ K, which is somewhat smaller than the estimated lattice temperature increase. The shapes and intensities of the curves are well reproduced. At the exact Bragg condition the intensity of the photoexcited

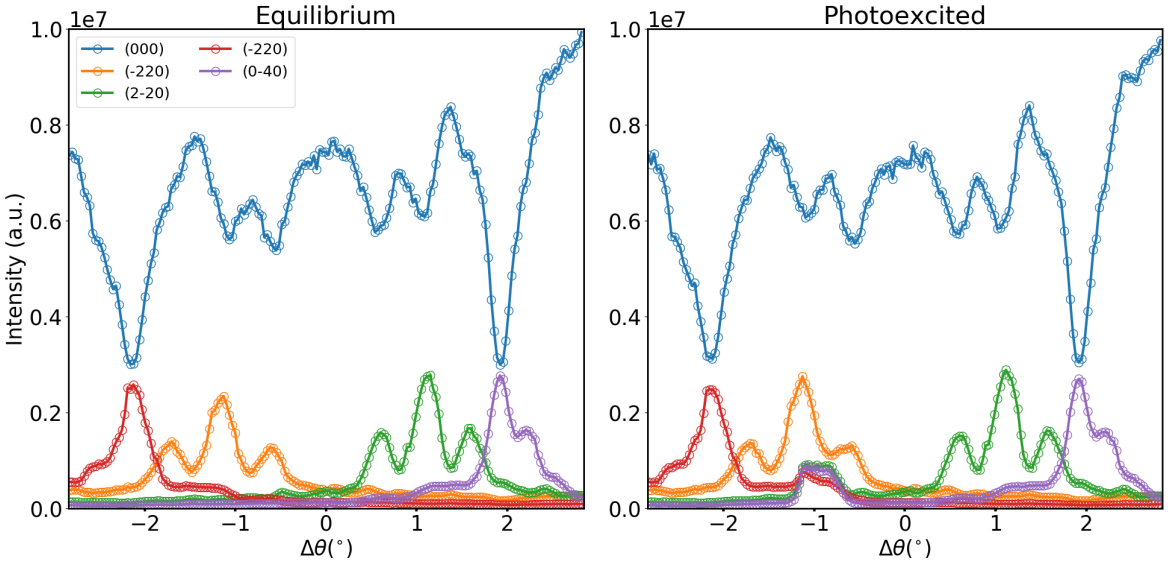

Figure 4.13: Rocking curve scans of a 30 nm sample at 30 keV electron beam energy, at equilibrium (left) and photoexcited (right) at a time delay of 100 ps. Note: In the photoexcited curves, a reflection of the pump beam in the sample holder gives rise to artifact in the intensity at $\Delta\theta \sim -1°$.

curve shows a slight increase, whereas it shows a decrease for other $s \neq 0$. The oscillatory fringe pattern of the rocking curve displays a larger distance between fringes than in the case of the 70 nm sample, as expected from the dynamical behaviour of the diffracted intensity (see section 2.1.2).

In light of these results, we can undoubtedly assign the observed intensity changes to the presence of multiple scattering effects. The proposed model, accounting for several interacting beams and lattice temperature increase, fits accurately the shapes of the rocking curves before and after photoexcitation. The final temperature estimation from our model, underestimates the temperature increase in comparison to the values obtained from equation 4.2. This fact most probably arises from obviating absorption effects in the model (usually accounted within the imaginary part of the crystal potential), which in our case has been regarded with a phenomenological gaussian background. Another possibility that could explain the discrepancy on the calculated temperatures could be related to an imperfect spatial pump-probe overlap on the sample.

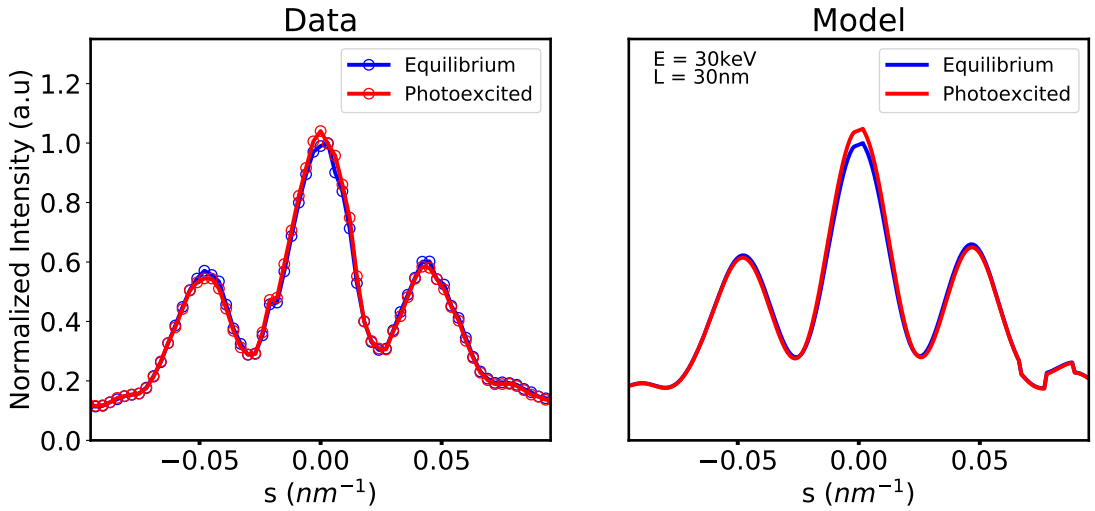

Figure 4.14: Rocking curve scans of a 30 nm sample at 30 keV electron beam energy at a time delay of 100 ps, at equilibrium (blue curve) and photoexcited (red curve). The results from the model after photoexcitation consider a value of $\Delta T = 450K$.

4.5 General behaviour

Finally, and as a way of summarizing our observations figure 4.15 shows the different non intuitive behaviors of dynamical diffraction effects. Figure 4.15 a) shows the evolution of the (220) peak at the Bragg angle, $s = 0$, as a function of thickness. The diffracted intensity oscillates along propagation in the sample which is one of the main feature of dynamical diffraction. Interestingly, the diffracted intensity in the high temperature case (red curve) shows a different behavior, indicating that the relative intensity changes are also expected to change sign depending on the sample thickness.

Note that for small thicknesses, one recovers kinematical theory and $\Delta I/I < 0$, i.e., the diffracted intensity is smaller at higher temperatures. Figure 4.15 b) shows a similarly complex behavior when the electron energy is varied. This indicates that the relative intensity $\Delta I/I$ has a varying amplitude and sign depending on the energy of the probing electrons.

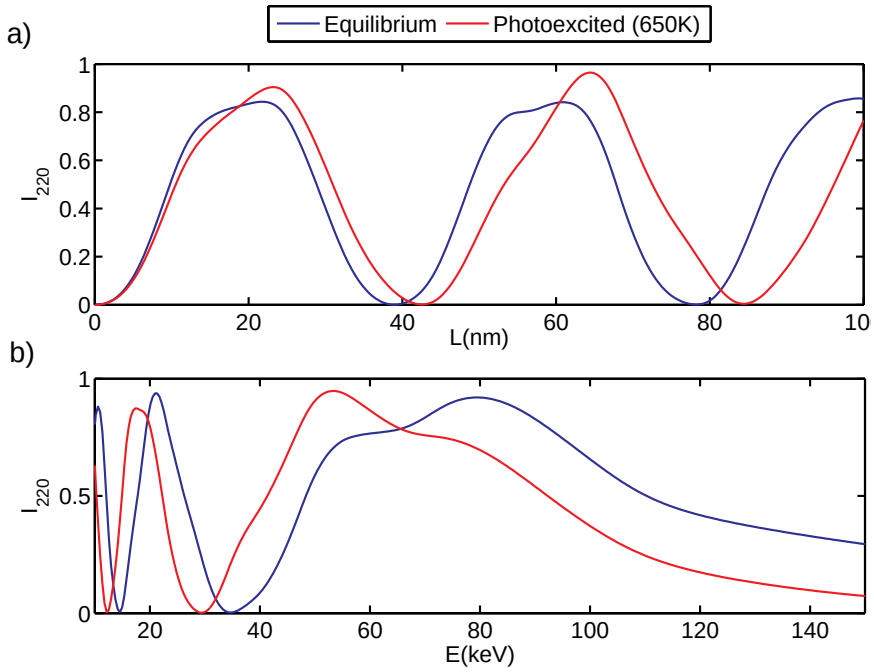

Figure 4.15: Results of dynamical diffraction theory including N=26 beams. a) Intensity of the (220) peak at the Bragg angle, I_{220} (s=0) for varying sample thicknesses, assuming 45 keV electrons. b) Intensity of the (220) peak at the Bragg angle, I_{220} (s=0) for varying electron energy, assuming a 70 nm thickness.

4.6 Conclusions and perspectives

Under the observations from the experimental data and simulations shown in this chapter, it is possible to conclude that the ultrafast response of the Bragg peak intensity within the dynamical diffraction framework is greatly dependent on the sample quality, thickness and the electron energy. While the results and simulations shown in the chapter were performed on silicon membranes, we can anticipate that multiple scattering processes are always present in the case of high quality samples with thicknesses comparable to the extinction distance. As a general rule, dynamical diffraction should be considered when $L > \xi_g/3$ [102]. The presence of such effects in time resolved experiments might hinder the interpretation of the structural dynamics. Dynamical effects, in turn, could potentially be used to obtain new information on the dynamics of the crystal potential after photoexcitation. Although, it requires to precisely know the crystal potential in the equilibrium state, which is not easily available for complex materials.

The rocking curve measurements performed in our UED setup are analogous to the convergent beam electron diffraction technique, which instead of rocking the sample it relies on a beam with a certain angle of convergence. This technique within an ultrafast framework has promising outlooks, since it can accurately measure not only the thickness of the sample but

also the presence of crystal defects or lattice strain at the nanoscale and so, their evolution on time [103].

Chapter 5

Dynamics of the charge density wave phase transition in $GdTe_3$

Contents

Charge density wave (CDW) phases are broken symmetry states characterized by a periodically ordered charge density concomitant to a periodic lattice distortion (PLD) and by a gap opening at the Fermi level in low-dimensional systems. The theoretical model that describes this type of phase transition was proposed by Peierls in 1955 in a linear metallic chain [104]. This model was the first approach that considered a coupling between electrons and lattice. Experimentally, the CDW state has clear electronic and structural features that reveal its existence in real materials under the probe of different techniques. Below a critical temperature, such a state manifests itself by a band gap opening in ARPES, the appearance of satellite reflections in diffraction, an increase of the resistivity in transport measurements or by a dip in the $R(\omega)$

reflectivity curves. A myriad of low-dimensional materials undergo a CDW phase transition: from the quasi-one-dimensional materials as blue bronze ($K_{0.3}MoO_3$) or $NbSe_3$ to quasi-two-dimensional layered compounds such as TaS_2 or the rare earth tritellurides (RTe_3, where R stands for the rare earth element).

CDW systems have gathered great attention in the time-resolved community due to these characteristic structural and electronic signatures. Tracking their evolution after photoexcitation allows to probe the phase transition in the relevant time scales. In the specific case of time resolved diffraction, the out-of-equilibrium dynamics of the CDW state can be followed from the intensity changes of the satellite reflections. A non-trivial open question about the triggering mechanism of the CDW formation relies on the respective contributions of electronic and lattice degrees of freedom. Indeed, the CDW transition involves the simultaneous transformation of the electronic and crystalline structures, but so far, it has not been clear which one is the main driving force, how they are entangled and what is the strength of the electron-phonon coupling [105]. Out-of-equilibrium experiments might shed some light on this matter and improve the understanding of how the phase transition develops.

One of the quasi-two-dimensional materials most representative of a CDW state are the RTe_3, a family of compounds extensively studied statically in the past decade [106, 107, 108]. This layered system shows a Peierls instability with a fairly simple electronic structure. Most of the compounds display a unidirectional CDW with a period that is incommensurate with the underlying atomic lattice, i.e., its period is an irrational fraction of the lattice period. The role of the rare earth ion acts as a chemical pressure factor [109], giving rise to different critical temperatures and even the presence of a second CDW depending on the rare earth ion. Recent studies in 2019 in the ultrafast diffraction domain have opened new questions on the mechanisms behind its dynamics and their possible relation to photoinduced topological defects [36]. By now, some of them are only accessible from *arXiv* [39, 40].

The chapter is divided as follows: in section 5.1, I introduce basic concepts to the understanding of the CDW emergence and characteristics of the RTe_3 compounds. A description of the crystal and electronic structures of the RTe_3 family of compounds is given in section 5.2 along with a brief review of recent experimental results on these compounds. In section 5.3, I describe the sample preparation procedure and section 5.4 is devoted to the experimental results obtained in $GdTe_3$ with the UED setup at LOA. Finally, a discussion with possible interpretations is given and main conclusions are drawn.

5.1 Charge density wave phase transition

The theoretical description of the CDW phase transition is based on the mean-field approximation, which makes use of a statistical treatment to overcome the N-body problem. In this framework, an electron is described in a potential constituted by the surrounding electrons and the underlying lattice. In order to understand the basics of the CDW formation, I briefly intro-

duce the Peierls mechanism and three important aspects involved: Fermi surface nesting, the susceptibility instability and the Kohn anomaly. Theoretical and experimental reviews covering the topic in depth can be found in [105, 110, 111, 112] and in several books [113, 114, 115].

5.1.1 The Peierls transition

As its name suggests, a CDW state is characterized by a periodically varying electron density which is concomitant to a periodic modulation of the underlying lattice, with a period that is related to the Fermi wavevector k_F [113]. In order to picture the mechanism as described by Peierls [104], imagine the simple case of a monoatomic metallic linear chain with a lattice spacing a between ions and one free electron per ion. Peierls realized that such system would become unstable against a lattice distortion such that the periodicity of the chain is doubled to $2a$, leading to a periodically distorted lattice of the form:

$$u(x) = \Delta u \, sin(2k_F x) \tag{5.1}$$

where Δu denotes the amplitude of the distortion and $k_F = \pi/2a$ the Fermi wavevector. The conduction electrons will tend to screen the new potential created by the displaced ions, resulting in a modulated charge density which is described as:

$$\rho(x) = \rho_0(r)[1 + \rho_1 \, cos(2k_F x + \phi)] \tag{5.2}$$

where ρ_0 describes the unmodulated charge density and ϕ the phase of the modulation with respect to the ion lattice.

The new periodicity introduced in the system results in a new Brillouin zone leading to a gap opening at the Fermi level. Figure 5.1 depicts the electronic energy along with the lattice distortion and electron density above and below the transition temperature. Above a critical temperature, the electronic dispersion mimics to that of a free electron gas, with a constant charge density along the atomic chain. As the temperature decreases, the linear atomic chain dimerizes and consequently the charge density is modulated. The gap opening in the energy spectrum results in a lowering of the energies of the filled one-electron states of the conduction band, while empty states are raised in energy. As we will see later, the gain in electron energy is larger than the cost of the elastic energy required to distort the lattice, and so the CDW state remains stable.

Susceptibility

As seen above, the spatial perturbations arising from the lattice distortion lead to an instability of the conduction electrons in a one-dimensional system. A way of describing the response of a free electron gas to an external periodic potential is given by the linear response function:

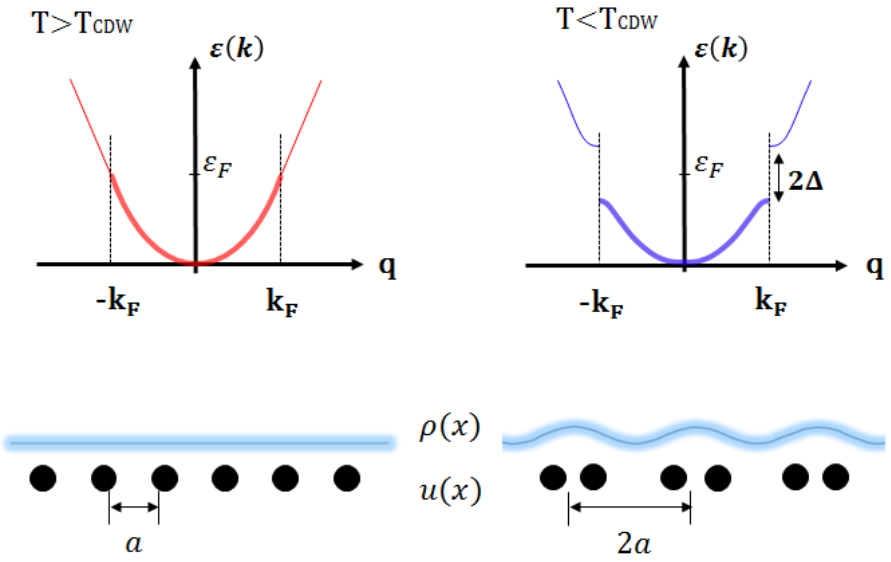

Figure 5.1: Left: Electron energy dispersion curves above the transition temperature $T > T_{CDW}$ without lattice distortion. Right: The same below the transition temperature $T < T_{CDW}$ with the distorted lattice and the 2Δ gap opening at the Fermi level and at $k_F = \pm\pi/2a$.

$$\rho_{ind}(\mathbf{q}) = \chi(\mathbf{q})\phi(\mathbf{q}) \tag{5.3}$$

where $\rho_{ind}(\mathbf{q})$ and $\phi_(\mathbf{q})$ are the Fourier components of the induced charge density and the potential, respectively:

$$\phi(\mathbf{r}) = \int_q \phi(\mathbf{q})\, e^{i\mathbf{q}\cdot\mathbf{r}} d\mathbf{q} \tag{5.4}$$

$$\rho_{ind}(\mathbf{r}) = \int_q \rho_{ind}(\mathbf{q})\, e^{i\mathbf{q}\cdot\mathbf{r}} d\mathbf{q} \tag{5.5}$$

with $\chi(\mathbf{q})$ the Lindhard function, which describes the electronic susceptibility of the conduction band:

$$\chi(\mathbf{q}) = \int \frac{d^d\mathbf{k}}{2\pi^d} \frac{f_k - f_{k+q}}{\varepsilon_k - \varepsilon_{k+q}} \tag{5.6}$$

where d stands for the dimension and $f_k = f(\varepsilon_k)$ is the Fermi function. The value of the susceptibility is largely influenced by the energy bands. By analyzing equation 5.6 we find that the largest changes in the susceptibility appear for a pair of electron and hole states which have the same energy. In the case of a one-dimensional electron gas, this condition is fulfilled in the vicinity of the Fermi level with $q = 2k_F$.

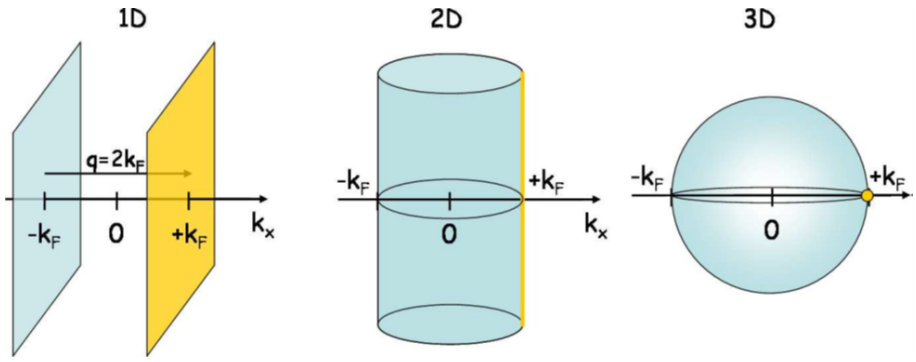

Figure 5.2: Fermi surface topology in different dimensions. The yellow shaded areas represent the nesting of states due to a translation of the Fermi surface by a wavevector $q = 2k_F$, image from [116].

By considering a linear dispersion relation $\varepsilon_k - \varepsilon_F = \hbar v_F(k - k_F)$ around the Fermi level, where v_F stands for the Fermi velocity, the susceptibility in 1D results in:

$$\chi_{1D}(\mathbf{q}) = -e^2 n(\varepsilon_F) ln\left|\frac{q + 2k_F}{q - 2k_F}\right| \tag{5.7}$$

where $n(\varepsilon_F)$ is the density of states at the Fermi level. Figure 5.2 depicts the topology of the Fermi surface in the different spatial dimensions and figure 5.3 shows the result of the corresponding susceptibility function.

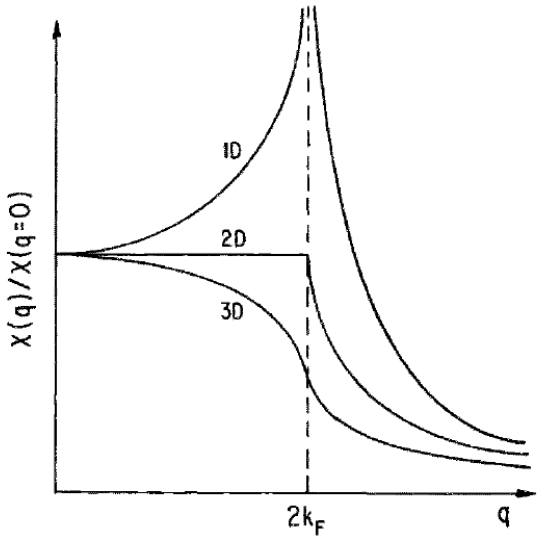

Figure 5.3: Susceptibility as a function of the wavevector at different dimensions [113].

The divergence of the susceptibility in 1D is a direct consequence of the Fermi surface topology. In the case of a 1D system, the Fermi surface consists of two parallel sheets: one formed of filled states and one of empty states, depicted in blue and yellow in figure 5.2, respectively. The excitation of an electron with wavevector $-k_F$ into an empty state located at $+k_F$ can be performed by a translation of $q = 2k_F$. This condition is perfectly fulfilled in the case of a 1D system, and that is why it is known as *perfect nesting*. The singularity in the susceptibility results in an instability of the electron gas leading to the formation of the periodically varying electron density and the gap opening. As the dimensions are incremented, the number of available nesting wavevectors decreases (a line in 2D or a dot in 3D), so the

nesting becomes partial or "imperfect" and accordingly, the singularity in the susceptibility curve is lost (see figure 5.3).

Although this purely electronic picture would look as the only CDW transition mechanism, in real materials the instability of the susceptibility is very fragile and it needs to be assisted by a strong electron-phonon coupling for the transition to develop [117]. Indeed, other ways to repopulate the empty bands is via phonon scattering through the electron-phonon interaction [118], leading to the Kohn anomaly.

The Kohn anomaly

The divergence at $q = 2k_F$ along with an electron-phonon interaction, results in a renormalization of the phonon spectrum, known as the Kohn anomaly [119]. This translates into a softening of the acoustic phonon mode ($\omega \longrightarrow 0$) when the temperature of the system approaches a critical value $T \longrightarrow T_c$. The Kohn anomaly gives rise to the periodic lattice distortion with $q = 2k_F$ wavevector, which itself constitutes the nesting wavevector in the Fermi surface.

In order to find the renormalized phonon spectrum, we introduce the energy of the system given by the Fröhlich Hamiltonian, which accounts for electron-phonon coupling neglecting Coulomb interactions [112]:

$$H = H_{el} + H_{ph} + H_{el-ph} = \sum_k \varepsilon_k a_k^\dagger a_k + \sum_q \hbar\omega_q b_q^\dagger b_q + \sum_{k,q} g_q a_{k+q}^\dagger a_k (b_{-q}^\dagger + b_q) \tag{5.8}$$

where $\varepsilon_k = \frac{\hbar^2 k^2}{2m}$ is the free electron energy, $a_k^\dagger$ and a_k are the electron creation and annihilation operators in state k (spin is not considered), $b_q^\dagger$ and b_q the phonon creation and annihilation operators with wavevector q and frequency ω_q and $g_q = i\left(\frac{\hbar}{2M\omega_q}\right)^{1/2} |q| V_q$ the electron-phonon coupling constant, and V_q is the Fourier component of the potential set by the lattice displacement. The renormalized phonon frequency is obtained from the equation of motion[1]:

$$\hbar^2 \ddot{Q}_q = -[[Q_q, H], H] \tag{5.9}$$

where $\ddot{Q}_q$ is the second time derivative of the position coordinate.

$$\ddot{Q}_q = -\omega_q^2 Q_q - g\left(\frac{2\omega_q}{M\hbar}\right)^{1/2} \rho_q \tag{5.10}$$

with $\rho_q = \sum_k a_{k+q}^\dagger a_k$ and assuming that g is independent of the wavevector q. By making use of the linear response function in equation 5.3 and the ionic potential $g(2M\omega_q/\hbar)^{1/2} Q_q$, the

[1]The Hamiltonian in normal coordinates and momenta is given by:

$$H_{ph} = \sum_q \frac{P_q P_{-q}}{2M} + \frac{M\omega_q^2}{2} Q_q Q_{-q} \quad and \quad H_{el-ph} = \rho_q \sum_q \left(\frac{2M\omega_q}{\hbar}\right)^{1/2} Q_q$$

equation of motion becomes:

$$\ddot{Q}_q = -\left[\omega_q^2 + \chi(q,T)\frac{2g^2\omega_q}{M\hbar}\right]Q_q = \omega_{ren,q}^2 Q_q \tag{5.11}$$

where $\omega_{ren,q}$ is the renormalized phonon frequency and with the susceptibility of the system at a finite temperature given by [113, 115]:

$$\chi(\mathbf{q},T) = -e^2 n(\varepsilon_F) ln\frac{1.14\varepsilon_0}{k_B T} \tag{5.12}$$

here ε_0 is an arbitrary cutoff energy, usually taken as the Fermi energy ε_F. Therefore, the renormalized phonon frequency at a finite temperature finally yields:

$$\omega_{ren,2k_F}^2 = \omega_{2k_F}^2 - \frac{2g^2\omega_{2k_F}}{\hbar} n(\varepsilon_F) ln\left(\frac{1.14\varepsilon_0}{k_B T}\right) \tag{5.13}$$

where $\omega_{2k_F}^2$ denotes the normal state phonon frequency. At the phase transition the renormalized frequency tends to zero, $\omega_{ren,2k_F}^2 = 0$, leading to a frozen lattice distortion with wavelength of $\lambda_0 = 2\pi/2k_F$, which defines the mean-field transition temperature:

$$k_B T_{CDW}^{MF} = 1.14\varepsilon_0 e^{-1/\lambda} \tag{5.14}$$

with the dimensionless electron-phonon coupling expressed as $\lambda = \frac{g^2 n(\varepsilon_F)}{\hbar\omega_{2k_F}}$.

This is the same formalism that describes BCS superconductivity, thus we are dealing with a second order phase transition with the complex order parameter described by:

$$\Delta = |\Delta| e^{i\phi} = g\left(\langle b_{2k_F}\rangle + \langle b_{-2k_F}^{\dagger}\rangle\right) = g\left(\frac{2M\omega_q}{\hbar}\right)^{1/2} Q_q \tag{5.15}$$

where $|\Delta|$ and ϕ represent the amplitude and phase of the order parameter, respectively. The displacement of the lattice in terms of the order parameter becomes:

$$\langle u(x)\rangle = \Delta u \, cos(2k_F x + \phi) \tag{5.16}$$

with

$$\Delta u = \left(\frac{2\hbar}{M\omega_{2k_F}}\right)^{1/2} \frac{|\Delta|}{g} \tag{5.17}$$

In this way the lattice strain energy as a function of the order parameter is defined as:

$$E_{latt} = \frac{1}{2} M\omega_{2k_F}^2 \Delta u^2 = \frac{\hbar\omega_{2k_F}|\Delta|^2}{g^2} \tag{5.18}$$

On the other hand, the electronic energy gain of the system as a function of the order parameter (considering the weak coupling limit with $\varepsilon_F >> \Delta$) is given by [113]:

$$E_{elec} = \frac{n(\varepsilon_F)}{2}\left[|\Delta|^2 ln\left(\frac{2\varepsilon_F}{|\Delta|}\right)\right] \tag{5.19}$$

The stability of the system in the CDW state becomes possible by compensation of the elastic energy cost $E_{latt} \propto |\Delta|^2$ by the gain of the electronic energy $E_{elec} \propto -|\Delta|^2 ln|\Delta|$.

5.1.2 Collective excitations: Amplitudons and Phasons

Due to the complex nature of the order parameter, excitations of the phase ϕ and the amplitude $|\Delta|$ are expected [113]. These excitations or fluctuations inherent to the CDW phase are known as phasons (phase modes) and amplitudons (amplitude modes), respectively. They are described within the Ginzburg-Landau formalism in the long range wavelength fluctuation limit.

The phase mode represents spatio-temporal fluctuations of the electron density modulation phase with respect to the ionic positions. These modes give rise to an acoustic branch in the phonon spectrum. As a main difference with respect to the amplitude mode, it can propagate in space.

The amplitude mode, on the other hand, accounts for the fluctuations of the ionic displacements Δu, which is proportional to the amplitude of the order parameter $|\Delta|$, as seen in equation 5.17. The resulting frequency dispersion of the mode corresponds in this case to an optic branch.

Figure 5.4 shows a simple schematic representation of the ionic positions and the modulated electronic density in both modes, related to their respective frequencies, which in the case of an incommensurate CDW, are given by:

$$\begin{aligned} \omega_\phi &= \left(\frac{m}{m^*}\right)^{1/2} v_F q \\ \omega_A &= \left(\lambda\omega_{2k_F}^2 + \frac{1}{3}\frac{m}{m^*}v_F^2 q^2\right)^{1/2} \end{aligned} \tag{5.20}$$

where m^* denotes the CDW effective mass, or Fröhlich normalized mass [112], given by:

$$m^* = m_0\left(1 + \frac{4\Delta^2}{\hbar^2\omega_{2k_F}}\right) \tag{5.21}$$

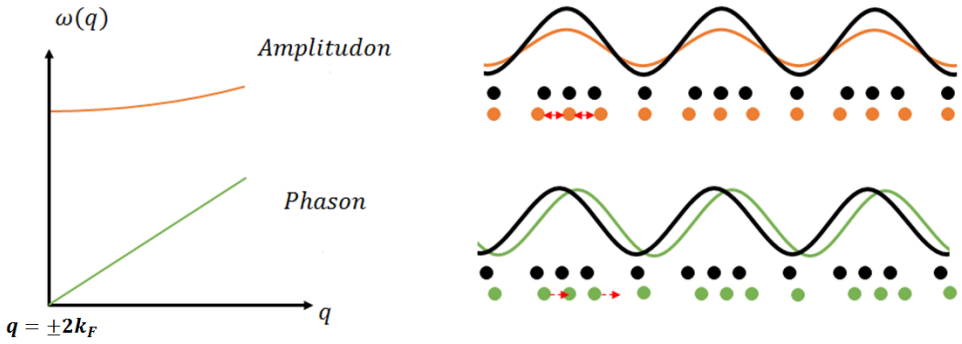

Figure 5.4: Schematic of the collective excitations present on the CDW along with their respective phonon branches; acoustic in the case of the phason (green) and optic in the case of the amplitudon (orange). Black circles and lines represent the equilibrium distorted chain.

Equilibrium collective excitations probed by diffraction

In diffraction, the presence of a the CDW state results in the appearance of satellite spots around the main Bragg reflections, with a wave vector Q = 2k$_F$. As the temperature of the system is increased, fluctuations of the amplitude and phase modes have large implications in the diffraction intensities. Giuliani [120] and Overhauser [121] shown theoretically the effects of such fluctuations on the diffraction intensities. In their works, they defined the equilibrium structure factor taking into consideration both phase and amplitude fluctuations, resulting in [120]:

$$F(\mathbf{q}) = \sum_{\mathbf{G}} \sum_{n=-\infty}^{\infty} \delta\big(\mathbf{q} - \big[\mathbf{G} + n\mathbf{Q}\big]\big) J_n^2(\mathbf{q}\cdot\mathbf{A}) F_n^{\phi} F_n^{A} \tag{5.22}$$

where $\boldsymbol{G}$ stands for the reciprocal lattice vector, $\boldsymbol{q}$ represents the electron scattering wavevector, $\boldsymbol{Q}$ the wavevector of the distortion, $\mathbf{A}$ the distortion amplitude of the CDW (termed as Δu in equation 5.1), J_n is the Bessel function of the first kind and order n, which assigns $n = 0$ for Bragg peaks and $n = 1$ for first-order satellites. This term sets the influence of the distortion amplitude in both Bragg and satellite peaks intensity, since J_1^2 and J_0^2 are out of phase (see figure 5.5).

Finally, the last two terms in equation 5.22, correspond to the collective modes attenuation factors being:

$$F_n^{\phi} = exp\big(-n^2\langle\delta_{\phi}^2\rangle\big)$$
$$F_n^{A} = exp\big(-(n^2 - |n|)\langle\delta_{A}^2\rangle\big)$$

where the terms $\langle\delta_i^2\rangle$ arise from the fluctuations of the phase and the amplitude and n sets the order of the satellite reflection.

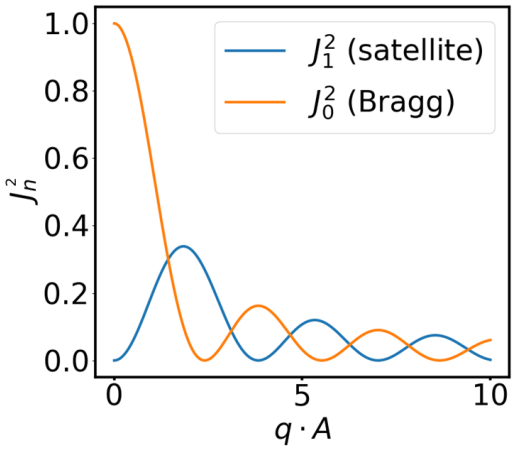

Figure 5.5: Squared of the Bessel functions for $n = 0$ (assigned to Braggs) and $n = 1$ (satellites).

Thus, the intensity of the Bragg reflections, with $n = 0$, in the presence of a CDW will be proportional to:

$$I_{bragg} \propto |J_0^2(\mathbf{q} \cdot \mathbf{A})|^2$$

This implies that large lattice distortions (i.e., large $\mathbf{A}$) decreases the intensity of the Bragg reflections. In the case of first order satellite reflections with $n = 1$, the intensity becomes:

$$I_{sat} \propto |J_1^2(\mathbf{q} \cdot \mathbf{A}) F_1^{\phi}|^2$$

from which we can clearly observe that ***its intensity only depends on phase fluctuations and not on amplitude fluctuations*** (since $F_{n=1}^{A} = 1$ in the case of first order satellites). Note that in this model the authors consider that the fluctuations are time-independent. Moreover, it is worth noticing the influence of the lattice distortion $\mathbf{A}$, that also tends to decrease as the temperature raises. In this way, a smaller lattice distortion reduces the structure factor even if the phase fluctuations are not present.

Out-of-equilibrium collective excitations probed by diffraction

In the case of time resolved experiments, where the time dependency has to be considered, the photoexcitation of the amplitude mode gives rise to oscillations in the diffraction satellite intensities with a frequency given by ω_A, usually on the order of few THz. This behaviour can be well explained within the phenomenological time-dependent Ginzburg-Landau formalism, as shown experimentally by Huber *et al.* where the order parameter of the phase transition is given by the amplitude of the lattice distortion [22]:

$$V(x) = \frac{1}{2}(\eta e^{-t/\tau} - 1)x^2 + \frac{1}{4}x^4$$

with x the order parameter, η a fluence dependent parameter $\eta \propto F$, and τ the temporal decay of the satellite intensity. The potential energy of the system at equilibrium ($\eta = 0$) displays a

Peierls barrier as depicted in the schematic of figure 5.6. As the incident fluence is increased, the shape of the double well changes up to $\eta \sim 1$, where the Peierls barrier collapses.

The amplitude mode fluctuations as a function of the time, can be described by the equation of motion within the Peierls barrier. By considering the Ginzburg-Landau potential V(x), it becomes:

$$\frac{1}{\omega_{DW}^2}\frac{\partial^2}{\partial t^2}x - \left(1-\eta e^{-t/\tau}\right)x + x^3 + \frac{2\gamma(t)}{\omega_{DW}}\frac{\partial}{\partial t}x = 0 \tag{5.23}$$

where ω_{DW} represents the angular frequency of the motion in the double-well ($\omega_{DW} \sim \omega_{AM}$) and a phenomenological damping parameter $\gamma(t) = \gamma_{assym}(1-e^{-t/\tau_R})$ considering the relaxation times from pump-probe reflectivity curves. Although the authors could not fully confirm the origin of this damping mechanism they pointed out to a strong time-dependent electron-phonon or phonon-phonon coupling.

The influence of the phase mode fluctuations is expected at longer time scales due to their lower excitation energies, and so they are not considered in the phenomenological model. At long time scales, the phason mode contributes to a satellite intensity decrease, as in the case of the equilibrium fluctuations shown the precedent subsection.

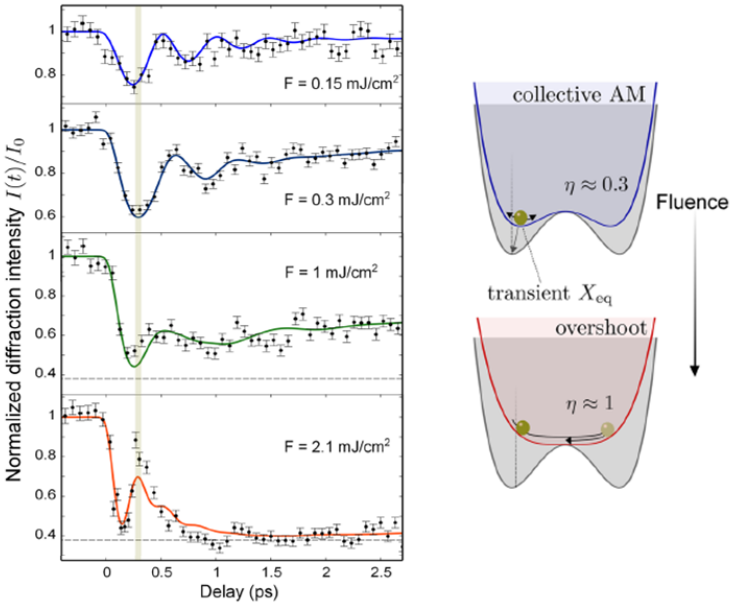

Figure 5.6: Temporal evolution of the satellite reflection intensity as a function of the incident fluence measured by Huber et al. in $K_{0.3}MoO_3$. The solid lines represent fits within a displacive model which agrees to the dynamics resulting from equation 5.23. The schematic on the right side represents the potential energy of the Peierls barrier as a function of the excitation parameter $\eta \propto F$. Figure adapted from [22].

5.2 The Rare-Earth Tritelluride family

5.2.1 Crystal and electronic structures

The crystalline structure of the RTe_3 compounds (here R stands for the rare earth element) is arranged in an orthorombic *Cmcm* space group (No. 63), nearly tetragonal with lattice parameters of $a \sim c \sim 4.3\,\AA$ and $b \sim 25.5\,\AA$ [122]. The unit cell consists of a set of stacked Te bi-layers sandwiched between corrugated RTe insulating slabs [106], as shown in figure 5.7. The interlayer bonds between Te nets located at $b/2$ of the unit cell are weakly bonded by Van der Waals forces [123], here a glide plane (which corresponds to a symmetry operation of a mirror reflection on the b axis and an in-plane translation of $c/2$) sets the weak orthorhombicity of the crystal structure. The Te layers host a unidirectional incommensurate CDW with a preferred ordering direction along the c-axis originated from the small anisotropy between the in-plane lattice parameters ($a/c \sim 0.99$).

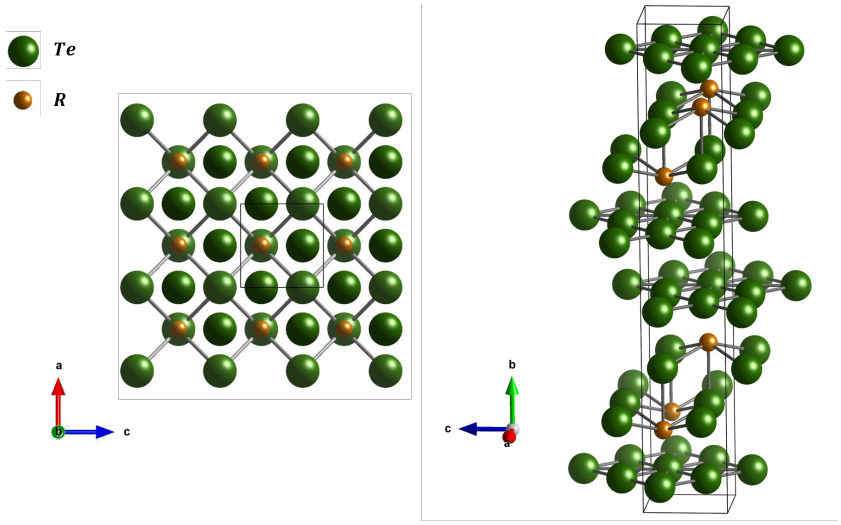

Figure 5.7: Top view (left) and side view (right) of the unmodulated unit cell. Black lines highlight the unit cell. The crystal structure is generated with VESTA software [124] from the X-ray data published by Malliakas et al. [125].

The electronic structure is dominated by the presence of the $5p_x$ and $5p_z$ orbitals within the square-planar Te layers. The weak interaction of the electrons gives rise to a simple electronic structure that is well described within a 2D tight-binding model [107, 126]. Figure 5.8 *a*) shows the real space in-plane cell in which the Te plane is oriented 45° with respect to the a,c axis. The Te p_x and p_z orbitals form linear chains perpendicular to each other, conferring a quasi 1D character to the Fermi surface. In reciprocal space, the resulting Fermi surface has a diamond shape within two different unit cells; a 3D Brillouin zone defined by the rare-earth atoms and a 2D Brillouin zone from the Te plane (see figure 5.8). Since its shape is mostly dominated by the Te orbitals, it is qualitatively the same for all the family compounds. Below the transition temperature, a nesting vector with $Q_{CDW} \sim 2/7c^*$ opens a bandgap at the tip of the diamond [107, 127, 128, 129]. The slight curvature of the bands leads to an imperfect nesting, so that

the material does not become insulating but it coexists with the metallic phase. Figure 5.9 shows the $TbTe_3$ ($T_c = 330$ K) Fermi surface measured with ARPES at two temperatures. At T = 100 K, the band dispersion (cut on the Fermi surface highlighted by the red line) clearly shows the opening of the bandgap with $\Delta \sim 250$ meV.

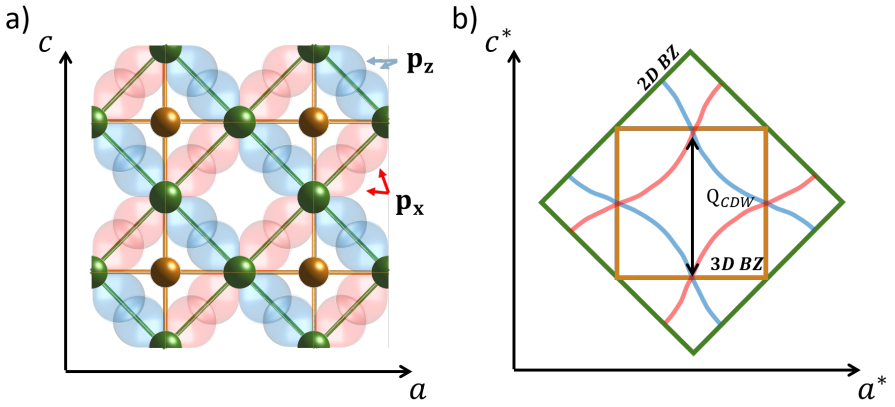

Figure 5.8: a) Real space in plane atomic positions represented along with the Te $5p_x$ (red) and $5p_z$ (blue) orbitals, with the Te net oriented 45° with respect to the ac axis. b) Schematic of the reciprocal space showing the 3D (orange) and 2D (green) Brillouin zones. Red and blue lines represent the FS arising from the Te $5p_z$ and $5p_x$ orbitals, respectively.

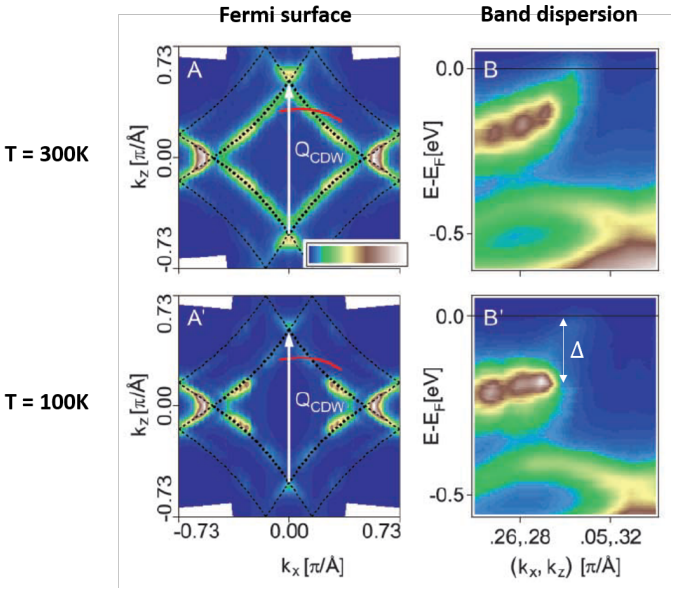

Figure 5.9: Measured equilibrium Fermi surface and energy band dispersion (cuts taken at the highlighted line in red in A and A') of $TbTe_3$. At 300 K (A and B) and at 100 K, well below the transition temperature (A' and B'). Image adapted from [129].

The rare earth ion has a key function on the structure as it sets the lattice parameters and most importantly, the transition temperature of the CDW phase. It can be seen as a chemical pressure parameter (an increasing lattice parameter leads to a decreasing chemical pressure) [109, 130], which allows to present the phase diagram as a function of temperature and the rare earth element, as shown in figure 5.10. In this way, the lightest ion (La) displays the largest lattice parameters with $a = 4.39\,\AA$ and $c = 4.41\,\AA$ leading to an anisotropy ratio of $a/c = 0.45\%$, whereas the heaviest (Tm), will display the shortest lattice constants with $a = 4.27\,\AA$ and $c = 4.28\,\AA$ that corresponds to $\sim 0.2\%$ anisotropy (room temperature values) [125]. Note that compounds with reduced anisotropy (heavier ions), result in a second CDW phase along the a-axis with a $T_{c2} < T_{c1}$ coexisting with the one along the c-axis, see figure 5.10. The transition temperatures to the CDW phase are decreasing with the atomic mass of the rare-earth ion in the case of Q_1 whilst they increase in the case of Q_2. The rather large transition temperatures of these compounds, allow to perform studies at room temperature.

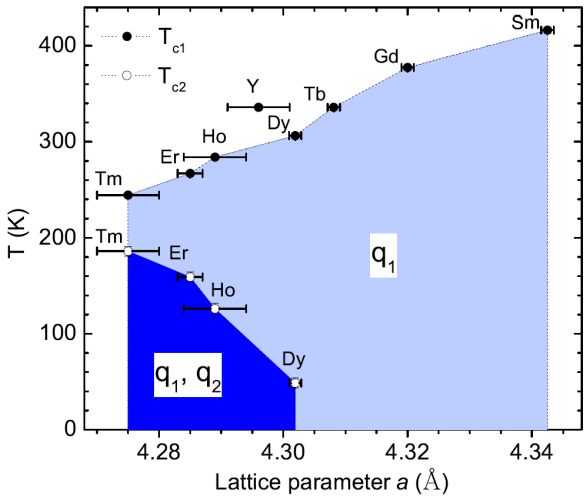

Figure 5.10: Phase diagram as a function of the temperature and the lattice parameter a. The transition temperatures for the CDW oriented along the c axis increases with increasing lattice parameter, whereas the transition temperature of the CDW along the a axis decreases. Graph from [122].

5.2.2 Recent literature review and motivation

Although the Peierls picture with the Fermi surface nesting as the main driving force inducing the phase transition has been widely accepted in RTe_3 materials [128], Johannes and Mazin argued theoretically that in real 2D materials the Fermi surface nesting itself can not predict the ordering direction. On the contrary, a strong $\mathbf{q}$-dependent electron-phonon coupling triggers the phase transition [117]. Experimentally, the combination of different time resolved techniques

probing each degree of freedom involved in the transition (lattice and electrons) and with their capability to follow the transition in time scales as short as few hundreds of femtoseconds are promising candidates to reveal the role of the lattice in the phase transition.

The understanding of the physical scenario ruling the photoinduced phase transition in these compounds has lead to an intense research during the last decade. Three main techniques with different sensitivities have been used to probe the dynamics at the electronic and structural levels unveiling the temporal dynamics of each degree of freedom.

Time resolved ARPES experiments with high sensitivity to the electronic structure, showed partial suppression of the gap after photoexcitation followed by a recovery of the order of few picoseconds depending on the incident excitation fluence. This temporal response to photoexcitation is common in several compounds of the RTe_3 family; on $TbTe_3$ [131], $CeTe_3$ [62], $DyTe_3$ and $HoTe_3$ [132] and $LaTe_3$ [36]. An example of the temporal evolution of the gap in $TbTe_3$ is shown in figure 5.11 [129] with the upper band associated to the CDW gap (shown in black in figure 5.11).

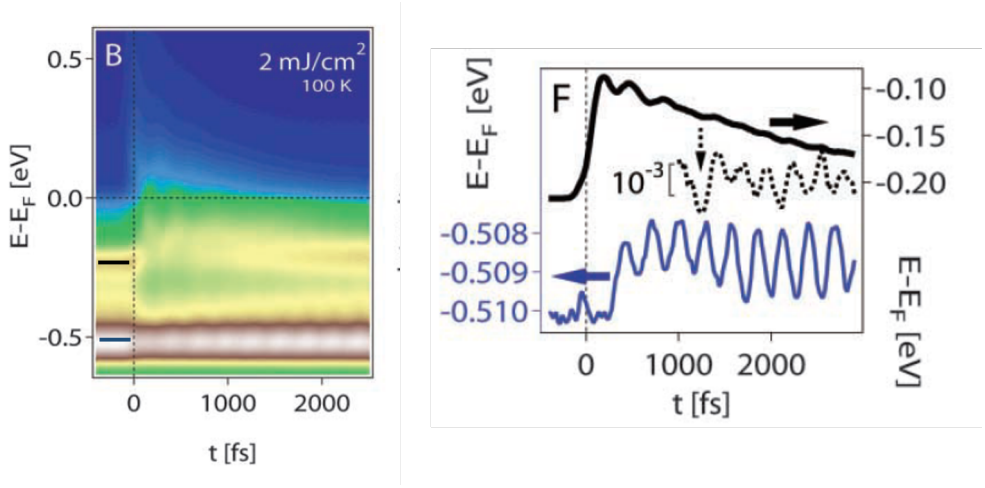

Figure 5.11: Left: Time resolved photoelectron intensity around the Fermi level of $TbTe_3$ with the black line corresponding to the conduction band (CB) and the blue line to the Te band. Right: Variations of the CB band (black line) and Te band (blue). The oscillations on the CB at $t < 1$ ps correspond to the CDW amplitude mode. Adapted figures from [129].

On the other hand, time resolved reflectivity experiments are sensitive not only to changes in the electronic structure, but also to lattice changes through coherent generation of phonons. This type of experiments shows a slowing down of the CDW gap relaxation as a function of the incident fluence on $LaTe_3$ with values of the recovery times ranging from hundred of femtoseconds to few picoseconds [36]. Interestingly, results from Yusupov *et al.* showed as well a slowing down in the relaxation of the reflectivity curves with increasing temperatures (also reported by Chen *et al.* [133], see figure 5.12) accompanied by a softening the of amplitude mode at $T \sim T_c$. Moreover, their experimental results pointed to a coupling between the amplitude mode and an optical phonon mode at a similar frequency [134], this effect is further discussed in section

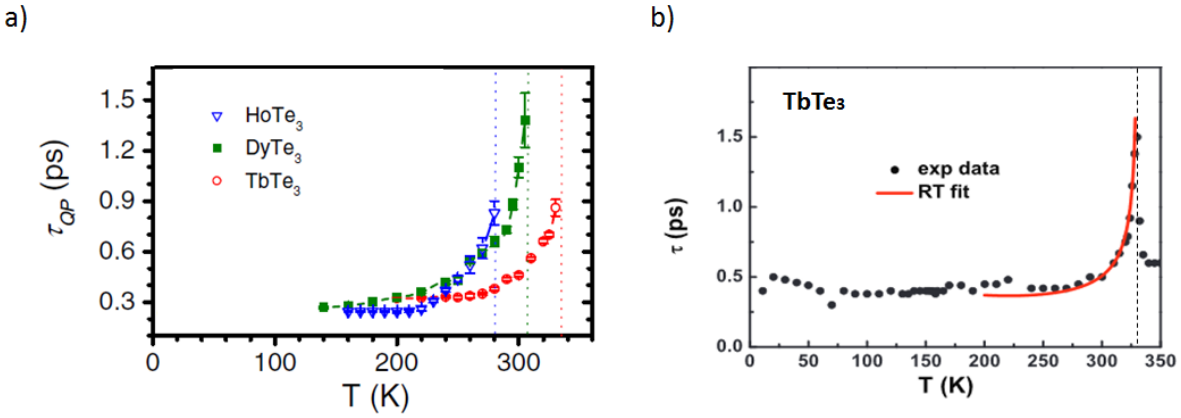

Figure 5.12: Measured relaxation time in reflectivity curves as a function of the sample temperature reported by a) Yusupov et al. [135] and b) Chen et al. [133]. Dashed lines mark the transition temperatures of each material. Adapted figures.

5.5. Later, a double pump-probe reflectivity experiment hinted toward the role of topological defects in the CDW dynamics of $TbTe_3$[2]. More precisely, the authors suggest that domain walls likely annihilate after a delay time of few picoseconds [135].

Critical slowing down: The results presented in figure 5.12 reveal an interesting effect at the onset of a phase transition that merits some mention. Critical slowing down is a universal behaviour observed in phase transitions of any type. When a system is subjected to a perturbation that pulls it away from its equilibrium state, the temporal recovery to that initial state will slow down, becoming most noticeable when the perturbation is performed close to a critical point. This is exactly what we observe in figure 5.12. Zong *et al.* have recently applied this concept in the decay times measured on $LaTe_3$ by various techniques [38].

The most interesting aspect of this phenomenon which occurs in complex systems is its universality in a wide variety of fields [136]. Critical slowing down has been observed in economy [137] before economical crises, in nature before climate changes [138], population collapse in ecosystems [139] or even in psychology before or after a depression episode [140]. Although the arrival of a "tipping point" before a drastic change is difficult to predict, the majority of these publications claim the possibility of detecting early warnings of "catastrophic" changes by studying critical slowing down.

Finally, ultrafast diffraction represents the probe which is only sensitive to the crystal structure. The increasing interest on these compounds in the diffraction community is reflected in the numerous publications with different proposed scenarios in the past years. All of these works present a similar behaviour on the CDW dynamics: the photoexcited satellite peaks undergo a fast suppression of the intensity followed by a slow recovery that increases with

[2]The experiment was also performed on other compounds (2H-$TaSe_2$ and $K_{0.3}MoO_3$) showing similar effects and indicates that it is a universal response in CDW systems.

fluence [36, 37, 108, 141]. The temporal evolution of the satellite reflections has opened new questions concerning the main structural mechanisms behind the photoinduced phase transition. Although the results are qualitatively the same, the controversy arises in the interpretation of the observed dynamics. Han *et al.* [141] and Trigo *et al.* [37] assign the CDW dynamics to changes of the order parameter (amplitude of the distortion) in $CeTe_3$ and $SmTe_3$, respectively. Zong *et al.* ($LaTe_3$) interpret their results as the emergence of a high density of photoinduced topological defects [36]. And finally, Moore *et al.* underline the role of lattice strain and coupling of the CDW amplitude mode to optical phonons in $TbTe_3$ [108].

At this point, it is interesting to note a main difference between both diffraction techniques. While UED measurements did not reveal any oscillatory behaviour of the satellite intensities, time resolved X-ray diffraction measurements detected the coherent excitation of the amplitude mode [37, 108]. This fact could arise either from the differences in temporal resolutions of each technique or from the different satellites under study. In UED, in transmission geometry, we are restricted to the observation of the (h0l) planes, so that information of the b^* axis can not be retrieved.

Out-of-equilibrium CDW phase: Here, it is worth mentioning as well some striking results recently uploaded to *arXiv*: the photoinduced emergence of a hidden CDW phase in the compounds $LaTe_3$ [39] and $CeTe_3$ [40]. The astonishing aspect of these results is that at thermal equilibrium, light compounds of the RTe_3 family have never shown the presence of a second CDW phase (c.f. figure 5.10). Both studies point to the formation of topological defects as the mechanism favouring the emergence of this transient non-equilibrium CDW phase.

With respect to the above-mentioned controversies, the goal of our experimental measurements was to provide a better understanding of the physical mechanisms behind the CDW dynamics. For this purpose, we performed a series of pump probe diffraction experiments on thin films of $GdTe_3$ at different incident fluences. We extended the temporal window of the scans to hundreds of picoseconds and analyzed the dynamics of the phase transition by looking at the effects of photo-excitation on the Bragg peaks and satellites intensities. Moreover, we investigated the implications of the initial conditions by analyzing two different initial temperatures on the sample, demonstrating that this has large effects on the CDW dynamics.

5.3 Sample preparation

Bulk $GdTe_3$ samples were grown by self-flux technique under purified argon atmosphere at the Néel Institute in Grenoble by P. Lejay [142]. The preparation of suitable thin films for the UED setup at LOA was performed with an ultramicrotome (Leica EM UC7) at *Laboratoire des Solides Irradies (LSI)*. This technique allowed me to cut thin sections down to 30 nm. A pair of diamond knives can be fitted in the ultramicrotome, each of them used in different steps. Firstly a trimming diamond knife with an inclination of 45° is used to shape the sample into a trapezoid block (flat pyramid, see figure 5.13). At this point, it is important to stress the main difficulty when preparing this type of samples: the dimensions of our electron probe are fairly large when compared to the beam of a regular electron microscope. Accordingly, the surface of the flat pyramid should be on the order of $\sim 300\,\mu m \times 300\,\mu m$.

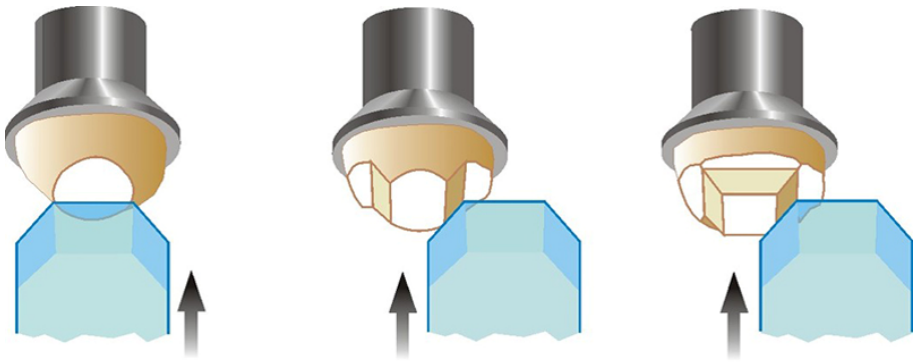

Figure 5.13: First steps to prepare sample sections. The bulk sample is glued on the sample holder and with a trimming knife it is shaped into a trapezoid block. The surface of the flat area should be on the order of $\sim 300\,\mu m \times 300\,\mu m$. *Image taken from [143].*

In a second step, a 35° knife provided with a small water container is fitted into the ultramicrotome and the water level is adjusted to create a perfectly flat surface. These samples are highly sensitive to surface oxidation, requiring a fast operation during the sectioning process. In order to get a "fresh" surface I usually cut a first section of $\sim 100\,\mu m$ and discard it. Subsequently, by adjusting the feed of the ultramicrotome to few tens of nm, the sample is sectioned into a single thin film which remains floating on the water surface. With the help of an eye lash the section is taken as far as possible from the knife blade to avoid damaging and retrieved with a *Perfect loop* tool (see figure 5.15).

Finally, the water drop containing the sample section is placed on the dull side of a copper TEM grid, which is in turn placed on an absorbing paper to remove it (see figure 5.15). The TEM grids containing the sections are then stored in a vacuum vessel to avoid degradation from surface oxidation until is needed for experiments.

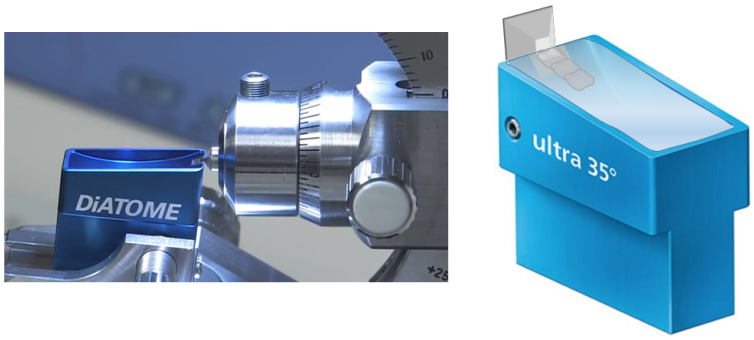

Figure 5.14: Left: Picture of an ultramicrotome with a 35° diamond knife. Right: Sketch of the knife with the water container filled with the floating sections. Adapted figure from [144].

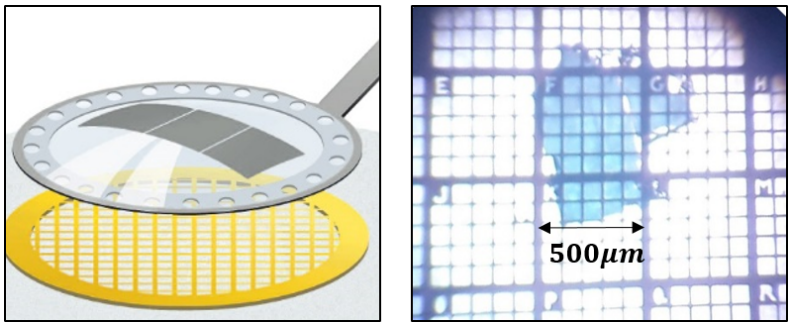

Figure 5.15: Left: Sketch of the Perfect loop tool containing the water drop and the sample sections, ready to be deposited on the TEM grid [144]. Right: Optic microscope image of a $GdTe_3$ section with an area of a $\sim 500\,\mu m \times 500\,\mu m$ and 50 nm thickness.

Figure 5.16 shows the diffraction pattern of an ultramicrotomed 50 nm $TbTe_3$ sample obtained with a TEM at 300 keV electrons prepared by a coworker. The positions of the satellites along the c-axis are highlighted by the red arrows on the diffraction image. The intensity ratio between the satellite peaks and the $k+l=2n+1$ Bragg peaks is of the order 30 % (depending on the diffraction order). Although RTe_3 compounds belong to the Cmcm space group, we can observe forbidden reflections with $h+l=2n+1$. This effect has been already observed in several electron diffraction experiments [36, 39, 122, 130, 141], and their appearance is believed to result from stacking disorder along the b crystallographic axis [130].

By the use of the ultramicrotome I prepared both materials $TbTe_3$ ($T_c = 330\,K$) and $GdTe_3$ ($T_c = 377\,K$) in thin films. Although $TbTe_3$ is a better known material with extensive characterization in the literature, we finally chose to perform the pump probe experiments on the neighbouring $GdTe_3$ compound since it presents a higher transition temperature. Consequently, the intensity of the satellites (which is proportional to the order parameter) is higher, requiring shorter exposure times to collect good quality diffraction patterns.

It is worth mentioning that the characteristics of our probe along with the high sensitivity of

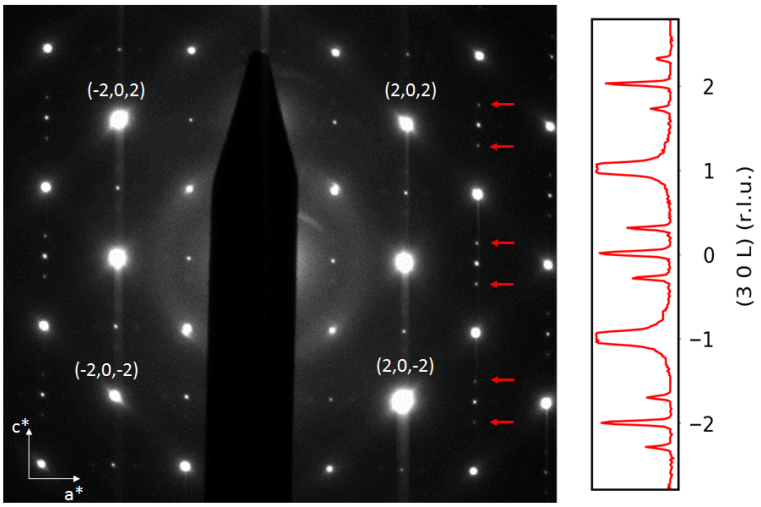

Figure 5.16: TEM diffraction pattern with 300 keV of an ultramicrotomed sample of $TbTe_3$ along the [010] axis at room temperature. Line profile of the (3 0 L) plane; satellites are marked by red arrows in the diffraction pattern.

these samples to oxidation, make the preparation very difficult. Several trials were necessary to obtain the samples presented in the following section which are monocristalline with nanometric thickness and mm^2 surface.

5.4 Experimental results

The pump probe experiments presented in this section were performed on $GdTe_3$ samples (T_c = 377 K) with a thickness of L~50 ± 2 nm at 155 K. The repetition rate was set to 1 kHz, at 41 keV electron energy and a pump wavelength of $\lambda = 800\,nm$. At every time step five images were collected and averaged, each of them recorded with an exposure time of 3 s. The penetration depth of the pump pulse can be estimated from the reflectivity and optical conductivity values reported by Sacchetti *et al.* [145], leading to a value of $\delta_{depth} \sim 41$ nm (see appendix D), so that we ensure quasi-uniform energy deposition along the thickness of the sample.

We start by reviewing the characteristics of the diffraction pattern at equilibrium conditions. Figure 5.17 shows the static diffraction pattern along the [010] crystallographic axis. Red arrows point to the position of the first order satellites appearing along the c-axis.

A line profile, which is taken at the position highlighted by the red box in the diffraction pattern is plotted on the right side of the figure. The satellites are centered at $Q_{CDW} = (1,0,\delta)$ where $\delta \sim \pm 2/7$ and with an intensity of 20% of the (1,0,0) Bragg peak. The line profile of the Bragg reflection and both satellite peaks is well fitted by the sum of three Lorentzian functions.

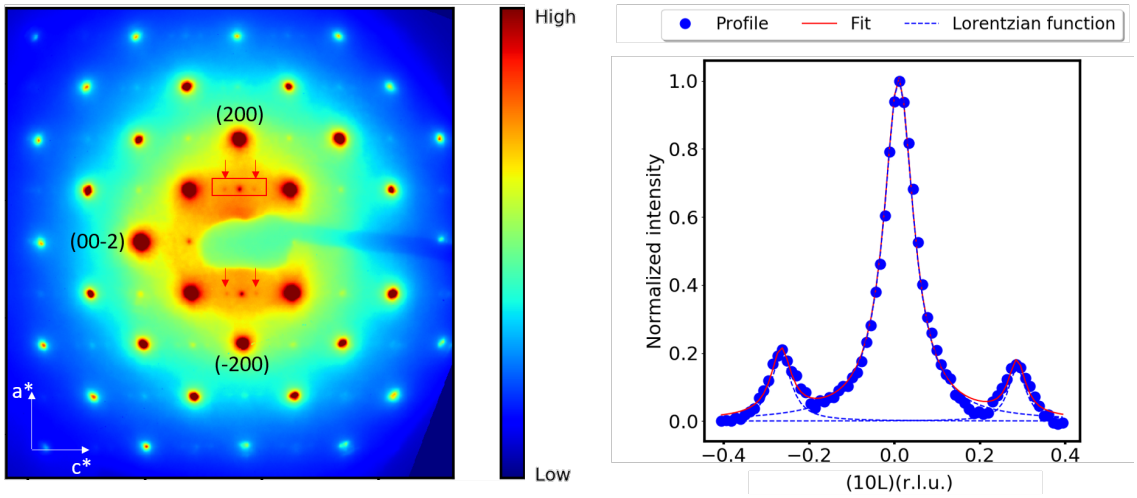

Figure 5.17: Static electron diffraction pattern of a 50 nm $GdTe_3$ sample collected at 41 keV. Red arrows point to the positions of the satellites with $Q_{CDW} = (\pm 1, 0, \pm\delta)$ where $\delta \sim 2/7$. Left: Line profile of the (1, 0, 0) Bragg peak and the neighbouring satellites (blue dots). The blue dashed lines are Lorentzian fits of each peak and the solid red line represents the complete fit.

Note that contrary to the silicon diffraction patterns shown in chapter 4, in this case it is necessary to use of a beam blocker due to the large intensity difference between the direct and diffraction peaks. We observe that first diffraction orders are about 50 times weaker that the direct beam, as shown in figure 5.18. This large intensity difference between the direct and diffraction peaks confirms that the measured diffraction patterns can be described within the kinematic diffraction regime. This is probably due to the sample quality that is inferior than industrial silicon wafers.

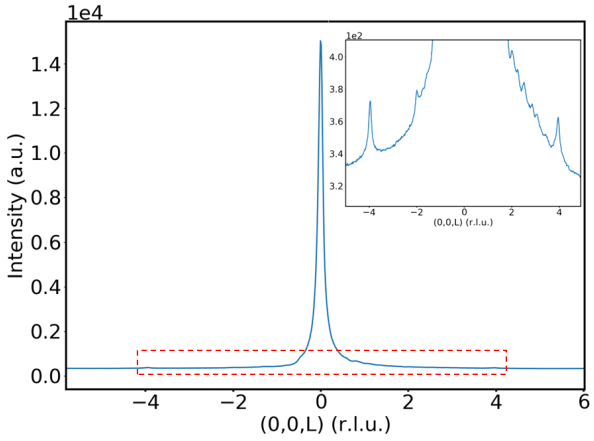

Figure 5.18: Line profile of the unblocked direct beam along the (0,0,l) direction. The inset shows a zoom of the highlighted region.

Now we turn our attention to the diffraction patterns of the photoexcited state. Figure 5.19 shows the diffraction pattern shortly after photoexcitation with an incident fluence of

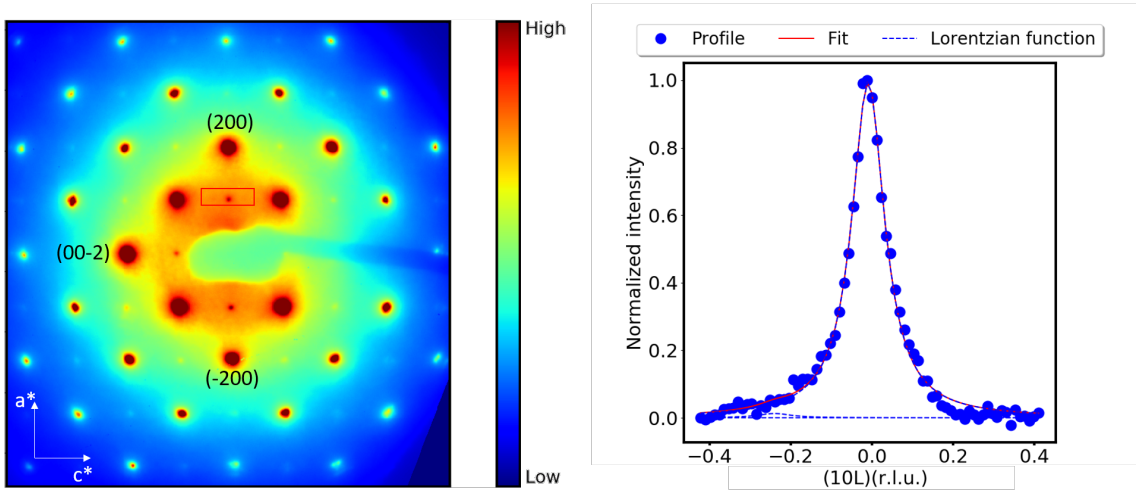

Figure 5.19: Left: Diffraction pattern after pump arrival at $t = 5\,ps$ with an incident fluence of $3.5\,mJ/cm^2$. Right: Corresponding line profile of the (1, 0, 0) Bragg peak, the intensity of the satellites is suppressed to the background level.

$F = 3.5\,mJ/cm^2$. The arrival of the excitation beam triggers the phase transition into the high symmetry state inferred from the satellite intensity suppression, clearly seen in the line profile.

Finally figure 5.20 presents the normalized difference between diffraction patterns with pump and without pump (at a time delay t = 5 ps and at a fluence of 3.5 mJ/cm^2). The red arrows are pointing to the position of the satellites. The intensity difference of the Bragg peaks and the satellites is negative after the pump arrival. On the other hand, the background signal reveals a slight positive intensity that increases at high scattering wave vectors, mostly due to thermal diffuse scattering.

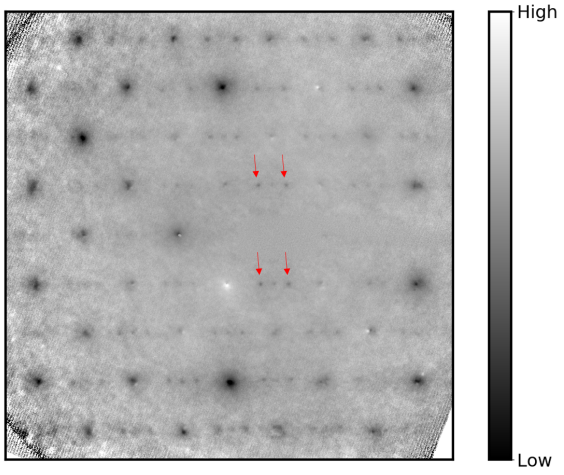

Figure 5.20: Diffraction pattern after pump arrival at $t = 5\,ps$ with an incident fluence of $3.5\,mJ/cm^2$.

It is important to point out that we do not observe the presence of new satellite reflections emerging along the a^* crystallographic axis at any pump fluence. This is in contrast to what was recently observed by Kogar *et al.* in $LaTe_3$ [39] and by Zhou *et al.* in $CeTe_3$ [40].

5.4.1 Bragg peak dynamics

In this section, I present the experimental results obtained at an initial sample temperature of $T_i = 155$ K under pump excitation fluences ranging from 0.5 to 3.5 mJ/cm^2. The time delays between pump and probe were typically measured in a range between -10 ps and 140 ps, with a time step between consecutive shots of few hundreds of femtoseconds. The curves of the temporal relative changes are the result of binning between two or three consecutive points (depending on the scan) in order to increase the signal to noise ratio.

Here, I retrieve the dynamical information of the lattice by analyzing the intensity changes of the Bragg reflections. The relative intensity changes of the $(k+l) = 2n$ Bragg peaks are presented in figure 5.21, which result from an average of the integrated intensity over thirty Bragg peaks. The temporal intensity decrease can be well described by a single exponential decay of the form:

$$\Delta I / I_0 = A(1 - e^{-t/\tau}) \cdot H(t)$$

where I_0 is the integrated intensity of the peak without pump, A the amplitude of the decay and τ the time decay constant. $H(t)$ is the Heaviside function centered at $t = 0$ ps.

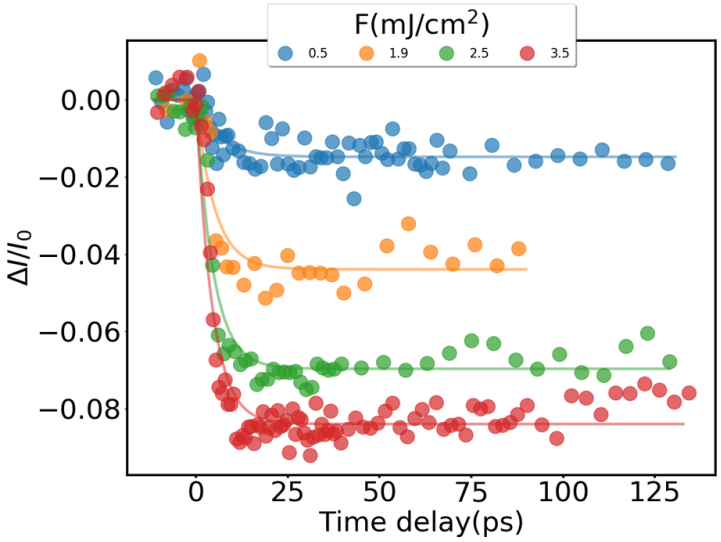

Figure 5.21: Relative intensity changes of the Bragg peaks, averaged over 30 Bragg peaks, as a function of the delay time between pump and probe at four different fluences. The initial sample temperature is $T_i = 155$ K. The solid lines are resulting from a single exponential decay fit.

The intensity of the Bragg reflections decreases with a typical time scale of $\tau = 6$ ps showing a weak dependence on incident fluence (see figure 5.22 a)). Following this intensity decay, the

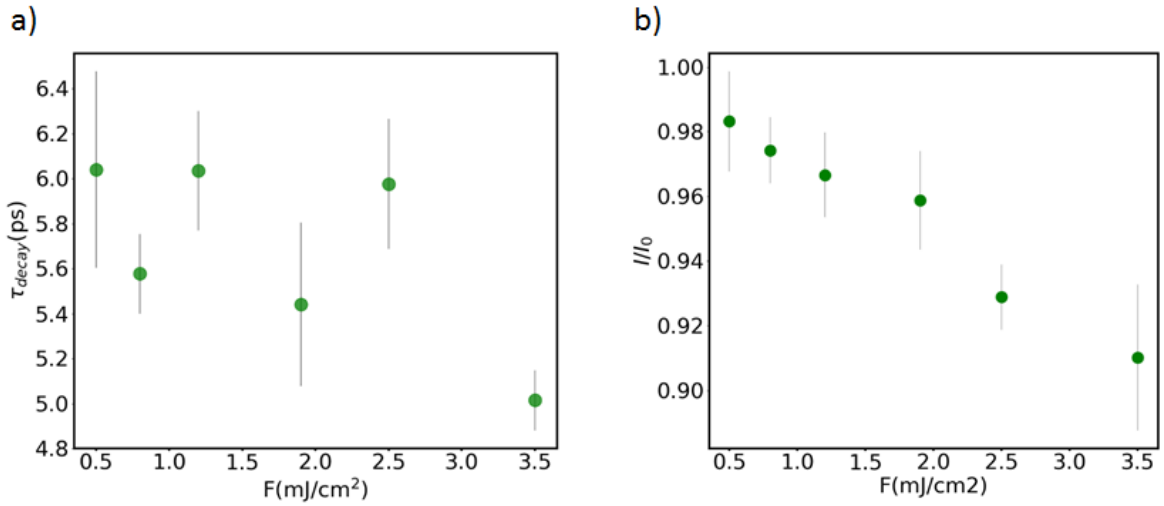

Figure 5.22: a) Decay times extracted from the fit. b) Intensity ratio averaged over several Bragg peaks and measured after the system has reached the quasi-equilibrium state.

system is brought into a quasi-equilibrium state, inferred from the constant intensity ratio of the Bragg peaks, which lasts as long as the temporal length of the scan, i.e., more than 125 ps.

While the time decay constant τ does not show a clear dependence with the incident fluence, the amplitude of the intensity decreases from $I/I_0 = 98\%$ to $I/I_0 = 90\%$ as shown in figure 5.22 b), suggesting that the Bragg dynamics are directly related to the lattice temperature increase. Scans taken within our temporal limit of the delay line reveal no relaxation of the process up to 2 ns. The fact that the relative intensity remains constant at those time scales implies that the lattice temperature evolves slowly due to the long thermal diffusion process, owing to the free-standing sample geometry. Note that figure 5.22 displays the average of the decay constants and the amplitudes of 30 Bragg peaks. The difference in the intensity changes between Bragg peaks along a^* and c^*, i.e., (h, 0, 0) and (0, 0, l) respectively, is shown in figure 5.23.

Figure 5.23 *a)* shows the integrated intensity changes at low fluence while 5.23 *b)* at the highest fluence, for three different Bragg peaks: (00-4), (-400) and (400) in green, blue and red, respectively.

This suggests that the intensity changes depend on the crystallographic axis, pointing to an anisotropic Debye-Waller effect. Figure 5.24 depicts the difference in intensity ratio between the (00-4), (-400) and (400) Bragg peaks at all studied fluences, with the intensity ratios measured after lattice thermalization. Here, we can clearly observe that the (4,0,0) and (-4,0,0) reflections present different values in their intensities, although they belong to the same crystallographic direction. A plausible explanation for this effect is related to residual multiple scattering effects. Since these effects may occur, we could not obtain quantitative information on the lattice anisotropy.

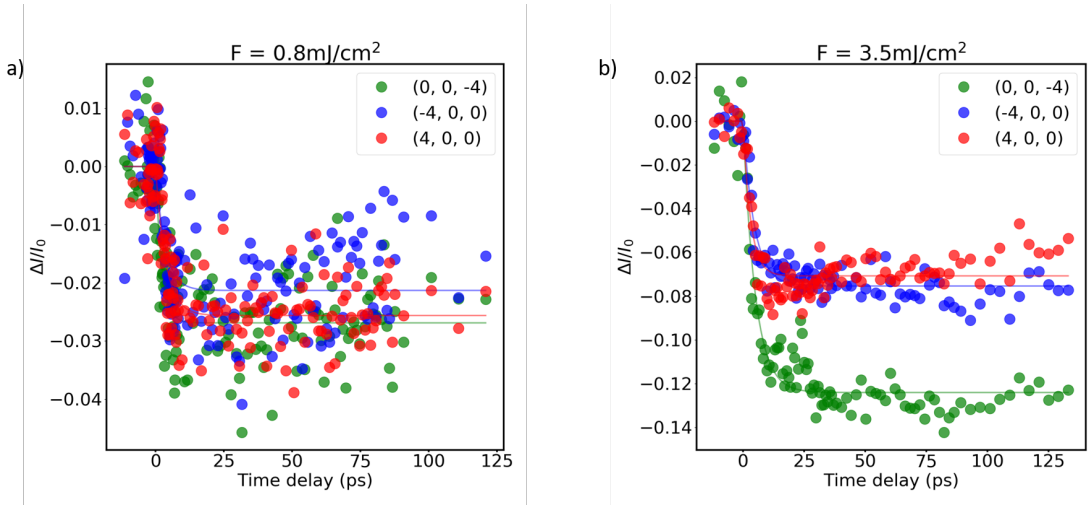

Figure 5.23: Comparison between the intensity changes of orthogonal Bragg peaks: (±400) and (00-4), with incident fluences of a) $F = 0.8\,mJ/cm^2$ and b) $F = 3.5\,mJ/cm^2$, and initial temperature $T_i = 155\,K$.

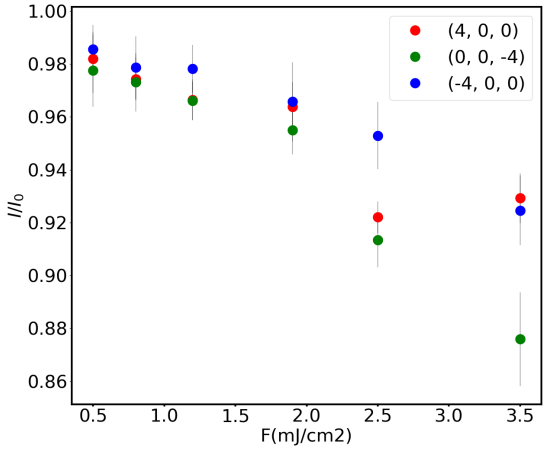

Figure 5.24: Intensity changes ratio I/I_0 where I is the intensity after full decay. The sample initial temperature is $T_i = 155\,K$.

5.4.2 Lattice temperature and Debye Waller effects

We have seen in section 2.1.1 that there is an intrinsic relation between the intensity ratio, lattice temperature and the scattering wave vector of the diffraction peak, given by the Debye-Waller equation:

$$I = I_0 e^{-M} \tag{5.24}$$

where $M = \frac{1}{2}Q_{hkl}^2\langle u^2\rangle = \frac{1}{2}\left(\frac{4\pi}{\lambda}\right)^2 sin^2\theta\langle u^2\rangle$ is the Debye-Waller factor with Q_{hkl} the scattering wave vector corresponding to the (hkl) Miller plane and $\langle u^2\rangle$ is the mean-squared amplitude

of the atomic displacement. Figure 5.25 shows the logarithm of the intensity ratio after the sample has reached the thermal quasi-equilibrium state $I(t \gg 6\,ps)$ and before photoexcitation I_0 as a function of $sin^2\theta/\lambda^2$ from several Bragg peaks for all studied incident fluences. Dashed lines are linear fits of the data[3]. These results undoubtedly confirm that the arrival of the pump induces an increase of the lattice temperature, being higher with stronger incident fluences, as expected.

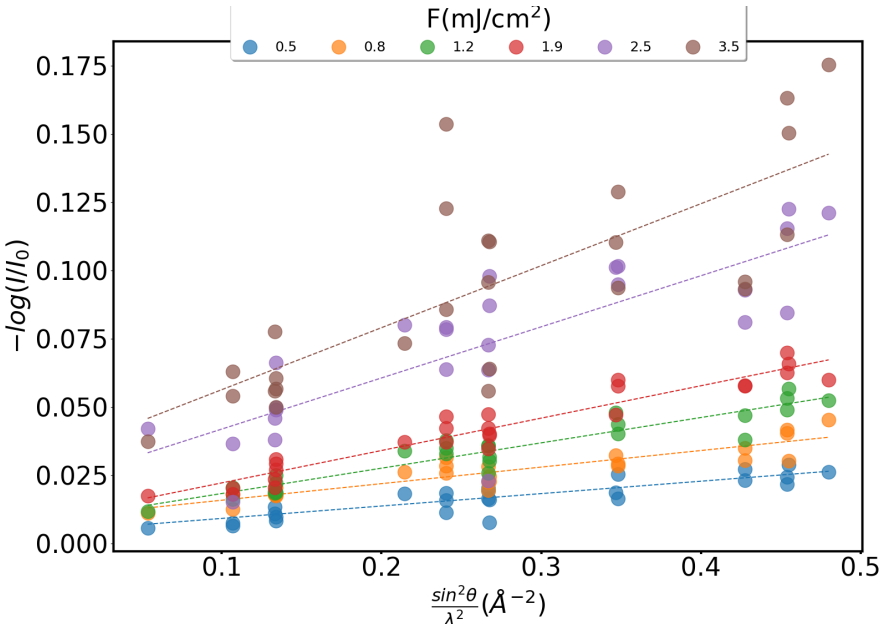

Figure 5.25: Logarithm of the intensity ratio after the quasi-equilibrium is reached $I(t = 75\,ps)$ and before photoexcitation (I_0) as a function of the squared of the wavevector. As expected from Debye-Waller theory, $log(I/I_0)$ vs. $sin^2\theta/\lambda^2$ follows a linear trend (dashed lines).

In the case of isotropic vibration the Debye-Waller factor becomes $M = B_T\left(\frac{sin\theta}{\lambda}\right)^2$ with $B_T = \frac{8\pi}{3}\langle u^2\rangle$. In this way, the lattice temperature increase after pump arrival ΔT can be easily extracted from the slope of the linear fit [44, 147]:

$$b = \frac{-log(I/I_0)}{\left(sin\theta/\lambda\right)^2} = \frac{8\pi^2}{3}\langle u^2\rangle = \frac{6\hbar^2\Delta T}{m_A k_B \Theta_D^2} \tag{5.25}$$

where $m_A = 8.96 \cdot 10^{-22}\,g$ represents the average mass of $GdTe_3$ and $\Theta_D = 144\,K$ the Debye temperature, measured by Banerjee *et al.* with X-ray diffraction [148]. Here, we consider that the anisotropy between the crystallographic axis a and c is marginal, so that the Debye-Waller

[3]Note that the intercept of the fit is finite. Results from the same analysis performed in bismuth by a different group lead to a similar behaviour [146]. Effects from residual dynamical effects on the diffraction process could potentially result in a non-zero intercept when plotting $log(\frac{I}{I_0})$ vs $sin^2\theta/\lambda^2$.

factor can be treated as isotropic and that the difference in atomic masses is small, so that we can approximate to a monoatomic solid. This approximation accurately fits the data at low incident fluences, where the intensity ratio at similar $sin^2\theta/\lambda^2$ is closely the same. As the incident fluence is increased above 1.9 mJ/cm^2, we can clearly notice a higher dispersion of the $ln(I/I_0)$ from the linear fit. This is considered in the following to calculate the error bars in the temperature estimation.

The results of the lattice temperature based on this calculation are plotted in figure 5.26, where the lattice temperature at the quasi-equilibrium state is defined as $T_{q.e.} = T_i + \Delta T$, with T_i=155 K. The red dots show the experimentally estimated lattice increase using equation 5.25. Along with the points retrieved experimentally, we plot the estimated temperature increase from absorbed heat (gray line) showing an excellent agreement with the results obtained from equation 5.25. The lattice temperature from absorbed heat is calculated from:

$$\Delta T = \frac{Q_{abs}}{m\,C_l} = \frac{F_{inc}(1-R)}{\rho\,\delta_{depth}\,C_l} \tag{5.26}$$

with Q_{abs} the absorbed energy, $\rho = 0.014$ mol/cm^3 the molar density, δ_{depth} ~41 nm the penetration depth, $R(\lambda = 800\,nm)$ =0.7 the reflectivity coefficient [145] and $C_l \sim 99.5$ J/K·mol the lattice heat capacity [106].

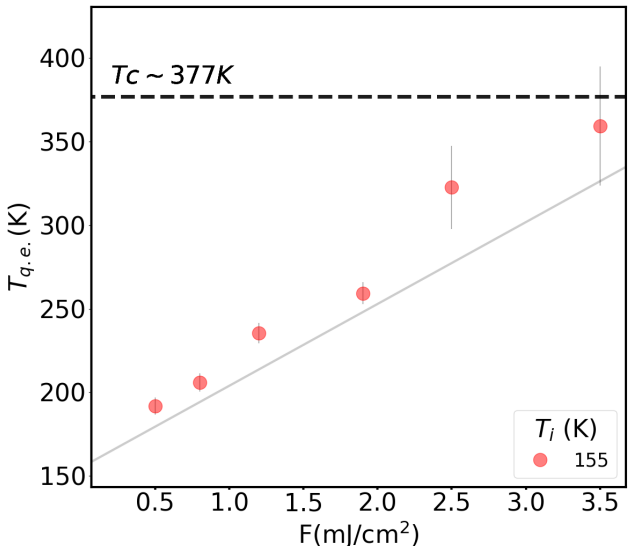

Figure 5.26: Lattice temperature estimation at the quasi-equilibrium state ($T_{q.e.} = T_i + \Delta T$, T_i=155 K) from the Debye-Waller effect (red dots) and from heat absorption (gray line) at the quasi-equilibrium state. The black dashed line marks the transition temperature of $GdTe_3$ [122].

These results confirm that the lattice temperature remains below the critical temperature after photoexcitation. Despite this fact, we have seen in figure 5.19 that the satellite reflections disappear below the background level at the highest incident fluence, suggesting that the photoinduced transition is not purely thermal.

5.4.3 Satellite dynamics

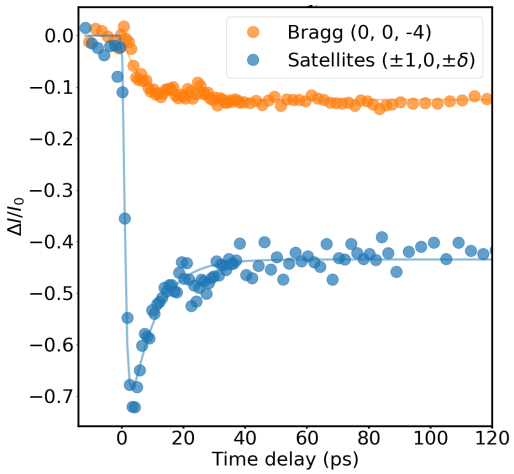

Figure 5.27: Relative intensity changes of the (00-4) Bragg peak (orange dots) and the averaged satellite peaks (blue dots, see text) at an incident fluence of 3.5 mJ/cm^2.

Quite differently to the dynamics of the Bragg peaks, the satellite reflections present a bi-exponential decay and recovery behaviour. Figure 5.27 shows the intensity changes of the $(00-4)$ Bragg peak (in orange) compared to that of the satellite peaks (in blue) with an excitation fluence of $F = 3.5\,mJ/cm^2$. To enhance the signal to noise ratio, I averaged the intensity of four satellite reflections with the same Q^2 value ($Q_{CDW} = (1,0,\pm\delta)$, and $Q_{CDW} = (-1,0,\pm\delta)$). The dynamical response of the satellite reflections to the laser excitation is described by an instantaneous intensity decrease, followed by a slower recovery to the quasi-equilibrium state. At this point, the intensity ratio remains constant up to the end of the scan, in the same manner as the intensity of the Bragg reflection.

The photoinduced intensity changes of the satellite reflections as a function of the incident pump fluence are shown in figure 5.28, where the dashed black line marks the background level. Figure 5.28 b) shows a zoom of the dynamics up to 40 ps. At all studied fluences, the photoexcitation induces a large intensity drop within the first picoseconds, followed by a recovery whose characteristic time increases linearly with the pump fluence, leading finally to a quasi-equilibrium state that lasts for several tens of picoseconds. The partial intensity recovery indicates the reformation of the CDW implying that the lattice temperature remains below the critical temperature of $GdTe_3$, in agreement with the results obtained from the Debye-Waller analysis on the Bragg peaks.

We can clearly observe in figure 5.28 that at large incident pump fluences with $F \geq 1.9\,mJ/cm^2$, the intensity of the satellite peaks is suppressed down to the background level, suggesting that the system has transited into the high symmetry phase. We can therefore define an experimental "critical fluence" F_c corresponding to the fact that the satellite peaks disappear in the background noise for $F \geq F_c$. Figure 5.29 shows the minimum intensity reached after pump arrival (dark blue) with the critical fluence value marked by the red dashed line at $F_c = 1.9\,mJ/cm^2$. In the same figure, $I_{q.e.}$ illustrates the intensity changes after reaching the quasi-equilibrium state (light blue dots) which decreases linearly with the incident fluence. As we will see in section 5.4.5, the peak width exhibits a similar critical fluence onset.

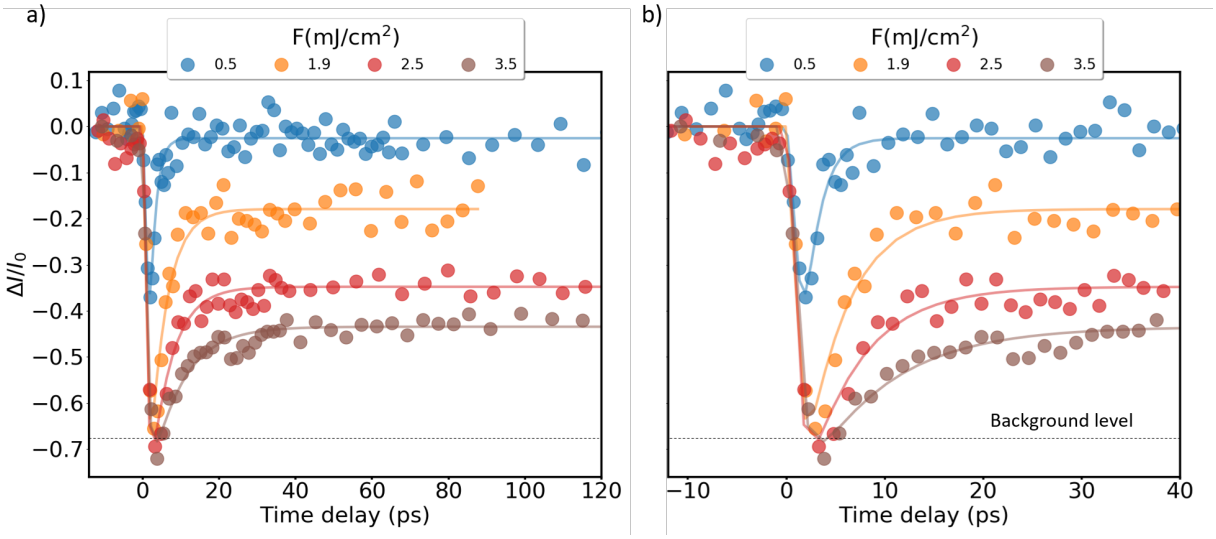

Figure 5.28: a) Relative intensity changes of the satellites at different incident fluences, b) zoom of first 40 ps. Solid lines are the best fits to the data and the black dashed line marks the background level.

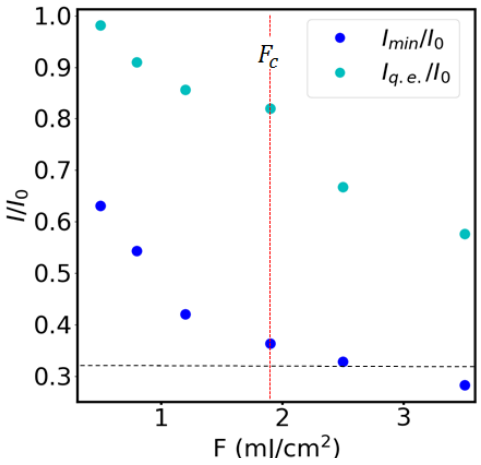

Figure 5.29: Intensity ratios at the minimum of the satellite intensity (dark blue) and at $t > 40$ ps (light blue). The dashed black line marks the background level and the red dashed line the critical fluence threshold.

The temporal intensity changes of the satellite reflections can be described by considering both decay and recovery processes convoluted with the probe beam [149]:

$$\Delta I/I_0(x) = F(t) * G(t,\sigma) = \int_0^\infty F(x-t_0)G(x,\sigma)dx$$

where F represents a decay and recovery function of the form:

$$F(t) = A_1(1 - e^{-t/\tau_1}) + A_2(1 - e^{-t/\tau_2})$$

and G(t, σ) represents the electron probe beam temporal distribution:

$$G(t,\sigma) = \frac{1}{\sigma\sqrt{(2\pi)}} e^{-t^2/\sigma^2}$$

where τ_1 stands for the temporal decay constant, τ_2 is the temporal recovery of the process and σ the r.m.s. width of the probe beam to consider the temporal resolution.

The amplitude of the intensity changes is accounted in the variables A_1 and A_2. The fits are performed with σ constrained to [0,2] ps, which represents the temporal resolution of the probe, τ_1 is constrained between [0,5] ps and τ_2 between [0,10] ps. The decay time constants extracted from the fits are shown in figure 5.30 a) and the recovery time constants in 5.30 b). The error bars result from the standard deviation of the four averaged satellites.

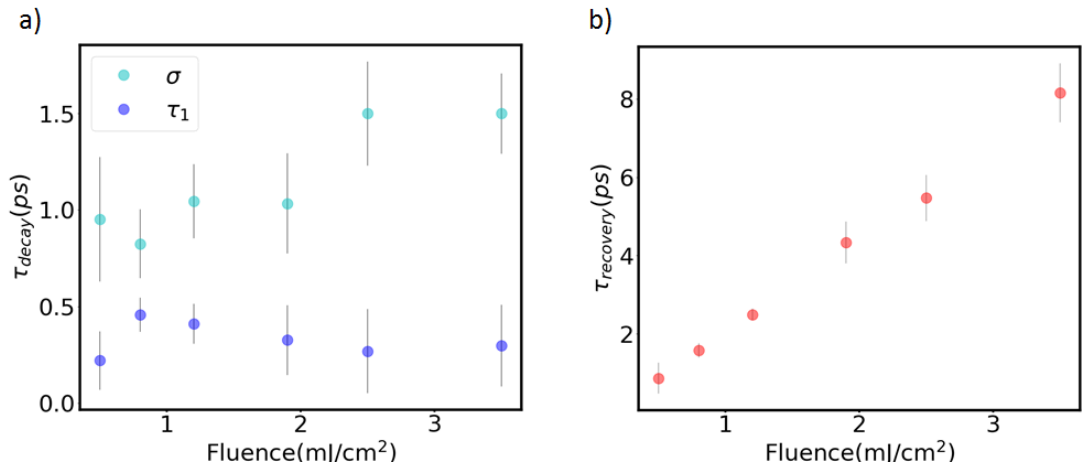

Figure 5.30: Time constants extracted from the bi-exponential fits on the satellites dynamics as a function of the incident fluence: a) Time constants corresponding to the probe temporal resolution σ (light blue) and τ_1 corresponding to the system response decay (dark blue). b) Recovery time constants extracted from the fits, showing a clear linear increase with fluence.

The temporal decay of the dynamics is extremely fast, being limited by the temporal resolution of our probe (σ). In order to confirm this result, a set of experimental data was collected with an electron bunch containing few thousands of electrons with a temporal resolution of ~ 400 fs. The time decay in this case resulted in values of the same order as the temporal width of the electron beam. Time resolved X-ray diffraction experiments performed by Trigo *et al.* in $SmTe_3$ [37] with a temporal resolution <80fs, showed time decays of the order of ~ 200 fs, which confirms again that in our case the decay time is limited by the resolution of our probe. As shown in

figure 5.30 a), we do not observe a clear influence of the incident fluence on the temporal decays.

On the other hand, the recovery time constants show values which are well above the temporal resolution, allowing us to study the recovery process. As inferred from the results shown in figure 5.28, the increment of the incident fluence has a direct impact on the recovery time scales: the CDW recovery slows down linearly from 1 ps to 8 ps with increasing fluence (see figure 5.30 b)). Notice that at high fluences, the recovery times of the CDW are similar to the τ_{decay} of the Bragg peaks, which means that the lattice temperature is already thermalized. This slow down seen in the recoveries is a typical signature of systems displaying a phase transition at temperatures close to the critical value, also known as critical slowing down. Our experimental results are in agreement with other UED studies performed on other compounds [36, 40]. Time resolved reflectivity measurements have shown the same behaviour of the recovery processes as a function of sample temperature measured by Yusupov *et al.* [134] and Chen *et al.* [133]. It is worth mentioning that in the case of reflectivity, and as pointed out by the authors in [134, 133], the recovery time can be theoretically related to the gap size as $\tau_{recovery} \propto 1/\Delta$ [150, 151], leading thus to slower recoveries as the system approaches the T_c.

5.4.4 Scans at different initial temperatures

In these experimental data sets, we demonstrate that the initial sample temperature is a key factor in the CDW dynamics, notably on their intensity changes and recovery times. For this purpose, I have performed a set of scans with an initial temperature of T_i = 295 K, a value which is closer to the critical temperature of our sample with $T_i / T_c \sim 0.8$. Here, I present the results from two different fluences F = 0.8 mJ/cm^2 and F = 1.2 mJ/cm^2. In this way we are able to compare how the system responds to a similar excitation level under different initial temprature conditions. Figure 5.31 shows the Bragg dynamics for each pump fluence and initial sample temperature.

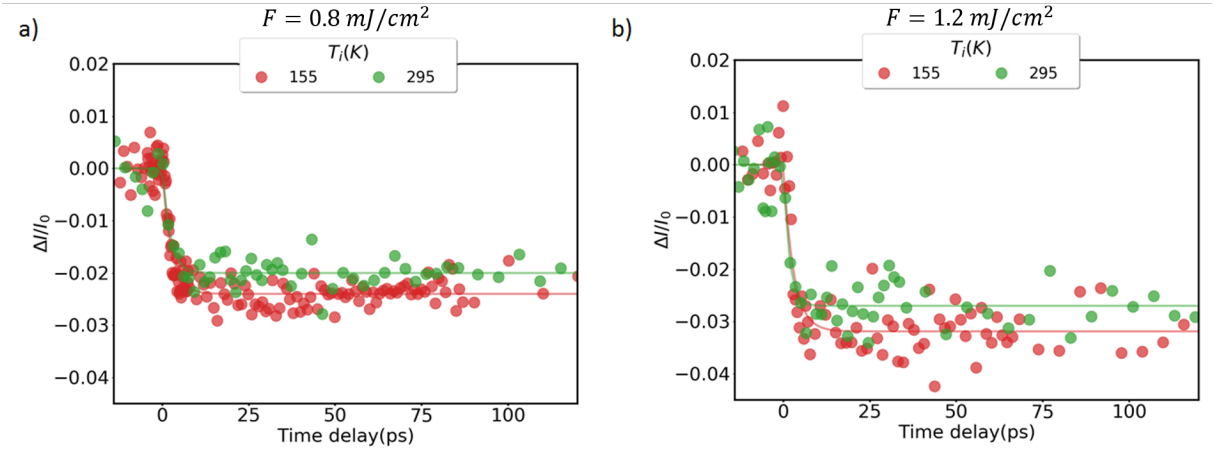

Figure 5.31: Bragg peak intensity changes at two different initial temperatures and at two incident fluences a) F = 0.8 mJ/cm^2 and b) F = 1.2 mJ/cm^2.

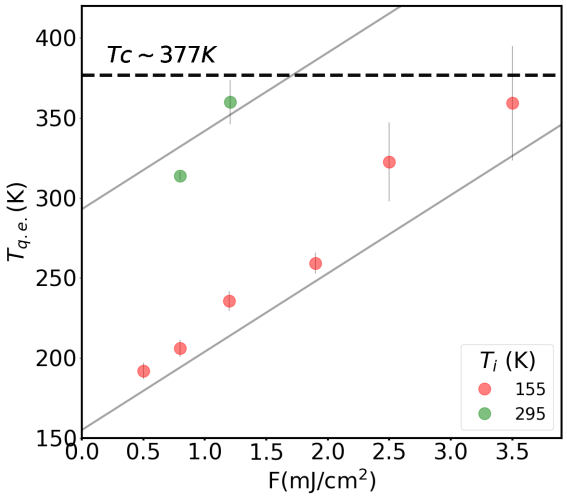

Figure 5.32: Lattice temperature estimation at the thermal quasi-equilibrium state, for two different initial temperatures. The procedure to estimate the lattice temperature is the same as the one presented in figure 5.25.

By comparing the intensity changes of the Bragg peaks in figure 5.31 we can observe that there is no significant disparity between the scans taken at low initial temperature and at room temperature. Following the same procedure as in section 5.4.2 we calculate the lattice temperature increase. At F = 0.8 mJ/cm^2 the temperature increase for both initial temperatures is $\Delta T \sim 35\,K$, and at F =1.2 mJ/cm^2 the lattice temperature increase is $\Delta T \sim 50\,K$. Figure 5.32 depicts the resulting values (green dots) which are again in good agreement with the estimated temperatures from heat absorption (gray line). Note that the incident pump energy is sufficiently low to maintain the lattice temperature below the transition temperature. Surprisingly, the response on the satellites is clearly different, as shown in figure 5.33.

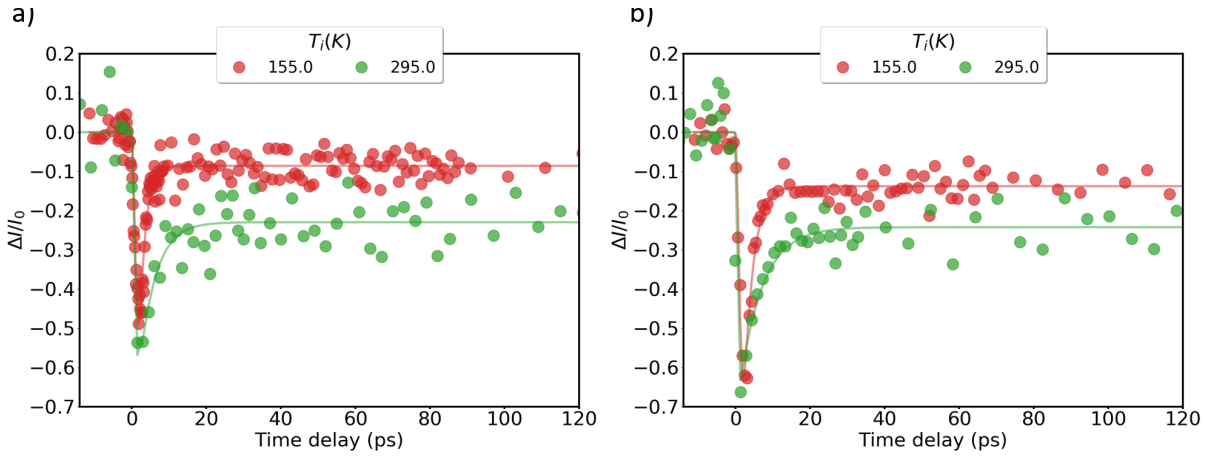

Figure 5.33: CDW peak intensity changes at two different initial temperatures and at two incident fluences a) F = 0.8 mJ/cm^2 and b) F = 1.2 mJ/cm^2. As in figure 5.28, the curves are resulting from an average over four satellite peaks with the same Q^2 wave vector.

Although the incident photoexcitation is the same in both scans, **the CDW recovery to the quasi-equilibrium state is slower when the system is initially closer to the transition temperature.** This is in qualitative agreement with the aforementioned reflectivity results from Yusupov *et al.* [134] and Chen *et al.* [133], where the relaxation times slow down when the system is closer to the critical temperature. Figure 5.34 *a*) depicts the recovery times of the satellite peaks at the two initial conditions: room temperature (green) and low temperature (red). Those taken at a higher initial temperature (i.e., at room temperature), present a recovery time of about 3.5 ps longer than when the system is initially further from the transition temperature. This suggests that the out-of-equilibrium dynamics of the CDW are strongly influenced not only by the effect of the laser excitation but also by the initial temperature. In light of these results, we plot in figure 5.34 *b*) the time constants of the CDW recovery times as a function of the ratio $T_{q.e.}/T_c$.

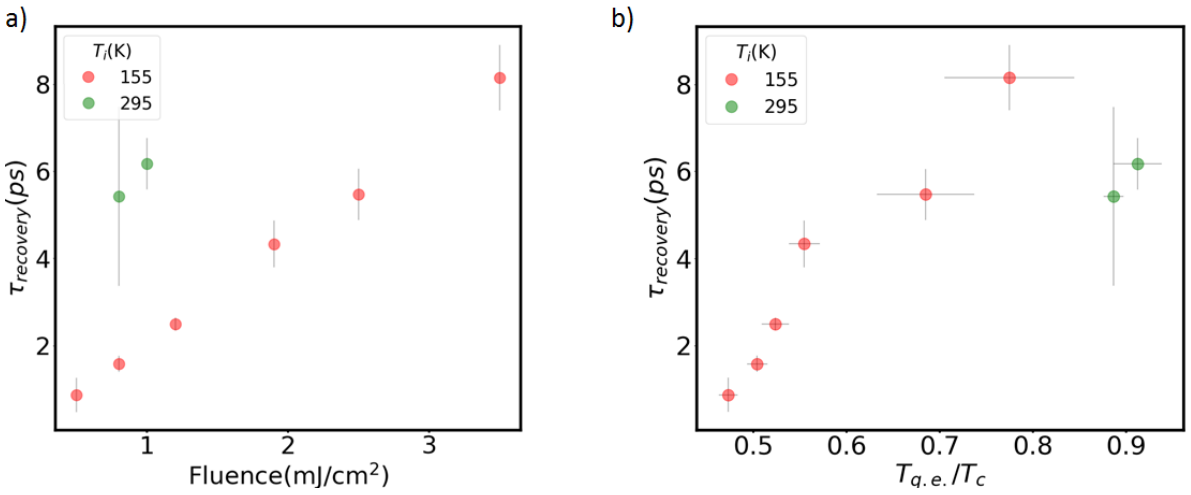

Figure 5.34: a) Recovery times of the satellite reflections as a function of the fluence at different initial lattice temperatures, b) recovery times as a function of the quasi-equilibrium and critical temperatures ratio.

From figure 5.34 b) we can conclude that the recovery time increases with higher $T_{q.e.}$.

5.4.5 Long-range order

Overall, the satellite intensity evolution presented in section 5.4.3 is in excellent agreement with those reported by Zong *et al.* on $LaTe_3$ with a similar UED setup [36]. In our case, we extended the temporal range to $\sim$ 125 ps, giving extra information on the long living quasi-equilibrium state.

The physical scenario proposed by Zong *et al.* involves the emergence of photoinduced topological defects. On the contrary, Trigo *et al.*, in a time resolved X-ray diffraction, explicitly states that the dynamics of the CDW are not influenced by the presence of such defects. The

origin of the controversy arises from the satellite peak shape, which shows large width changes in the former whereas it remains constant in the latter.

In diffraction, the FWHM of the Bragg reflections contains information on the crystal quality [44]. In the particular case of a CDW peak, they represent the long-range order, i.e., the covered distance at which the CDW maintains its periodicity, also known as correlation length. Within the Fukuyama-Lee-Rice theory [152, 153], the correlation length arises from phase fluctuations of the form $e^{\langle i[\phi(x)-\phi(0)]\rangle}$ which Fourier transform corresponds to a Lorentzian function. Thus the correlation length is inversely proportional to the FWHM of the diffraction peak:

$$\xi = \frac{1}{FWHM} \tag{5.27}$$

When the temperature of the sample is decreased towards the critical value T_c (with $T > T_c$), the correlation length is:

$$\xi \propto \frac{1}{(T - T_c)^{\gamma}} \tag{5.28}$$

with $\gamma = 2/3$ for systems in three dimensions with a complex order parameter within the XY universality class. At equilibrium conditions, the thermal evolution of the CDW peak leads to an enlarged correlation length (narrowed FWHM) as the temperature decreases towards T_c, as demonstrated by X-ray diffraction in $TbTe_3$ [109]. On the microscopic level, the increase of ξ can be understood as growth and nucleation of domains.

To take into consideration this last fact in our experimental data, I analyze in the following the FWHM temporal changes at all studied fluences. The peak profiles were taken along the a crystallographic axis by projecting the intensity of a ROI of 29×3 pixels containing the satellite reflection (see inset in figure 5.35). Note that the width of the peak is not given by a rocking curve but it is rather a projection on the Ewald sphere. The fit of the profile is performed by adding a Pseudo-Voigt function to a linear function that accounts for the background. We start by analyzing the satellite shape at equilibrium conditions at the different initial temperatures T_i.

Figure 5.35 depicts the equilibrium profiles after background subtraction at two different initial temperatures: $T_i = 155$ K and $T_i = 295$ K. These profiles clearly demonstrate that the satellite width at equilibrium increases when $T \sim T_c$.

In the following, we compare the steady state satellite peak widths. Figure 5.36 shows the normalized peak profiles after background subtraction at negative time delays for four different incident fluences. Interestingly, the FWHM of the equilibrium profiles present broadening at high incident fluences. Every scan was collected with the same number of electrons per bunch and chronologically disordered with respect to the increasing fluence, so that we can discard sample deterioration with time. The reason for this slight broadening might be cumulative heating. Indeed, because of the slow time scale of heat dissipation, the sample does not fully

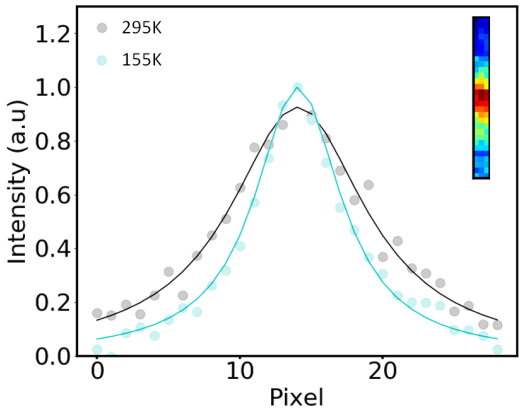

Figure 5.35: Peak shape of the (-10δ) satellite peak at equilibrium (at negative time delays and with the pump beam blocked) at $T_i = 155$ K (cyan) and at $T_i = 295$ K. Inset: selected ROI around the satellite peak, the profile corresponds to the intensity integrated along the vertical axis.

relax between two laser shots, leading eventually to a residual cumulative heating. This observed effect in the FWHM implies that there is a slight deviation in the estimated lattice temperature increase in section 5.4.2. Nevertheless, at this millisecond time scale we can consider that the temperature remains well below T_c.

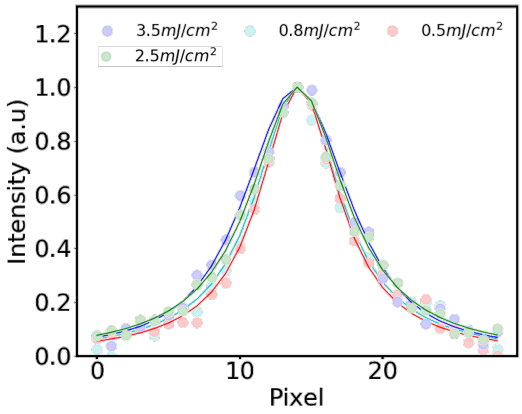

Figure 5.36: Peak shape of the (-10δ) satellite peak in the steady state (at negative time delays) for different incident fluences.

We now turn to the dynamics of the CDW peak width after photoexcitation. Figure 5.37 shows the satellite intensity profiles at several delay times at equilibrium and at the photoexcited state. The blue dots correspond to the equilibrium profile (collected with the pump beam blocked) while the red dots correspond to the photoexcited profile. We can clearly observe that at low fluence ($F = 0.8$ mJ/cm^2, left column), the FWHM does not present evident changes at any delay time, while its intensity is decreased without full recovery up to 138 ps. On the other hand, at high incident fluence ($F = 3.5$ mJ/cm^2, right column), shortly after the pump arrival, the FWHM clearly broadens with respect to the equilibrium profile. Here, it is interesting

to notice that at negative delays (figure 5.37 *e*)) the photoexcited and equilibrium profiles do not completely match, which confirms that the system does not reach full thermal relaxation between consecutive pump pulses at high fluences.

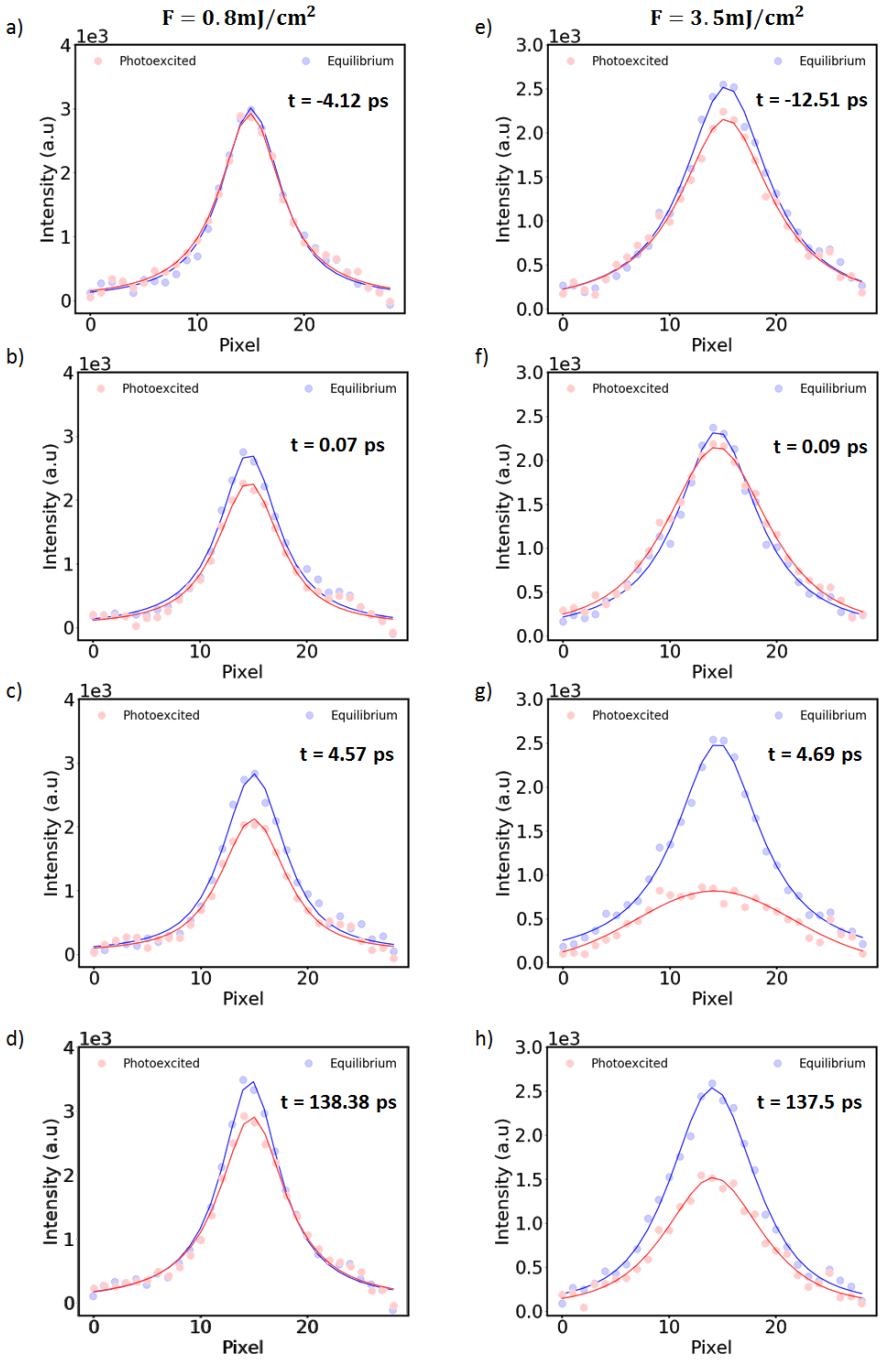

Figure 5.37: Line profiles of the (-10δ) satellite peak at equilibrium (blue) and after photoexcitation (red) at different time delays. Left column: $F = 0.8\,mJ/cm^2$. Right column: $F = 3.5\,mJ/cm^2$.

The complete dynamics of the FWHM are shown in figure 5.38 *a)*: at low fluence, below the

critical value $F < F_c$, the FWHM shows small changes $\Delta w/w_0 < 8\%$, that quickly recover to the initial values. On the other hand, above the critical value $F > F_c$ the peak broadens significantly without full relaxation to initial values within the temporal range of the scan. This is clearly seen in figure 5.38 *b)* in which dark blue dots represent the maximum relative changes (averaged over four points around the maximum) and light blue dots represent the FWHM changes after the recovery time (averaged over the last twenty points of the curves). The error bars are calculated from their standard deviation.

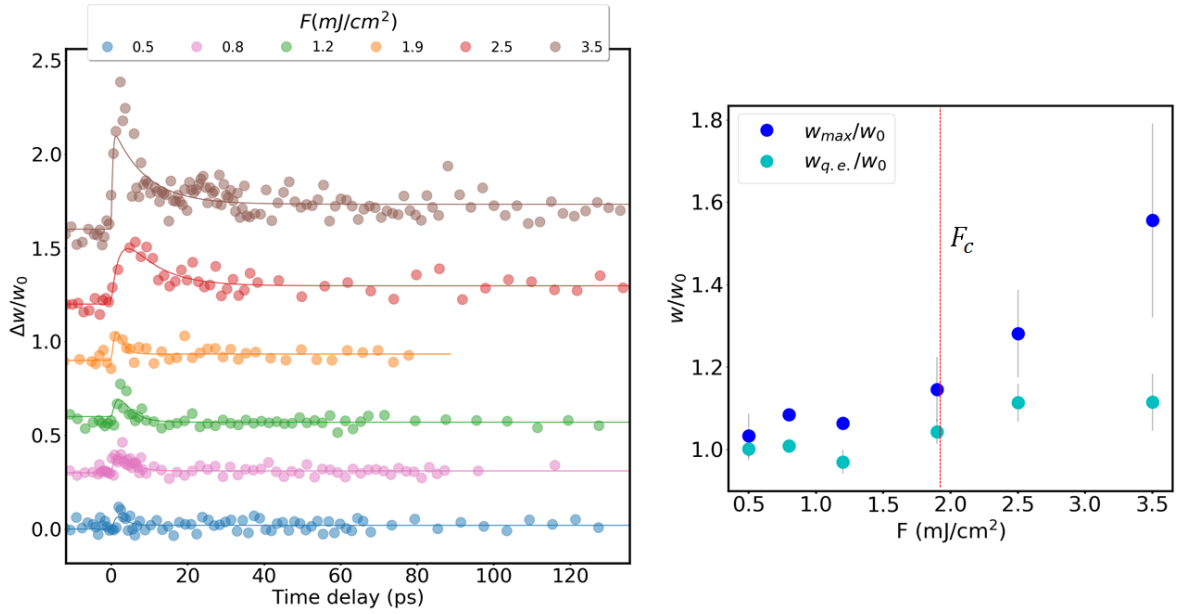

Figure 5.38: a) Relative FWHM changes at different incident fluence. Curves are vertically shifted for clarity. b) Relative changes of the FWHM at the maximum (averaged over the four points around the maximum) and after the time recovery (averaged over the last twenty points of each curve in a)).

The temporal decay and recovery time constants of the relative peak widths follow the dynamics of the CDW peak intensities. Figure 5.39 summarizes and displays the recovery times of both intensity and FWHM, which increase linearly with incident fluence. In order to compare directly the temporal traces of both parameters, figure 5.40 depicts the intensity and FWHM temporal changes. While the temporal constants are on the same order, the relative changes to initial values are quite different. Below the critical fluence, the relative changes of the peak width present a fast increase followed by a complete relaxation to initial values, whilst the intensity of the peak does not fully recover. Experimentally, the fact that the peak width presents small differences after the recovery time, might be related to the finite coherence length of the probe (~5 nm). On the other hand, above the critical fluence, neither the intensity nor the FWHM return to their initial values.

In summary, we have observed that both initial lattice temperature T_i and incident fluences have strong implications on the satellite peak widths. At equilibrium conditions, the FWHM of the satellite peak widths is broader when $T \sim T_c$. In the steady state, we have observed slight

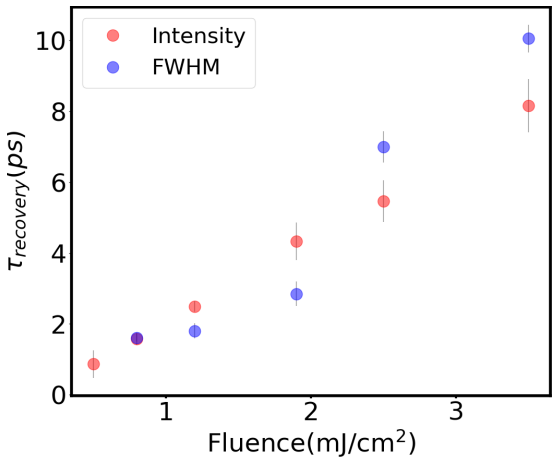

Figure 5.39: Recovery times of the CDW peak width and intensity as a function of the incident fluence. At $F = 0.5\,mJ/cm^2$ no changes of the peak width are observed.

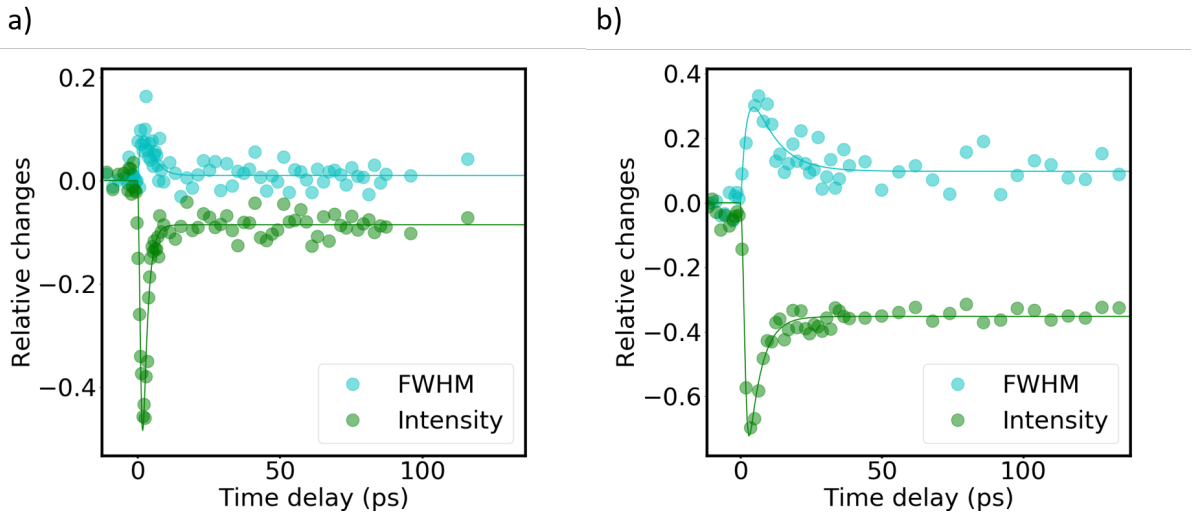

Figure 5.40: Temporal evolution of the intensity and FWHM changes at a) $F = 0.8\,mJ/cm^2$ and b) at $F = 2.5\,mJ/cm^2$.

broadening at higher fluences, probably due to cumulative heating effects. Finally, the temporal dynamics of the intensity and width have similar time scales.

5.5 Discussion

In this chapter we have shown a series of pump-probe electron diffraction experiments at different excitation energies and at different initial conditions. An extensive analysis of the Bragg reflections intensities has allowed us to retrieve information on the state of the main lattice after photoexcitation. The temperature of the quasi-equilibrium state $T_{q.e.}$ has been

estimated from the Debye-Waller effect and from laser heat absorption, both results are in good agreement. At all incident fluences, the quasi-equilibrium temperature satisfies $T_{q.e.}$<T_c. The typical time to reach $T_{q.e.}$ is $\tau_{thermal} \sim 6$ ps and shows a weak temporal dependence on incident fluence. Our experiments, performed at two different initial lattice temperatures (shown in section 5.4.4), have demonstrated that the lattice temperature increase is similar under the same incident fluence.

On the other hand, the satellite peak intensities, inherent to the CDW dynamics, present a fast decay (∼1 ps) and a clear slowing down of the recovery times. The dynamics is closely related to the $T_{q.e.}$ as shown with the results starting at higher initial temperatures. This behaviour is consistent with the universal critical slowing down in phase transitions. For fluences $F_c \geq 1.9\,\mathrm{mJ/cm^2}$, the intensity of the satellite is decreased to the background level suggesting that, although the lattice is below the $T_c = 377$ K, the system transits to the high symmetry state by photoexcitation.

Finally, an analysis of the satellite reflection profiles have shown that the width of the satellite peaks is broader at thermal equilibrium with initial temperature $T_i \sim T_c$. After photoexcitation, the width of the CDW peak increases, witnessing the loss of long range order. The temporal dynamics of the CDW peak width follows the one of the intensity.

In light of these results, the chronology of the photoexcitation and relaxation processes can be summarized as follows: **(1)** electron excitation is followed by fast electron-phonon coupling. This creates a large disorder in the system resulting in the decrease of the satellite intensity and an increase of the FWHM in t∼1.5 ps → **(2)** Lattice temperature increase (inferred from Bragg peak intensity loss) and partial reformation of the satellite intensity in few picoseconds → **(3)** lattice temperature stabilization at $T_{q.e.}$. The temporal relaxation of the CDW with respect to the lattice thermalization depends on two critical values F_c and T_c.

Several possible mechanisms could be responsible for our experimental observations, listed in the following categories:

a) Lattice strain

b) CDW amplitude suppression and phase fluctuations

c) Loss of long range order due to:

- c1) Domain nucleation and growth
- c2) Photoinduced topological defects: CDW dislocations or vortex
- c3) Pinning of the CDW on crystal impurities

d) Strong mixing with photoexcited optical modes

In the following I review one by one the possible effects in the diffraction signal from the different mechanisms listed above:

a) Lattice strain.
We have seen in the phase diagram of the RTe_3 family that the lattice parameters play an important role in the transition to the CDW state. Since our sample is a thin film, we could argue that the arrival of the laser pulse may trigger coherent breathing oscillations along the b crystallographic axis, perpendicular to the Te nets containing the CDW, and thus perturbing the CDW formation. Such a mechanism have been already observed in 1T-TaSeTe [33], another layered CDW compound. Thin films of layered materials usually respond to the laser excitation by coherent breathing oscillations launched from photoinduced pressure as demonstrated in several metals by Thomsen *et al.* in reflectivity measurements [67]. In our diffraction results, such acoustic oscillations are present in the lattice planes perpendicular to the probing beam, which can not be observed in transmission geometry. Despite this geometrical constraint, such a compression and expansion along the stacking axis should induce a stretching of the a and c lattice parameters.

A study of the peak positions of all Bragg peaks did not reveal any presence of lattice changes within our spatial resolution that could support this interpretation.

b) CDW Amplitude suppression and CDW phase fluctuations.
Time resolved X-ray diffraction experiments have shown in several CDW systems that the laser excites coherently the amplitude mode of the CDW [22, 37] on a sub-picosecond time scale (see figure 5.6). The frequency of the amplitude mode in the RTe_3 compounds is $\nu_{AM} \sim 2$ THz, which tends to soften at $T \sim T_c$ or with increasing pump excitation. Our temporal resolution does not allow us to measure the amplitude mode oscillations, so that a decrease of the distorted amplitude can only be retrieved from the loss of the satellite intensity accompanied by an increase of the Bragg peak intensity (see equation 5.22). The latter was not appreciable in our data sets, probably masked by the background level.

On the other hand, and as we have seen in section 5.1.2 at thermal equilibrium, the changes of the CDW peak intensity (not accompanied by an increase of the Bragg peak intensity) are a clear signature of excitation of phason modes. Vibrational excitations of the phase (phason mode) weaken the satellite reflections analogously to the Debye-Waller effect resulting from phonon scattering in the Bragg peaks. Considering that these phase modes are lower energy excitations than the amplitude mode, we can expect them to appear at longer temporal scales. Most likely after lattice thermalization, at the quasi-equilibrium state.

Accordingly, the loss of intensity on the satellite peaks at short temporal time scales can be attributed to a reduction of the CDW amplitude (and so the lattice distortion). At longer time scales, i.e., after the lattice temperature is stabilized in the quasi-equilibrium state, we attribute the intensity loss to an increase of the phason population and a partial reformation of the lattice distortion, i.e., the order parameter is not fully recovered.

c) Loss of long range order.
Loss of long range order in the CDW leads to broadening of the FWHM of the satellite reflections,

clearly apparent at high initial temperature ($T_i \sim T_c$) and at high incident fluence ($F \geq F_c$). Phase transitions at thermal equilibrium are characterized by the presence of topological defects or domains when the temperature approaches the critical value $T \sim T_c$. This is exactly what we observe at high excitation fluences and at higher initial sample temperature, where the FWHM of the satellite peak does not fully recover to original values at any time delay.

As a consequence, we assign the presence of topological defects to higher lattice temperatures, similarly to what is observed at thermal equilibrium. This suggests that, if topological defects are the key in the slower relaxation process, they are not only photoinduced by the pump, but also intrinsically linked to the lattice temperature. Whether these defects are dislocations or vortex, as discussed by Zong *et al.* [36], can not be distinguished in our diffraction experiments. Most likely, we observe multiple domain nucleation followed by a growth of these domains. Domain growth at long time delays has been demonstrated experimentally in 1T-TaS_2 by Laulhé *et al.* [24].

The fact that the dynamics of the FWHM and the intensity follow similar time scales could point to a relation between the order parameter and the correlation length. Indeed, Dicarlo *et al.* in an experimental study on CDW pinning on crystal impurities on $NbSe_3$, found a direct relation between the amplitude of the CDW distortion and the correlation length of the form [154]:

$$\xi \propto \Delta^2$$

d) Mixing with phonon modes.
Finally, mixing of the CDW amplitude with optical modes is a possible mechanism explaining the observed satellite dynamics. The works performed by Yusupov *et al.* showed in a pump probe reflectivity experiment that the sample temperature plays a crucial role on the amplitude of the CDW state, mostly driven by couplings of the amplitude mode with excited optical phonons [134]. In their experiments, they have shown that when the system crosses a critical temperature (termed as T_{cr} in the figure) the intensity associated to the CDW in the reflectivity curves is highly decreased, implying that the gap of the CDW is reduced. $TbTe_3$ is a neighbouring compound of $GdTe_3$ (see figure 5.10), so we can expect similar behaviour in our material. The critical fluence observed in our experimental results in a temperature of the lattice of T~250 K, in close agreement with the T_{cr} value given by Yusupov *et al.*. They assigned this response to a strong coupling between the amplitude mode and the 1.75 THz phonon, as clearly shown in figure 5.41. The mixing of the two modes strongly disturbs the Te ion displacements (i.e. the amplitude mode) by introducing other displacements corresponding to the 1.75 THz phonon.

This could potentially lead to CDW gap renormalization by the 1.75 THz mode, presenting a smaller order parameter even though the system is below the critical temperature $T < T_c$. These results have been supported experimentally by Lavagnini *et al.* by Raman

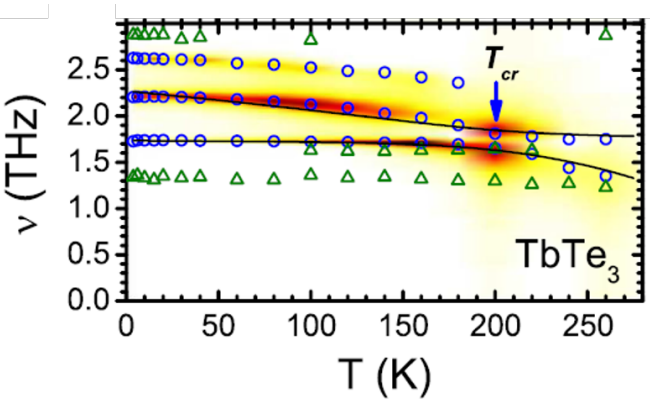

Figure 5.41: Phonon intensity map as a function of the sample temperature in $TbTe_3$. The color map, circles and triangles are the experimentally retrieved frequencies while black lines result from calculations. Mode mixing is evident between the amplitude mode (whose frequency is $\nu = 2.2$ THz at low T) and the 1.75 THz mode at intermediate temperatures and with the 2.6 THz phonon at low temperatures. Figure from [134].

spectroscopy [155]. In our experimental results we do not observe the presence of any oscillation, so that we can not conclude in this respect.

Extrapolating these interpretations to our data, we can assign the possible reviewed mechanisms to different time scales. At low incident fluences $F < F_c$, the lattice distortion is reduced (and so the order parameter) in a time scale below our temporal resolution (i.e., t<1 ps). Disorder induced by the pump generates multiple domains which nucleate before the system reaches the quasi-equilibrium state (i.e.,before 6 ps). At this point, the order parameter is practically recovered and the loss of intensity at long time delays can be associated to a high population of phasons. As the incident fluence is increased, the order parameter is largely reduced, being fully suppressed for $F > F_c$. The recovery time of the CDW is similar to the time the system needs to reach the quasi-equilibrium state. At these conditions, the thermal increase prevents the system to recover both the initial amplitude and the long range order within the time range of the scans.

In conclusion, the energy energy difference ΔE of the system can be divided into three main contributions: the lattice (with its dynamics encoded in the intensity of the Bragg peaks), the amplitude and the phase of the CDW (with their dynamics encoded in the intensity and width of the satellite peaks). Similarly to the scenario proposed by Lee *et al.* [30], figure 5.42 shows a schematic of the temporal energy difference of the system divided into the three parts.

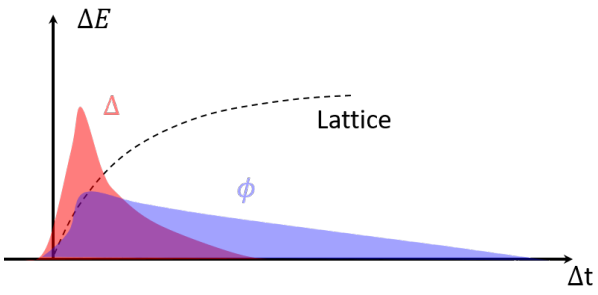

Figure 5.42: Schematic of the temporal energy changes at the lattice and CDW levels with Δ denoting the amplitude of the CDW and phi the phase.

5.6 Conclusion and perspectives

The presence of topological defects in CDW phase transitions at thermal equilibrium has been widely discussed theoretically and experimentally [135, 156]. In the case of photoinduced phase transitions probed by diffraction, their appearance is still under debate and several groups probing different compounds do not reach an agreement [30, 34, 36, 37].

Our results performed at different initial temperatures showed that the slowing down in the CDW relaxation is mostly related to the lattice temperature rather than to the density of absorbed photons, which we have maintained constant by pumping at the same incident fluences, as shown in section 5.4.4. **This suggests that, if topological defects are the key in the slower relaxation process, they are not only photoinduced by the pump, but also intrinsically linked to the lattice temperature**. The results given by Zong *et al.* on $LaTe_3$ could also reflect this effect, since their experiments were performed at a higher repetition rate of 5 kHz. As we have seen in our experimental results (notably in figure 5.36) such repetition rates are seemingly too high for a complete heat evacuation of the thin films at high incident fluences. A possible way of excluding laser heating effects might be verified by performing time resolved experiments with a pump wavelength of the same order as the CDW gap and the optical mode, i.e., a few THz. Moreover, direct imaging by means of time-resolved STM or electron imaging on thin films could further enlighten this scenario.

From optical measurements on several RTe_3 compounds [134] one thing seems to be certain: the photoexcitation triggers the appearance of optical lattice modes that couple to the charge-density state, which likely affects the lattice distortion. This scenario fits well with the interpretations given by Trigo *et al.* and Moore *et al.* [37, 108]. Time resolved reflectivity and diffraction experiments (with sufficiently short temporal resolution) at different incident fluences and temperatures could confirm the strength of this coupling.

Finally it is important to point to further investigations on sample geometry. All the reflectivity results in literature are performed on bulk samples, which makes it difficult to directly compare to our experimental results on free-standing thin films. Moreover, pump-probe reflectivity experiments performed in transmission geometry could reveal if the presence of acoustic modes within the thin films are affecting anyhow the amplitude mode related to the CDW state.

Chapter 6

Displacive phase transition of Nb_3Sn

Contents

A15 phases have attracted the scientific attention since the 1960s due to their particular structural and electronic properties. Around 45 of the A_3B compounds with this structure (with A a transition element) are superconductors of potential interest [157]. Amongst them, Nb_3Sn and V_3Si are the most representative alloys. Two of their most noticeable features are a structural phase transition from a cubic symmetry $Pm3n$ to a tetragonal $P4_2/mmc$ at a certain temperature $T_m \sim 45$ K and the superconducting transition occurring at lower temperatures at $T_c \sim 18$ K [158]. For several years, until the discovery of the cuprates in 1984, these compounds held the largest superconducting temperatures [159].

The structural phase transition, also known as a martensitic phase transition, is a diffusionless phase transition associated with a lattice distortion at constant volume of the unit cell. The study of the relation between the structural transition and the superconducting state has been a central question for many years in the scientific community [158]. The martensitic phase transition, was also proposed theoretically as a triggering mechanism of a CDW likely in competition with the superconducting state [160]. Despite the extensive investigations performed in these compounds during the 1970s and 1980s, the discovery of the perovskite cuprates shifted the attention from the A15 structures leaving some remaining open questions; as for example, what is the relation between the martensitic transition and the plausible appearance of a CDW state [161].

The development of time resolved techniques is turning back the interest on the A15 structures. In the particular case of the superconducting phase, terahertz pump-probe reflectivity has recently revealed the appearance of the hidden competing CDW state only accessible by non-thermal photoexcitation [162, 163]. The dynamics of the structural phase transition remains

however unknown. Time resolved X-rays sources as synchrotrons are well suited to perform this kind of studies.

In this chapter, I briefly introduce the structural and electronic properties of Nb_3Sn, a sample on which we have performed a series of pump-probe X-ray diffraction experiments in the CRISTAL beamline at SOLEIL. In section 6.2, the experimental results are presented and compared with the phase transition at thermal equilibrium. Section 6.3 gives a summary and future work to be performed.

6.1 Nb_3Sn properties

The crystal structure of Nb_3Sn at high temperature presents a cubic structure belonging to the space group $Pm3n$ (No.223) with lattice parameter $a = 5.282\,\mathring{A}$ [164]. The unit cell in the cubic phase is composed by two Sn atoms and six Nb atoms. The latter forms orthogonal 1-dimensional chains located at the faces of the cubic cell with an interatomic separation within the chains (intrachain) of $a/2$. On the other hand, the Sn atoms are located at the BCC sites of the unit cell as shown in figure 6.1.

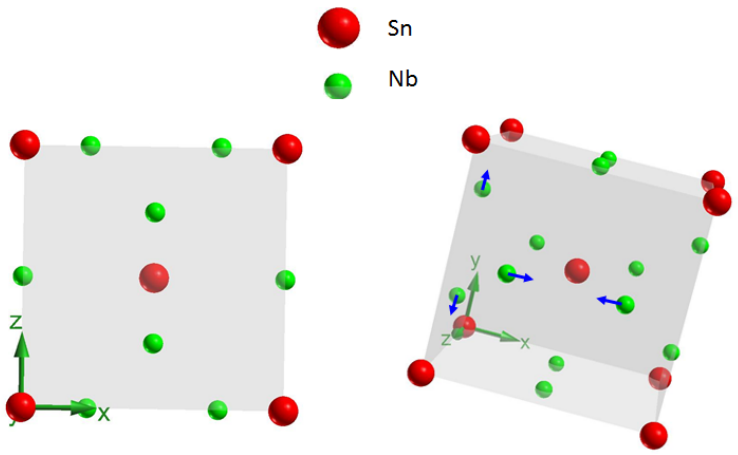

Figure 6.1: Unit cell of Nb_3Sn in the cubic phase.

On cooling down, the crystal structure undergoes a large softening in all lattice modes, which is particularly prominent for shear waves (acoustic) propagating along the [110] direction with [1-10] polarization. The softening becomes maximal at a $T_m \sim 45$ K, which varies between 40 K and 50 K depending on stoichiometric conditions on the sample [158]. At this point, the crystal becomes unstable and accommodates in the tetragonal phase with space group $P4_2/mmc$ (No.131).

Along with the acoustic phonon softening, the transition to the tetragonal phase arises with a dimerization of the Nb atoms within the linear chains and a weak distortion of the cubic phase. These atomic distortions correspond to an optical phonon with symmetry Γ_{12}, as pointed by the

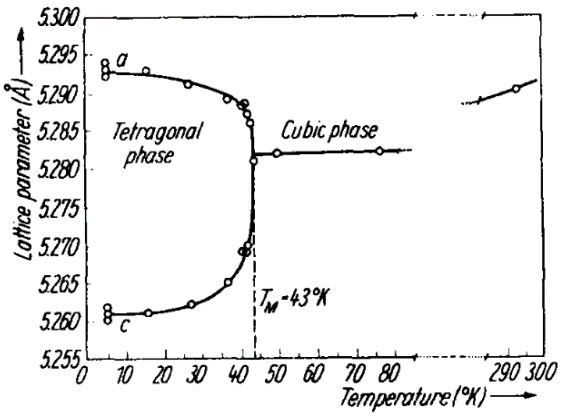

Figure 6.2: Lattice parameter measured as a function of the temperature. T_M corresponds to the temperature at which the crystal transits to the tetragonal phase. Figure from [164]

blue arrows in figure 6.1. The maximum atomic displacement of the Nb atoms in the chains corresponds to a $\delta = 0.00315\,\mathring{A}$ at T = 4 K, as reported by Shirane and Axe [165]. The distorted lattice results in a lattice parameter ratio in the tetragonal phase of $a/c = 1.0062$ [164, 165]. This type of structural transition is known as martensitic. In the particular case of Nb_3Sn, the volume of the unit cell in the cubic phase is maintained constant through the transition to the tetragonal phase, so that the following condition is fulfilled:

$$V = a_0^3 = a^2 c \tag{6.1}$$

where a_0 is the lattice parameter of the cubic cell and a, c the lattice parameters of the tetragonal phase. Both parameters are related by the tetragonal strain [166]:

$$\varepsilon = a_0/c - 1$$

Figure 6.2 shows the lattice parameters as a function of the temperature measured by Shirane *et al.* at the cubic and tetragonal phase [165].

The electronic bands of these structures have a strong 1-dimensional character arising from the Nb linear chains. The electronic density of states in the cubic phase presents a singularity of the d-bands from the Nb atoms near the Fermi level, as shown in figure 6.3 a). Labbé and Friedel proposed theoretically that the origin of the structural instability was behind this electronic singularity. A splitting of the density of states into two sub-peaks (a break of the d-band degeneracy) leads to an electronic gain at the vicinity of Fermi level. This electronic rearrangement favours the tetragonal structural phase against the cubic structure.

At the T_m transition temperature, the distances between Nb atoms is altered in such a way that the chain along the [100] direction tends to stretch (contract) the atomic distances while the other two chains along [010] and [001] tend to contract (stretch), fulfilling the conditions of constant volume through the transition. The degeneracy of the bands in the tetragonal phase is

thus "broken" raising the electronic energy and the density of states at the Fermi level. Figure 6.3 illustrates a sketch of the band degeneracy in both phases [167].

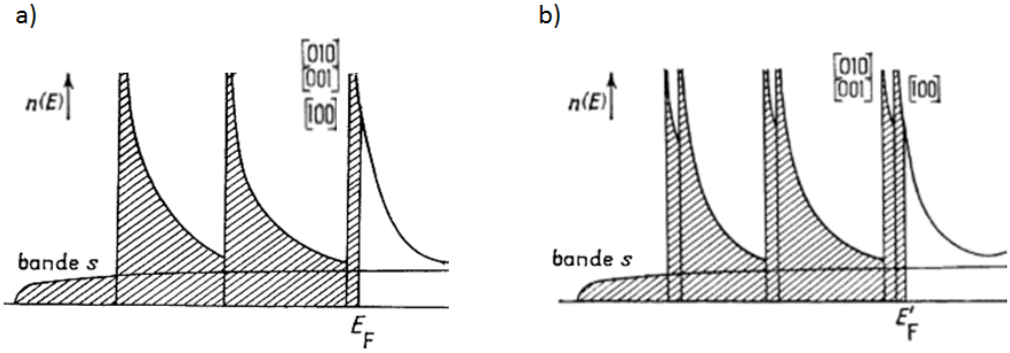

Figure 6.3: Electronic d bands from the Nb atoms in the linear chains in a) the cubic phase and b) the tetragonal phase. Image taken from [167].

Although several compounds of the A15 family have similar density of states at the Fermi level, their critical temperatures to the superconducting state are largely different, as an example Nb_3Au presents a $T_c = 11.5\,K$, while Nb_3Ir $T_c = 1.7\,K$. This observation suggests that the superconducting properties of these compounds can not only be explained by the density of states itself [168].

6.2 Experimental results

On a first experiment we characterized the structural phase transition at equilibrium conditions and compared it later with the time resolved measurements. The measurements were performed with an X-ray energy of 8 keV ($\lambda = 1.55\mathring{A}$). The sample is oriented along the [110] crystallographic axis, coincident with the vertical axis of the diffractometer. The measurements were performed at grazing geometry with an angle of incidence $\alpha_i = 1°$, resulting in a X-ray penetration depth of $\delta_X \sim 100\,nm$. A schematic of the diffraction geometry is given in figure 6.4. The blue shaded region corresponds to the Ewald sphere, $\{XYZ\}$ axis represent the laboratory framework centered at the sample position, the crystallographic direction perpendicular to the surface is highlighted in red. We have performed a series of scans by turning the sample around the azimuthal angle ϕ (i.e., the normal to the surface). The vertical and horizontal position of the diffracted peak can be retrieved from the angles δ and γ, respectively. The detector was located at a distance of 780 mm from the sample, resulting in an spatial resolution of 9.5 mdeg/pixel.

In order to cool down the sample we used a Helium cryostat; the temperature control was given by the Helium flow together with a heating wire connected to a PID controller. The minimum measured temperature at the sample position was T = 16 K, well below the martensitic phase transition temperature T_m reported in literature. The cryostat was mounted on the 6-circle

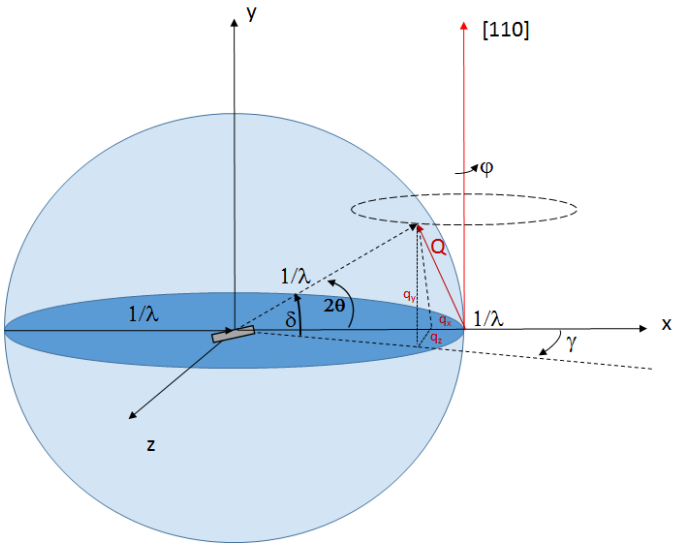

Figure 6.4: Schematic of the experimental grazing geometry.

diffractometer of the beamline. Detection of the Bragg reflections was achieved with the 2D pixel XPAD detector (detailed description in chapter 3).

6.2.1 Martensitic phase transition at equilibrium

We start by analyzing the equilibrium behaviour of the material. This will serve as a basis for comparison with the time resolved experiments presented later. We performed a series of rocking scans around the azimuthal angle ϕ (see figure 6.4) at different sample temperatures. As a way of correcting any possible intensity loss arising from contraction at low temperatures, we have carefully adjusted the vertical position of the sample at every temperature. Due to a "miscut" of the sample, there is a small deviation of about 5° between the [110] and the vertical axis. This makes the indexation of the peak very difficult in grazing incidence. Nevertheless, the Bragg angle can be easily retrieved from the δ and γ angles from the relation:

$$cos(2\theta_B) = cos\,\delta\ cos\,\gamma \tag{6.2}$$

Considering a lattice parameter $a = 5.285\ \AA$, the most plausible reflection is of the type (201) or equivalent reflections with the same norm. When lowering the temperature phase, several splittings are possible due to the presence of different variants in the sample. Knowing that there is no preferred direction in the cubic phase, the contraction/dilatation which appears at low temperature can be observed along the three equivalent directions: $\{a+\delta, a+\delta, a-2\delta\}$, $\{a+\delta, a-2\delta, a+\delta\}$ or $\{a-2\delta, a+\delta, a+\delta\}$. As a consequence, the (201) Bragg reflection would then split in three peaks, in principle: $(2+2dq, 0, 1-dq)$,$(2-2dq, 0, 1+dq, 0)$ and $(2-dq, 0, 1-dq)$ with $dq = \Delta a/a$. A detailed calculation of the possible splitting geometry of the (201) reflection

is given in Appendix E.

Figure 6.5 depicts the resulting rocking curves at different temperatures. The curves are vertically shifted for clarity. The evolution of the Bragg reflection shows a loss of intensity accompanied by a large broadening until T = 35 K. Below this temperature the emergence of a second reflection at higher azimuthal angles becomes evident. In the following and as a way to distinguish both reflections, each of them is referred as ϕ_1 and ϕ_2, as marked in figure 6.5. The emergence of reflection ϕ_2 can result either from a splitting of the cubic reflection or by surface domain contribution, as discussed later.

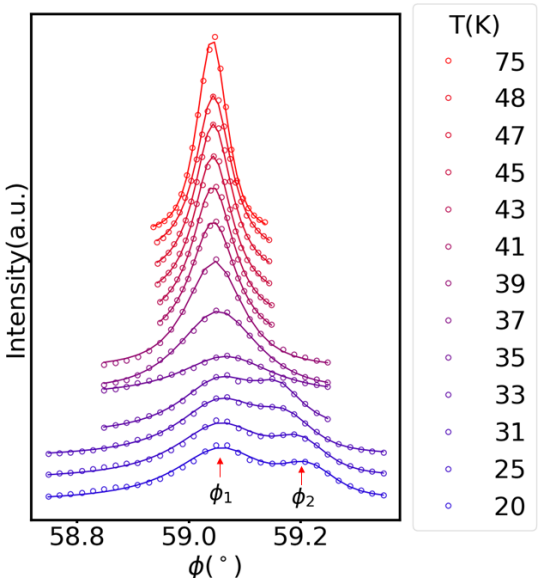

Figure 6.5: Equilibrium rocking curves of the (210) Bragg reflection measured at grazing incidence and at different temperatures. Curves are vertically shifted for clarity. Below T = 35 K, a second reflection emerges with constant FWHM and its position evolves towards higher azimuthal angles.

The experimental results are fitted by a single Pseudo-Voigt fit for temperatures T ≥ 35 K and a double Pseudo-Voigt for T < 35 K. The resulting parameters are presented in figure 6.6.

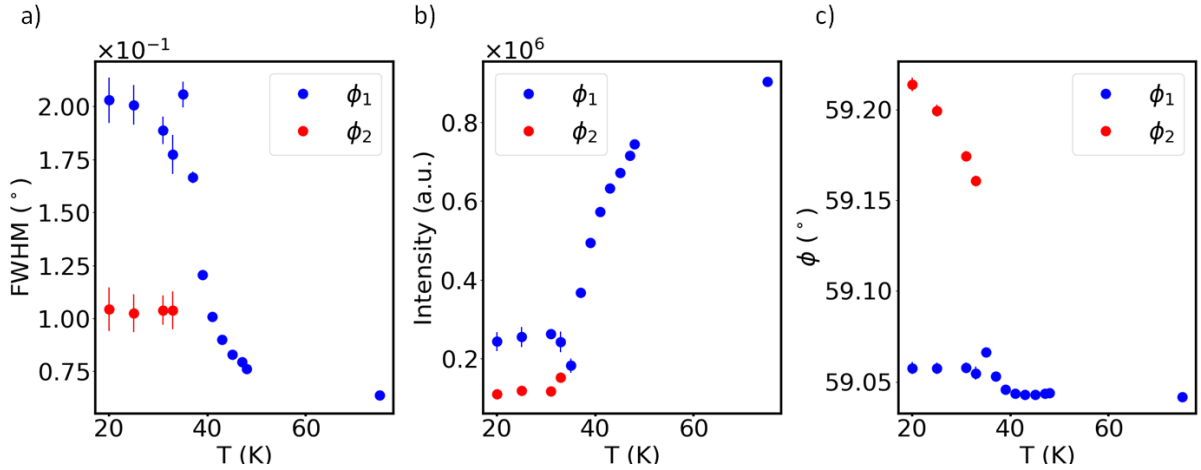

Figure 6.6: Fit parameters of the rocking scans at equilibrium temperatures: a) FWHM, b) maximum intensity (height parameter) and c) center.

Interestingly, the FWHM of reflection ϕ_1 (figure 6.6 a)) shows an exponential increase, that ceases with the emergence of the second reflection ϕ_2 at T = 35 K. On the other hand, the width corresponding to ϕ_2 remains constant. The intensity of the Bragg reflection ϕ_1 displays a fast drop down to 35 K that partially recovers at lower temperatures. The intensity gain of the second reflection ϕ_2 remains constant (see figure 6.6 b)). Finally, figure 6.6 c) depicts the thermal evolution of the positions of each Bragg reflection. The position of the cubic reflection ϕ_1 presents a tip at T = 35 K followed by a constant value, whereas the position of ϕ_2 increases continuously up to the lowest measured temperature.

The width broadening observed in reflection ϕ_1 is likely a consequence of the appearance of new domains in the tetragonal phase. A closer inspection of the detector images reveals a clear splitting along the vertical direction of the image. Figure 6.7 shows the detector images at the position of reflection ϕ_1. At T =37 K the Bragg reflection presents an obvious change in shape followed by a splitting which evolves along the vertical axis, pointed by the red arrows.

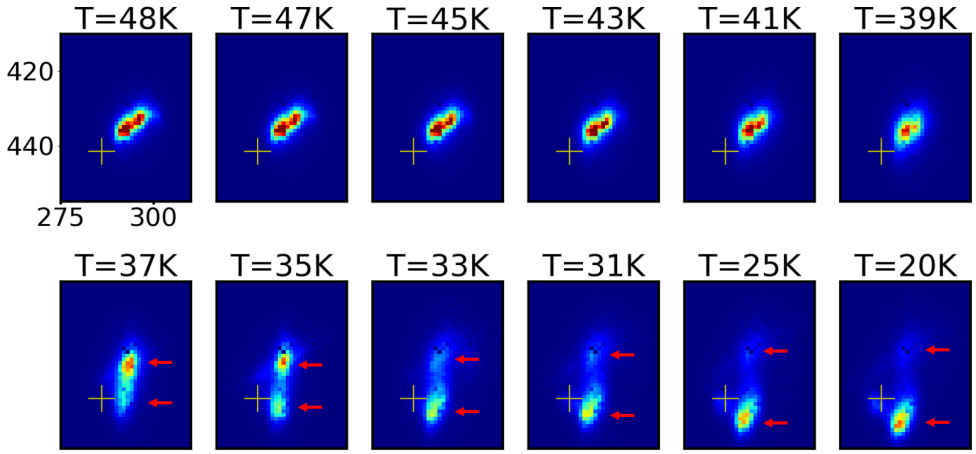

Figure 6.7: Detector images (linear scale) corresponding to the peak located at ϕ_1 in the rocking curve. The white cross marks the position of the high temperature Bragg reflection, used as the origin to retrieve the vertical and horizontal positions. Red arrows point to the position of the emergent peaks after splitting at T = 37 K. Color maps are normalized to the maximum of each image for clarity.

The position of the center of mass of each reflection allows us to extract the corresponding lattice parameters from the Bragg law and the angular relation given by equation 6.2.

The behaviour of the second reflection at ϕ_2 on the detector images is shown in figure 6.8. Note here that in contrast to peak ϕ_1, the azimuthal angles vary with decreasing temperature, with their corresponding value given in each image. The peak in this case does not present further splitting or large displacements along the vertical or horizontal positions.

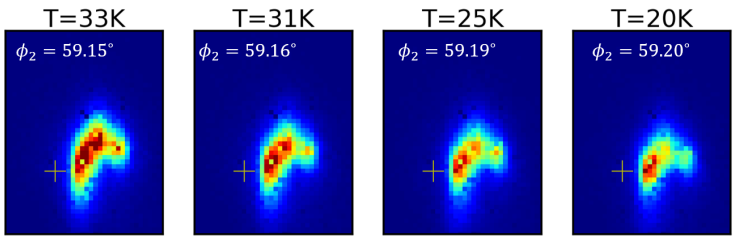

Figure 6.8: Detector images corresponding to the peak located at ϕ_2 in the rocking curve. In this case the color map scale is the same for all images.

Figure 6.9 shows the calculated lattice parameters retrieved from the center of mass of the peaks in ϕ_1 on the detector images. The position of the peaks highlighted by arrows in figure 6.7 gives rise to an increment and a decrease of the lattice parameters, as expected from literature (see figure 6.2). On the other hand, the center of mass corresponding to ϕ_2 depicted in figure 6.8 shows little changes. Since we have some uncertainty on the indexation of the peak, we rely on the position of ϕ_1 to retrieve the lattice parameter.

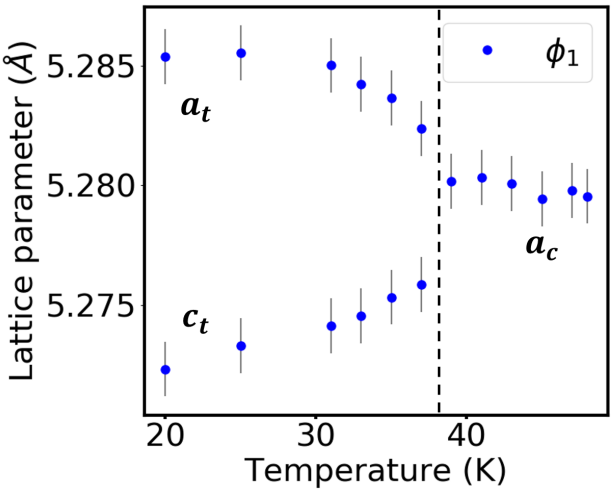

Figure 6.9: Calculated lattice parameters from the images on the detector. The error bars correspond to the spatial resolution given by the pixel size.

These lattice parameter values point to a transition temperature of our sample of $T_m = 39$ K, in close agreement with the values reported in literature.

The lattice parameters retrieved from ϕ_1 satisfy the constant volume condition in both phases: in the cubic phase with $a_c = 5.2801 \pm 0.0012$ Å and $V_c = 147.202 \pm 0.095$ Å^3, and in the tetragonal phase with $a_t = 5.2854 \pm 0.0012$ Å, $c_t = 5.2723 \pm 0.0012$ Å and $V_t = 147.284 \pm 0.064$ Å^3. The tetragonal values are measured at 20 K.

6.2.2 Time resolved structural phase transition with 75 ps temporal resolution

After the analysis of the thermal evolution of the phase transition, we have performed a series of pump-probe measurements with a temporal resolution of 75 ps, given by the 8-bunch filling mode of the Synchrotron. The laser beam impinged the sample perpendicularly to its surface with a spot size on the sample of 3.1 mm by 2.1 mm. The X-ray beam footprint was ~1.7 mm along the incident beam direction and 0.5 mm in the perpendicular direction. The penetration depth of the laser at this wavelength ($\lambda = 800$ nm) is estimated to be $\delta_{laser} \sim 40$ nm.

In this case, we have increased the X-ray angle of incidence to $\alpha_i = 1.5°$, yielding to a penetration depth of $\delta_{X-ray} \sim 150\,nm$. This difference of penetration depths results in a mismatch between the excited and probed volumes, so we may expect some contributions from the unexcited volume in the time resolved measurements.

In a first step, we have measured the influence of the pump excitation on reflection ϕ_1. Figure 6.10 shows the temporal evolution of the Bragg reflection intensity at three different incident fluences. The relative intensity changes are calculated from the intensity value measured at negative time delays:

$$I/I_0 = \frac{I(t)}{I(-2.5\,ns)}$$

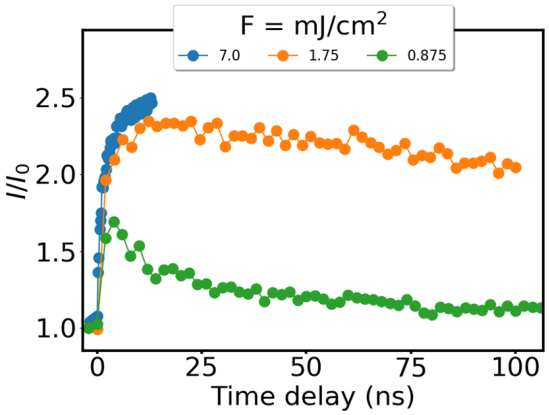

Figure 6.10: Relative intensity changes as a function of the time delay at constant ϕ angle ($\phi = \phi_1$) and at a sample temperature of $T = 20$ K.

The intensity of the Bragg reflection displays a large increase within the first 4.5 ns. The relaxation time to initial values decreases with decreasing incident fluence, showing a typical time scale of 150 ns for the lowest fluence F = 0.875 mJ/cm^2. The large relative intensity increase displayed in the curves is associated to a transition into the cubic phase. Indeed, the images in the detector display a merging of the diffracted spots into a single spot, as expected in this phase transition. Considering the probed depth of 150 nm and taking into account the typical heat diffusivity in solids (10^{-6}m^{2}s^{-1}), we can assign the observed dynamics to a heat diffusion process.

In order to extract the full information of the dynamics of both Bragg reflections, we performed a series of rocking curves collected at different time delays. The position of the delay line was randomly generated as a way of preventing any possible artifacts from laser thermal drifts or fluctuations. Each rocking curve was collected with a step of $\Delta\phi = 0.015°$ and an exposure time of 3 s per time delay step. Figure 6.11 shows the intensity maps of the rocking curves below the transition temperature at T = 25 K and at two different incident fluences: *a)* F = 0.16 mJ/cm^2 and *b)* F = 0.7 mJ/cm^2. In both cases the position of the peak located at

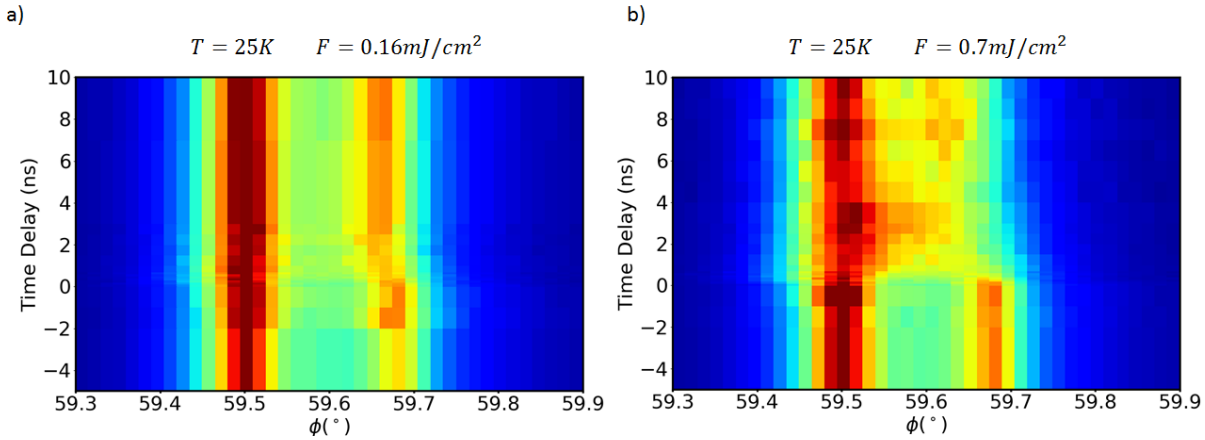

Figure 6.11: Rocking curves at T = 25 K as a function of the time delay between pump and probe for incident fluences a) F = 0.16 mJ/cm^2 and b) F = 0.7 mJ/cm^2.

ϕ_1 remains constant, while the position of the second reflection located at ϕ_2 shows a strong sensitivity to photoexcitation. A closer inspection of their dynamics is presented in figures 6.12 and 6.13. Every rocking curve was fitted by two Pseudo-Voigt functions, one corresponding to each peak ϕ_1 and ϕ_2, and a linear function to account for the background. The resulting fits are depicted in figures 6.12 and in 6.13. At both incident fluences, the largest changes of the peak position are observed in reflection ϕ_2. Within the first 1.5 ns after pump excitation, the center of ϕ_2 shifts towards lower angles with a maximum displacement of $\Delta\phi = 0.04°$ at 4 ns and a typical relaxation time t > 10 ns. Surprisingly, the FWHM of both peaks present a large broadening after photoexcitation with a maximum difference of 0.04° at 1.5 ns and a relaxation time to initial values with a typical time of 10 ns.

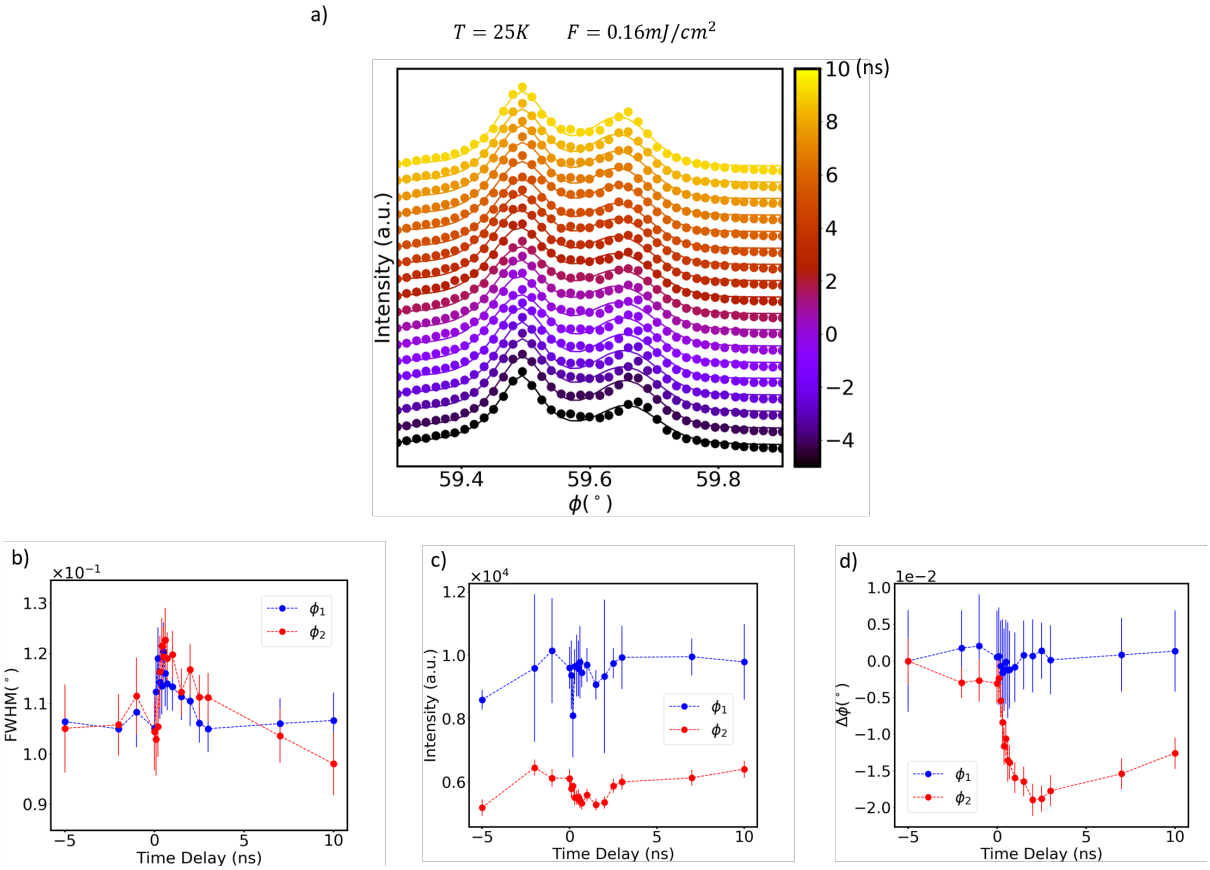

Figure 6.12: a) Experimental time resolved rocking curves (dots) collected at a sample temperature of $T = 25\,K$ and an incident fluence of $F = 0.16\,mJ/cm^2$ with their corresponding fits (lines), b) width peak values resulting from the fits and c) center position of both reflections.

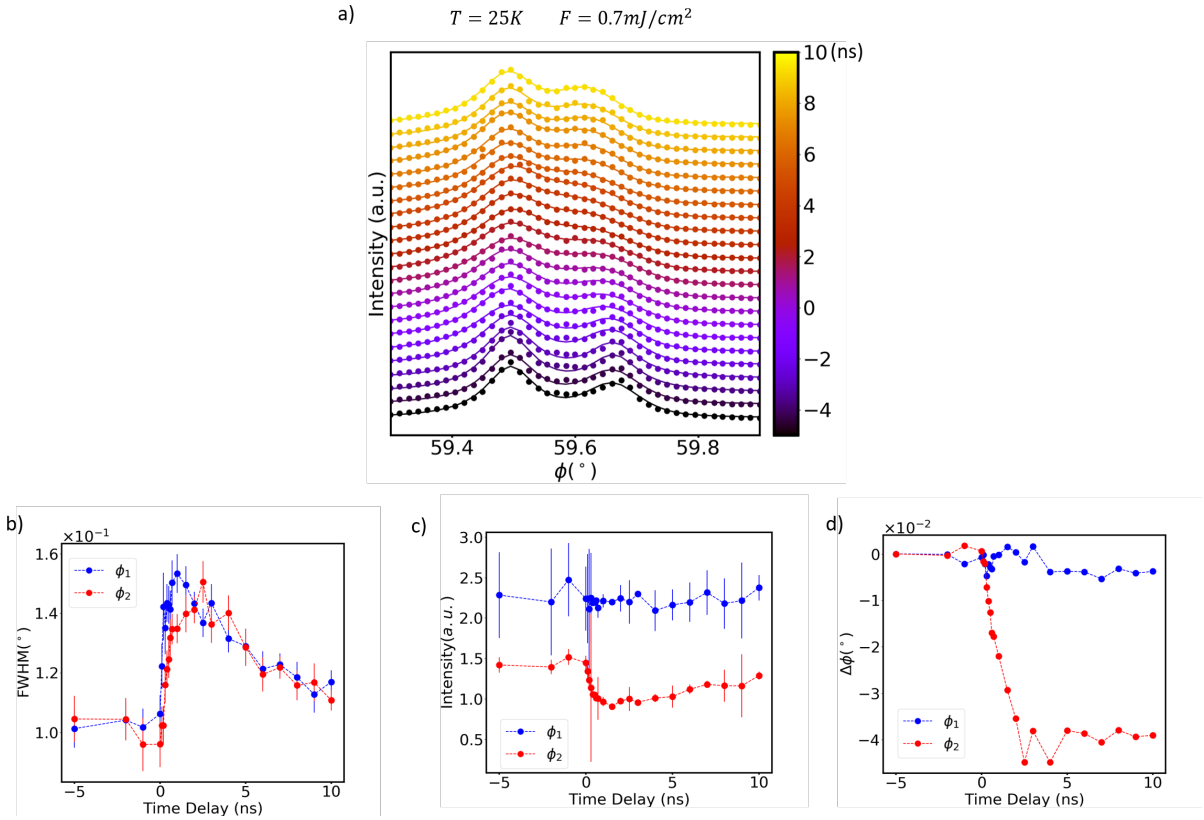

Figure 6.13: a) Experimental time resolved rocking curves (dots) collected at a sample temperature of $T = 25\,K$ and an incident fluence of $F = 0.7\,mJ/cm^2$ with their corresponding fits (lines), b) width peak values resulting from the fits and c) center position of both reflections.

In a next step we lowered the temperature to T = 16 K while keeping an incident fluence of F = 0.7 mJ/cm^2. The dynamics of the curves after pump arrival displays again a shift in position of the ϕ_2 reflection and a broadening of the FWHM. At this temperature, the temporal evolution of the position and of the FWHM reach their maximum changes at 1 ns in a similar trend as observed at higher lattice temperature under the same incident fluence.

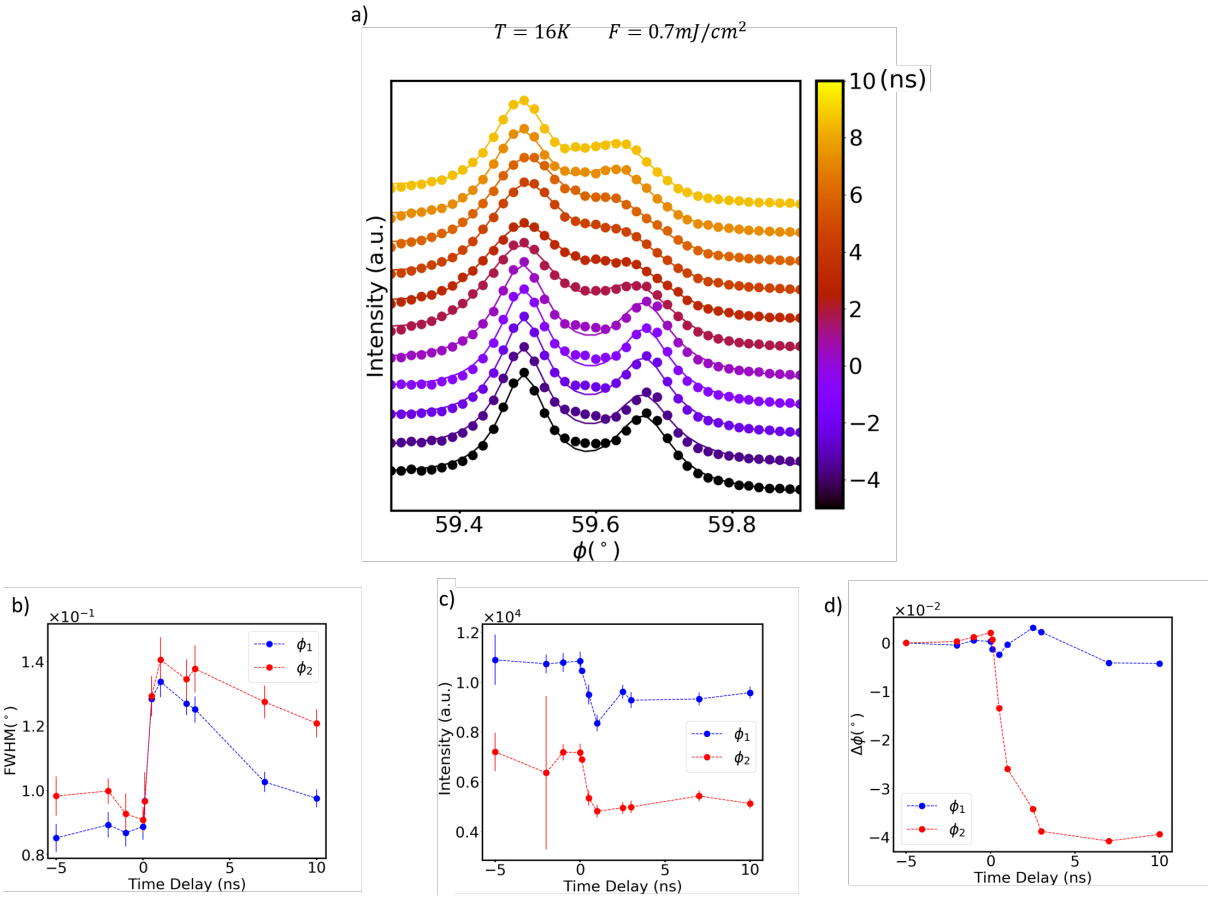

Figure 6.14: a) Experimental time resolved rocking curves (dots) collected at a sample temperature of T=16 K and an incident fluence of F = 0.7 mJ/cm^2 with their corresponding fits (lines), b) width peak values resulting from the fits and c) center position of both reflections.

This interesting increase of the FWHM after photoexcitation is not observed at thermal equilibrium. An increase of the lattice temperature induced from photoexcitation should lead, on the contrary, to a narrower FWHM as observed in figure 6.6 a). This effect might be originated by photoinduced disorder or a hysteresis effect.

An analysis of the detector images at ϕ_1 reveals a similar behaviour of the peak position as observed at thermal equilibrium, which suggest that the lattice parameter changes upon pump arrival.

From the experimental results presented in this section we can conclude that:

- At these temporal scales, the dynamics of the phase transition is dominated by thermal effects: the intensity and position of the Bragg peaks as a function of the time present a similar behaviour as at thermal equilibrium. The estimated lattice temperature increase induced by the pump is $\Delta T \sim 10\,\mathrm{K}$ for an incident fluence of $\mathrm{F} = 0.7,\mathrm{mJ/cm^2}$.
- The FWHM of the reflections present a large broadening after photoexcitation, opposite to what we observed at thermal equilibrium. We could attribute this difference to a large disorder induced by the pump or to a hysteresis effect.

6.2.3 Time resolved structural phase transition with 15 ps temporal resolution

The results presented before motivated us to perform a second study with a better temporal resolution. In this case, the pump probe scans were implemented in the low-alpha mode with a temporal resolution of 15 ps. Due to the complexity of the reflection studied before, we analyzed the dynamics of the (200) Bragg peak.

The expected position of the new reflections appearing in the tetragonal phase can be retrieved by considering the splitting of a wave vector belonging to the (h00) direction. We start by calculating the position of the cubic reflection in grazing incidence. Consider a wavevector $\mathbf{Q}_{h00}$ at 45° from the [110] crystallographic direction (i.e., perpendicular to the sample surface):

$$\mathbf{Q}_{h00} = \frac{1}{d_{h00}\sqrt{2}}\begin{pmatrix}-1\\1\\0\end{pmatrix}$$

with d_{h00} the interplanar distance. The rocking curves are performed around the vertical axis y, so that we can apply a rotation of the form:

$$\mathbf{Q'}_{h00} = \mathfrak{R}_y(\varphi)\vec{Q}_{h00}$$

where $\mathfrak{R}_y(\varphi)$ is the rotation matrix and φ the azimuthal angle:

$$\mathfrak{R}_y(\varphi) = \begin{pmatrix}\cos\varphi & 0 & \sin\varphi\\0 & 1 & 0\\-\sin\varphi & 0 & \cos\varphi\end{pmatrix}$$

In this way the position of the Bragg peak is defined in terms of the azimuthal angle as:

$$\mathbf{Q'}_{h00} = \frac{1}{d\sqrt{2}}\begin{pmatrix}-\cos\varphi\\1\\\sin\varphi\end{pmatrix}$$

The diffraction condition is fulfilled when the wave vector intercepts the Ewald sphere, so we can calculate its position on the detector as the intersection between two spheres of radius

$R_1 = 1/\lambda$ and center $C_1 = (0,0,0)$, and a second sphere with radius $R_2 = ||Q'_{h00}||$ and centered at $C_2 = (1/\lambda,0,0)$:

$$\frac{1}{\lambda^2} = \left(q_x + \frac{1}{\lambda}\right)^2 + q_y^2 + q_z^2 \tag{6.3}$$

By replacing Q'_{h00} in equation 6.3, we find the azimuthal angle:

$$\cos\varphi = -\frac{\lambda}{d\sqrt{2}} \tag{6.4}$$

$$\tag{6.5}$$

On the other hand, the vertical and horizontal positions of the Bragg on the detector are given by:

$$\sin\delta = \lambda q_y = \frac{\lambda}{d\sqrt{2}} \tag{6.6}$$

$$\tan\gamma = \frac{q_z}{\frac{1}{\lambda} - q_x} = \frac{1}{d\sqrt{2}} \frac{\sin\varphi}{\frac{1}{\lambda} - \cos\varphi} \tag{6.7}$$

with $d_{200} = a/2$, $a = 5.29\,\mathring{A}$ and $\lambda = 1.756\,\mathring{A}$, we find:

$$\begin{pmatrix} \delta = 28^\circ \\ \gamma = 28^\circ \end{pmatrix}$$

These values are in agreement with the detected position. Upon cooling we expect changes of the lattice parameter on the order of $\Delta a \lesssim 0.02\,\mathring{A}$, so that the deviation on the azimuthal angle becomes:

$$\Delta\varphi \lesssim 0.11^\circ$$

As expected from this small deviation, we did not observe the emergence of a clear new reflection on the rocking curves on cooling. Instead, the (200) Bragg peak presented a large broadening.

At this point we lowered the temperature of the sample to 10 K and performed a series of rocking scans at different time delays with an incident fluence of 0.63 mJ/cm^2. Figure 6.15 shows the rocking curves at different time delays with an angle of incidence of $\alpha = 1^\circ$.

The best fit of the rocking curves is found with two Pesudo-Voigt functions. Their centers are separated by $\Delta\phi = 0.11^\circ$ as expected in this Bragg reflection. The increase of the peak width in this case, can be explained by an increase of the intensity or position of one of the Pseudo-Voigt profiles. The most noticeable results are seen in the position of the peak on the detector. After pump arrival the Bragg reflection shifts vertically, a direct consequence of a decrease of the lattice parameter. Figure 6.16 shows the intensity difference in the detector images at every time delay.

The changes of the center of mass on the detector images are clearly shifting towards higher vertical angles. No changes along the γ angle are evident, as shown in figure 6.17.

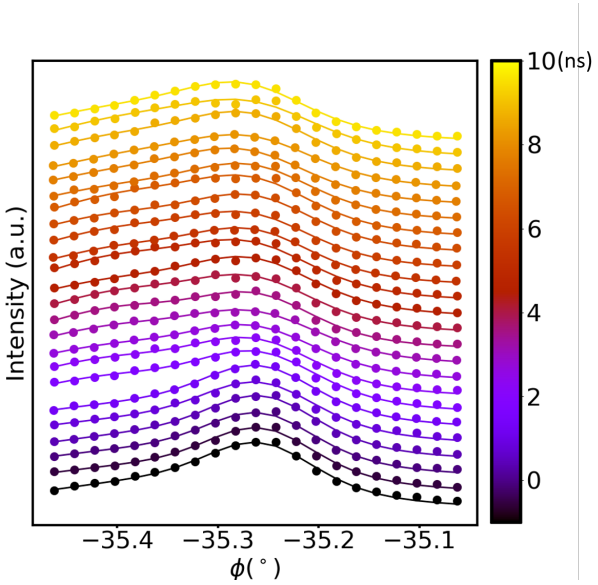

Figure 6.15: Rocking curves at different time delays at $T = 10\,K$ and $F = 0.63 mJ/cm^2$.

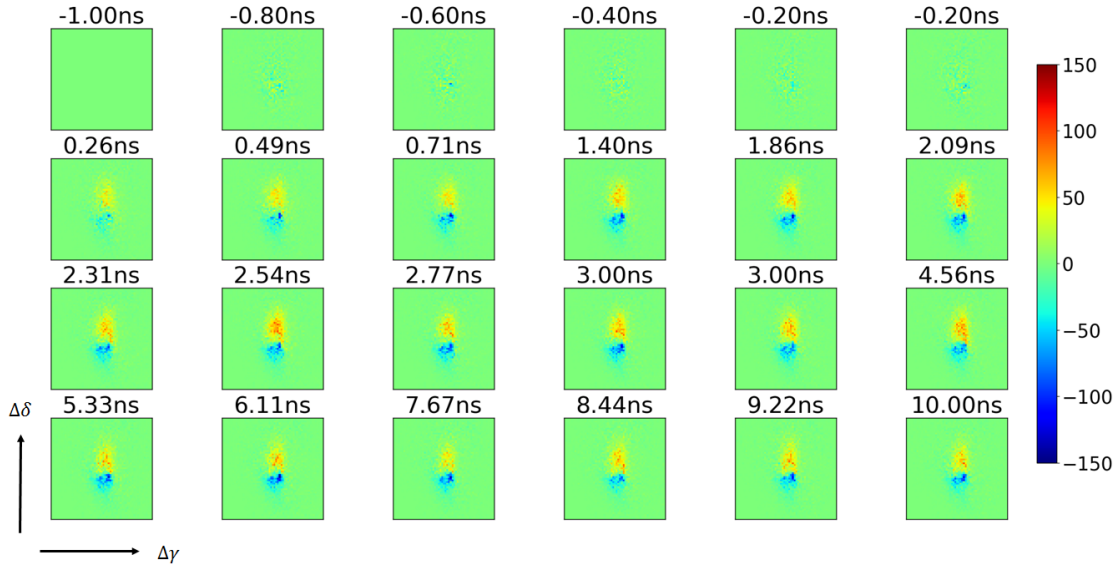

Figure 6.16: Detector images of the integrated rocking curve at different times delays. The sample temperature was $T = 10\,K$ and the incident fluence $F = 0.63\,mJ/cm^2$. Every image is a result after subtracting the image at negative time delays with t = -1 ns.

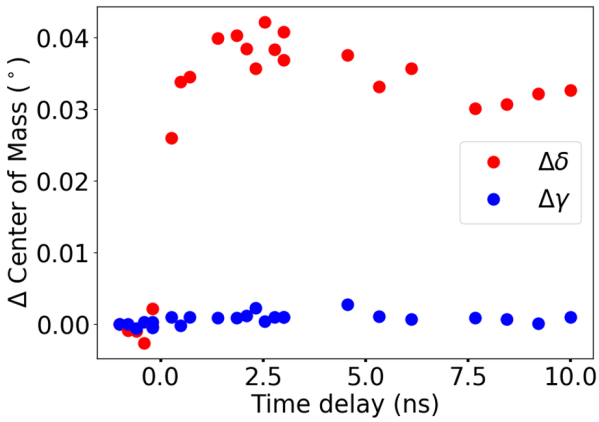

Figure 6.17: Changes of the center of mass along the vertical ($\Delta\delta$) and horizontal ($\Delta\gamma$) of the detector images.

With the purpose of investigating the changes of the Bragg reflection position after photoexcitation, we performed a pump probe scan at a constant $\phi = -35.32°$ at different temperatures and at two incident fluences[1]. Figure 6.18 presents the relative changes of the lattice parameter at two incident fluences and for three different temperatures. Following the center of mass of the Bragg spot in the detector images, we find that the vertical position increases with typical time scale of 1 ns without full relaxation within the length of the scan.

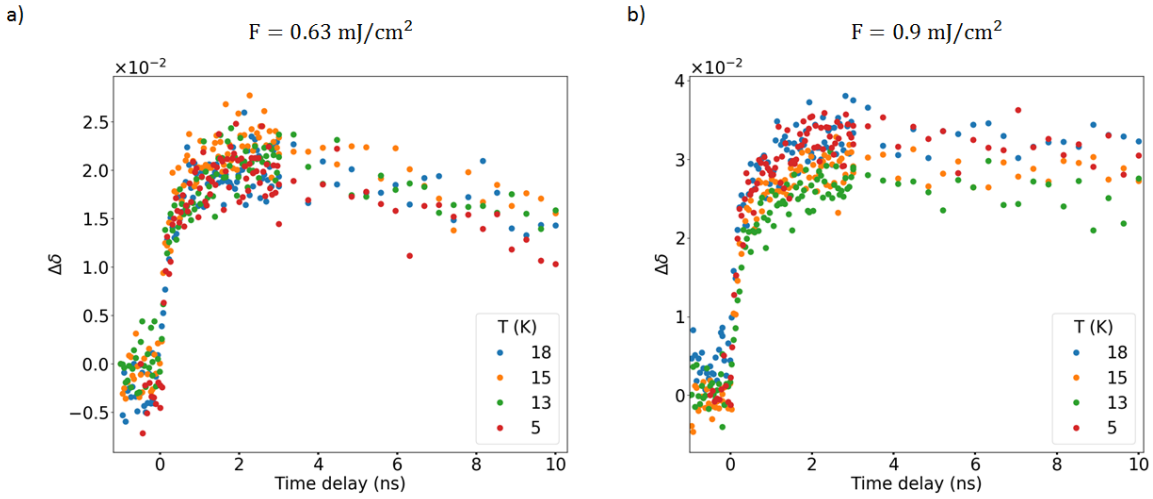

Figure 6.18: Changes on the vertical center of mass retrieved from the detector images at different sample temperatures and at two incident fluences: a) $F = 0.63$ mJ/cm^2 and b) $F = 0.9$ mJ/cm^2.

The temporal dynamics of the peak position suggest again heat diffusion as the main mechanism

[1]Note here that we do not explicitly calculate the lattice parameter, since we are measuring on the side of the rocking curve; corresponding to the position at which a "shoulder" in the rocking curve appears.

after photoexcitation. In light of these results, we observe that the lattice is more sensitive to changes on the incident fluence rather than on sample temperature.

6.3 Conclusions and future work

In this chapter, I presented preliminary results performed in Nb_3Sn, a compound that displays a martensitic phase transition from cubic to tetragonal structure at $T_m = 39$ K. Pump probe X-ray diffraction scans were performed on the tetragonal phase and compared to the equilibrium structural transition. The temporal dynamics of the position and intensity changes follows a similar behaviour as observed in thermal equilibrium, with typical time scales characteristic of thermal diffusion. Interestingly, the arrival of the pump broadens the peak width, differently to what was observed at thermal equilibrium. This effect could be related to a thermal hysteresis effect or to a large induced disorder after photoexcitation.

In both experiments we have observed that the lattice is more sensitive to large incident fluences rather than initial sample temperature. At this temporal resolutions and incident fluences, we did not detect any oscillation that could be related to the acoustic phonon related to the phase transition.

Further experiments on this compound are recommended. In particular, pump probe diffraction experiments with a temporal resolution of at least 1 ps could reveal photoinduced coherent oscillations arising from the phonon softening associated to this transition. In order to facilitate the studies in grazing incidence, new samples with perfect [110] orientation are required. It is worth mentioning that there are certain reflections that only exist in the tetragonal phase, as for instance the (300). Provided that the X-ray flux is high enough (since the intensity of this reflection is rather low) an experiment on this reflection would provide more insightful information on the photoinduced phase transition. Time resolved reflectivity experiments to complement the diffraction measurements are recommended as well.

Chapter 7

Conclusion

Contents

7.1 Summary

The experimental work presented in this thesis was centered around the dynamics of out-of-equilibrium structural phase transitions. Two experimental approaches were followed. On the one hand, I studied the martensitic phase transition on Nb_3Sn at SOLEIL Synchrotron, and on the other hand I investigated the photoinduced charge density wave phase transition on $GdTe_3$ with the UED experimental setup at LOA.

The first part was dedicated to an introduction to time-resolved diffraction and the description of the experimental setups employed to reveal the structural dynamics of phase transitions. In particular, the characteristics of the CRISTAL beamline at SOLEIL were introduced and the main capabilities of the UED setup at LOA were analyzed in chapter 3. In the latter, the spatio-temporal resolutions of the resulting electron bunches, estimated by GPT simulations, resulted in a minimum pulse length of 300 fs with a spatial coherence of 5 nm. These parameters are found to be optimal for pump-probe diffraction studies.

The first results obtained with this experimental setup were presented in chapter 4. The UED experimental setup at LOA proved an ideal tool to perform pump-probe scans on single crystal silicon nanomembranes. In these experiments we observed a giant photoinduced response on the Bragg peaks' intensities. The relative intensity changes presented a stunning increase of the order of $\Delta I/I \sim 60\%$, with large sensitivity to the angle of incidence. These values were surely impossible to explain within the kinematical theory of diffraction. Further experiments as a function of the angle of incidence complemented with simulations revealed that multiple scattering of the incident electron beam was responsible for this puzzling response. Indeed, when high quality samples are under study, dynamical diffraction effects may lead to the unexpected Bragg peak intensity dynamics. Under certain conditions of thickness and electron energies, lattice heating following photoexcitation results in the non-intuitive increase of the Bragg peak intensities, in contradiction with the well-known Debye-Waller effect. We reiterated the study

on another sample with a different thickness, which confirmed our interpretation. We thus demonstrated that a quantitative interpretation of phenomena occurring in high quality crystals requires multiple electron scattering effects to be taken into account.

The second part of this thesis was devoted to the study of the photoinduced structural phase transition of the CDW state in $GdTe_3$, presented in chapter 5. These experiments were performed with the UED experimental setup at LOA. The main aim of this study was to answer the following questions:

- On which time scales does lattice dynamics take place?
- What is the response of the system to different excitation fluences?
- How does the initial temperature of the lattice influence the dynamics of the CDW?
- How can our results resolve conflicting interpretations existing in the literature?

Our experimental results showed evidence of an increase of the lattice temperature after pump arrival with a typical time scale of 6 ps. We observed that for all studied fluences, the lattice temperature never exceeded the critical temperature T_c. For more than 125 ps, we could observe that the Bragg peaks' relative intensity was not changing, which led us to infer the persistence of a quasi-equilibrium state. We ascribed this phenomenon to a long heat diffusion process.

Concerning the first two questions, the observed dynamics of the CDW diffraction peaks showed a fast decay, limited by our temporal resolution. At high incident fluence, the intensity of the satellite peak was reduced to the background level, suggesting that the system transits to the metallic phase by optical excitation. Interestingly, this photoinduced transition occurs below the critical temperature. On the other hand, the relaxation to the initial CDW state presented a slowing down from 2 ps to 8 ps. These values were directly proportional to the incident fluence, in good agreement with previous results reported in literature on another RTe_3 compound.

Experiments performed at two different sample temperatures revealed that when the system is initially at $T \sim T_c$, the relaxation dynamics of the CDW tends to slow down with respect to the low initial temperature. These interesting results in combination with an analysis performed on the CDW correlation lengths suggest that if topological defects are the key in the slower relaxation process, they are not photoinduced by the pump but inherent to the lattice temperature. This interpretation, if proven true, may resolve the ongoing debate about the role of topological defects in the dynamics of charge density waves. Most likely, the slowing down in the relaxation of the CDW state is a consequence of an increase of the lattice temperature. Such an effect would prevent both the nucleation of domains and the complete recovery of the order parameter.

The last part of this thesis presented preliminary results on the photoinduced martensitic structural phase transition in Nb_3Sn performed by X-ray pump-probe diffraction at SOLEIL.

The capabilities of the beamline with a temporal resolution of several picoseconds, were well suited to study the martensitic phase transition on Nb_3Sn. The sample was firstly characterized at thermal equilibrium while cooling down the sample. These measurements served as a basis for comparison with the photoinduced phase transition. Two studies were carried out at two different temporal resolutions of 75 ps and 15 ps, respectively. In both cases, laser excitation triggered distinctive changes on the lattice structure (inferred from the Bragg peak position) related to the structural phase transition. The position and intensities of the diffracted peaks showed similar changes to those observed at thermal equilibrium with temporal time scales that pointed to thermal diffusion as the main mechanism behind the structural dynamics. Interestingly, the changes of the peak width presented the opposite behaviour, a broadening that could not be simply explained by lattice temperature increase, but pointed rather to either a hysteresis effect or to photoinduced disorder.

7.2 Future work

There are several paths to improving and furthering the studies presented in this manuscript. The main experimental improvement that could be performed on the UED experimental setup at LOA is an enhancement of the signal to noise ratio (SNR) of the detection scheme. Indeed, while the inherent properties of the DC gun would allow for a certain SNR, the system itself is strongly limited by the detection system (currently multi-channel plates) when measuring low diffracting samples. An effective way of improving the SNR without compromising the temporal resolution is based on the installation of a more efficient electron detector, such as sCMOS (scientific Complementary Metal Oxide Semiconductor) camera or a phosphor screen with a cooled intensified charge-coupled device (iCCD). In order to extend the capabilities of this setup to the study of structural phase transitions with very low critical temperatures, it would be interesting to install a cryostat. Such an improvement would furthermore allow to perform studies at several initial temperatures, necessary to investigate other interesting phenomena as critical slowing down.

With respect to the structural dynamics in the photoinduced CDW to metallic phase transition, there are still some questions to be answered. Firstly, how does the sample geometry affect the temporal dynamics? So far, all the transient reflectivity experiments present in literature are performed on bulk samples. With the purpose of comparing the temporal time scales measured in UED, it is necessary to perform time-resolved reflectivity studies on thin films. Particularly, it would be worth investigating the presence of photoinduced coherent acoustic modes propagating along the thickness of the sample to verify whether it has or not implications on the relaxation of the order parameter. Furthermore, temperature and fluence dependent studies are recommended to reveal the strength of the coupling between the CDW amplitude and optical phonons. It has been proven in literature that the amplitude mode of the CDW couples to other optical phonons with a strength that depends on the sample temperature. This coupling may

result in a renormalization of the order parameter [134]. To my knowledge, so far there are no results as a function of both the incident fluence and temperature that could provide more information to this matter. These studies should be performed in time-resolved reflectivity and compared preferably with time-resolved electron diffraction with a temporal resolution below 100 fs. Secondly, heating effects from the pump on the observed behaviour have not been ruled out, and THz pump-probe spectroscopy would thus provide enlightening complementary results. While trying to answer the questions mentioned in the previous section, we opened up a new one. We did not observe the emergence of a second transient CDW phase, differently to what has been recently reported on lighter compounds of the RTe_3 family. This transient CDW phase in lighter compounds has never been observed at thermal equilibrium conditions. Consequently, it opens the question on whether it depends on the compound under study or if it occurs in all the RTe_3 family. Thus, further experimental and theoretical studies on different compounds are needed to shed more light on this astonishing effect.

Finally, concerning the studies performed on the structural phase transition on Nb_3Sn, complementary measurements should be carried out. An attempt to conduct time-resolved reflectivity measurements was not possible due to the low reflecting sample, most likely due to surface roughness. These experiments could directly detect the phonon softening associated with the displacive martensitic phase transition. To do so, a pristine sample surface is required. As a way of furthering these studies, time-resolved diffraction with a temporal resolution below 1 ps should be performed, ideally on a diffraction spot belonging to the [110] crystallographic axis, i.e., the direction which presents the largest softening in the transition, or on a forbidden Bragg reflection in the cubic phase, for example the (300). These experiments would confirm whether the photoinduced transition follows an order-disorder path as may suggest our experimental results, or if in contrary, it follows a displacive process as observed at thermal equilibrium.

Appendix A

Charge measurements and detector calibration

As shown in section 3.1.3, the charge contained in the electron bunch was measured as a function of the third harmonic beam intensity impinging the photocathode. In this appendix I give more details and information about the parameters used during the calibration.

The beam charge measurements were performed with a repetition rate of 5 kHz to enhance the signal. The number of electrons per pulse is directly given by $N_e = \frac{I}{Rep.Rate} = \frac{Q}{e}$, being I the measured current, Q the charge of the bunch and e the electron charge.

In the case of the images recorded on the CCD, the repetition rate was lowered to 1kHz (the actual value that is used when performing experiments). The MCP voltage was maintained to 0.93 kV, the phosphor plate to 5 kV and the electron energy to 35 keV, the current on the solenoid was maintained to I = 0.98 A (V = 6.1 V). We took five images of the electron beam per waveplate angle and averaged them. It is interesting to notice that as the number of electrons rises in the electron bunch the number of counts becomes more unstable, giving rise to a non negligible standard deviation as shown in figure A.2, this value was used to compute the error bars in the fit presented in figure 3.11 in section 3.1.3 .

Figure A.1 shows an image of the direct beam and the corresponding Voigt fits of the vertical and horizontal line profiles. The fits were performed with the VoigtModel function from Python Lmfit package, information about the function and parameters can be found in [169].

In order to estimate the number of electrons as a function of the number of counts in the detector, I used the maximum of the fit curve, i.e. the height parameter, since values of the FWHM could not be easily fitted, as shown in figure A.4, indeed the FWHM of the electron beam should decrease as the number of electrons decreases. This effect might be due to a focusing effect since the current of the solenoid was maintained constant. Moreover, the variation of the FWHM is around 2pixels in the entire series of data points, this small variations are limited by the spatial resolution of the detector. Effects in the FWHM of the beam as a function of the number of electrons contained in the bunch will be much more notorious in the case of unfocused electron beam. Because of this, the number of counts at the maximum might be a more appropriate estimation in the case of a collimated beam.

Figure A.3 shows the measured number of electrons and the corresponding maximum of counts on the detector as a function of the waveplate angle. Similar trends are followed in both, current and number of counts, as expected from the resulting quantum efficiency from the photoemitted electrons at the photocathode.

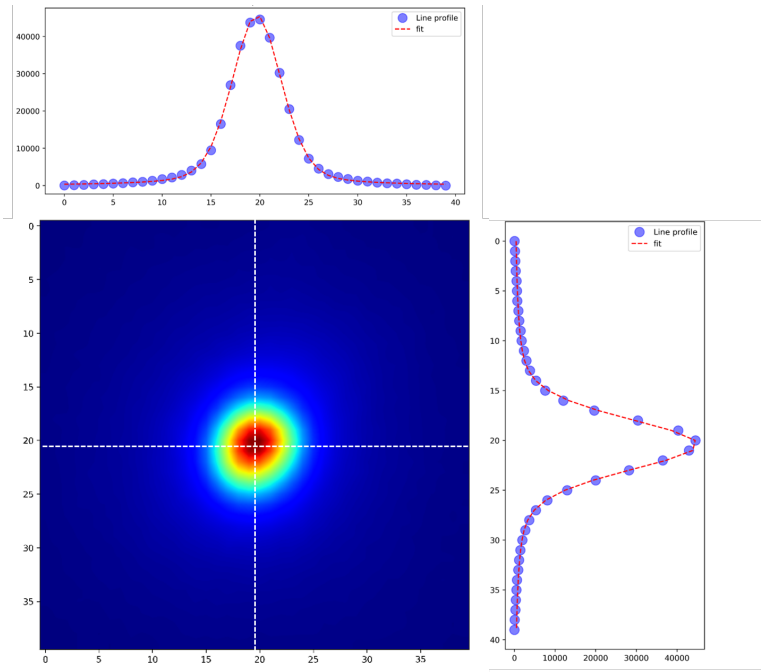

Figure A.1: Image recorded on the camera of the focused electron beam and its corresponding vertical and horizontal line profiles fitted with a Voigt function.

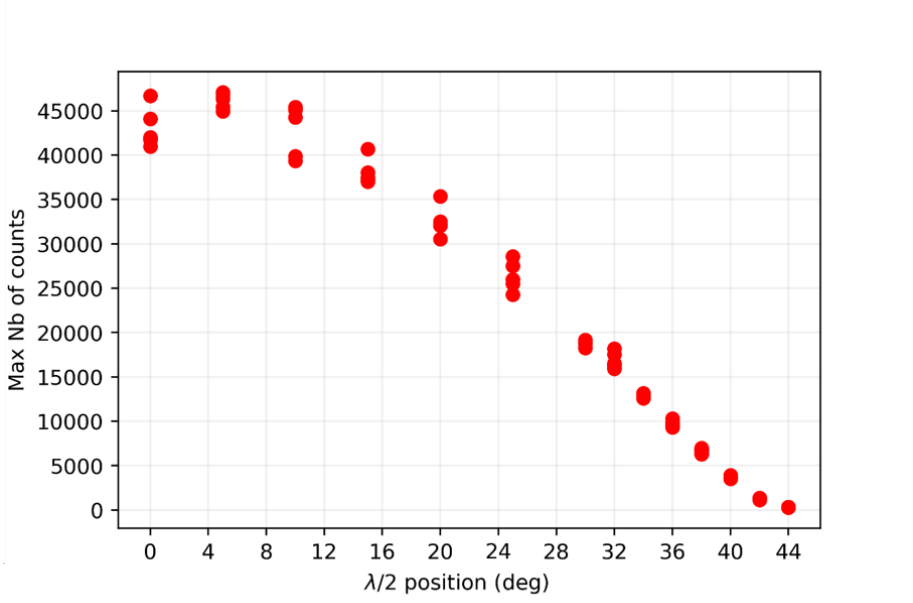

Figure A.2: Maximum number of counts at each image as a function of the waveplate angle. Note that the deviation in the number of counts increases as the current of the bunch is incremented.

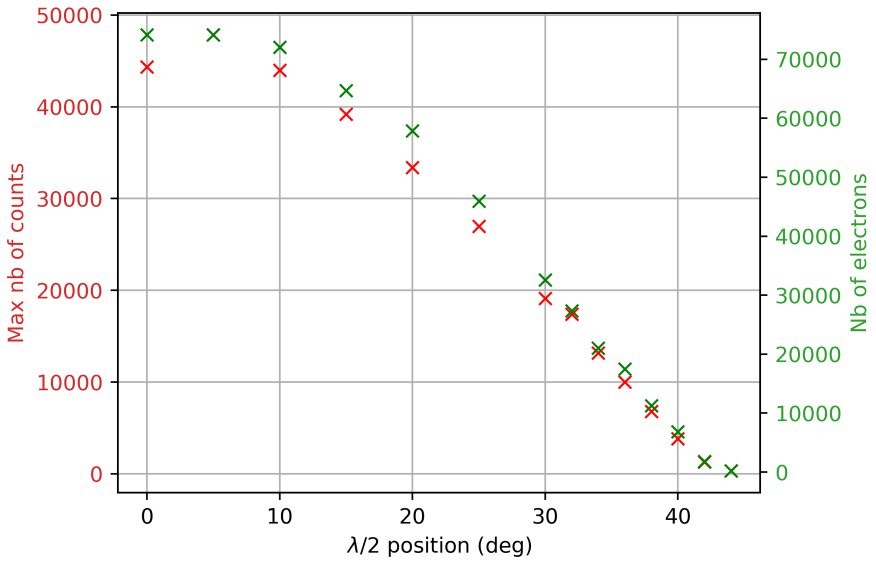

Figure A.3: Number of measured electrons with the Faraday cup and the corresponding averaged height from the Voigt fit as a function of the waveplate angle.

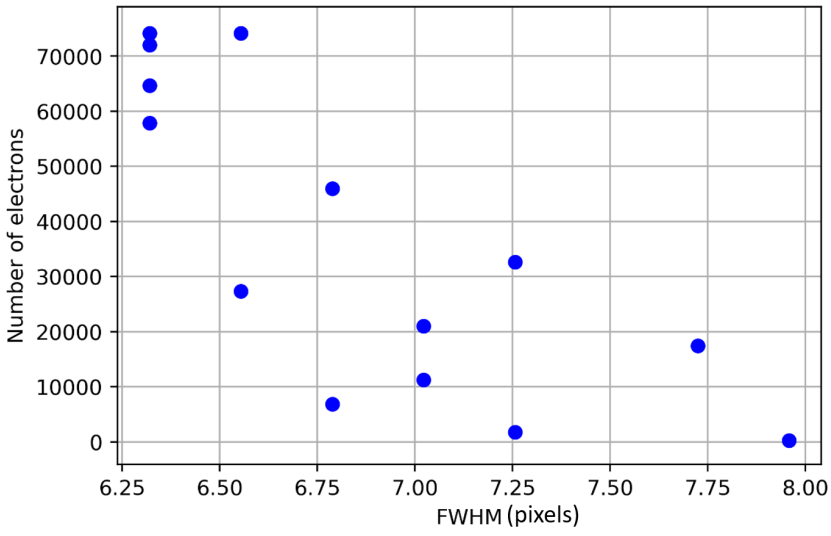

Figure A.4: Number of electrons as a function of the FWHM (given in pixels) of the focused direct beam.

Appendix B

Effects of electron beam size on the diffraction patterns

The size of the electron beam can be easily adjusted with the telescope in the beamline and monitored at the virtual focal plane of the photocathode. Figure B.1 shows the changes of the electron beam at a distance of D = 8.6 mm between lenses in the telescope and at D = 9.45 mm, corresponding to an electron FWHM size of $\sim 73 \mu m$ and $\sim 50\ \mu m$, respectively. The images of the direct electron beam seen on the camera (left), the diffracted signal from a polycrystalline aluminum sample (center) and the laser spot of the third harmonic recorded on the virtual plane of the photocathode.

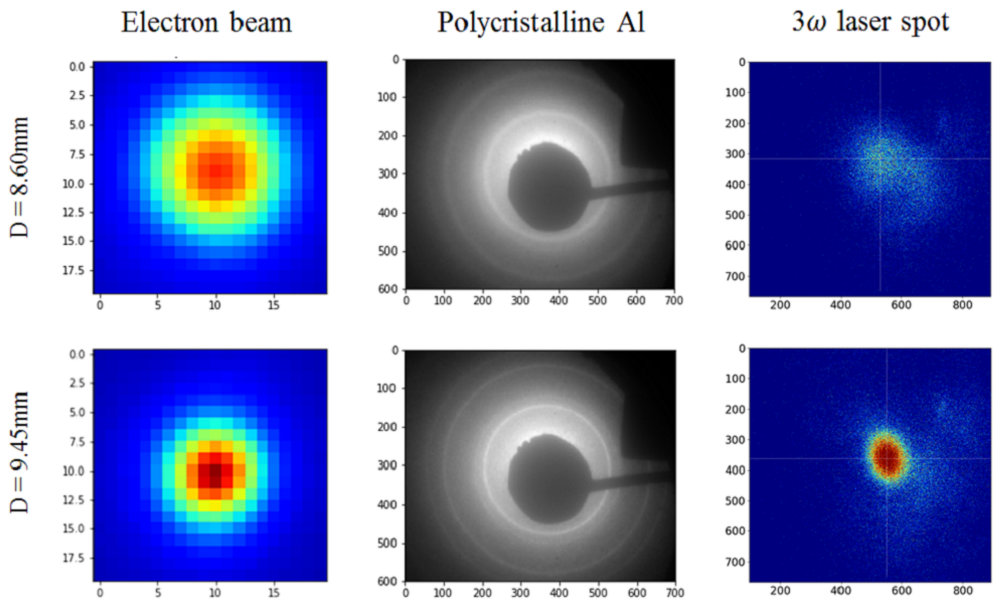

Figure B.1: Images of the direct electron beam (left), diffracted electron beam on a polycrystalline aluminium sample (center) and of the third harmonic laser spot (right, in log scale) as a function of the distance between the telescope lenses. The upper row corresponds to a third harmonic beam size of ~ 73 µm whereas the lower row correspond to ~ 53 µm.

The effect of the electron beam size in the spatial resolution is clearly seen in the diffracted images of the polycrystalline sample; the larger the beam the lower the quality of the diffraction pattern. As seen in section 3.1.1.3, an increasing size of the electron beam will increase

its emittance and thus lower the coherence length, resulting in lower intensities and broader diffracted spots or rings.

Appendix C

Static CBED measurements on 70 nm silicon nanomembranes

In order to measure the thickness of the nanomembranes by the CBED technique, a section of one of the samples was sectioned and deposited on a TEM grid, as shown in figure C.1. Figure C.2 shows the measured (left) and simulated (right) CBED diffraction patterns of (400) diffraction spot at 300 keV. The fringe pattern shown in figure C.3 was obtained from a line profile of the measured diffraction pattern and compared with the simulated CBED. Figure C.3 depicts the line profiles of the (400) and transmitted electron beam. The simulations were performed for several thicknesses between 30 nm and 130 nm. Best accordance between simulation and measurements is achieved between 69 nm and 70 nm, with an accuracy of 1 nm.

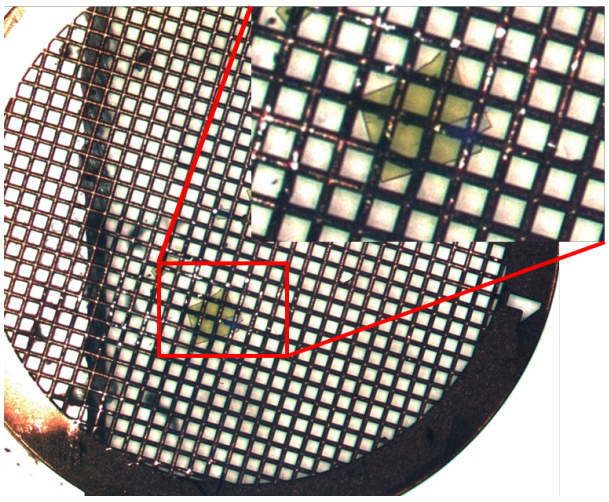

Figure C.1: Section of the silicon nanomembrane deposited on a TEM grid for CBED measurements.

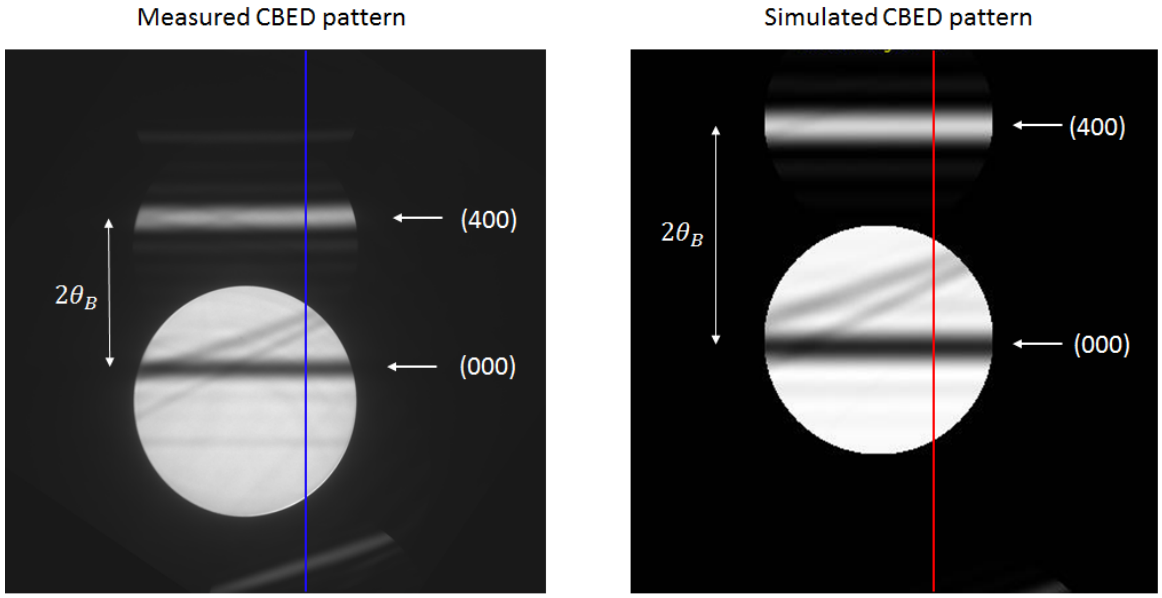

Figure C.2: Excess (400) and deficiency (000) lines of the silicon at 300 keV, measured (left) and simulated by JEMS (right). Red and blue lines correspond to the line profiles showed in C.3.

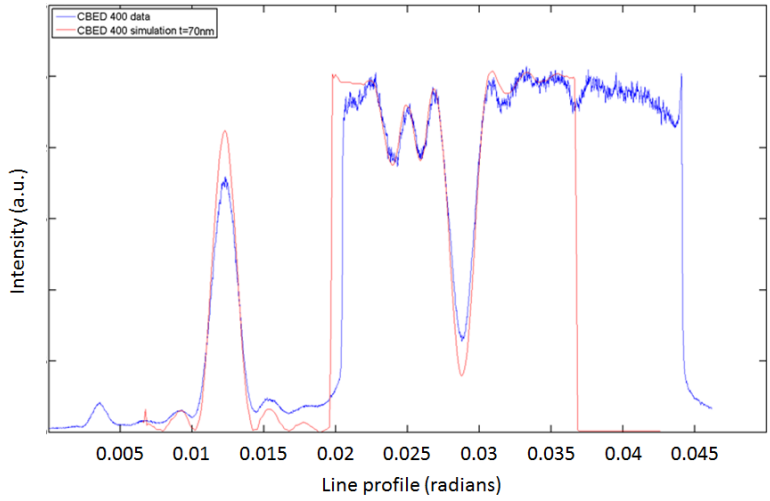

Figure C.3: Comparison between simulated (red) and measured (blue) line profiles for a thickness of 70 nm.

Appendix D

Laser penetration depths from optical conductivity values

The penetration depth of the laser into the material can be estimated from optical measurements, as the reflectivity and attenuation coefficient. It is obtained from the Beer-Lambert law, which states that the intensity of an electromagnetic wave in a material decreases exponentially as:

$$I = I_0 e^{-\alpha L}$$

with α the attenuation constant and L the material thickness.

The attenuation constant is inversely proportional to the penetration depth and so it can be linked to the extinction coefficient by:

$$\delta = \frac{1}{\alpha} = \frac{\lambda}{4\pi\kappa(\lambda)}$$

where λ is the wavelength and $N = n + i\kappa$ the refractive index. The imaginary part of the refractive index can be obtained from the optical conductivity value. From the complex dielectric function:

$$\varepsilon = \varepsilon' + i\varepsilon'' = \varepsilon' + i\frac{\sigma\lambda}{2\pi c}$$

and the refractive index relation:

$$N^2\varepsilon_0 = \varepsilon$$

The imaginary part as a function of the conductivity:

$$\kappa = \frac{\sigma\lambda}{4\pi\varepsilon_0 cn}$$

The reflectivity of the material can be expressed from Fresnel equation:

$$R = \left|\frac{1-N}{1+N}\right|^2 = \frac{(1-n)^2+\kappa^2}{(1+n)^2+\kappa^2}$$

Finally combining the above equations the imaginary part of the refractive index becomes:

$$\kappa^4 + \kappa^2 + \frac{R+1}{R-1}\frac{\sigma\lambda}{2\pi\varepsilon_0 c}\kappa + \frac{\sigma^2\lambda^2}{16\pi^2\varepsilon_0^2 c^2} = 0$$

with two possible imaginary and real solutions, where only one of them has physical meaning.

Appendix E

Relation between the physical angles and the Q vector in grazing incidence geometry

Let us consider the Q_{201} reflection in the laboratory frame, with the y axis vertical, parallel to the (1-10) axis of the sample and the q_{110} and q_{001} defining the surface:

$$\vec{Q}_{201} = \frac{1}{d_{201}} \begin{pmatrix} \sin\alpha \sin\beta \\ \cos\alpha \\ \sin\alpha \cos\beta \end{pmatrix}$$

with $d_{201} = a/\sqrt{5}$, $a = 5.29\,\mathring{A}$ and the angles $\alpha = 50.76°$ and $\beta = 63.4°$ (see figure). We have now to rotate the sample with the ϕ angle around the [h-h0] direction normal to the surface (see figure E.1 a)). We use the rotation matrix $\mathfrak{R}_y(\varphi)$ to get the new position $\vec{Q}'_{201}$:

$$\vec{Q}'_{201} = \mathfrak{R}_y(\varphi)\vec{Q}_{201}$$

with

$$\mathfrak{R}_y(\varphi) = \begin{pmatrix} \cos\varphi & 0 & \sin\varphi \\ 0 & 1 & 0 \\ -\sin\varphi & 0 & \cos\varphi \end{pmatrix}$$

By turning φ the wave vector crosses the Ewald sphere, so that:

$$\frac{1}{\lambda^2} = \left(q_x + \frac{1}{\lambda}\right)^2 + q_y^2 + q_z^2$$

We get:

$$\sin(\varphi+\beta) = -\frac{\lambda}{2d}\frac{1}{\sin\alpha} \tag{E.1}$$

$$\sin\delta = \lambda q_y = \frac{\lambda}{d}\cos\alpha \tag{E.2}$$

$$\tan\gamma = \frac{q_z}{\frac{1}{\lambda} - q_x} = \frac{\sin\alpha\cos(\beta-\varphi)}{d/\lambda - \sin\alpha\sin(\beta+\varphi)} \tag{E.3}$$

For the Q_{201} reflection, there are three different possible variants (see figure E.1 c)):

$$\begin{pmatrix} 2+2dq, & 0, & 1-dq \\ 2-dq, & 0, & 1+2dq \\ 2-dq, & 0, & 1-dq \end{pmatrix}$$

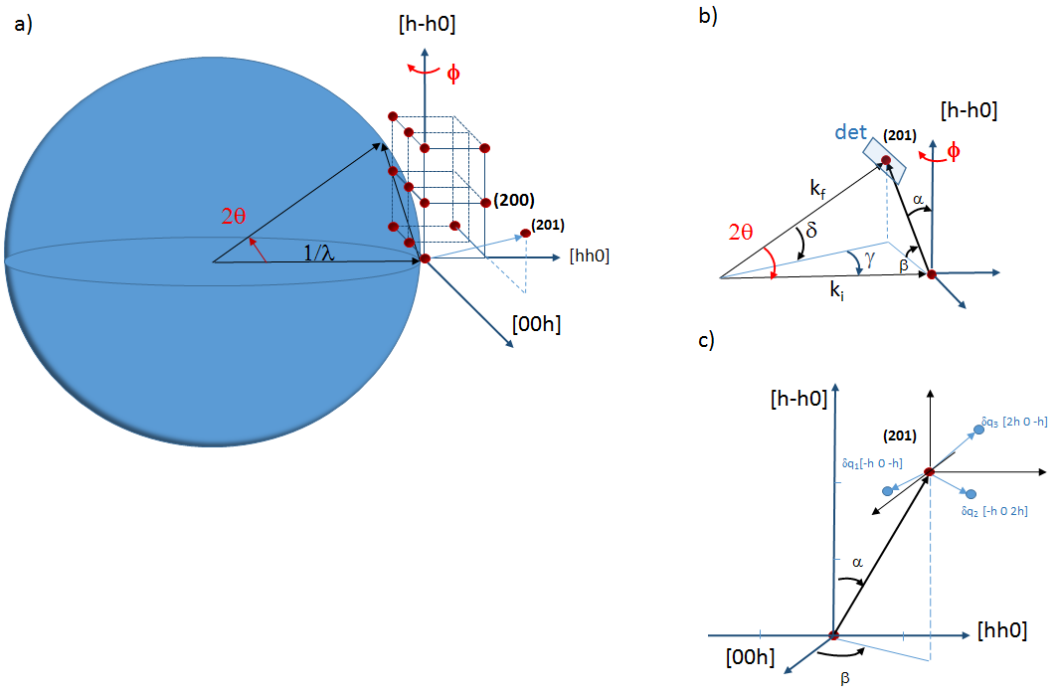

Figure E.1: a) Grazing incidence geometry with the Nb_3Sn sample orientation. The rotation around the ϕ angle is used in order to intersect the (201) reflection on the Ewald sphere. b) Angular configuration with the section of the reciprocal lattice defined by the detector. c) The three possible variants observable in Nb3Sn at low temperature.

with $dq = \frac{\Delta a}{a}$. We can see that the variation in δ corresponds to the variations of the lattice parameter perpendicular to the surface since:

$$\sin(\delta + d\delta) = \lambda(q_{1-10} + dq_{1-10}) \tag{E.4}$$

$$\sin\delta + d\delta\cos\delta \approx \lambda q_{1-10} + \lambda dq_{1-10} \tag{E.5}$$

$$d\delta = \frac{\lambda}{\cos\delta} dq_{1-10} \tag{E.6}$$

As a conclusion, the two peaks in δ seen at φ_1 mainly correspond to an expansion-dilatation of the lattice perpendicular to the surface, i.e. along the (1-10) direction.

The peak at φ_2 remains however not clear. Although that this contribution is clearly related to the phase transition, the absence of any shift in δ but two peaks in ϕ is not very compatible with the bulk phase transition described here. The absence of change of correlation length close to T_c could be explained by the appearance of the phase transition occurring on very thin layer on the surface, that is, a distortion within the surface and not in the bulk of the sample.

Résumé en français

Lorsqu'un matériau traverse un changement entre deux états electroniques et/ou structurales, on dit qu'il subit une transition de phase. Les transitions de phase sont le résultat d'un stimulus externe tel qu'un changement de température, de pression ou même d'une excitation optique. Les techniques pompe-sonde reposent sur ce dernier stimulus, dans lequel une courte impulsion optique (la pompe) déclenche une cascade de processus hors équilibre dans les électrons et le réseau. Au niveau du réseau cristallin, tous les événements suivis de l'excitation optique peuvent être directement mesurés par la diffraction des impulsions d'électrons ou de rayons X (la sonde). La courte durée temporelle de la sonde permet d'observer la dynamique de la structure en suivant l'intensité, la position et la forme des pics de Bragg dans des échelles de temps aussi courtes que quelques centaines de femtosecondes.

Mon travail de thèse était consacré à l'étude de la dynamique structurale des transitions de phase par diffraction résolue en temps des électrons et des rayons X. Plus précisément, ce manuscrit présente des études sur deux composés présentant une transition de phase structurale: $GdTe_3$ et Nb_3Sn. Afin de comprendre leur dynamique structurale hors équilibre, j'ai réalisé des expériences pompe-sonde par diffraction d'électrons au Laboratoire d'Optique Appliquée (LOA) et par diffraction de rayons X au Synchrotron SOLEIL avec mon groupe du Laboratoire de Physique des Solides (LPS).

Motivation et objectifs principaux: La compréhension des mécanismes physiques impliqués dans les transitions de phases structurales photoinduites est devenue une question centrale dans la communauté de l'ultrarapide. Les systèmes présentant une forte coopération entre les différents degrés de liberté (charge, spin, orbitales et réseau) sont particulièrement intéressants. Les principales questions concernant les transitions de phase qui ont lieu dans ces systèmes peuvent être énumérées comme suit :

- Quel est le principal propulseur de la transition de phase?
- Quelle est la force du couplage entre les différents degrés de liberté ?
- Quelles sont les différentes échelles de temps associées à chaque degré de liberté et leur couplage ?
- Est-ce que la compréhension de la dynamique nous aide à mieux comprendre la physique de base de la transition de phase ?

Les expériences résolues en temps, avec leur capacité à suivre la transition de phase dans les échelles de temps pertinentes, sont les techniques idéales pour éclairer ces questions. Un bon exemple de transition de phase structurale coopérative se trouve dans les matériaux présentant une onde de densité de charge (ODC). Les ODC sont des états quantiques macroscopiques

stables à basse température dans des matériaux de faible dimension, qui ne peuvent se produire que par le couplage entre les electrons et le réseau cristallin.

Lorsqu'un système métallique subit une transition vers la phase ODC à une certain temperature T_c, une ouverture dans la bande d'énergie électronique apparaît accompagnée d'une distorsion dans le réseau. Cette distortion donne une nouvelle periodicité qui, en diffraction, se traduit par l'émergence de nouveaux pics de diffraction, appelés réflexions satellites. Leur intensité est directement liée au paramètre d'ordre de la transition de phase.

L'excitation optique peut entraîner la suppression de la phase ODC. En diffraction, cela peut être directement déduit de la suppression de l'intensité du satellites. Différentes voies de relaxation dans cette transition ont été proposées. Dans certains cas, ces voies ont été attribuées à des mécanismes qui sont différents de ceux observés à l'équilibre thermique [30]. Une bonne preuve de l'intérêt croissant pour ces systèmes se reflète dans la grande quantité de travaux de recherche sur les dichalcogénures des métaux de transition [23, 24, 31, 32, 33, 34, 35]. Ces composés présentent des réflexions satellites de haute intensité qui, d'un point de vue expérimental, ont un grand avantage en termes de détection. Un des "inconvénients" de ces composés est leur complexe diagramme de phase, dans lequel plusieurs phases ODC peuvent être présentes selon le composé. **Par conséquent, les études sur des matériaux ayant des diagrammes de phase relativement simples pourraient donner une image plus directe de la transition de phase photoinduite vers l'état métallique.** Les candidats possibles avec des diagrammes de phase moins complexes sont les bronzes bleus ($K_{0,3}MoO_3$) et les composés de tritelluride de terre rare (RTe_3).

Cette thèse est encadré dans une collaboration entre le LOA et le LPS. Les deux laboratoires sont largement reconnus pour leur expertise dans le domaine des sources ultra-rapides et de la physique de l'état solide, respectivement. Le développement du premier dispositif expérimental compact de diffraction électronique ultrarapide (DEU) en France au LOA a ouvert la possibilité d'étudier la dynamique structurale hors équilibre d'un sujet bien connu au LPS: la transition de phase ODC dans les composés RTe_3. Au début des travaux présentés ici (mi 2016), la dynamique structurale de la transition de phase photoinduite dans les composés RTe_3 était peu connue, la collaboration entre le LOA et le LPS a donc donné les conditions idéales pour étudier ce sujet.

L'objectif de cette thèse était triple:

Tout d'abord, nous avons testé les capacités de l'experience de diffraction d'electrons ultrarapide récemment développée au LOA. Pour ce faire, nous avons réalisé une série d'expériences de pompe-sonde sur des nanomembranes monocristallines de silicium de haute qualité. Lors de la réalisation de ces expériences, nous avons découvert la grande influence des effets de diffusion multiples sur les intensités diffractées résolues dans le temps, un aspect qui a été suggéré précédemment par d'autres groupes de recherche mais qui n'a jamais été étudié en détail [29, 33].

Le deuxième et principal objectif de cette thèse est centré sur l'étude de la transition de phase photoinduite de $GdTe_3$ avec l'experience DEU. J'ai ainsi abordé plusieurs questions :

- Quelles sont les principales différences entre l'équilibre thermique et les transitions de phase photoinduites ?
- Sur quelles échelles de temps la dynamique du réseau a-t-elle lieu ?
- Quelle est la réponse du système aux différentes fluences d'excitation ?
- Comment la température initiale du réseau influence-t-elle la dynamique de l'ODC?

Ici, il a fallu relever plusieurs défis. En particulier, la préparation d'échantillons appropriés pour la mise en place de l'experience DEU et les moyens de détecter les réflexions de satellite de faible intensité. Un autre aspect difficile du travail présenté ici était son actualité, car un grand nombre de données de haute qualité ont été publiées sur le sujet pendant que je réalisais ces expériences [36, 37, 38, 39, 40] (certaines d'entre elles sont encore sur *arXiv*).

Le dernier objectif de la thèse est de comprendre la dynamique de la transition de phase structurelle sur Nb_3Sn, un matériau qui présente une transition de phase *martensitique* induite par des déplacements déformants du réseau. Dans ce cas, nous avons centré notre attention sur les principales différences entre la transition de phase structurelle à l'équilibre thermique et après photoexcitation avec des résolutions temporelles de plusieurs picosecondes. Les expériences ont été réalisées dans la ligne de faisceaux CRISTAL du synchrotron SOLEIL.

Résultats principaux: La première partie de la thèse est consacrée à une introduction à la diffraction en temps résolu et à la description des dispositifs expérimentaux utilisés pour révéler la dynamique structurelle des transitions de phase. En particulier, les caractéristiques de la ligne de lumière CRISTAL à SOLEIL ont été présentées et les principales capacités du dispositif expérimental DEU développé au LOA sont analysées dans le chapitre 3. Dans ce dernier, les résolutions spatio-temporelles des faisceaux d'électrons, estimées par des simulations GPT, ont permis d'obtenir une longueur temporelle d'impulsion minimale de 300 fs avec une cohérence spatiale de 5 nm. Ces paramètres se sont avérés optimaux pour les études de diffraction pompe-sonde. Les premiers résultats obtenus avec ce dispositif expérimental sont présentés au chapitre 4, suivis d'une deuxième étude présentée au chapitre 5.

Les effets de la diffusion multiple observés dans la diffraction résolue en temps. Le dispositif expérimental DEU s'est révélé être idéal pour effectuer des expériences pompe-sonde sur des nanomembranes de silicium monocristallin. Les échantillons ont été préparés par nos collaborateurs Max Lagally et Shelley Scott à l'université du Wisconsin. Ces nanomembranes ont une épaisseur de 70 nm et une surface de 300 μm $\times$ 300 μm avec une haute qualité cristalline. Dans les diagrammes de diffraction à l'équilibre et à certains angles d'incidence entre la surface de l'échantillon et le faisceau d'électrons entrant, nous avons observé que

l'intensité du pic de diffraction (220) montrait une intensité comparable au pic direct, c'est-à-dire le pic (000). Après l'excitation optique avec une fluence de F = 12 mJ/cm^2, nous avons observé une réponse photoinduite géante sur l'intensité du pic de Bragg, avec une augmentation étonnante de l'ordre de $\Delta I/I \sim 60\%$. Cette augmentation a également montré une grande dépendance avec l'angle d'incidence. Ces valeurs étaient certainement impossibles à expliquer dans le cadre de la théorie cinématique de la diffraction. Afin d'expliquer nos observations, j'ai réalisé d'autres expériences complementaires en fonction de l'angle d'incidence (rocking curves). Ces résultats complétés par des simulations ont révélé que la diffusion multiple du faisceau d'électrons incident était responsable de cette réponse surprenante. En effet, lorsque des échantillons de haute qualité sont mesurés, les effets dynamiques de la diffraction peuvent conduire à l'augmentation inattendue de l'intensité du pic de Bragg. Dans le contexte de la théorie dynamique de la diffraction et dans certaines conditions d'épaisseur et d'énergie des électrons, le chauffage du réseau après la photoexcitation entraîne une augmentation d'intensité non intuitive, en contradiction avec l'effet Debye-Waller. Nous avons réitéré l'étude sur un autre échantillon d'épaisseur différente, ce qui a confirmé notre interprétation. Nous avons ainsi démontré que dans les expériences de diffraction résolues en temps sur des cristaux de haute qualité, il est impératif de prendre en compte les effets de diffusion multiples pour donner une interprétation quantitative.

Transition de phase ODC-metallique photoinduite dans le composé $GdTe_3$.
La deuxième partie de cette thèse a été consacrée à l'étude de la transition de phase structurale dans $GdTe_3$, présentée dans le chapitre 5. Ces expériences ont été réalisées aussi avec le dispositif expérimental DEU au LOA. Le composé $GdTe_3$ est un matériau quasi-2D qui possède une structure orthorombique avec $a \sim c \ll b$ et qui présente une transition de phase metallique-ODC aux températures inférieures à T_c ~377 K [122]. La modulation du réseau correspondant à l'état ODC apparaît le long de l'axe cristallographique c. Nos résultats expérimentaux ont montré la preuve d'une augmentation de la température du réseau après l'arrivée de la pompe avec une échelle de temps typique de 6 ps. En analysant les pics de Bragg du réseau principal, nous avons observé que pour toutes les fluences étudiées (entre F = 0.5 mJ/cm^2 et F = 3.5 mJ/cm^2), la température du réseau n'a jamais dépassé la température critique T_c. Après la diminution initial de l'intensité et pendant plus de 125 ps, nous avons observé que l'intensité relative des pics de Bragg ne changeait pas, ce qui nous a conduit à déduire la persistance d'un état de quasi-équilibre. D'autre part, la dynamique observée des pics de diffraction correspondant a l'etat d'ODC a montré une décroissance de l'intensité très rapide, limitée par notre résolution temporelle. Pour des fluences incidentes élevées (F>1.9 mJ/cm^2), l'intensité du pic du satellite a été réduite au niveau du bruit de fond, ce qui suggère que le système passe à la phase métallique par excitation optique. Il est important de souligner ici que cette transition photoinduite se produit en dessous de la température critique, elle est donc considérée comme une transition de phase non thermique. D'autre part, nous avons observé que la relaxation vers l'état initial de l'ODC était variable, allant de 2 ps à 8 ps. Ce ralentissement vers l'etat intial était proportionnel

à la fluence incidente, en bon accord avec les résultats précédents rapportés dans la littérature sur un autre composé de la même famille $LaTe_3$ [35]. Ce ralentissement a été considéré comme le résultat de l'apparition de défauts topologiques photo-induits, ce qui est en contradiction avec l'interprétation donnée par Trigo et al. [37] qui ont étudié le composé $SmTe_3$. Afin de mieux comprendre cet effet, j'ai réalisé des expériences à deux températures d'échantillon différentes. Ces derniers résultats ont révélé que lorsque le système est initialement à $T \sim T_c$, la dynamique de relaxation de l'ODC a tendance à ralentir par rapport à la relaxation lorsque la température initiale est basse $T < T_c$. Ces intéressantes observations, combinés à une analyse effectuée sur les longueurs de corrélation d'ODC, suggèrent que si les défauts topologiques sont la clé du processus de lente relaxation, ils ne sont photoinduits par la pompe mais aussi inhérents à la température du réseau. Cette interprétation, si elle s'avère vraie, pourrait résoudre le débat en cours sur le possible rôle des défauts topologiques photo-induits dans la dynamique des ondes de densité de charge. Il est très probable que le ralentissement de la relaxation vers l'état ODC soit la conséquence d'une augmentation de la température du réseau. Un tel effet empêcherait à la fois la croissance des domaines ODC et la récupération complète du paramètre d'ordre. À la vue de nos résultats, il est recommandé de procéder à de futures expériences pompe-sonde à plusieurs températures d'échantillon. Ces expériences, de préférence avec une résolution temporelle plus courte (de l'ordre de 100 fs ou moins), donneraient plus d'informations sur les mécanismes à l'origine de défauts topologiques.

Transition de phase structurale dans le composé Nb_3Sn.

La dernière partie de cette thèse présente des résultats préliminaires sur la transition de phase martensitique structurelle photoinduite dans le composé Nb_3Sn. Ce matériau montre deux transitions de phase distinctes: une transition de phase structurale d'une structure cubique à une structure tétragonale (connue sous le nom de transition de phase martensitique) et une phase supraconductrice apparaissant à une température critique inférieure. Dans nos études, nous nous sommes concentrés sur la transition de phase martensitique à l'équilibre thermique et après photoexcitation. Ces experiences on été réalisée par diffraction résolue en temps de rayons X dans la ligne de lumière CRISTAL à SOLEIL. Les caractéristiques de CRISTAL avec une résolution temporelle de plusieurs picosecondes, étaient bien adaptées pour étudier cette transition de phase. L'échantillon a d'abord été caractérisé à l'équilibre thermique en refroidissant largement en dessous de la température critique ($T_c \sim 39$ K). Ces mesures ont servi comme référence pour comparaison avec la transition de phase photoinduite. À l'équilibre thermique, le pic de Bragg mesuré a montré une diminution de l'intensité suivie d'un "splitting" très évident à la température de transition. De plus, la largeur de chaque pic de Bragg après le "splitting" était plus petite à $T \sim T_c$. Pour les mesures pompe-sonde, deux études ont été réalisées avec deux résolutions temporelles différentes de 75 ps et 15 ps, respectivement. Dans les deux cas, l'excitation laser a déclenché des changements distincts sur la structure du réseau ("splitting" du pic de Bragg) liés à la transition de phase structurale. La position et les intensités des pics de diffraction ont montré des changements similaires à ceux observés à l'équilibre thermique avec

des échelles de temps temporelles qui indiquaient la diffusion thermique comme le principal mécanisme derrière la dynamique structurelle. Il est intéressant de noter que les changements de la largeur du pic ont présenté le comportement opposé, un élargissement qui ne pouvait pas être simplement expliqué par l'augmentation de la température du réseau, mais qui indiquait plutôt un effet d'hystérésis ou un désordre photoinduit. Au vu de ces résultats, nous proposons des études avec des résolutions temporelles plus courtes pour s'assurer que la transition de phase photoinduite suit une voie différente de la transition de phase à l'équilibre thermique. D'autres techniques en temps résolu, comme la réflectivité pompe-sonde, sont recommandées pour compléter les données de diffraction.

Bibliography

[1] M. Planck. *Über irreversible Strahlungsvorgänge. Sitzungsberichte der Königlich Preussischen Akademie der Wissenschaften zu Berlin.*, volume Jan-Juni 1899, p.479-480 (1899).

[2] L. Xu, W. W. Zhang and S. R. Nagel. *Drop Splashing on a Dry Smooth Surface*. Phys. Rev. Lett. 94, 184505 (2005).

[3] G. Mourou and S. Williamson. *Picosecond electron diffraction*. Appl. Phys. Lett. 41, 44 (1982).

[4] A. A. Ischenko, V. V. Golubkov, V. P. Spiridonov, A. V. Zgurskii, A. S. Akhmanov, M. G. Vabischevich and V. N. Bagratashvili. *A stroboscopical gas-electron diffraction method for the investigation of short-lived molecular species*. Appl. Phys. B 32, 161 (1983).

[5] A. H. Zewail. *Femtochemistry: Atomic-Scale Dynamics of the Chemical Bond Using Ultrafast Lasers (Nobel Lecture)*. Angewandte Chemie International Edition 39, 2586 (2000).

[6] A. H. Zewail and J. M. Thomas. *4D electron microscopy* (Imperial College Press, London, 2009).

[7] G. Sciaini and R. J. D. Miller. *Femtosecond electron diffraction: heralding the era of atomically resolved dynamics*. Rep. Prog. Phys. 74, 96101 (2011).

[8] R. J. D. Miller. *Femtosecond crystallography with ultrabright electrons and X-rays: capturing chemistry in action*. Science 343, 1108 (2014).

[9] M. M. MURNANE, H. C. KAPTEYN, M. D. ROSEN and R. W. FALCONE. *Ultrafast X-ray Pulses from Laser-Produced Plasmas*. Science 251, 531 (1991).

[10] C. Rischel, A. Rousse, I. Uschmann, P. A. Albouy, J. P. Geindre, P. Audebert, J. C. Gauthier, E. Forster, J. L. Martin and A. Antonetti. *Femtosecond time-resolved X-ray diffraction from laser-heated organic films*. Nature 390, 490 (1997).

[11] A. Rousse, C. Rischel, S. Fourmaux, I. Uschmann, S. Sebban, G. Grillon, P. Balcou, E. Förster, J. P. Geindre, P. Audebert, J. C. Gauthier and D. Hulin. *Non-thermal melting in semiconductors measured at femtosecond resolution.* Nature 410, 65 (2001).

[12] A. A. Zholents and M. S. Zolotorev. *Femtosecond X-ray pulses of synchrotron radiation*. Phys. Rev. Lett. 76, 912 (1996).

[13] R. W. Schoenlein, S. Chattopadhyay, H. H. W. Chong, T. E. Glover, C. V. Shank, A. A. Zholents and M. S. Zolotorev. *Generation of Femtosecond Pulse of Synchrotron Radiation*. Science 287, 2237 (2000).

[14] M. Harmand, R. Coffee, M. R. Bionta, M. Chollet, D. French, D. Zhu, D. M. Fritz, H. T. Lemke, N. Medvedev, B. Ziaja, S. Toleikis and M. Cammarata. *Achieving few-femtosecond time-sorting at hard X-ray free-electron lasers*. Nat. Photonics 7, 215 (2013).

[15] K. Sokolowski-Tinten, C. Blome, J. Blums, A. Cavalleri, C. Dietrich, A. Tarasevitch, I. Uschmann, E. Förster, M. Kammler, M. Horn-von Hoegen and D. Von Der Linde. *Femtosecond X-ray measurement of coherent lattice vibrations near the Lindemann stability limit.* Nature 422, 287 (2003).

[16] S. L. Johnson, P. Beaud, C. J. Milne, F. S. Krasniqi, E. S. Zijlstra, M. E. Garcia, M. Kaiser, D. Grolimund, R. Abela and G. Ingold. *Nanoscale depth-resolved coherent femtosecond motion in laser-excited bismuth.* Phys. Rev. Lett. 100, 155501 (2008).

[17] C. Rose-Petruck, R. Jimenez, T. Guo, A. Cavalleri, C. W. Siders, F. Ráksi, J. A. Squier, B. C. Walker, K. R. Wilson and C. P. Barty. *Picosecond-milliangstrom lattice dynamics measured by ultrafast X-ray diffraction*. Nature 398, 310 (1999).

[18] M. Harb, A. Jurgilaitis, H. Enquist, R. Nüske, C. V. Schmising, J. Gaudin, S. L. Johnson, C. J. Milne, P. Beaud, E. Vorobeva, A. Caviezel, S. O. Mariager, G. Ingold and J. Larsson. *Picosecond dynamics of laser-induced strain in graphite*. Phys. Rev. B 84, 045435 (2011).

[19] A. Cavalleri, C. Tóth, C. W. Siders, J. A. Squier, F. Ráksi, P. Forget and J. C. Kieffer. *Femtosecond Structural Dynamics in* VO_2 *during an Ultrafast Solid-Solid Phase Transition*. Phys. Rev. Lett. 87, 237401 (2001).

[20] P. Baum, D. S. Yang and A. H. Zewail. *4D visualization of transitional structures in phase transformations by electron diffraction*. Science 318, 788 (2007).

[21] V. R. Morrison, R. P. Chatelain, K. L. Tiwari, A. Hendaoui, A. Bruhács, M. Chaker and B. J. Siwick. *A photoinduced metal-like phase of monoclinic* VO_2 *revealed by ultrafast electron diffraction*. Science 346, 445 (2014).

[22] T. Huber, S. O. Mariager, A. Ferrer, H. Schäfer, J. A. Johnson, S. Grübel, A. Lübcke, L. Huber, T. Kubacka, C. Dornes, C. Laulhe, S. Ravy, G. Ingold, P. Beaud, J. Demsar and S. L. Johnson. *Coherent Structural Dynamics of a Prototypical Charge-Density-Wave-to-Metal Transition*. Phys. Rev. Lett. 113, 026401 (2014).

[23] M. Eichberger, H. Schäfer, M. Krumova, M. Beyer, J. Demsar, H. Berger, G. Moriena, G. Sciaini and R. J. D. Miller. *Snapshots of cooperative atomic motion in the optical suppression of charge density waves*. Nature 468, 799 (2010).

[24] C. Laulhé, T. Huber, G. Lantz, A. Ferrer, S. O. Mariager, S. Grübel, J. Rittmann, J. A. Johnson, V. Esposito, A. Lübcke, L. Huber, M. Kubli, M. Savoini, V. L. R. Jacques, L. Cario, B. Corraze, E. Janod, G. Ingold, P. Beaud, S. L. Johnson and S. Ravy. *Ultrafast Formation of a Charge Density Wave State in 1T-TaS_2 : Observation at Nanometer Scales Using Time-Resolved X-Ray Diffraction*. Phys. Rev. Lett. 118, 247401 (2017).

[25] C. W. Siders, A. Cavalleri, K. Sokolowski-Tinten, C. Tóth, T. Guo, M. Kammler, M. Horn Von Hoegen, K. R. Wilson, D. Von Der Linde and C. P. Barty. *Detection of nonthermal melting by ultrafast X-ray diffraction*. Science 286, 1340 (1999).

[26] B. J. Siwick, J. R. Dwyer, R. E. Jordan and R. J. D. Miller. *An Atomic-Level View of Melting Using Femtosecond Electron Diffraction*. Science 302, 1382 (2003).

[27] R. Ernstorfer, M. Harb, C. T. Hebeisen, G. Sciaini, T. Dartigalongue and R. J. D. Miller. *The formation of warm dense matter: Experimental evidence for electronic bond hardening in gold*. Science 323, 1033 (2009).

[28] G. Sciaini, M. Harb, S. G. Kruglik, T. Payer, C. T. Hebeisen, F. J. Z. Heringdorf, M. Yamaguchi, M. H. V. Hoegen, R. Ernstorfer and R. J. D. Miller. *Electronic acceleration of atomic motions and disordering in bismuth*. Nature 458, 56 (2009).

[29] M. Harb, W. Peng, G. Sciaini, C. T. Hebeisen, R. Ernstorfer, M. A. Eriksson, M. G. Lagally, S. G. Kruglik and R. J. D. Miller. *Excitation of longitudinal and transverse coherent acoustic phonons in nanometer free-standing films of (001) Si*. Phys. Rev. B 79, 094301 (2009).

[30] W. S. Lee, Y. D. Chuang, R. G. Moore, Y. Zhu, L. Patthey, M. Trigo, D. H. Lu, P. S. Kirchmann, O. Krupin, M. Yi, M. Langner, N. Huse, J. S. Robinson, Y. Chen, S. Y. Zhou, G. Coslovich, B. Huber, D. A. Reis, R. A. Kaindl, R. W. Schoenlein, D. Doering, P. Denes, W. F. Schlotter, J. J. Turner, S. L. Johnson, M. Först, T. Sasagawa, Y. F. Kung, A. P. Sorini, A. F. Kemper, B. Moritz, T. P. Devereaux, D. H. Lee, Z. X. Shen and Z. Hussain. *Phase fluctuations and the absence of topological defects in a photo-excited charge-ordered nickelate*. Nat. Commun. 3, 838 (2012).

[31] N. Erasmus, M. Eichberger, K. Haupt, I. Boshoff, G. Kassier, R. Birmurske, H. Berger, J. Demsar and H. Schwoerer. *Ultrafast Dynamics of Charge Density Waves in* $4H_b$−$TaSe_2$ *Probed by Femtosecond Electron Diffraction*. Phys. Rev. Lett. 109, 167402 (2012).

[32] T. R. T. Han, F. Zhou, C. D. Malliakas, P. M. Duxbury, S. D. Mahanti, M. G. Kanatzidis and C. Y. Ruan. *Exploration of metastability and hidden phases in correlated electron crystals visualized by femtosecond optical doping and electron crystallography*. Sci. Adv. 1, 5 (2015).

[33] L. Wei, S. Sun, C. Guo, Z. Li, K. Sun, Y. Liu, W. Lu, Y. Sun, H. Tian, H. Yang and J. Li. *Dynamic diffraction effects and coherent breathing oscillations in ultrafast electron diffraction in layered 1T-TaSeTe*. Struct. Dyn. 4, 044012 (2017).

[34] S. Vogelgesang, G. Storeck, J. G. Horstmann, T. Diekmann, M. Sivis, S. Schramm, K. Rossnagel, S. Schäfer and C. Ropers. *Phase ordering of charge density waves traced by ultrafast low-energy electron diffraction*. Nat. Phys. 14, 184 (2017).

[35] A. Zong, X. Shen, A. Kogar, L. Ye, C. Marks, D. Chowdhury, T. Rohwer, B. Freelon, S. Weathersby, R. Li, J. Yang, J. Checkelsky, X. Wang and N. Gedik. *Ultrafast manipulation of mirror domain walls in a charge density wave*. Sci. Adv. 4, 10 (2018).

[36] A. Zong, A. Kogar, Y. Q. Bie, T. Rohwer, C. Lee, E. Baldini, E. Ergeçen, M. B. Yilmaz, B. Freelon, E. J. Sie, H. Zhou, J. Straquadine, P. Walmsley, P. E. Dolgirev, A. V. Rozhkov, I. R. Fisher, P. Jarillo-Herrero, B. V. Fine and N. Gedik. *Evidence for topological defects in a photoinduced phase transition*. Nat. Phys. 15, 27 (2019).

[37] M. Trigo, M. E. Kozina, T. Henighan, M. P. Jiang, H. Liu, J. N. Clark, M. Chollet, J. M. Glownia, D. Zhu, T. Katayama, D. Leuenberger, P. S. Kirchmann, I. R. Fisher, Z. X. Shen and D. A. Reis. *Coherent order parameter dynamics in $SmTe_3$*. Phys. Rev. B 99, 104111 (2019).

[38] A. Zong, P. E. Dolgirev, A. Kogar, E. Ergeçen, M. B. Yilmaz, Y.-Q. Bie, T. Rohwer, I.-C. Tung, J. Straquadine, X. Wang, Y. Yang, X. Shen, R. Li, J. Yang, S. Park, M. C. Hoffmann, B. K. Ofori-Okai, M. E. Kozina, H. Wen, X. Wang, I. R. Fisher, P. Jarillo-Herrero and N. Gedik. *Dynamical Slowing-Down in an Ultrafast Photoinduced Phase Transition*. Phys. Rev. Lett. 123, 97601 (2019).

[39] A. Kogar, A. Zong, P. E. Dolgirev, X. Shen, J. Straquadine, Y.-Q. Bie, X. Wang, T. Rohwer, I.-C. Tung, Y. Yang, R. Li, J. Yang, S. Weathersby, S. Park, M. E. Kozina, E. J. Sie, H. Wen, P. Jarillo-Herrero, I. R. Fisher, X. Wang and N. Gedik. *Light-Induced Charge Density Wave in $LaTe_3$*. arXiv:1904.07472 (2019).

[40] F. Zhou, J. Williams, C. D. Malliakas, M. G. Kanatzidis and A. F. Kemper. *Nonequilibrium dynamics of spontaneous symmetry breaking into a hidden state of charge-density wave*. arXiv:1904.07120 (2019).

[41] R. E. Franklin and R. G. Gosling. *Molecular configuration in sodium thymonucleate*. Nature 171, 740 (1953).

[42] G. Thomson. *The early history of electron diffraction*. Contemp. Phys. 9, 1 (1968).

[43] C. Kittel. *Introduction to Solid State Physics* (Wiley, 2004), 8th edition.

[44] J. Als-Nielsen and D. McMorrow. *Elements of Modern X-ray Physics* (John Wiley & Sons, Ltd, 2011).

[45] S. Ravy. *Lecture notes: "Structure de la matière condensée"* (2015-2016).

[46] L. Reimer and H. Kohl. *Transmission electron microscopy* (Springer Series in Optical Sciences, New York, 2008).

[47] B. Fultz and J. Howe. *Transmission electron microscopy and diffractometry of materials* (Springer Series in Graduate Texts in Physics, Berlin, Heidelberg, 2013).

[48] K. Nasu. *Photoinduced Phase Transitions* (WORLD SCIENTIFIC, 2004).

[49] W. Bragg. *X-rays and Crystals*. Nature 90, 219 (1912).

[50] W. Bragg. *X-rays and Crystals*. Nature 90, 360 (1912).

[51] E. Maslen, A. Fox and M. O'Keefe. *X-ray scattering*. International Tables of Crystallography C, 6.1.1., 554 (2006).

[52] B. Warren. *X-ray Diffraction*. Addison-Wesley series in metallurgy and materials (Addison-Wesley, 1969).

[53] R. M. Nicklow and R. A. Young. *Lattice Vibrations in Aluminum and the Temperature Dependence of X-Ray Bragg Intensities*. Phys. Rev. 152, 591 (1966).

[54] D. Delille, R. Pantel and E. Van Cappellen. *Crystal thickness and extinction distance determination using energy filtered CBED pattern intensity measurement and dynamical diffraction theory fitting*. Ultramicroscopy 87, 5 (2001).

[55] P. M. Kelly, A. Jostsons, R. G. Blake and J. G. Napier. *The determination of foil thickness by scanning transmission electron microscopy*. Phys. Stat. Sol. (a) 31, 771 (1975).

[56] F. S. Allen. *Foil thickness measurements from convergent-beam diffraction patters. an experimental assessment of errors.* Phil. Mag. A 43, 325 (1981).

[57] S. I. Anisimov, B. L. Kapeliovich and T. L. Perel'man. *Electron emission from metal surfaces exposed to ultrashort laser pulses*. Sov. Phys. -JETP 39, 375 (1974).

[58] R. W. Schoenlein, W. Z. Lin, J. G. Fujimoto and G. L. Eesley. *Femtosecond studies of nonequilibrium electronic processes in metals*. Phys. Rev. Lett. 58, 1680 (1987).

[59] H. E. Elsayed-Ali, T. B. Norris, M. A. Pessot and G. A. Mourou. *Time-resolved observation of electron-phonon relaxation in copper*. Phys. Rev. Lett. 58, 1212 (1987).

[60] E. Beaurepaire, J.-C. Merle, A. Daunois and J.-Y. Bigot. *Ultrafast Spin Dynamics in Ferromagnetic Nickel*. Phys. Rev. Lett. 76, 4250 (1996).

[61] L. Perfetti, P. A. Loukakos, M. Lisowski, U. Bovensiepen, H. Eisaki and M. Wolf. *Ultrafast Electron Relaxation in Superconducting* $Bi_2Sr_2CaCu_2O_{8+\delta}$ *by Time-Resolved Photoelectron Spectroscopy*. Phys. Rev. Lett. 99, 197001 (2007).

[62] D. Leuenberger, J. A. Sobota, S. Yang, A. F. Kemper, R. G. Moore, I. R. Fisher, P. S. Kirchmann, T. P. Devereaux and Z. Shen. *Classification of collective modes in a charge density wave by momentum-dependent modulation of the electronic band structure*. Phys. Rev. B 91, 201106(R) (2015).

[63] D. C. Joy, J. I. Goldstein and A. D. Romig, editors. *Principles of Analytical Electron Microscopy* (Springer Sci. Media New York, 1986).

[64] R. Henderson. *The potential and limitations of neutrons, electrons and X-rays for atomic resolution microscopy of unstained biological molecules*. Q. Rev. Biophys. 28, 171–193 (1995).

[65] C. Hauf, A.-A. Hernandez Salvador, M. Holtz, M. Woerner and T. Elsaesser. *Phonon driven charge dynamics in polycrystalline acetylsalicylic acid mapped by ultrafast X-ray diffraction*. Struct. Dyn. 6, 014503 (2019).

[66] *FXE Instrument Parameters for Early User Operation* . https://www.xfel.eu/sites/sites_custom/site_xfel/content/e35165/e46561/e46879/e59227/e59229/xfel_file59230/FXE-Poster2017-01-16_eng.pdf. Accessed: 2019-09-30.

[67] C. Thomsen, H. T. Grahn, H. J. Maris and J. Tauc. *Surface generation and detection of phonons by picosecond light pulses*. Phys. Rev. B 34, 4129 (1986).

[68] R. P. Chatelain, V. R. Morrison, B. L. M. Klarenaar and B. J. Siwick. *Coherent and Incoherent Electron-Phonon Coupling in Graphite Observed with Radio-Frequency Compressed Ultrafast Electron Diffraction*. Phys. Rev. Lett. 113, 235502 (2014).

[69] G. Sciaini, M. Harb, S. G. Kruglik, T. Payer, C. T. Hebeisen, F. M. Heringdorf, M. Yamagushi, M. H. Hoegen, R. Ernstorfer and R. J. D. Miller. *Electronic acceleration of atomic motions and disordering in bismuth*. Nature 458, 458 (2009).

[70] T. van Oudheusden. *Electron source for subrelativistic single-shot femtosecond diffraction*. Ph.D. thesis, Eindhoven:Technische Universiteit Eindhoven (2010).

[71] *Eksma optics*. https://eksmaoptics.com/out/media/Femtokit.pdf.

[72] D. H. Dowell and J. F. Schmerge. *Quantum efficiency and thermal emittance of metal photocathodes*. Phys. Rev. Spec. Top. - Accel. Beams 12, 074201 (2009).

[73] M. Aidelsburger, F. O. Kirchner, F. Krausz and P. Baum. *Single-electron pulses for ultrafast diffraction*. Proc. Natl. Acad. Sci. 107, 19714 (2010).

[74] S. B. van der Geer and M. J. de Loos. *Pulsar Physics and the General Particle Tracer (GPT) code*. http://www.pulsar.nl/gpt.

[75] T. Van Oudheusden, E. F. De Jong, S. B. Van Der Geer, W. P. Op 't Root, O. J. Luiten and B. J. Siwick. *Electron source concept for single-shot sub-100 fs electron diffraction in the 100 keV range*. J. Appl. Phys. 102, 093501 (2007).

[76] S. Humphreis Jr. *Charged particle beams* (Wiley, 1990).

[77] C. Gerbig, A. Senftleben, S. Morgenstern, C. Sarpe and T. Baumert. *Spatio-temporal resolution studies on a highly compact ultrafast electron diffractometer*. New J. Phys. 17, 43050 (2015).

[78] A. Gahlmann, S. Tae Park and A. H. Zewail. *Ultrashort electron pulses for diffraction, crystallography and microscopy: Theoretical and experimental resolutions*. Phys. Chem. Chem. Phys. 10, 2894 (2008).

[79] J. L. Wiza. *Michrochannel plate detectors*. Nucl. Instrum. Meth. 162, 587 (1979).

[80] J. G. Timothy. *Photon-Counting Detector Arrays Based on Microchannel Array Plates* (Springer, 1975).

[81] H. Park, Z. Hao, X. Wang, S. Nie, R. Clinite and J. Cao. *Synchronization of femtosecond laser and electron pulses with subpicosecond precision*. Rev. Sci. Instrum. 76, 083905 (2005).

[82] J. R. Dwyer, C. T. Hebeisen, R. Ernstorfer, M. Harb, V. B. Deyirmenjian, R. E. Jordan and R. J. D. Miller. *Femtosecond electron diffraction: 'Making the molecular movie'*. Philos. Trans. R. Soc. A Math. Phys. Eng. Sci. 364, 741 (2006).

[83] *Soleil beamlines: Cristal*. https://www.synchrotron-soleil.fr/en/beamlines/cristal.

[84] M. Gao, C. Lu, H. Jean-Ruel, L. C. Liu, A. Marx, K. Onda, S. Koshihara, Y. Nakano, X. Shao, T. Hiramatsu, G. Saito, H. Yamochi, R. R. Cooney, G. Moriena, G. Sciaini and R. J. D. Miller. *Mapping molecular motions leading to charge delocalization with ultrabright electrons*. Nature 496, 343 (2013).

[85] M. Harb, R. Ernstorfer, T. Dartigalongue, C. T. Hebeisen, R. E. Jordan and R. J. D. Miller. *Carrier relaxation and lattice heating dynamics in silicon revealed by femtosecond electron diffraction*. J. Phys. Chem. B 110, 25308 (2006).

[86] S. Lahme, C. Kealhofer, F. Krausz and P. Baum. *Femtosecond single-electron diffraction*. Struc. Dynam. 1, 034303 (2014).

[87] S. Schäfer, W. Liang and A. H. Zewail. *Structural dynamics of surfaces by ultrafast electron crystallography: Experimental and multiple scattering theory*. J. Chem. Phys. 135, 214201 (2011).

[88] *Silicon electronic structure*. https://warwick.ac.uk/fac/sci/physics/current/postgraduate/regs/mpagswarwick/ex5/bandstructure.

[89] S. Jeong, H. Zacharias and J. Bokor. *Ultrafast carrier dynamics on the Si(100)2×1 surface*. Phys. Rev. B 54, R17300 (1996).

[90] C. V. Shank, R. Yen and C. Hirlimann. *Time resolved reflectivity measurements of femtosecond-optical-pulse-induced phase transitions in silicon*. Phys. Rev. Lett. 50, 454 (1983).

[91] K. G. Svantesson and N. G. Nilsson. *The temperature dependence of the Auger recombination coefficient of undoped silicon*. J. Phys. C Solid State Phys. 12, 5111 (1979).

[92] X. Gonze, B. Amadon, P. Anglade, J. Beuken, F. Bottin, P. Boulanger, F. Bruneval, D. Caliste, R. Caracas, M. Côté, T. Deutsch, L. Genovese, P. Ghosez, M. Giantomassi, S. Goedecker, D. Hamann, P. Hermet, F. Jollet, G. Jomard, S. Leroux, M. Mancini, S. Mazevet, M. Oliveira, G. Onida, Y. Pouillon, T. Rangel, G.-M. Rignanese, D. Sangalli, R. Shaltaf, M. Torrent, M. Verstraete, G. Zerah and J. Zwanziger. *Abinit: First-principles approach to material and nanosystem properties*. Comp. Phys. Commu. 180, 2582 (2009).

[93] B. Arnaud, S. Lebègue and M. Alouani. *Excitonic and quasiparticle lifetime effects on silicon electron energy loss spectra from first principles*. Phys. Rev. B 71, 035308 (2005).

[94] J. Dziewior and W. Schmid. *Auger coefficients for highly doped and highly excited silicon*. Appl. Phys. Lett. 31, 346 (1977).

[95] M. Harb. *Investigating Photoinduced Structural Changes in Si using Femtosecond Electron Diffraction*. Ph.D. thesis, University of Toronto (2009).

[96] Y. Okada and Y. Tokumaru. *Precise determination of lattice parameter and thermal expansion coefficient of silicon between 300 and 1500 K*. J. Appl. Phys. 56, 314 (1984).

[97] J. Morniroli, M. Nó, P. Rodríguez, J. S. Juan, E. Jezierska, N. Michel, S. Poulat and L. Priester". *CBED and LACBED: characterization of antiphase boundaries*. Ultramicroscopy 98, 9 (2003).

[98] A. Howie and M. J. Whelan. *Diffraction contrast of electron microscope images of crystal lattice defects - II. The development of a dynamical theory*. Proc. R. Soc. Lond. A 263, 217 (1961).

[99] P. A. Stadelmann. *JEMS-EMS java version* (2004).

[100] A. Howie and U. Valdrè. *Temperature dependence of the extinction distance in electron diffraction*. Philos. Mag. 15, 777 (1967).

[101] S. Takagi. *On the Temperature Diffuse Scattering of Electrons I. Derivation of General Formulae*. J. Phys. Soc. Japan 13, 278 (1958).

[102] J. P. Morniroli. *Large-Angle Convergent-Beam Electron Diffraction Applications to Crystal Defects* (Société Française des Microscopies, New York, 2002).

[103] A. Feist, N. Rubiano da Silva, W. Liang, C. Ropers and S. Schäfer. *Nanoscale diffractive probing of strain dynamics in ultrafast transmission electron microscopy*. Struct. Dyn. 5, 014302 (2018).

[104] R. E. Peierls. *Quantum Theory of Solids* (Oxford classic texts in the physical sciences, 1955).

[105] K. Rossnagel. *On the origin of charge-density waves in select layered transition-metal dichalcogenides*. J. Phys.: Cond. Matt. 23, 213001 (2011).

[106] N. Ru and I. R. Fisher. *Thermodynamic and transport properties of YTe_3 , $LaTe_3$, and $CeTe_3$* . Phys. Rev. B 73, 3 (2006).

[107] V. Brouet, W. L. Yang, X. J. Zhou, Z. Hussain, N. Ru, K. Y. Shin, I. R. Fisher and Z. X. Shen. *Fermi Surface Reconstruction in the CDW State of* $CeTe_3$ *Observed by Photoemission*. Phys. Rev. Lett. 93, 126405 (2004).

[108] R. G. Moore, W. S. Lee, P. S. Kirchman, Y. D. Chuang, A. F. Kemper, M. Trigo, L. Patthey, D. H. Lu, O. Krupin, M. Yi, D. A. Reis, D. Doering, P. Denes, W. F. Schlotter, J. J. Turner, G. Hays, P. Hering, T. Benson, J. H. Chu, T. P. Devereaux, I. R. Fisher, Z. Hussain and Z. X. Shen. *Ultrafast resonant soft X-ray diffraction dynamics of the charge density wave in $TbTe_3$*. Phys. Rev. B 93, 024304 (2016).

[109] N. Ru, C. L. Condron, G. Y. Margulis, K. Y. Shin, J. Laverock, S. B. Dugdale, M. F. Toney and I. R. Fisher. *Effect of chemical pressure on the charge density wave transition in rare-earth tritellurides RTe_3*. Phys. Rev. B 77, 035114 (2008).

[110] G. Grüner. *The dynamics of charge-density waves*. Rev. Mod. Phys. 60, 1129 (1988).

[111] S. Van Smaalen. *The Peierls transition in low-dimensional electronic crystals*. Acta Crystallogr. Sect. A Found. Crystallogr. 61, 51 (2005).

[112] P. Monceau. *Electronic crystals: an experimental overview*. Adv. Phys. 61, 325 (2012).

[113] G. Grüner. *Density waves in solids* (Adison Wesley, 1994).

[114] L. Gor'kov and G. Grüner. *Charge density waves in solids* (Elsevier Science Publishers B.V., 1989).

[115] S. Kagoshima, H. Nagasawa and T. Sambongi. *One-Dimensional Conductors* (Springer Series in Solid-State Sciences, 1982).

[116] V. Jacques. *Application de la diffraction coherente des rayons X a l'etude de defauts topologiques dans les structures atomiques et electroniques.* Ph.D. thesis, Université Paris Sud (2009).

[117] M. D. Johannes and I. I. Mazin. *Fermi surface nesting and the origin of charge density waves in metals*. Phys. Rev. B 77, 165135 (2008).

[118] S. Chan and V. Heine. *Spin density wave and soft phonon mode from nesting Fermi surfaces*. J. Phys. F: Met. Phys. 3, 795 (1973).

[119] W. Kohn. *Image of the Fermi Surface in the Vibration Spectrum of a Metal*. Phys. Rev. Lett. 2, 393 (1959).

[120] G. F. Giuliani and A. W. Overhauser. *Structure factor of a charge-density wave*. Phys. Rev. B 23, 3737 (1971).

[121] A. W. Overhauser. *Observability of Charge-Density Waves by Neutron Diffraction*. Phys. Rev. B 3, 3173 (1971).

[122] N. Ru. *Charge density wave formation in rare-earth tritellurides*. Ph.D. thesis, Stanford University (2008).

[123] C. Malliakas, S. J. L. Billinge, H. J. Kim and M. G. Kanatzidis. *Square Nets of Tellurium: Rare-Earth Dependent Variation in the Charge-Density Wave of $RETe_3$ (RE = Rare-Earth Element)*. J. Am. Chem. Soc. 127, 6510 (2005).

[124] K. Momma and F. Izumi. *Vesta: a three-dimensional visualization system for electronic and structural analysis*. J. Appl. Crystallogr. 41, 653 (2008).

[125] C. D. Malliakas and M. G. Kanatzidis. *Divergence in the Behavior of the Charge Density Wave in $RETe_3$ (RE = Rare-Earth Element) with Temperature and RE Element*. J. Am. Chem. Soc. 128, 12612 (2006).

[126] V. Brouet, W. L. Yang, X. J. Zhou, Z. Hussain, R. G. Moore, R. He, D. H. Lu, Z. X. Shen, J. Laverock, S. B. Dugdale, N. Ru and I. R. Fisher. *Angle-resolved photoemission study of the evolution of band structure and charge density wave properties in RTe_3 (R = Y, La, Ce, Sm, Gd, Tb, and Dy)*. Phys. Rev. B 77, 235104 (2008).

[127] G.-H. Gweon, J. D. Denlinger, J. A. Clack, J. W. Allen, C. G. Olson, E. DiMasi, M. C. Aronson, B. Foran and S. Lee. *Direct Observation of Complete Fermi Surface, Imperfect Nesting, and Gap Anisotropy in the High-Temperature Incommensurate Charge-Density-Wave Compound* $SmTe_3$. Phys. Rev. Lett. 81, 886 (1998).

[128] J. Laverock, S. B. Dugdale, Z. Major, M. A. Alam, N. Ru, I. R. Fisher, G. Santi and E. Bruno. *Fermi surface nesting and charge-density wave formation in rare-earth tritellurides*. Phys. Rev. B 71, 085114 (2005).

[129] F. Schmitt, P. S. Kirchmann, U. Bovensiepen, R. G. Moore, M. K. L. Rettig, J.-H. Chu, N. Ru, L. Perfetti, D. H. Lu, M. Wolf, I. R. Fisher and Z.-X. Shen. *Transient Electronic Structure and Melting of a Charge Density Wave in $TbTe_3$*. Science 321, 1649 (2008).

[130] E. DiMasi, M. C. Aronson, J. F. Mansfield, B. Foran and S. Lee. *Chemical pressure and charge-density waves in rare-earth tritellurides*. Phys. Rev. B 52, 14516 (1995).

[131] F. Schmitt, P. S. Kirchmann, U. Bovensiepen, R. G. Moore, J. H. Chu, D. H. Lu, L. Rettig, M. Wolf, I. R. Fisher and Z. X. Shen. *Ultrafast electron dynamics in the charge density wave material $TbTe_3$*. New J. Phys. 13, 063022 (2011).

[132] L. Rettig, R. Cortés, J. H. Chu, I. R. Fisher, F. Schmitt, R. G. Moore, Z. X. Shen, P. S. Kirchmann, M. Wolf and U. Bovensiepen. *Persistent order due to transiently enhanced nesting in an electronically excited charge density wave*. Nat. Commun. 7, 10459 (2016).

[133] R. Y. Chen, B. F. Hu, T. Dong and N. L. Wang. *Revealing multiple charge-density-wave orders in $TbTe_3$ by optical conductivity and ultrafast pump-probe experiments*. Phys. Rev. B 89, 075114 (2014).

[134] R. V. Yusupov, T. Mertelj, J.-H. Chu, I. R. Fisher and D. Mihailovic. *Single-Particle and Collective Mode Couplings Associated with 1- and 2-Directional Electronic Ordering in Metallic RTe_3 (R = Ho, Dy, Tb)*. Phys. Rev. Lett. 101, 246402 (2008).

[135] R. Yusupov, T. Mertelj, V. V. Kabanov, S. Brazovskii, P. Kusar, J. H. Chu, I. R. Fisher and D. Mihailovic. *Coherent dynamics of macroscopic electronic order through a symmetry breaking transition*. Nat. Phys. 6, 681 (2010).

[136] M. Scheffer, J. Bascompte, W. A. Brock, V. Brovkin, S. R. Carpenter, V. Dakos, H. Held, E. H. Van Nes, M. Rietkerk and G. Sugihara. *Early-warning signals for critical transitions*. Nature 461, 53 (2009).

[137] C. Diks, C. Hommes and J. Wang. *Critical slowing down as an early warning signal for financial crises?* Empir. Econ. 57, 1201 (2018).

[138] V. Dakos, M. Scheffer, E. H. Van Nes, V. Brovkin, V. Petoukhov and H. Held. *Slowing down as an early warning signal for abrupt climate change*. Proc. Natl. Acad. Sci. 105, 14308 (2008).

[139] A. J. Veraart, E. J. Faassen, V. Dakos, E. H. Van Nes, M. Lürling and M. Scheffer. *Recovery rates reflect distance to a tipping point in a living system*. Nature 481, 357 (2012).

[140] I. A. Van De Leemput, M. Wichers, A. O. Cramer, D. Borsboom, F. Tuerlinckx, P. Kuppens, E. H. Van Nes, W. Viechtbauer, E. J. Giltay, S. H. Aggen, C. Derom, N. Jacobs, K. S. Kendler, H. L. Van Der Maas, M. C. Neale, F. Peeters, E. Thiery, P. Zachar and M. Scheffer. *Critical slowing down as early warning for the onset and termination of depression*. Proc. Natl. Acad. Sci. 111, 87 (2014).

[141] T.-R. T. Han, Z. Tao, S. D. Mahanti, K. Chang, C.-y. Ruan, C. D. Malliakas and M. G. Kanatzidis. *Structural dynamics of two-dimensional charge-density waves in $CeTe_3$ investigated by ultrafast electron crystallography*. Phys. Rev. B 86, 075145 (2012).

[142] A. A. Sinchenko, P. Lejay and P. Monceau. *Sliding charge-density wave in two-dimensional rare-earth tellurides*. Phys. Rev. B 85, 241104 (2012).

[143] *Diamond trim knifes, howpublished* = https://www.labtech-em.com/em/diamond-trim-knives, *note* = *Accessed: 2019-09-01*.

[144] *Diatome knifes, howpublished* = https://www.diatome.ch/, *note* = *Accessed: 2019-09-01*.

[145] A. Sacchetti, L. Degiorgi, T. Giamarchi, N. Ru and I. R. Fisher. *Chemical pressure and hidden one-dimensional behavior in rare-earth tri-telluride charge-density wave compounds*. Phys. Rev. B 74, 125115 (2006).

[146] V. Tinnemann, C. Streubühr, B. Hafke, A. Kalus, A. Hanisch-Blicharski, M. Ligges, P. Zhou, D. Von Der Linde, U. Bovensiepen and M. Horn-Von Hoegen. *Ultrafast electron diffraction from a Bi(111) surface: Impulsive lattice excitation and Debye-Waller analysis at large momentum transfer*. Struct. Dyn. 6, 035101 (2019).

[147] R. D. Horning and J.-L. Staudenmann. *The Debye–Waller factor for polyatomic solids. Relationships between X-ray and specific-heat Debye temperatures. The Debye–Einstein model*. Acta Cryst. A 44, 136 (1988).

[148] A. Banerjee, Y. Feng, D. M. Silevitch, J. Wang, J. C. Lang, H. H. Kuo, I. R. Fisher and T. F. Rosenbaum. *Charge transfer and multiple density waves in the rare earth tellurides*. Phys. Rev. B 87, 155131 (2013).

[149] D. J. Hilton. *Ultrafast pump-probe spectroscopy*. In *Optical Techniques for Solid-State Materials Characterization*, edited by R. P. Prasankumar and A. J. Taylor (CRC Press, 2011).

[150] V. V. Kabanov, J. Demsar, B. Podobnik and D. Mihailovic. *Quasiparticle relaxation dynamics in superconductors with different gap structures: Theory and experiments on* $YBa_2Cu_3O_{7-\delta}$. Phys. Rev. B 59, 1497 (1999).

[151] J. Demsar, K. Biljaković and D. Mihailovic. *Single Particle and Collective Excitations in the One-Dimensional Charge Density Wave Solid* $K_{0.3}MoO_3$ *Probed in Real Time by Femtosecond Spectroscopy*. Phys. Rev. Lett. 83, 800 (1999).

[152] H. Fukuyama and P. A. Lee. *Dynamics of the charge-density wave. I. Impurity pinning in a single chain*. Phys. Rev. B 17, 535 (1978).

[153] P. A. Lee and T. M. Rice. *Electric field depinning of charge density waves*. Phys. Rev. B 19, 3970 (1979).

[154] D. DiCarlo, R. E. Thorne, E. Sweetland, M. Sutton and J. D. Brock. *Charge-density-wave structure in* $NbSe_3$. Phys. Rev. B 50, 8288 (1994).

[155] M. Lavagnini, H.-M. Eiter, L. Tassini, B. Muschler, R. Hackl, R. Monnier, J.-H. Chu, I. R. Fisher and L. Degiorgi. *Raman scattering evidence for a cascade evolution of the charge-density-wave collective amplitude mode*. Phys. Rev. B 81, 081101 (2010).

[156] T. Mertelj, P. Kusar, V. V. Kabanov, P. Giraldo-Gallo, I. R. Fisher and D. Mihailovic. *Incoherent topological defect recombination dynamics in* $TbTe_3$. Phys. Rev. Lett. 110, 156401 (2013).

[157] D. Dew-Hughes. *Superconducting a-15 compounds: A review*. Cryogenics 15, 435 (1975).

[158] L. R. Testardi. *Structural instability an superconductivity in A-15 compounds*. Rev. Mod. Phys. 47, 637 (1975).

[159] G. R. Stewart. *Superconductivity in the A15 structure*. Physica C Supercond. 514, 28 (2015).

[160] G. Bilbro and W. L. McMillan. *Theoretical model of superconductivity and the martensitic transformation in A15 compounds*. Phys. Rev. B 14, 1887 (1976).

[161] R. N. Bhatt and W. L. McMillan. *Landau theory of the martensitic transition in A-15 compounds*. Phys. Rev. B 14, 1007 (1976).

[162] X. Yang, C. Vaswani, C. Sundahl, M. Mootz, P. Gagel, L. Luo, J. H. Kang, P. P. Orth, I. E. Perakis, C. B. Eom and J. Wang. *Terahertz-light quantum tuning of a metastable emergent phase hidden by superconductivity*. Nat. Mater. 17, 586 (2018).

[163] X. Yang, X. Zhao, C. Vaswani, C. Sundahl, B. Song, Y. Yao, D. Cheng, Z. Liu, P. P. Orth, M. Mootz, J. H. Kang, I. E. Perakis, C. Z. Wang, K. M. Ho, C. B. Eom and J. Wang. *Ultrafast nonthermal terahertz electrodynamics and possible quantum energy transfer in the Nb_3Sn superconductor*. Phys. Rev. B 99, 094504 (2019).

[164] R. Mailfert, B. W. Batterman and J. J. Hanak. *Observations Related to the Order of the Low Temperature Structural Transformation in V_3Si and Nb_3Sn*. Phys. Stat. Sol. (b) 32, K67 (1969).

[165] G. Shirane and D. J. Axe. *Neutron Scattering Study of the Lattice-Dynamical Phase Transition in Nb_3Sn*. Physcial Rev. B 4, 2957 (1971).

[166] L. J. Vieland, R. W. Cohen and W. Rehwald. *Evidence for a First-Order Structural Transformation in* Nb_3Sn. Phys. Rev. Lett. 26, 373 (1971).

[167] J. Labbe and J. Friedel. *Instabilite electronique et changement de phase cristalline des composes du type V_3Si a basse temperature*. J. Phys. France 27, 153 (1966).

[168] H. Tütüncü, H. Uzunok, G. Srivastava, V. Özdemir and G. Uğur. *The effect of martensitic phase transition from cubic to tetragonal on the physical properties of V_3Si superconductor*. Intermetallics 96, 25 (2018).

[169] M. Newville, T. Stensitzki, D. B. Allen and A. Ingargiola. *LMFIT: Non-Linear Least-Square Minimization and Curve-Fitting for Python* (2014).

List of Figures

List of Tables

université PARIS-SACLAY

ÉCOLE DOCTORALE
Physique en Île-de-France (EDPIF)

Titre : Études de la dynamique structurale des transitions de phase par diffraction des électrons et des rayons X résolue en temps.

Mots clés : Dynamique structurale, Diffraction résolue en temps, Transition de phase structurale, Onde de densité de charge

Résumé : L'application d'une perturbation externe à certains matériaux (tels que la température, la pression ou la lumière) provoque souvent l'émergence de nouvelles propriétés macroscopiques dont l'origine se situe au niveau atomique. Par conséquent, une étude détaillée de la dynamique atomique devient essentielle pour la compréhension de processus tels que les transformations chimiques ou les transitions de phase. Dans le cas particulier des transitions de phase structurales, la symétrie du cristal est soumise à une transformation entre deux états différents à une valeur critique. Les échelles de temps typiques de la dynamique structurale sont de l'ordre de quelques centaines de femtosecondes à plusieurs picosecondes. Le développement des impulsions laser femtoseconde a permis aux chercheurs d'accéder aux échelles de temps nécessaires pour explorer la dynamique structurale ultra-rapide. Plus précisément, la diffraction résolue en temps s'est révélée être une technique idéale pour suivre et dévoiler les voies hors équilibre suivies par le réseau après une courte impulsion laser. Cette thèse présente des études expérimentales réalisées par des techniques de diffraction d'électrons et de rayons X résolues en temps sur deux transitions de phase structurelles différentes. Dans une première partie, nous démontrons les capacités du montage expérimental de diffraction d'électrons ultra-rapide (DEU) développé au Laboratoire d'Optique Apliquée. Nos résultats expérimentaux réalisés sur des échantillons monocristallins de haute qualité sont présentés ainsi qu'une étude quantitative des implications des effets de diffraction dynamique dans les expériences DEU. Dans une deuxième partie, nous présentons un ensemble d'expériences de diffraction d'électrons pompe-sonde réalisée sur $GdTe_3$, un composé appartenant à la famille des tritellurides de terres rares qui présente un état d'onde de densité de charge. L'arrivée d'une excitation optique déclenche la transition de phase de manière non thermique. La dynamique de relaxation est caractérisé par un ralentissement qui augmente avec la fluence incidente ainsi qu'avec la température initiale de l'échantillon. Ces résultats éclairent les interprétations controversées actuelles concernant l'émergence de défauts topologiques photo-induits. Dans une troisième partie, nous présentons des expériences de diffraction des rayons X en temps résolu réalisées à la ligne CRISTAL du synchrotron SOLEIL. Dans ce cas, nous avons étudié le composé A15 Nb_3Sn, qui présente une transition de phase d'une symétrie cubique à une symétrie tétragonale à l'équilibre thermique. Les résultats de notre expérience pompe-sonde mettent en évidence une réponse différente du réseau par rapport à la transition d'équilibre thermique, ce qui encourage les futures recherches sur la dynamique structural de ce matériau.

Title : Study of the structural dynamics of phase transitions using time resolved electron and X-ray diffraction.

Keywords : Structural dynamics, Time-resolved diffraction, Structural phase transitions, Charge-density-wave materials

Abstract : The application of an external perturbation in certain materials (such as temperature, pressure or light) often gives rise to the emergence of new macroscopic properties with their origin at the atomic level. Therefore, a detailed study of the atomic dynamics becomes essential to the understanding of processes such as chemical transformations or phase transitions. In the particular case of structural phase transitions, the symmetry of the crystal undergoes a transformation between two different states at a given critical value. The typical time scales of the structural dynamics occur on the order of few hundreds of femtoseconds to several picoseconds. The development of femtosecond laser pulses has enabled scientists to access the required time scales to explore the ultrafast dynamics of the lattice structure in the relevant time scales. More precisely, time-resolved diffraction has proven to be an ideal technique to track and unveil the out-of-equilibrium pathways followed by the lattice after a short laser pulse. This thesis presents experimental studies performed by time-resolved electron and X-ray diffraction techniques on two different structural phase transitions. In a first part, we demonstrate the capabilities of the ultrafast electron diffraction (UED) experimental setup developed at Laboratoire d'Optique Apliquée. Our UED experimental results performed on high quality single crystal samples are presented along with a quantitative study of the implications of dynamical diffraction effects in UED experiments. In a second part, we present a set of pump-probe electron diffraction experiments performed on $GdTe_3$, a compound belonging to the rare-earth tritellurides family which presents a charge density wave state. The arrival of an optical excitation triggers the phase transition non-thermally with the out-of-equilibrium relaxation dynamics of the charge density wave state characterized by slowing down that increases with incident fluence as well as with initial sample temperature. These results shed more light on current controversial interpretations involving the emergence of photoinduced topological defects. In a third part, we present time resolved X-ray diffraction experiments performed at CRISTAL beamline at SOLEIL synchrotron. In this case we have studied the A15 compound Nb_3Sn, which displays a displacive phase transition evolving from cubic to tetragonal symmetry at thermal equilibrium. Our pump-probe results present evidence of a different lattice response with respect to the thermal equilibrium transition, encouraging future investigations on the dynamics of this material.

Université Paris-Saclay
Espace Technologique / Immeuble Discovery
Route de l'Orme aux Merisiers RD 128 / 91190 Saint-Aubin, France